



**HAL**  
open science

# Theoretical and experimental studies of the processability of ultra-high molecular weight polyethylene

Jing-Gang Gai

► **To cite this version:**

Jing-Gang Gai. Theoretical and experimental studies of the processability of ultra-high molecular weight polyethylene. Other. Institut National Polytechnique de Lorraine, 2009. English. NNT : 2009INPL039N . tel-01748912

**HAL Id: tel-01748912**

**<https://hal.univ-lorraine.fr/tel-01748912>**

Submitted on 29 Mar 2018

**HAL** is a multi-disciplinary open access archive for the deposit and dissemination of scientific research documents, whether they are published or not. The documents may come from teaching and research institutions in France or abroad, or from public or private research centers.

L'archive ouverte pluridisciplinaire **HAL**, est destinée au dépôt et à la diffusion de documents scientifiques de niveau recherche, publiés ou non, émanant des établissements d'enseignement et de recherche français ou étrangers, des laboratoires publics ou privés.



## AVERTISSEMENT

Ce document est le fruit d'un long travail approuvé par le jury de soutenance et mis à disposition de l'ensemble de la communauté universitaire élargie.

Il est soumis à la propriété intellectuelle de l'auteur. Ceci implique une obligation de citation et de référencement lors de l'utilisation de ce document.

D'autre part, toute contrefaçon, plagiat, reproduction illicite encourt une poursuite pénale.

Contact : [ddoc-theses-contact@univ-lorraine.fr](mailto:ddoc-theses-contact@univ-lorraine.fr)

## LIENS

Code de la Propriété Intellectuelle. articles L 122. 4

Code de la Propriété Intellectuelle. articles L 335.2- L 335.10

[http://www.cfcopies.com/V2/leg/leg\\_droi.php](http://www.cfcopies.com/V2/leg/leg_droi.php)

<http://www.culture.gouv.fr/culture/infos-pratiques/droits/protection.htm>

Nancy-Université  
INPL

en co-tutelle avec l'Université du Sichuan

Ecole Nationale Supérieure des  
Industries Chimiques  
(ENSIC)

Ecole Doctorale  
Ressources Procédés Produits Environnement  
(RP2E)

Laboratoire des Sciences  
du Génie Chimique  
(LSGC-CNRS UPR 6811)

# ETUDES THEORIQUES ET EXPERIMENTALES DE LA PROCESSABILITE DU POLYETHYLENE A ULTRA-HAUTE MASSE MOLAIRES

## THESE

présentée en vue de l'obtention du

DOCTORAT DE L'INSTITUT NATIONAL POLYTECHNIQUE DE LORRAINE

Spécialité : Génie des Procédés et des Produits

par

**Jing-Gang GAI**  
Master en Chimie Physique  
Université du Sichuan, Chengdu, Chine

*Soutenance prévue le 16 juillet 2009 à 9h*

### Composition du jury :

<i>Rapporteurs :</i>	M. Christian CARROT	Professeur (Université Jean Monnet de Saint-Etienne)
	M. Hong-Lai LIU	Professeur (East-China University of Science and Technology, Shanghai, Chine)
<i>Examinateurs :</i>	M. Guo-Hua HU	Professeur (Nancy-Université, INPL) et membre de l'IUF
	M. Hui-Lin LI	Professeur (Sichuan University, Chengdu, Chine)

# Abstract

Ultra-high molecular weight polyethylene (UHMWPE) has a number of outstanding properties. Its application, however, is limited due to its exceedingly high viscosity and its poor processability.

This work aims at improving the processability of UHMWPE by decreasing its viscosity upon retaining whenever possible its outstanding properties. The idea is to judiciously add a compound or a mixture of compounds to it. It is validated both experimentally and by dissipative particle dynamics (DPD) and MesoDyn theories. The main conclusions are as follows:

Adding HDPE or LDPE is much more efficient at disentangling the UHMWPE chains than PP. However, adding PP is much more efficient at reducing its viscosity than HDPE and LDPE, implying that when a normal molecular weight polymer (NMWP) is added, the formation of a lubricating layer between the UHMWPE particles leads to a significant decrease in viscosity. As the plasticating time increases, the viscosity of the UHMWPE/PP (50/50) blend decreases whereas that of the UHMWPE/LDPE (50/50) increases. This is because the former forms a two-phase structure while the latter a homogeneous one. Phase diagrams are constructed in order to quantitatively investigate the effects of the composition, the parameter  $\chi$  and the molecular weights on the lubricating phase and the viscosity of the blends. It is recommended that the optimum composition should be located in the critical sensitive region (CSR) of the blends at low shear rates, and above and close to the corresponding binodal curve at high shear rates. The phase diagram also shows that for a polymer blend with a given parameter  $\chi$ , both the corresponding binodal and spinodal curves shift downwards with increasing  $N_1$ , indicating that increasing the molecular weight of NMWP to a certain degree can promote the phase separation and improve the processability of blends. These results may be served as guidelines for other ultra-high molecular weight polymers.

Considering the remarkable viscosity reduction of the UHMWPE/PP blend, other

properties of the blend are also investigated by DPD. The results indicate that the UHMWPE/PP blend forms a homogeneous phase structure when the concentration of PP is below 10%; above that concentration, two-phase structures appear. In the latter cases, no UHMWPE is located in the PP-rich phase while a significant amount of PP is located in the UHMWPE-rich domains. This distribution favors disentanglement of UHMWPE molecules and prevents the viscosity increasing of the PP-rich phase. It is confirmed experimentally that the melt apparent viscosity of the UHMWPE/PP blend decreases with increasing PP content. Besides, for the UHMWPE/NMWPE/HMWPP/NMWPP blends with different compositions, both UHMWPE and HMWPP tend to be located in their own rich phases. The other normal molecular weight components (NMWPE and NMWPP) are not only located in their own rich phases but also in the interfaces. The physical reason of the accumulation of small chains might be attributed to the fact that small chains play a role of surfactant and reduces the interfacial tension. Moreover, an increase in the concentration of small chains significantly increases the interface thickness of the blend.

NMWP that improves the processability of UHMWPE may deteriorate some of its outstanding properties such as mechanical properties. The addition of a hybrid of PMM (PEG/MDAB/MMT) results in a good balance. WAXD analysis and TEM observation indicate the formation of exfoliated and intercalated structure for the UHMWPE/PP/PMM composites. The structure of PMM in the matrix is probably attributed to the effect of the complex intercalator (PEG/MDAB) on the intercalation and exfoliation of MMT. The addition of a small amount of PMM can significantly decrease the melt viscosity of UHMWPE/PP (90/10) blend. The magnitude of viscosity reduction increases with increasing PMM content. The UHMWPE nanocomposites exhibit remarkable improvement in mechanical properties such as tensile strength, elongation at break and yield strength compared with the matrix without clay. The dispersed PMM particles have a large two-dimensional aspect ratio, which plays an important role in enhancing mechanical properties of UHMWPE composites.

Both the SCFT and F-H theories are used to study a general binary *A/B* polymer

system. Results indicate that thermodynamic properties, such as free energy of mixing, interfacial tension and the interface thickness, are insensitive to  $N_B$  when  $N_B$  is large enough. Consider a polymer blend with  $N_A = 250$  and  $\chi = 0.009$ . When  $N_B > 6620$ , which corresponds to a molecular weight of  $1.4 \times 10^6$  for PE,  $C_R(N_B)$  (relative contribution of each part of interfacial tension) will be less than 1%, indicating that the effect of the variation of  $N_B$  on the interfacial tension of the blend may be neglected for  $N_B > 6620$ . This critical value of  $1.4 \times 10^6$  for PE is consistent with most reports in the literature. For the binary polymer systems with a given polymer A and a fixed value of  $\chi$ , exchange chemical potential curves all pass through a common point and the corresponding volume fraction is  $\phi_A = 1-1/e$  ( $\approx 0.63$ ), whatever the value of  $N_B$ , implying that the exchange chemical potentials at  $\phi_A = 1-1/e$  are independent of  $N_B$ . Moreover, as  $N_B$  decreases the minimum free energy of mixing monotonously decreases and  $\phi_{Am}$  asymptotically approaches  $\phi_A = 1-1/e$  if  $\chi N_A \neq 2.05$  or is located at  $\phi_A = 1-1/e$  if  $\chi N_A = 2.05$  and  $\chi N_B < 2.65$ . This indicates that  $\phi_{Am}$  for a polymer solution with a good solvent is close to  $1-1/e$ . It is also worth noting that  $\mu_c$  (exchange chemical potentials corresponding to the common points) is crucially dependent on the value of  $\chi N_A$ . More specifically, if  $\chi N_A$  is less than, equal to, or greater than 2.05, the corresponding  $\mu_c$  is positive, zero and negative, respectively.

## Résumé

Le polyéthylène à très haute masse molaire (UHMWPE) possède de nombreuses propriétés extraordinaires. Cependant, ses applications sont limitées en raison de sa très haute viscosité et de sa mauvaise processabilité.

Les travaux présentés dans ce mémoire de thèse ont pour objet d'améliorer la processabilité d'un UHMWPE par le biais de la diminution de sa viscosité tout en conservant autant que ce peut ses propriétés. L'idée est d'y ajouter un composé ou un mélange de composés. Elle est validée par des expériences et par les théories de la dynamique des particules dissipatives (DPD) et de MesoDyn. Les principales conclusions de ces travaux sont les suivantes :

Le polyéthylène haute densité (PEHD) ou le polyéthylène basse densité (PEBD) est plus efficace pour désenchevêtrer l'UHMWPE que le polypropylène (PP), tandis que le PP est plus efficace pour diminuer sa viscosité que le PEHD ou le PEBD. Cela signifie que l'ajout d'un polymère à masse molaire normale (NMWP) conduit à la formation d'une couche lubrifiante entre les particules UHMWPE. Elle est responsable de la très forte diminution de la viscosité de l'UHMWPE. Au fur et à mesure que le temps de plastification avance, la viscosité du mélange UHMWPE/PP (50/50) diminue alors que celle du mélange UHMWPE/PEBD augmente. Ceci est dû au fait que le premier mélange forme une structure biphasique alors que le deuxième mélange forme une structure homogène. Des diagrammes de phase ont été construits afin d'étudier quantitativement les influences de la composition du mélange, du paramètre d'interaction  $\chi$  ainsi que de la masse molaire de chacun des polymères dans le mélange sur la formation de la phase lubrifiante et la viscosité du mélange. Il est recommandé qu'à faible taux de cisaillement la composition optimale se situe dans un domaine dit critique et sensible alors qu'à fort taux de cisaillement elle soit au-dessus mais proche de la courbe binodale correspondante. Ces diagrammes de phase montrent également que pour un mélange avec une valeur de  $\chi$  donnée, quand  $N_1$  augmente les courbes binodale et spinodale se déplacent vers le bas, indiquant que

l'augmentation de la masse molaire du NMWP dans une certaine fourchette peut promouvoir la séparation de phase et améliorer la processabilité de l'UHMWPE. Ces résultats peuvent être utilisés comme guides pour améliorer la processabilité d'autres types de polymères à très haute masse molaire.

Comme l'ajout du PP est très efficace pour diminuer la viscosité de l'UHMWPE, d'autres propriétés du mélange UHMWPE/PP ont été étudiées par la méthode DPD. Les résultats montrent que ce mélange constitue une structure homogène quand la teneur en PP est inférieure à 10% ; au-delà de cette teneur, une structure biphasique apparaît. Dans ce dernier cas, il est à noter que l'UHMWPE est absent dans la phase riche en PP alors qu'une quantité importante de PP est localisée dans les domaines riches en UHMWPE. La dissolution du PP dans la phase riche en UHMWPE contribue au désenchevêtrement des macromolécules UHMWPE en diminuant sa viscosité alors que l'absence d'UHMWPE dans la phase riche en PP permet le maintien de la faible viscosité du PP. Il a été confirmé expérimentalement que la viscosité apparente du mélange UHMWPE/PP diminue avec l'augmentation de la teneur en PP. Par ailleurs, pour le mélange UHMWPE/NMWPE/HMWPP/NMWPP, les UHMWPE and HMWPP ont tendance à se localiser dans les phases riches en eux-mêmes. Les deux autres polymères de masses molaires normales sont localisés non seulement dans les phases riches en eux-mêmes mais aussi aux interfaces. La raison en est que les chaînes courtes jouent le rôle d'agent compatibilisant en diminuant la tension interfaciale. De surcroît, la concentration des chaînes courtes aux interfaces augmente considérablement leur épaisseur.

Un NMWP capable d'améliorer la processabilité de l'UHMWPE peut détériorer certaines de ses propriétés telles que propriétés mécaniques. L'ajout d'une faible quantité d'un hybride PMM (PEG/MDAB/MMT) dans le mélange conduit à un bon compromis. Les analyses DRX et MET montrent la formation de structure exfoliée et intercalée dans le cas du mélange UHMWPE/PP/PMM. La structure du PMM dans le mélange dépend de l'influence de l'agent intercalant PEG/MDAB sur l'intercalation et l'exfoliation de la MMT. L'ajout d'une faible quantité de PMM peut

considérablement diminuer la viscosité du mélange UHMWPE/PP (90/10). L'ampleur de cette diminution est d'autant plus grande que la teneur en PMM est importante. Par rapport au mélange UHMWPE/PP, les nanocomposites UHMWPE/PP/PMM présentent des propriétés mécaniques améliorées telles que la contrainte limite apparente d'élasticité, l'allongement à la rupture et la contrainte maximale avant rupture. Les particules PMM ont un facteur de forme important, ce qui joue un rôle important dans l'amélioration des propriétés mécaniques de ces nanocomposites.

Les théories de SCFT et de F-H sont employées pour étudier le comportement d'un mélange binaire A/B. Les résultats montrent que les propriétés thermodynamiques, telles que l'énergie libre de mélange, la tension interfaciale et l'épaisseur interfaciale, sont insensibles à  $N_B$  quand celui-ci est suffisamment grand. Prenons l'exemple d'un mélange de polymères avec  $N_A = 250$  et  $\chi = 0.009$ . Quand  $N_B > 6620$ , ce qui correspond à une masse molaire de  $1,4 \times 10^6$  g/mole pour le PE, la tension interfaciale ne varie pratiquement plus avec l'augmentation de  $N_B$ . Cette valeur critique de  $1,4 \times 10^6$  g/mole pour le PE est en accord avec la plupart des études de la littérature. Pour les mélanges binaires pour lesquels la masse molaire du polymère A et la valeur de  $\chi$  sont fixées, toutes les courbes du potentiel chimique d'échange passent par un point commun dont la fraction volumique  $\Phi_A = 1-1/e \approx 0,63$ , quelque soit la valeur de  $N_B$ . Ceci indique que les potentiels chimiques d'échange à  $\Phi_A = 1-1/e$  sont indépendants de la valeur de  $N_B$ . De plus, quand  $N_B$  diminue le minimum de l'énergie libre de mélange diminue continuellement et  $\Phi_{Am}$  s'approche vers  $\Phi_A = 1-1/e$  quand  $\chi N_A \neq 2,05$  ou vaut  $\Phi_A = 1-1/e$  quand  $\chi N_A = 2,05$  ou  $\chi N_B < 2,65$ . Ceci montre que  $\Phi_{Am}$  pour une solution polymère avec un bon solvant est proche de  $1-1/e$ . Il est aussi intéressant de noter que le potentiel chimique d'échange correspondant à point commun,  $\mu_c$ , dépend étroitement de la valeur de  $\chi N_A$ . Plus précisément, quand la valeur de  $\chi N_A$  est inférieure, égale ou supérieure à 2,05, la valeur de  $\mu_c$  est positive, zéro et négative, respectivement.

# Acknowledgments

First and foremost, I wish to express my sincere gratitude to my thesis advisors, Professors Guo-Hua Hu and Hui-Lin Li, from whose hard work I have benefited at each stage in my authoring of the present thesis. Every bit of my progress is the result of their encouragement, inspiration, guidance and support.

My special thanks also extend to Prof. Cornelius SCHRAUWEN and Prof. Sandrine HOPPE for their kind assistance.

I am also grateful to Professor Xi Xu. With his profound knowledge and upright personality, he has been and will always be an excellent example for me to learn from.

Other teachers, fellows and friends I owe a lot and wish to thank are Prof. Ya Cao, Lin Ye, Dr. Cai-Liang Zhang, Rui-Fen Liu, Sara Ronasi, Penu Christian, Yuan Fang, Xiao-Bo Song, Wei Li, Jin-Yao Chen, Jian-Jun Chen, Lin Yang, Shi-Peng Zhu, Jiang Lan, Jian Kang, Shao-Hua Chen, Geng Li.

Without the opportunity and financial support provided by China Scholarship Council, it may be impossible for me to complete the present thesis.

I am greatly indebted to my family. It is their spiritual and material support that kept me going.

I would also like to express my appreciation to all the people who have given me their love and help.

# Table of contents

<b>Abstract.....</b>	<b>i</b>
<b>Acknowledgements.....</b>	<b>iv</b>
<b>Table of Contents.....</b>	<b>v</b>
<b>List of Figures.....</b>	<b>ix</b>
<b>List of Tables.....</b>	<b>xvii</b>
<b>Nomenclature .....</b>	<b>xviii</b>
<b>CHAPTER 1 Introduction .....</b>	<b>1</b>
1.1 UHMWPE properties and Applications .....	1
1.2 Improvement in UHMWPE processability.....	3
1.2.1 Processing methods of UHMWPE .....	4
1.2.1.1 Gel-spinning .....	4
1.2.1.2 Compression moulding .....	5
1.2.1.3 Ram extrusion molding .....	7
1.2.1.4 Screw extrusion molding .....	8
1.2.2 Flowability improvement of UHMWPE .....	9
1.2.2.1 Viscosity reduction of UHMWPE with processing aids .....	9
1.2.2.2 Blends with low viscosity resins .....	11
1.2.2.3 Viscosity reduction of UHMWPE with ultrasonic irradiation .....	14
1.2.3 UHMWPE/clay nanocomposites .....	15
1.3 DPD Method and its applications on polymer research .....	16
1.3.1 Introduction to DPD .....	17
1.3.2 Applications of DPD to polymers .....	17
1.4 Scope of this thesis .....	19
1.4.1 Content of the thesis .....	19
1.4.2 Relevant results of this work .....	20
1.5 References .....	21

<b>CHAPTER 2 Experiments and Simulation Methods .....</b>	<b>26</b>
2.1 Experimental Section .....	26
2.1.1 Materials .....	26
2.1.2 Sample preparation .....	26
2.1.2.1 Preparation of MP (Chapter 5) .....	26
2.1.2.2 Preparations of MDAB, PM, MM and PMM (Chapter 6) .....	27
2.1.2.3 Preparations of UHMWPE blends and composites.....	27
2.1.3 Instruments .....	28
2.2 Theoretical background .....	30
2.2.1 Thermodynamics of mixing .....	30
2.2.1.1 Flory-Huggins theory .....	30
2.2.1.2 Phase diagrams .....	32
2.2.2 DPD simulation .....	34
2.2.3 MesoDyn simulation .....	37
2.3 References .....	40
<b>CHAPTER 3 Phase Morphologies and Rheological Behaviors of UHMWPE/ NMWP Blends .....</b>	<b>43</b>
3.1 Introduction .....	43
3.2 Results and discussion .....	43
3.2.1 Morphology of the UHMWPE/NMWP blends.....	43
3.2.1.1 UHMWPE/HDPE blends .....	44
3.2.1.2 UHMWPE/LDPE blends .....	49
3.2.1.3 UHMWPE/PP blends .....	55
3.2.2 Mechanisms of the viscosity reduction of the UHMWPE/NMWP blends..	59
3.2.3. Rheological behaviors predictions based on phase diagram .....	63
3.3 Conclusion .....	70
3.4 References .....	71
<b>CHAPTER 4 Structures and Properties of UHMWPE/PP blends .....</b>	<b>74</b>
4.1 Introduction .....	74
4.2 Results and Discussion .....	74

4.2.1 Effects of initial configurations.....	74
4.2.2 Effect of temperature.....	79
4.2.3 Effects of shears rates on morphologies.....	83
4.2.4 Effect of polydispersity on interface properties .....	85
4.3 Conclusions .....	91
4.4 References .....	92
<b>CHAPTER 5 The UHMWPE/PP/MP Composites .....</b>	<b>95</b>
5.1 Introduction .....	95
5.2 Results and discussion.....	96
5.2.1 The dispersion characteristics of OMMT in the UHMWPE/PP/MP composites.....	96
5.2.2 Analysis of phase structure formation.....	99
5.2.2.1 Phase structure of the UHMWPE/PP/PEG blends.....	99
5.2.2.1.1 Phase behaviors in the Absence of shear.....	99
5.2.2.1.2 Phase behaviors in the presence of shear.....	100
5.2.2.1.3 Effects of molecular weight of UHMWPE .....	105
5.2.2.2 Phase structure of the UHMWPE/PP/MP composites .....	107
5.2.3 Rheological behaviors and mechanism of viscosity reduction .....	114
5.2.4 Crystal structure and crystallinity .....	116
5.2.5 Mechanical Properties .....	117
5.3 Conclusions .....	118
5.4 References .....	119
<b>CHAPTER 6 UHMWPE/PP/PMM Nanocomposites .....</b>	<b>121</b>
6.1 Introduction .....	121
6.2 Results and discussion .....	121
6.2.1 Structure of OMMT platelets in the composites .....	121
6.2.1.1 Structure analysis on the bases of WAXD results .....	122
6.2.1.2 Structure analysis on the bases of TEM .....	124
6.2.2 Rheological behaviors .....	132
6.2.3 Mechanical properties .....	134

6.3 Conclusions.....	135
6.4 References.....	136
<b>CHAPTER 7 Unique Thermodynamic Properties of Binary Polymer Blends and Solutions at the Volume Fraction <math>\phi_A = 1-1/e</math>.....</b>	<b>138</b>
7.1 Introduction .....	138
7.2 Results and discussion.....	140
7.2.1 Effects of $N$ and $\chi$ on the free energy of mixing .....	140
7.2.2 Effects of $N$ and $\chi$ on the interface properties .....	141
7.2.3 Effects of $N$ and $\chi$ on $\phi_{Am}$ .....	145
7.2.4 Comparison of the F-H calculations for polymer solutions with experiments and other calculations.....	153
7.3 Conclusions .....	153
7.4 References .....	154
<b>CHAPTER 8 Conclusions.....</b>	<b>158</b>

# List of Figures

<b>Figure 1.1</b>	Coefficient of friction of various polymers.....	1
<b>Figure 1.2</b>	Wear properties of UHMWPE and other material.....	2
<b>Figure 1.3</b>	The applications of UHMWPE and its composites.....	3
<b>Figure 1.4</b>	Schematic illustration of the major components of an apparatus adapted to carry out the process of this invention.....	9
<b>Figure 2.1</b>	Scheme for the synthesis of MDAB.....	28
<b>Figure 2.2</b>	Schematic diagram of the apparatus used for the preparation of OMMT.....	30
<b>Figure 2.3</b>	Lees–Edwards boundary conditions. The infinite periodic system is subjected to a uniform shear in the $xy$ plane. The simulation box and its images centred at $(x, y) = (\pm kL, 0)$ , ( $k$ is positive integer), (e.g. A, E) are taken to be stationary. Boxes in the layer above, $(x, y) = (\pm kL, mL)$ , ( $m$ is positive integer), (e.g. B, C, D) are moving at a speed $(dv_x/dr_y)L$ in the positive $x$ direction. Boxes in the layer below, $(x, y) = (\pm kL, -mL)$ , (e.g. F, G, H) move at a speed $-(dv_x/dr_y)L$ in the negative $x$ direction.....	36
<b>Figure 2.4</b>	SEM of UHMWPE powder.....	37
<b>Figure 3.1</b>	SEM micrographs of cryogenically fractured surfaces of UHMWPE after etching. The scale bars in (a) and (b) are 10 and 1 $\mu\text{m}$ , respectively.....	44
<b>Figure 3.2</b>	SEM micrographs of cryogenically fractured surfaces after etching for the HDPE. The scale bars in (a) and (b) are 100 and 10 $\mu\text{m}$ , respectively.....	44
<b>Figure 3.3</b>	SEM micrographs of cryogenically fractured surfaces after etching for the UHMWPE/HDPE blend mixed for 5 minutes. The scale bars in (a), (b), (c) and (d) are 200, 100, 20 and 10 $\mu\text{m}$ , respectively.....	45
<b>Figure 3.4</b>	SEM micrographs of cryogenically fractured surfaces after etching for the UHMWPE/HDPE blend mixed for 40 minutes. Scale bars are like in Figure 3.3.....	46
<b>Figure 3.5</b>	The UHMWPE/HDPE (50/50) blend is simulated from a core-shell initial configuration (UHMWPE and HDPE are the core and shell, respectively). (i): time evolution of iso-density surfaces of HDPE, The outward surfaces of the HDPE phases are colored with green, and the	

rests are UHMWPE phases; (s): the corresponding slices perpendicular to y axis (the legend shows the magnitudes of density in the slices denoted by different colors that vary from 0.000 to 3.000); the high density region of the UHMWPE are colored with red; the iso-density line of the UHMWPE for  $\rho = 1.00$  and  $2.00$  are colored with white...47

<b>Figure 3.6</b>	Density profiles of the simulated UHMWPE/HDPE (50/50) blend after $1.1 \times 10^4$ time steps.....48
<b>Figure 3.7</b>	The UHMWPE/HDPE (50/50) blend is simulated from a random initial configuration. The others are the same as those in Figure 3.5...49
<b>Figure 3.8</b>	SEM micrographs of cryogenically fractured surfaces of LDPE after etching. The scale bars in (a) and (b) are 100 and 10 $\mu\text{m}$ , respectively.....50
<b>Figure 3.9</b>	SEM micrographs of cryogenically fractured surfaces after etching for the UHMWPE/LDPE (50/50) blend mixed for 3 mins. The scale bars in (a), (b), (c) and (d) are 200, 100, 20 and 10 $\mu\text{m}$ , respectively.....50
<b>Figure 3.10</b>	SEM micrographs of cryogenically fractured surfaces after etching for the UHMWPE/LDPE (50/50) blend mixed for 9 mins. Scale bars are like in Figure 3.9.....51
<b>Figure 3.11</b>	SEM micrographs of cryogenically fractured surfaces after etching for the UHMWPE/LDPE blend mixed for 15 mins. Scale bars are like in Figure 3.9.....52
<b>Figure 3.12</b>	The UHMWPE/LDPE (50/50) blend is simulated from a core-shell initial configuration (UHMWPE and LDPE are core and shell, respectively). (i): time evolution of iso-density surfaces of LDPE; (s): the corresponding slices. Others are same with Figure 3.5.....54
<b>Figure 3.13</b>	SEM micrographs of cryogenically fractured surfaces of the UHMWPE/PP (70/30) after etching mixed for 3 minutes. The scale bars in (a), (b), (c) and (d) are 50, 10, 5 and 1 $\mu\text{m}$ , respectively.....56
<b>Figure 3.14</b>	Time evolution of iso-density surfaces of PP in the UHMWPE/PP (70/30) blends simulated from the core-shell initial configuration (UHMWPE and PP are core shell, respectively). The outward surfaces of PP phase are colored with green, and the rests are UHMWPE phase. (i) the blends with morphology of (h) is simulated under shear rate of 0.8 for $1 \times 10^5$ steps, and then without shear rate for $4 \times 10^5$ steps.....57
<b>Figure 3.15</b>	The time evolution of iso-density surfaces of PP for the UHMWPE/PP blend simulated from a core-shell initial configuration. The outward surfaces of PP phases are colored with green, and the rests are UHMWPE phases. Each system contains $8.1 \times 10^4$ DPD beads: (a) UHMWPE/PP (60/40), (b) UHMWPE/PP (50/50).....58

<b>Figure 3.16</b>	The UHMWPE/PP (50/50) blend is simulated from a core-shell initial configuration for $4 \times 10^5$ steps. The green and red beads represent PP and UHMWPE, respectively.....	59
<b>Figure 3.17</b>	Plot of the logarithm of the apparent viscosity versus the logarithm of the apparent shear rate for (a) HDPE, (b) LDPE, (c) UHMWPE/LDPE (50/50), (d) PP, and (e) UHMWPE/PP (50/50). Both blends are mixed for 15 minutes.....	60
<b>Figure 3.18</b>	Extrudates of the UHMWPE/HDPE (50/50) blend.....	61
<b>Figure 3.19</b>	Extrudates of the UHMWPE/PP (50/50) blend mixed for 15 mins.....	61
<b>Figure 3.20</b>	SEM micrographs of cryogenically fractured surfaces after etching for the UHMWPE /PP (90/10) blend mixed for 3 minutes. The scale bars in (a), (b), (c) and (d) are 50, 10, 5 and 1 $\mu\text{m}$ , respectively.....	62
<b>Figure 3.21</b>	Binodals (solid curves) and spinodals (dashed curves) of polymer blends with fixed $N_2$ (11600) and various $N_1$ . (a), (b) and (c) are critical points, and the bold solid curve are composed of critical points.....	63
<b>Figure 3.22</b>	SEM micrographs of cryogenically fractured surfaces after etching for the UHMWPE /PP (50/50) blend mixed for 3 minutes. The scale bars in (a), (b), (c) and (d) are 200, 100, 20 and 10 $\mu\text{m}$ , respectively.....	64
<b>Figure 3.23</b>	SEM micrographs of cryogenically fractured surfaces after etching for the UHMWPE /PP (50/50) blend mixed for 9 minutes. Scale bars are like in Figure 3.22.....	65
<b>Figure 3.24</b>	SEM micrographs of cryogenically fractured surfaces after etching of the UHMWPE /PP (50/50) blend mixed for 15 minutes. Scale bars are like in Figure 3.22.....	66
<b>Figure 3.25</b>	Plot of the logarithm of the apparent viscosity versus the logarithm of the apparent shear rate for (a) PP, and (b), (c), (d) are UHMWPE/PP (50/50) blend mixed for 3, 9 and 15 minutes, respectively.....	67
<b>Figure 3.26</b>	Plot of the logarithm of the apparent viscosity versus the logarithm of the apparent shear rate for (a) LDPE, and (b), (c), (d) are UHMWPE/LDPE blend (50/50) mixed for 3, 9 and 15 minutes, respectively.....	67
<b>Figure 3.27</b>	Plot of the apparent viscosity versus the concentration of PP for UHMWPE/PP (50/50) blend mixed for 3 mins.....	69
<b>Figure 3.28</b>	Binodals (solid curves) and spinodals (dashed curves) of polymer blends with fixed $N_1$ (250) and various $N_2$ . (a), (b) and (c) are critical points, and the bold solid curve are composed of critical points.....	70
<b>Figure 4.1</b>	Iso-density surfaces of PP for the UHMWPE/PP blends obtained after $4 \times 10^5$ steps DPD simulation from random initial configuration. The	

	outward surfaces of PP phases are colored with green, and the rests are UHMWPE phases.....	76
<b>Figure 4.2</b>	Time evolution of iso-density surfaces of PP in the UHMWPE/PP (50/50) blends from random initial configuration. The outward surfaces of PP phases are colored with green, and the rests are UHMWPE phases.....	78
<b>Figure 4.3</b>	Time evolution of diffusivities of PP and UHMWPE in the UHMWPE/PP blends with varying the proportion of the UHMWPE/PP blends from 90/10 to 10/90.....	79
<b>Figure 4.4</b>	Time evolution of the dimensionless order parameters of the UHMWPE/PP (50/50) blends at different temperatures: (a) 298, (b) 503 and (c) 573K.....	81
<b>Figure 4.5</b>	Mixed enthalpy of the UHMWPE/PP (50/50) blends with time evolution at temperatures of (a) 298, (b) 503 and (c) 573K.....	82
<b>Figure 4.6</b>	Mixed free energy of the UHMWPE/PP (50/50) blends with time evolution at temperatures of (a) 298, (b) 503 and (c) 573K.....	82
<b>Figure 4.7</b>	Iso-density surfaces of PP for the UHMWPE/PP (50/50) blends obtained after $4 \times 10^5$ steps DPD simulation. The outward surfaces of PP phases are colored with green, and the rests are UHMWPE phases. (a) and (b) 0.005 (DPD units), (c) and (d) 0.01, (e) and (f) 0.1, (g) and (h) 0.2, (i) and (j) 0.5. In this work, x-axis and z-axis are shear direction and the shear gradient direction, respectively.....	85
<b>Figure 4.8</b>	Density profiles of each component for the blends: (a) UHMWPE/HMWPP (50/50); (b) UHMWPE/ NMWPE/ HMWPP/ NMWPP (45/5/45/5); (c) UHMWPE/ NMWPE/ HMWPP/ NMWPP (35/15/35/15); (d) UHMWPE/ NMWPE/ HMWPP/ NMWPP (15/35/15/35).....	86
<b>Figure 4.9</b>	The sum of the densities of NMWPE and NMWPP for the blends: (a) UHMWPE/ NMWPE/ HMWPP/ NMWPP (45/5/45/5); (b) UHMWPE/ NMWPE/ HMWPP/ NMWPP (35/15/35/15); (c) UHMWPE/ NMWPE/ HMWPP/ NMWPP (15/35/15/35).....	87
<b>Figure 4.10</b>	The sum of the densities of UHMWPE and HMWPP for the blends: (a) UHMWPE/ NMWPE/ HMWPP/ NMWPP (45/5/45/5); (b) UHMWPE/ NMWPE/ HMWPP/ NMWPP (35/15/35/15); (c) UHMWPE/ NMWPE/ HMWPP/ NMWPP (15/35/15/35).....	88
<b>Figure 4.11</b>	The small chain excess (NMWPE and NMWPP) for the blends: (a) UHMWPE/ NMWPE/ HMWPP/ NMWPP (15/35/15/35); (b) UHMWPE/ NMWPE/ HMWPP/ NMWPP (45/5/45/5).....	89
<b>Figure 4.12</b>	Interfacial tension in each slab calculated from Eqs. (4.3) and (4.4) for:	

	(a) UHMWPE/ HMWPP (50/50); (b) UHMWPE/ NMWPE/ HMWPP/ NMWPP (45/5/45/5); (c) UHMWPE/ NMWPE/ HMWPP/ NMWPP (35/15/35/15); (d) UHMWPE/ NMWPE/ HMWPP/ NMWPP (15/35/15/35).....	91
<b>Figure 5.1</b>	Wide-angle X-ray diffraction patterns of (a) DK-1, (b) MP21, (c) MP11, (d) UHMWPE/PP/MP21 (90/10/3) and (e) UHMWPE/PP/MP11 (90/10/3).....	96
<b>Figure 5.2</b>	Transmission electron micrographs of (a1) and (a2) UHMWPE/PP/MP11 (90/10/3), (b1) and (b2) UHMWPE/PP/MP21 (90/10/3), (c) MP11 and (d) MP21.....	97
<b>Figure 5.3</b>	FTIR spectra for DK-1.....	98
<b>Figure 5.4</b>	Iso-density surfaces of PP and PEG for UHMWPE/PP blends obtained after $4 \times 10^5$ steps DPD simulation. The outward surfaces of PP phases are colored with green, the outward surfaces of PEG phases are colored with blue, and the rests are UHMWPE phases.....	99
<b>Figure 5.5</b>	Density profiles of each component for the blends UHMWPE/PP/PEG (30/70/2).....	100
<b>Figure 5.6</b>	Iso-density surfaces of PP and PEG for the UHMWPE/PP/PEG (50/50/2) blends obtained after $4 \times 10^5$ steps DPD simulation. The outward surfaces of PP phases are colored with green, the outward surfaces of PEG phases are colored with blue, and the rests are UHMWPE phases. (a) and (b) 0.005 (shear rate), (c) and (d) 0.01, (e) and (f) 0.05, (g) and (h) 0.3, (i) and (j) 0.5. x-axis and z-axis are shear direction and the shear gradient direction, respectively.....	103
<b>Figure 5.7</b>	Time evolution of diffusivities of UHMWPE in the UHMWPE/PP/PEG (50/50/2) blends with varying the shear rate: (a) 0.2 (DPD units), (b) 0.1, (c) 0.05, (d) 0.01, (e) 0.005, (f) 0.001 and (g) 0.0.....	103
<b>Figure 5.8</b>	Iso-density surfaces of PP and PEG for the UHMWPE/PP/PEG (90/10/2) blends obtained after $2 \times 10^5$ steps DPD simulation. The outward surfaces of PP phases are colored with green, the outward surfaces of PEG phases are colored with blue, and the rests are UHMWPE phases. (a) and (b) 0.01 (shear rate), (c) and (d) 0.05, (e) and (f) 0.1, (g) and (h) 0.2. x-axis and z-axis are shear direction and the shear gradient direction, respectively.....	104
<b>Figure 5.9</b>	Iso-density surfaces of PP and PEG for UHMWPE/PP blends obtained after $4 \times 10^5$ steps DPD simulation. The outward surfaces of PP phases are colored with green, the outward surfaces of PEG phases are colored with blue, and the rests are UHMWPE phases.....	106

<b>Figure 5.10</b>	Time evolution of the dimensionless order parameters for: (a) UHMWPE (11600)/PP (50/50/2); (b) UHMWPE (11600)/PP (90/10/2); (c) UHMWPE (2320)/PP (50/50/2); (d) UHMWPE (2320)/PP (90/10/2).....	107
<b>Figure 5.11</b>	SEM micrographs of cryogenically fractured surfaces of the UHMWPE/PP (80/20) after etching mixed for 3 minutes. The scale bars in (a), (b) and (c) are 10, 5 and 1 $\mu\text{m}$ , respectively.....	110
<b>Figure 5.12</b>	SEM micrographs of cryogenically fractured surfaces of the UHMWPE/PP/MP11 (70/30/3) after etching mixed for 3 minutes. Dish arrows denote MMT layer direction. Scale bars are like in Figure 5.11 .....	111
<b>Figure 5.13</b>	SEM micrographs of cryogenically fractured surfaces of the UHMWPE/PP/MP11 (80/20/3) after etching mixed for 3 minutes. Dish arrows denote MMT layer direction. Scale bars are like in Figure 5.11 .....	112
<b>Figure 5.14</b>	SEM micrographs of cryogenically fractured surfaces of the UHMWPE/PP/MP11 (90/10/3) after etching mixed for 3 minutes. Dish arrows denote MMT layer direction. Scale bars are like in Figure 5.11 .....	113
<b>Figure 5.15</b>	Plot of the logarithm of the apparent viscosity versus the logarithm of the apparent shear rate for UHMWPE/PP/MP11.....	114
<b>Figure 5.16</b>	Plot of the logarithm of the apparent viscosity versus the logarithm of the apparent shear rate for UHMWPE/PP/MP11.....	115
<b>Figure 5.17</b>	DSC curves of (a) PP, (b) UHMWPE/PP (70/30), (c) UHMWPE/PP/MP11 (90/10/5), (d) UHMWPE/PP/MP11 (90/10/3), (e) UHMWPE/PP/MP11 (90/10/1), (f) UHMWPE /PP (90/10), (g) UHMWPE.....	117
<b>Figure 6.1</b>	Wide-angle X-ray diffraction patterns: (a) Na <sup>+</sup> -MMT; (b) PM; (c) MM; (d) UHMWPE/PP/MM (90/10/5); (e) UHMWPE/PP/MM (90/10/3) and (f) UHMWPE/PP/MM (90/10/1).....	122
<b>Figure 6.2</b>	Wide-angle X-ray diffraction patterns: (a) PMM; (b) UHMWPE/ PP/ PMM (90/10/5); (c) UHMWPE/PP/PMM (90/10/3) and (d) UHMWPE /PP/PMM (90/10/1).....	123
<b>Figure 6.3</b>	Transmission electron micrographs of the UHMWPE/PP/MM (90/10/3) composites.....	125
<b>Figure 6.4</b>	Transmission electron micrographs of the UHMWPE/PP/MM (90/10/3) composites. The micrographs of (a) – (l) denote the different positions of the sample.....	126
<b>Figure 6.5</b>	The distributions of: (a) the MM layer length (nm), (b) thickness (nm)	

	and (c) parameter $L_{\text{clay}}/d_{\text{clay}}$ in the UHMWPE/PP/MM (90/10/3) composite.....	127
<b>Figure 6.6</b>	Transmission electron micrographs of the UHMWPE/PP/PMM (90/10/3) composites. The micrographs of (a) – (d) denote the different positions of the sample.....	128
<b>Figure 6.7</b>	Transmission electron micrographs of the UHMWPE/PP/PMM (90/10/3) composites. The micrographs of (a) – (i) denote the different positions of the sample.....	129
<b>Figure 6.8</b>	Transmission electron micrographs of the UHMWPE/PP/PMM (90/10/3) composites. The micrographs of (a) – (i) denote the different positions of the sample.....	130
<b>Figure 6.9</b>	The distributions of: (a) the PMM layer length (nm), (b) thickness (nm) and (c) parameter $L_{\text{clay}}/d_{\text{clay}}$ in the UHMWPE/PP/PMM (90/10/3) composite.....	131
<b>Figure 6.10</b>	Plot of the logarithm of the apparent viscosity versus the logarithm of the apparent shear rate for (a) UHMWPE/PP (90/10), (b) UHMWPE/PP/PM (90/10/1), (c) UHMWPE/PP/PM (90/10/3) and (d) UHMWPE/PP/PM (90/10/5).....	132
<b>Figure 6.11</b>	Plot of the logarithm of the apparent viscosity versus the logarithm of the apparent shear rate for (a) UHMWPE/PP (90/10), (b) UHMWPE/PP/PMM (90/10/1), (c) UHMWPE/PP/PMM (90/10/3) and (d) UHMWPE/PP/PMM (90/10/5).....	133
<b>Figure 6.12</b>	The bar and pipe of the UHMWPE/PP/PMM (90/10/5) composites.	133
<b>Figure 7.1</b>	Dependence of free energy of mixing on the volume fraction of component A, for $N_A = 250$ , $\chi = 0.009$ , and $N_B$ is 100, 250, 500 and 2500, respectively.....	140
<b>Figure 7.2</b>	Dependence of free energy of mixing on $N_B$ , for $N_A = 250$ , $\chi = 0.009$ , and $\phi_A = 0.10, 0.30$ , and $0.50$ , respectively. The relatively larger values of $N_B$ are used to represent the chain lengths of ultrahigh molecular weight polymers.....	141
<b>Figure 7.3</b>	(a) Interface tension from Eq. (7.5) and (b) interface thickness from Eq. (7.6) in binary polymer blends with various $N_B$ .....	142
<b>Figure 7.4</b>	The critical $N_B$ from thermodynamic criteria (7.7) plotted against $N_A$ , for $V = 0.02$ and $\chi = 0.009$ .....	143
<b>Figure 7.5</b>	The critical $N_B$ from thermodynamic criteria (7.7) plotted against the parameter $\chi$ , for $V = 0.02$ and $N_A = 250$ .....	144
<b>Figure 7.6</b>	Interface tension from Eq. (7.5) in binary polymer blends with various $N_B$ , (a): $N_A = 200$ ; (b): $N_A = 350$ ; (c): $N_A = 500$ .....	145

<b>Figure 7.7</b>	Interface thickness from Eq. (7.6) in binary polymer blends with various $N_B$ , (a): $N_A = 200$ ; (b): $N_A = 350$ ; (c): $N_A = 500$ .....	145
<b>Figure 7.8</b>	Exchange potential from Eq. (2.6) plotted against the volume fraction of component A, for $N_A = 250$ , $\chi = 0.009$ and $N_B$ varies from 1 to 10000.....	146
<b>Figure 7.9</b>	Same as Figure 7.8 but with $\chi = 0.9$ .....	146
<b>Figure 7.10</b>	Same as Figure 7.8 but with $N_A = 200$ .....	147
<b>Figure 7.11</b>	Same as Figure 7.8 but with $N_A = 250$ and $\chi N_A = 2.05$ .....	147
<b>Figure 7.12</b>	Plot of $\chi$ from Eq. (7.9) vs. $N_A$ at $\phi_A = 1-1/e$ . (a) the region with $\chi N_A > 2.0486$ , $\mu_c < 0$ ; (b) the line with $\chi N_A = 2.0486$ , $\mu_c = 0$ ; (c) the region with $\chi N_A < 2.0486$ , $\mu_c > 0$ .....	148
<b>Figure 7.13</b>	Plot of $\phi_{Am}$ vs. $N_B$ for $N_A = 250$ and $\chi = 0.009$ . The $N_B$ and $\phi_{Am}$ corresponding to the critical point of the disappearance of the left minima are calculated from the thermodynamic criteria (7.1) and (7.10).....	149
<b>Figure 7.14</b>	Same as Figure 7.13 but with $\chi = 0.9$ .....	149
<b>Figure 7.15</b>	Same as Figure 7.13 but with $N_A = 200$ .....	150

# List of Tables

<b>Table 1.1</b>	The impact strengths of several engineering plastics.....	1
<b>Table 1.2</b>	The water absorptions of several engineering plastics.....	2
<b>Table 1.3</b>	Physical properties of UHMWPE.....	4
<b>Table 1.4</b>	Properties of UHMWPE/processing aid agents.....	12
<b>Table 2.1</b>	Main materials and the relative information.....	26
<b>Table 2.2</b>	Characteristic ratios, molecular weights and the corresponding DPD chain lengths of the species in the UHMWPE blends.....	37
<b>Table 5.1</b>	(001) diffraction peaks and corresponding d-spacing of DK-1 and various composites.....	96
<b>Table 5.2</b>	Surface tensions at 200°C of the polymers and filler used.....	108
<b>Table 5.3</b>	Interfacial Tensions ( $\gamma_{A-B}$ ) and Wetting Coefficients ( $W_a$ ) of all possible polymer- polymer- and polymer-filler-pairs.....	108
<b>Table 5.4</b>	DSC analysis of pure UHMWPE, UHMWPE/PP and UHMWPE/PP /MP11.....	116
<b>Table 5.5</b>	The mechanical properties of pure UHMWPE, UHMWPE/PP and UHMWPE/PP/MP11.....	117
<b>Table 6.1</b>	(001) diffraction peaks, corresponding d-spacing, $h_{001}$ , and $n_C$ of various MMT and their composites.....	123
<b>Table 6.2</b>	The mechanical properties of pure UHMWPE and its composites....	134

# Nomenclature

Abbreviation	Meaning
UHMWPE	Ultra-high molecular weight polyethylene
HMWPP	High molecular weight polypropylene
NMWPE	Normal molecular weight PE
NMWPP	Normal molecular weight PP
DPD	Dissipative particle dynamics
MMT	Na <sup>+</sup> - montmorillonite
OMMT	Organophilic montmorillonite
NMWP	Normal molecular weight polymers such as normal HDPE, LDPE and PP whose molecular weights are far less than that of UHMWPE.
PEG	Poly(ethylene glycol)
MDAB	2-Methacryloyloxyethyl dodecyldimethylammonium bromide
MP	Hybrid DK-1/PEG
PMM	PEG/MDAB/MMT
MM	MDAB/MMT
PM	PEG/MDAB/MMT
DM	2-(Dimethylamino)ethyl methacrylate
MFR	Melt flow rate
UCST	Upper critical solution temperature
MD	Molecular dynamics
CSR	Composition sensitive region of low shear rates
PL	Perforated lamella
$k_B$	Boltzmann constant
$T$	Absolute temperature
$\phi_i$	Volume fractions
$N_i$	Numbers of segments per molecule

---

$\chi$	Interaction parameter
$F_{\text{mix}}$	Free energy
$\delta$	Solubility parameter
$\mathbf{F}^{\text{C}}, \mathbf{F}^{\text{D}}, \mathbf{F}^{\text{R}}$	Conservative force, dissipative force, random force
$r_c$	Cutoff radius
$\alpha_{ij}$	Conservative interaction strength
$\gamma$	Friction coefficient
$C_n$	Characteristic ratio
$M$	Bead mobility parameter
$\gamma$	Interfacial tension
$D$	Interfacial thickness
$C_R$	Relative contribution of each part of interfacial tension
$\mu_c$	Exchange chemical potentials corresponding to the common points
$\phi_{Am}$	Volume fraction of component A corresponding to the minimum free Energy of mixing
$\lambda$	X-ray wavelength
$W_a$	Wetting coefficient
$P$	Order parameter
$\varepsilon(x)$	Small-chain excess
$P_n(x), P_t(x)$	Normal and transversal components of the pressure tensor
$u(r)$	Interaction energy potential
$g(r)$	Radial distribution function
$v_0$	Lattice site volume
$v_i,$	$i$ molecular volume

---

# CHAPTER 1 Introduction

## 1.1 UHMWPE properties and Applications

Ultra-high molecular weight polyethylene (UHMWPE) is a linear polyethylene with a molecular weight more than 1.5 million. It is regarded as an amazing material. UHMWPE has very high impact strength of any engineering plastics, about three times that of nylon, two times that of PC, five times that of ABS, withstands repeated impact. It remains tough even at  $-196^{\circ}\text{C}$ . Besides, it dampens noise and vibration because of the best impact absorbing property (Table 1.1).

**Table 1.1** The impact strengths of several engineering plastics

Material	UHMWPE	PA-66	POM	PC	ABS	PBT
Impact strength ( $\text{kJ/m}^2$ )	140 - 160	5 - 30	5 - 15	60 - 110	4 - 35	5 - 10

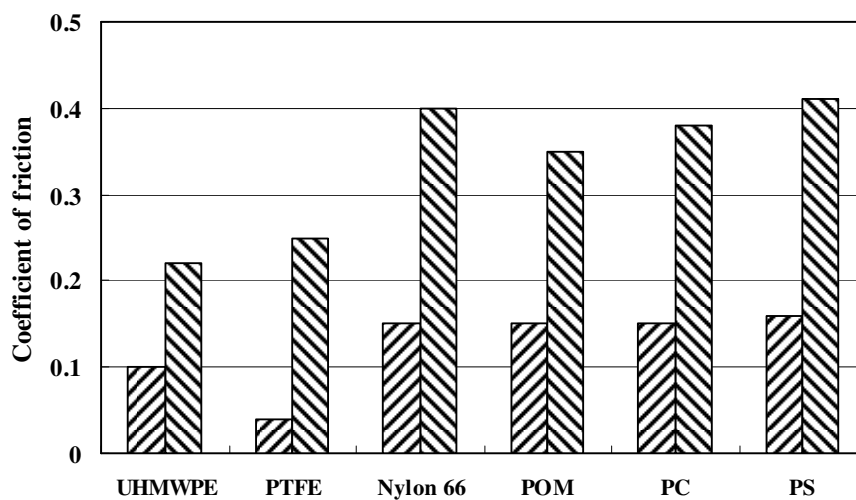


**Figure 1.1** Coefficient of friction of various polymers.

It has a very low coefficient of friction, and is self-lubricating. Its coefficient of friction is significantly lower than that of nylon and POM, and is comparable to that of PTFE (Figure 1.1). UHMWPE is highly resistant to abrasion, about four times more resistant to abrasion than nylon (Figure 1.2). UHMWPE friction parts need no lubricant, operate smoothly, and cause no damage to opponent, is a superb material

for using wear parts in machinery and equipment. Its water absorption is less than 0.01% which is only 1% that of nylon66 (Table 1.2). In water environment, it is very stable, resists to the attachment of algae and fungus. UHMWPE has better sanitary and can be in direct contact with drug and food (approved by FAD/USDA). Moreover, it is highly resistant to corrosive chemicals, with exception of oxidizing acids.

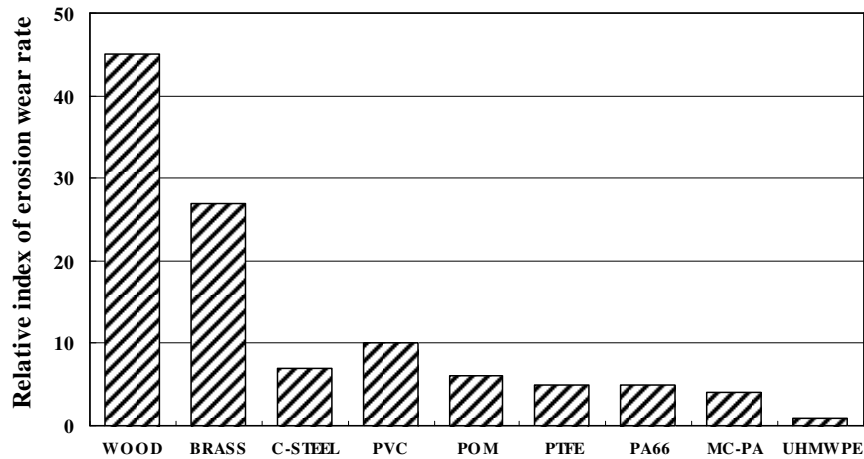


**Figure 1.2** Wear properties of UHMWPE and other material.

\*Sand slurry composition(weight ratio): sand/water = 2/3; Rotation speed of specimen: 900rpm;

Time: 7h

**Table 1.2** The water absorptions of several engineering plastics

Material	UHMWPE	PA-66	POM	PC	ABS	PTFE
Water absorption (%)	<0.01	1.5	0.25	0.15	0.2-0.45	<0.02

In the field of abrasion, selflubrication, impaction, vibration, corrosion, nonsticking etc, it's the best material for the substitution of bronze and stainless steel. UHMWPE and its composites are widely used as ballistic helmets and ballistic vehicle protection, gears, rollers, mixer paddles, pump impeller, bearing, chain and belt guides, wear strips, high-performance sails, etc (Figure 1.3). Since the 1960s, UHMWPE has also been the material of choice for total joint arthroplasty in orthopedic and spine implants (Figure 1.3) <sup>[1,2]</sup>.

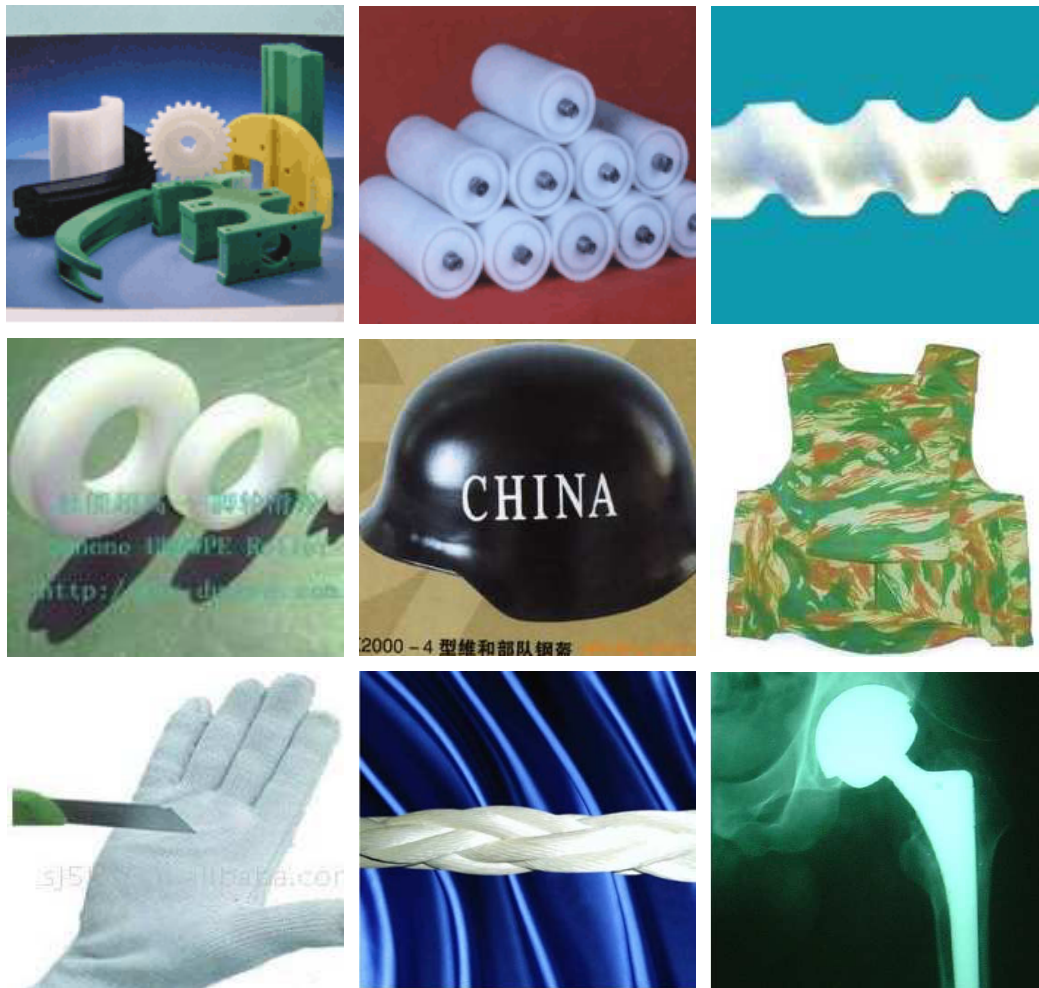


**Figure 1.3** The applications of UHMWPE and its composites.

## **1.2 Improvement in UHMWPE processability**

UHMWPE is a polymer with a number of technically important properties including notched impact strength, energy absorption capacity at high loading rates, tensile impact strength at elevated temperatures, resistance to stress cracking and extremely low embrittlement temperatures due to its very high molecular weight. It has an exceedingly high viscosity and pronounced viscoelastic characteristics in the melt. In fact, above its crystalline melting point (Table 1.3), UHMWPE is not a liquid but behaves much like a rubbery solid. Thus the processing techniques used for UHMWPE are limited to compression molding and ram extrusion in which shear flow is not important. Classical processing techniques like extrusion and injection molding are not applicable.

**Table 1.3** Physical properties of UHMWPE

Items	UHMWPE	ASMT methods
Relative molecular weight ( $10^4$ )	200	D2857
Average particle size ( $\mu\text{m}$ )	100 - 200	-
Density ( $\text{g}/\text{cm}^3$ )	0.935	D1505
Thermal conductivity ( $\text{W}/(\text{m}\cdot\text{k})$ )	8.5	D117
Coefficient of linear expansion ( $10^{-4}/^\circ\text{C}^{-1}$ )	1.5 - 2.5	D696
Melting point ( $^\circ\text{C}$ )	136	D2117
Heat distortion temperature ( $^\circ\text{C}$ )	85	D648
Wear rate ( $\text{mg}/1000$ times)	70	D1175
Rockwell Hardness (HRM)	40 - 60	D747
Flexural modulus (MPa)	600	D747
Volume resistivity ( $\Omega\cdot\text{cm}$ )	10	D257
Dielectric Constant	2.3	D150

## 1.2.1 Processing methods of UHMWPE

### 1.2.1.1 Gel-spinning

Gel spinning, swell drawing and die-free gel spinning involve the swelling or dissolution of polyethylene in solvent at elevated temperatures to reduce the entanglement density, followed by crystallization or gelation and then orientation of the lower entanglement material. Zwijnenburg and Pennings<sup>[4, 5]</sup> developed a technique for growing single polyethylene crystals longitudinally from flowing solutions using *p*-xylene as a solvent. They achieved growth rates of up to 31 cm/min, dependent on the polymer solution concentration and the rotor speed. Smith and Lemstra<sup>[3, 6, 7]</sup> developed the only commercial process, gel-spinning, with processing rates  $>10$  m/min. This involves the dissolution of polyethylene in decalin at elevated temperatures followed by recrystallization, drawing of the resulting unentangled gel and drying. To induce orientation, the fibre is subsequently hot drawn. Further

developments of this process are swell drawing and die-free gel spinning <sup>[8, 9]</sup>. Polyethylene crystal mats have also been hot drawn using coextrusion techniques <sup>[10]</sup>. The main disadvantage of these techniques is the use of harmful organic solvents, e.g. decalin and *p*-xylene, of the order of ~10 kg solvent/kg polymer, which require removal and recycling. A number of solid state processing techniques have been investigated using nascent UHMWPE, e.g. compression molding for films <sup>[11]</sup>, coextrusion of crystal mats <sup>[12]</sup> and films, ram extrusion <sup>[13]</sup> and rolldrawing <sup>[14]</sup>. Those processes involving compaction or compression of the UHMWPE powder particles are aiming to mechanically fuse the particles together.

### **1.2.1.2 Compression moulding**

Compression moulding is the most primitive and important processing method for UHMWPE because there is no limitation of molecular weight with this method. Molding temperature, time and pressure are the main influencing factors of the consolidation degree of UHMWPE product.

Farrar and Brain <sup>[15]</sup> investigated the effect of molding temperature on the consolidation degree of UHMWPE product. The specimen moulded at 170°C shows a highly granular structure in which the original powder particles are clearly evident, appearing as ~100µm grains, which are in turn composed of ~1 µm particles. The fracture has passed between the powder particles, indicating that these are only weakly bonded. All these features indicate a poorly consolidated sample. The specimen moulded at 180°C is shown. This material shows better consolidation since the fracture has passed through the original powder particles, rather than between them as in the previous sample. However, the boundaries between the 100 µm grains are clearly evident. Samples moulded at 190 and 200°C appeared very similar. The grain boundaries are much less evident than in the samples moulded at lower temperatures. The polyethylene powder particles are now well consolidated with very little evidence of voids around grain boundaries. Nevertheless, even in this sample an occasional defect could be found.

Wu and Buckley <sup>[16, 17]</sup> have studied the microscopic structural features of

compression moulding UHMWPE with varying time and temperature in the melt state during processing. Two distinct types of fusion defect were identified in their investigation. Type 1 defects were residual inter-particle voids arising from incomplete powder compaction, and were observed only for the lower moulding temperatures (145, 150, 155 and 165°C /15 min). Type 2 defects were regions of enhanced deformability at inter-particle boundaries in apparently fully compacted mouldings. They persisted up to 200°C. These defects were attributed to the slow self-diffusion of UHMWPE in the melt, leading to incomplete homogenization, even after compaction is complete. For the whole range of melt temperature 145-200°C, pressure 20-30MPa and time 10-90 min, higher moulding temperatures reduced the density of Type 1 defects and/or reduced the severity of Type 2 defects, producing a rapid rise in elongation-to-break.

Effects of compaction pressure on cohesive strength and chain mobility of low temperature compacted nascent UHMWPE were investigated by Gao and Mackley<sup>[18]</sup>. The studies showed an optimum compaction pressure at 30 MPa with Young's modulus = 5.3 GPa. They also stated that initially the Young's modulus increased with compaction pressure because of void reduction. Too high a compaction pressure reduced the volume available for chain movement and hindered inter-particle chain diffusion, and resulted in a decrease in particle cohesive strength.

Parasnis and Ramani<sup>[19]</sup> reported that an increase in the pressure applied at melt could improve the sintering and consolidation of polymer powder. However, the increased pressure also increased the melting point of the polymer. Hence, the pressure applied at melt increased the crystallinity and modulus, until a certain pressure was reached, beyond which the crystallinity and modulus reduced. Moreover, the increase in crystallinity and stiffness was accompanied by an increase in oxidation within the part. For obtaining the highest crystallinity and modulus, the processing should be carried out within a narrow window of applied pressure. If the applied pressure was significantly higher or lower than that window, parts of low crystallinity and modulus were produced, often accompanied by incomplete consolidation.

They also reported<sup>[19]</sup> that an increase in crystallinity and modulus were

accompanied by an increase in oxidation. The increased crystallinity caused an improvement in the tensile modulus of the part, and a concomitant decrease in the energy absorbed during failure, as the brittleness within the part increased. Stresses within the part increased because the applied pressure was high, leading to chain scission. Chain scissions provided additional sites for oxidation, leading to an increase in the oxidative index. Recrystallization of broken tie chains occurred immediately following chain scission in amorphous regions. Oxidation brings about a decrease in tensile strength and reduction in ultimate elongation. By filling the die in a nitrogen atmosphere instead of air, the oxidation level in the moulded parts was reduced by almost 60%, without adversely affecting the crystallinity and the modulus.

Hot isostatic pressing is a reliable method to process UHMWPE, and optimizing processing parameters, a well-consolidated material can be obtained. Gul and McGarry<sup>[20]</sup> reported that processing temperature was the most important variable affecting consolidation; fusion defects could be eliminated by increasing the processing temperature. However, an increase in heat soaking time from 2 to 4 hours at 210°C and 138 MPa did not produce any changes in the degree of consolidation. Consolidation was not affected by the processing pressure as shown by the similar structure present in the samples processed at 138 MPa and 69 MPa at a constant temperature of 210°C and heat soaking time of 2 hours.

The compression moulding has advantage of low cost, less investment, simple device, and no limits of molecular weight. However, there are a lot of shortcoming about this method such as low production efficiency, great labour intensity and uneasy control of product quality.

### **1.2.1.3 Ram extrusion molding**

When compaction is followed by extrusion, to orient the material, the samples produced are less brittle than when using compaction alone. The relative contributions of compaction and extrusion to this adhesion will depend on the initial compaction pressure prior to flow, according to the remarks of Gao et al<sup>[21]</sup>. Compacted and extruded UHMWPE powder is tougher than compacted alone because of increased

contact surface area brought about by extrusion <sup>[22]</sup>. Reports of ram extrusion of nascent, i.e. unmelted, UHMWPE indicate that the compaction/extrusion pressures used are of the order of 1000–2000 bar <sup>[23]</sup>. In many reports of the ram extrusion of polyethylene below its melting point, the compaction preceding the extrusion takes place at a temperature above the melting point <sup>[24, 25]</sup>. This is done to melt the material and eliminate any previous thermal history. It also increases the mobility of PE chains, which might increase the entanglement density on recrystallization and removes any existing chain extension or order brought about by the polymerization reaction.

Compaction and extrusion are not sufficient to bring about the amount of inter-particle penetration necessary to prevent or delay the onset of cohesive failure. Therefore, an additional technique is required. For UHMWPE most of the ram extrusion experiments are carried out with processing aids. *n*-Paraffins, up to a concentration of 33%, have also been used as processing aids in the solid-state extrusion of linear PE up to a temperature of 80°C <sup>[26]</sup>. However, despite the frictional coefficient decreasing with increasing *n*-paraffin content and extrusion temperature, the blended material exhibited lower orientation than the pure homopolymer, as shown by X-ray scattering experiments. In Refs. <sup>[26 - 29]</sup> the preparation of the polyethylene prior to ram extrusion involved melting of the polymer to produce shaped billets.

#### **1.2.1.4 Screw extrusion molding**

When UHMWPE is processed by screw extrusion molding, the melt covers on the screw and rotates with the screw together, and then UHMWPE can not be extruded due to its very low friction coefficient and exceedingly high viscosity. Besides, the critical shear rate of UHMWPE is very low. Much effort has been made for the screw extrusion molding of UHMWPE, which usually include two aspects: enhancing melt flowability and improving equipment.

USP 5399308 <sup>[30]</sup> reported on a process for producing a high modulus article of UHMWPE with an average molecular weight between about  $5 \times 10^5$  and about  $1.5 \times 10^6$ , g/mole through a passage of which the cross-sectional area diminishes in the forward

direction of the flow, thus producing an extrudate. Figure 1.4 shows a schematic illustration of the major components of the apparatus. The plastic material is extruded while it is close to or at its melt temperature. It is lubricated to obtain substantial plug flow through the passage. The extrudate can be deformed by drawing while it is maintained at or close to its melt temperature, thus producing an oriented, deformed extrudate. The oriented extrudate is then quickly cooled to preserve the orientation.

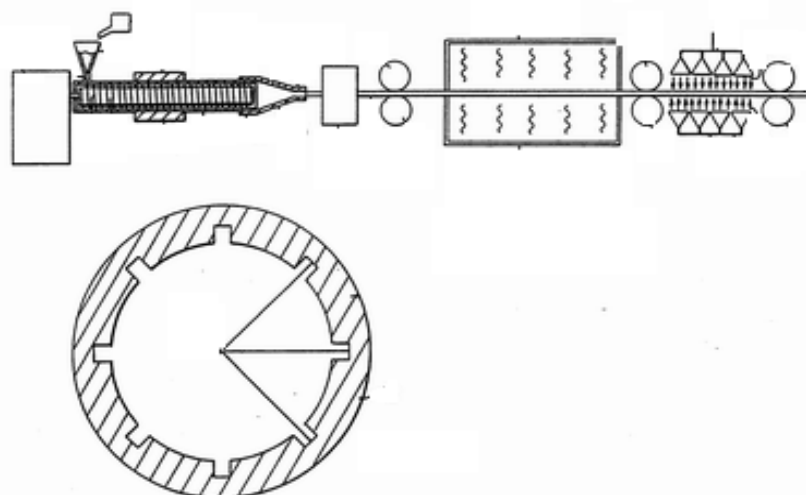


**Figure 1.4** Schematic illustration of the major components of an apparatus adapted to carry out the process of this invention.

## **1.2.2 Flowability improvement of UHMWPE**

Many attempts of reducing the viscosity of UHMWPE to a processable value while retaining as much as possible its mechanical properties have been made, mainly by blending it with processing aids or other low viscosity polyethylenes under a variety of experimental conditions.

### **1.2.2.1 Viscosity reduction of UHMWPE with processing aids**

There is a wide interest in the use of aids to improve the processing properties of polymers. A particular case concerns LLDPE, a widely applied commodity polymer but one known for its difficult melt processability. At shear rates suited for extrusion, flow defects are observed, which severely limit the economical benefit of processing. Defects are generally identified as shark-skin and cyclic, or slip-stick melt fracture.

The use of fluoroelastomer (FE) or related fluoropolymer additives has proven to be effective in suppressing both the surface defect (shark-skin) and the unstable extrusion (slip-stick) problems referred to above. Much progress has been made towards understanding the role of FE. There is consensus that FE polymers blended into LLDPE improve the appearance of extrudates at high output rates and decrease the polymer melt viscosity. The concurrent view on the mechanism for the changes in processing, due to the presence of FE, considers the additive to act as a die lubricant, allowing the host polymer to slip along the die wall. FE can effectively act as processing aid not only for LLDPE, but also for UHMWPE <sup>[31 - 34]</sup>.

Roberto and Francesco <sup>[35]</sup> improved the processability of a UHMWPE sample by using a liquid crystal polymer (LCP) sample and FE as lubricants. Both die pressure and torque decreased with increasing concentration of the two processing aids. The reduction of the die pressure was more pronounced. Moreover, the two polymer additives give similar effects but the FE is slightly more efficient. The torque decreased mostly at low contents of the two processing aids. As the concentration rised, the torque composition curves tended to flatten, in particular that of the system with the FE. Moreover, the processing aids, causing a reduction of the mechanical stress acting on the melt, decreased the degradation of the UHMWPE.

Gibson and co-workers <sup>[27, 28]</sup> used hydrostatic extrusion at 100°C to produce extrudates of polyethylene up to a molecular weight of  $3.5 \times 10^6$  with castor oil as the extrusion fluid and silicone vacuum grease as a lubricant coating on the PE billets. Extrusion draws ratios (EDRs) of up to 25 were obtained with extrusion pressures in the range ~ 400 to ~ 2700 bar and extrusion speeds of up to 2 cm/min at low EDRs <sup>[27]</sup>. For the UHMWPE the highest extrusion draw ratio was 6 with an extrusion pressure of ~ 1000 bar. Even for EDR = 2, the extrusion pressure was 144 bar. Die swell was in the range 13.4 to 17.8%. These researchers found that the silicone grease and the castor oil were stress-cracking agents for polyethylene. Predecki and Statton <sup>[29]</sup> found that the use of a fluorocarbon lubricant (along with die angle) was critical to their extrusion of a low-molecular weight PE at extrusion pressures between ~ 6900 and 20690 bar and temperatures between ambient and 130°C. Their extrusion rates were

from 0.00254 up to 2.54 cm/s. They concluded that the lubricant was actually reducing the efficiency of molecular orientation. The lubricant reduced the contribution of simple shear flow by reducing the shear stresses at the polymer-die interface.

The extrudability of UHMWPE can be effectively improved by adding a certain kind of lubricant. However, in order not to damage its mechanical properties, the amount of the lubricant has been limited to at most 5 phr (5 parts by weight per 100 parts by weight of UHMWPE), with which it has been impossible to improve the extrudability sufficiently <sup>[36]</sup>.

### **1.2.2.2 Blends with low viscosity resins**

In an attempt to make UHMWPE processable at lower temperatures, an intermediate molecular weight polyethylene (IMWPE) that behaves more like a liquid above its melting point was mixed with UHMWPE <sup>[39]</sup>. When the mixture was heated to above the melting point of the IMWPE, a pumpable slurry-like material resulted, in which the UHMWPE molding powders were suspended in the liquid phase of the IMWPE. The mixture was processable in conventional injection molding machines and screws extruders.

Vadhar's study <sup>[37]</sup> indicated that rheological and mechanical properties of the UHMWPE/LLDPE were profoundly affected by mixing process. Two mixing processes, namely simultaneous and sequential mixing, were employed. In the former case, the two polymer components were simultaneously loaded at 180°C and mixed. The latter allowed the UHMWPE component to diffuse at 250°C and cooled it down to 180°C, then the LLDPE component was added subsequently and mixed. LLDPE effectively reduced the UHMWPE viscosity for the two mixing processes. The tensile strength and elongation at break, on the other hand, exhibit negative departure from the linear additivity rule in the case of simultaneously prepared blends. Due to a very large viscosity difference, it was desirable to mix them by sequential mixing (or viscosity matching) to obtain homogeneous composites. Unfortunately, the tensile strength at break and tensile modulus decreased with increasing concentrations of

LLDPE for the sequential mixing process.

A composition improved in extrudability was prepared by intimately mixing 100 parts by weight of UHMWPE having a molecular weight of  $5 \times 10^5$  with 10-50 parts by weight of a low molecular weight polyethylene(LMWPE) having a molecular weight of 1500-3000 by the following complicated mixing procedure. LMWPE and a powdery UHMWPE were mixed together with thorough stirring at a temperature at which only the LMWPE could melt and the UHMWPE could not. The stirring was continued until the UHMWPE powder was intimately mixed with the molten LMWPE and had taken up all of the molten LMWPE between and on the UHMWPE particles. The resulting composition remained powdery or readily friable to a powder when allowed to cool. When a composition was prepared according to one example of the above-mentioned patent by mixing 100 parts by weight of UHMWPE having a molecular weight of  $2.2 \times 10^6$  with 25 parts by weight of a LMWPE having a molecular weight of 2000, the molded article was markedly inferior to UHMWPE itself in wear resistance and impact strength. Moreover, the mixing procedure was complicated. Nevertheless, the extrudability of the product was improved <sup>[38]</sup>.

**Table 1.4** Properties of UHMWPE/processing aid agents

PAA content (%)	Impact strength (J/m)	Wear loss (%)	Strength at break (MPa)	Elongation at break (%)
-	500	0.50	39.0	440
A (25%)	590	0.72	31.5	480
B (25%)	645	0.65	35.0	470
C (25%)	340	0.70	20.0	350
A (5%)+B (15%)+C (5%)	640	0.65	25.0	430
A (4%)+B (4%)+C (4%)	650	0.55	31.0	430
A (20%)+B (20%)+C (20%)	400	1.20	15.0	400
A (10%)+B (20%)+C (10%)	570	0.65	23.0	430

A composition improved in extrudability which comprises 100 parts by weight of an UHMWPE having a molecular weight of  $1 \times 10^6$ - $6 \times 10^6$  and 10-50 parts by weight of modifier which was selected from the group consisting of (A) only, (B) only, combination (A)+(B), combination (A)+(C), combination (B)+(C) and combination (A)+(B)+(C), wherein (A) is a saturated aliphatic alcohol having 15-30 carbon atoms, (B) is a petroleum hydrocarbon cyclopentadiene type resin having a molecular weight of 500-2,000 and a softening point of 70°C - 130°C and (C) is a low molecular weight polyethylene having a molecular weight of 1000 - 20000. The properties of various composites are shown in Table 1.4. The results showed that with the large amount of modifiers added, the molded articles prepared from the composition of this invention are hardly inferior to those prepared from UHMWPE alone in impact strength and wear resistance. However, its tensile strength is dramatically decreased <sup>[36]</sup>.

The use of an IMMWPE to improve the melt processability of UHMWPE is concomitant with disadvantages. Effective amounts of IMMWPE cause a marked decrease in some of the most desirable properties of the UHMWPE, such as impact strength and abrasion resistance. For this reason, the addition of IMMWPE to UHMWPE does not, in itself, present a practical way to improve the melt processability of UHMWPE. Nucleating agent is usually used to solve the contradiction between the improvement of processability and the mechanical properties of UHMWPE.

USP 4281070 reported an UHMWPE molding composition comprised of 70 to 95 percent by weight of UHMWPE, 5 to 30 percent IMMWPE having a molecular weight in a range from about  $4 \times 10^5$  to  $6 \times 10^5$ , and 0.1 to 10 percent by weight of a pyrogenic silica nucleating agent <sup>[39]</sup>. Pyrogenic silicas are generally described as having particle sizes in the range of 5 to 50 nm and surface areas in a range of about 100 to 400 m<sup>2</sup>/g. It was found that the addition of the IMMWPE not only improves the melt processability of UHMWPE, but also did not seriously compromise the physical properties of the UHMWPE when the nucleating agent was included in the formula.

Liu et al. <sup>[40 - 42]</sup> studied the effects of PP on the rheological behavior of

UHMWPE. The results showed that PP was enriched between the blend and the barrel wall, thus increased the frictional force on the wall, the conveying of the solid down to the channel could be carried out. During the melting and plasticating of UHMWPE/PP blend in the barrel, PP melted first and a melt film was formed on the barrel wall. The melt flowed from the melt-film toward the active flight flank to form a melt pool, exerting considerable pressure on the UHMWPE powder in the passive flight flank. The hard-compacted problem of UHMWPE was thus overcome. Microstructure analysis showed that PP was located in the amorphous zone (or low crystallinity zone) among UHMWPE crystal domains. Thus the chain entanglement density of UHMWPE was decreased and its flowability increased prominently. However, the melt fluidity of the UHMWPE/PP blend was still low. For example, the melt flow index of the UHMWPE/PP (75/25) was 0.66 g/10 min under the condition of 230°C and 21.6 kg load. Besides, the anti-wear property of UHMWPE could be improved by blending it with an appropriate amount of PP. Long scratch grooves and cracks occurred in the worn surface of UHMWPE, while no such serious damage is observed in the worn surface of the UHMWPE/PP blend.

### **1.2.2.3 Viscosity reduction of UHMWPE with ultrasonic irradiation**

Polymer processing aided by ultrasonic vibration has attracted attention for many years. Isayev et al. reported that during extrusion a high-intensity ultrasonic vibration could reduce the pressure and die swell and postpone melt fracture<sup>[43 - 45]</sup>. Oda<sup>[46]</sup> applied a 20 - 100 kHz ultrasound vibration in a direction vertical to the rubber discharging direction through extrusion and attained rubber sheets with better dimensional accuracy. Peshkovskii et al.<sup>[47]</sup> described a method for eliminating the unstable flow of a polybutene melt by the application of ultrasonic irradiation, and they discovered that the average size of fillers was smaller and the size distribution more homogeneous with ultrasonic treatment than without in kaolin clay filled HDPE.

Liu et al.<sup>[42]</sup> studied the effects of ultrasonic irradiation on the processing and mechanical properties of UHMWPE/PP blends. Ultrasonic vibration applied near the die can effectively reduce the die pressure and the melt apparent viscosity and thus

increase the extrusion effect of UHMWPE/PP blends. An appropriate ultrasonic intensity and extrusion rate can further improve the Young's modulus and Izod notched impact strength. However, an overdose of irradiation will harm the impact and yield strengths.

### **1.2.3 UHMWPE/clay nanocomposites**

In recent years, polymer/layered silicate nanocomposites have attracted great interest, both in industry and in academia, because they often exhibit remarkable improvement in materials properties when compared with virgin polymers or conventional micro and macro-composites. These improvements can include high moduli <sup>[48 - 50]</sup>, increased strength and heat resistance <sup>[51]</sup>, decreased gas permeability <sup>[52 - 54]</sup> and flammability <sup>[55, 56]</sup>, and increased biodegradability of biodegradable polymers <sup>[57]</sup>. However, the nanolayers are not easily dispersed in most polymers due to their preferred face-to-face stacking in agglomerated tactoids. Dispersion of the tactoids into discrete monolayers is further hindered by the intrinsic incompatibility between hydrophilic layered silicates and hydrophobic polymers. Therefore, layered silicates first need to be organically modified to produce polymer compatible clay (organoclay). In fact, it has been well-established that the replacement of the inorganic exchange cations in the cavities or "galleries" of the native clay silicate structure by alkylammonium surfactants can compatibilize the surface chemistry of the clay and a hydrophobic polymer matrix <sup>[58]</sup>.

Wang and Wu <sup>[59]</sup> investigated the rheological behaviour of UHMWPE/Kaolin composites prepared by a polymerization-filling process. Common elastic-viscous flow was absent for the composites with Kaolin content <10% in weight. Their flow curves had only two regions. The pressure oscillated at very low shear rate, accompanied by melt fracture. As for UHMWPE/Kaolin composites with Kaolin content >16% in weight, their melt behaved like normal polymer melts and were successfully extruded at low shear rates. Common elastic-viscous flow of UHMWPE melt was found. Besides, the higher the Kaolin content in the composite, the lower the apparent viscosity. They believed that the polymerization-filling method differed from

melt mixing technology in providing good interface adhesion or wettability between inorganic fillers and polymer chains. The strong interaction led to reduced polymer chain flexibility and a decrease in the chain entanglement density. As a result, the viscosity of UHMWPE melt decreased.

UHMWPE was reinforced with modified montmorillonite (o-MMT) in different contents <sup>[60]</sup>. The experimental conditions were a contact pressure of 7.0 MPa, a stroke length of 15 mm, and a reciprocating frequency of 1 Hz. Under the oilfield sewage condition, the friction coefficient and wear rate of the 10 wt.% o-MMT reinforced UHMWPE composite were all very much lower than those of PA material. The o-MMT particulates played an important role in impeding large-scale fragmentation of UHMWPE.

### **1.3 DPD Method and its applications on polymer research**

Computer simulations have been used to study polymer blend <sup>61 - 65</sup> and diblock copolymer properties <sup>[66 - 68]</sup>. On different scales, there are series of well developed simulation methods such as molecular dynamics (MD) and Monte Carlo methods on an atomistic level, as well as dissipative particle dynamics (DPD), lattice Boltzmann methods (LBMs), and dynamic mean field (MF) theory on the mesoscopic scale. Using atomistic simulation tools, the molecular structure and dynamic behavior of molecules can be analyzed. Because they are limited in the time and length scales in simulation and cannot effectively prevent a configuration from being trapped at a local minimum energy, it is difficult to observe the phase transformation process of a polymer blend and diblock copolymer system. Besides, an atomic-level description becomes prohibitively expensive. Therefore, atom-based simulations cannot predict more realistic structures on a mesoscopic scale. One way to circumvent this problem is to coarse-grain a group of atoms into a single “bead” and to replace the atomic-level interactions by simpler bead–bead interactions. For structural predictions on this scale, mesoscopic simulations such as DPD, LBM, and MF are more effective methods to reflect the mixing process between two or more polymers.

### 1.3.1 Introduction to DPD

Dissipative particle dynamics (DPD) is a mesoscopic simulation technique and was put forward by Hoogerbrugge and Koelman in the early 1990s <sup>[69, 70]</sup>. This method was applied to polymeric systems by introducing bead-spring-type models <sup>[71, 72]</sup>. In 1995, Español and Warren <sup>[73]</sup> carried out detailed formulation of DPD, i.e., all particles interact with three pairwise forces: (1) a conservative force, which is taken to be a soft repulsion and conserves the energy; (2) a dissipative force, which is proportional to the relative velocity of the particles and act to slow down the particles and remove the energy; and (3) a random force, necessary to add energy to the system on average. For polymeric systems, one has to include an additional interaction due to the “springs.” They carried out a detailed analysis using the fluctuation dissipation theorem, and showed that the relative amplitudes of the dissipative and random forces have to satisfy a certain relation in order to ensure that the hydrodynamic simulation follows the canonical ensemble (the ensemble with fixed  $N$ ,  $V$  and  $T$  can be defined as canonical ensemble). While the dissipative and random forces act in unison as a thermostat for the simulation, it is the conservative soft repulsive force that embodies the essential chemistry of the system. Ideally, one would like to derive the conservative force from detailed atomistic interactions. In 1997, Groot and Warren <sup>[74]</sup> applied a coarse-grained method to build the mapping relation of force parameters in DPD with the energy parameters in Flory-Huggins theory <sup>[75]</sup>. There are established theories in polymer science that link the  $\chi$ -parameter to solubilities and mixing energies of the polymeric components <sup>[76, 77]</sup>. The latter can be obtained either from atomistic simulations or from experiments. Thus, the Groot–Warren work provided a sound basis on which the conservative repulsion used in DPD could be derived starting from an atomistic description.

### 1.3.2 Applications of DPD to polymers

Recently, the DPD method has been applied in many areas, such as the investigation of the immiscibility property of polymer blends <sup>[78]</sup>, the formation of

micelle in the solvent<sup>[79]</sup>, shear force that induces the structural transformation of the lamellar phase<sup>[80]</sup>, and the viscosity property of polymer<sup>[81]</sup>.

Groot and Madden first applied DPD to examine the microphase separation behavior of linear  $A_mB_n$  diblock copolymer melts<sup>[65]</sup>. By varying the  $A$  composition and the effective  $A/B$  segregation parameter, various ordered structures, such as lamellae (L), gyroid (G), perforated lamellae (PL), hexagonally packed cylinders (C), and spheres (S), were obtained via DPD. Furthermore, the phase diagram constructed by DPD is in a near quantitative agreement with that predicted by self-consistent mean-field theory<sup>[82]</sup>. Qian et al.<sup>[83]</sup> applied DPD to construct the phase diagram of cyclic  $AB$  diblock copolymers. They found it very similar to that of linear diblock copolymers. In amphiphilic molecule solutions, current DPD studies were mainly focused on the less concentrated regimes. For example, Cao et al. employed DPD to simulate the aggregation behavior of poly(ethylene oxide)epoly(propylene oxide) block copolymers in aqueous solutions<sup>[84]</sup>. In particular, the effects of the copolymer architecture and concentration on the formed micelle type and size were examined. Their results are in a qualitatively good agreement with experiments<sup>[85]</sup>. As to examine the phase behavior of miktoarm star copolymers via DPD, only a few related studies have been reported recently. For example, Xu et al.<sup>[86]</sup> compared the phase behavior of four-arm star copolymers  $(AB)_4$  and  $(A_2B_2)$ , and observed that  $(A_2B_2)$  is more likely than  $(AB)_4$  to undergo a microphase separation. Rekvig et al. have demonstrated that the DPD simulations can successfully describe the partitioning behavior of the surfactant along the interface between water and oil<sup>[87]</sup>. Schulz et al. applied DPD to simulate the self-assembling behavior of surfactant  $C_{10}E_4$  in the presence of water and oil<sup>[88]</sup>. The simulated structure results by varying the water/oil ratio are in good agreement with the experimental phase diagram<sup>[89]</sup>. Qian et al.<sup>[90, 92]</sup> studied the effects of the stiffness of  $B$  blocks within  $AB_2$  miktoarm star copolymers on the microphase separation. They found that the increase of the stiffness of the  $B$  arms enables the randomly-distributed spheres to pack into an ordered BCC array. Although these studies demonstrated that the DPD simulation method is an appropriate technique to examine the phase behavior of amphiphilic molecules in the

presence of two solvents, their results are neither extend to the concentrated regimes nor consider the effects of solvent miscibility degree.

A few studies concern the morphology of polymer melt in confined systems. Malfreyt and Tildesley <sup>[92]</sup> studied the grafted polymer chains between two walls by DPD and obtained results identical to those from other methods. Recently, Xu et al. <sup>[93]</sup> used DPD to investigate the meso-scale structure of symmetric diblock copolymer in a slit or a nano-tube. However, the effect of the repulsion parameters and asymmetry of diblock copolymer on the morphology have not been considered.

To conclude, DPD simulation has been widely used to investigate the physical properties of polymers and their blends. However there are not any studies on UHMWPE based on DPD simulation. In this work, in addition to doing experiments, we adopt DPD simulation to investigate the structures and properties of UHMWPE and its blends.

## **1.4 Scope of this thesis**

### **1.4.1 Content of the thesis**

Both computer simulation and experimental analysis are used here to investigate the structures and processability of UHMWPE and its composites.

1. The effects of NMWP on the morphology and rheological behavior of the UHMWPE blend have been studied experimentally and theoretically. The phase diagram approach is adopted here to investigate in detail the effects of the composition, the parameter  $\chi$  and the molecular weight on the lubrication phase and the viscosity of blends.

2. The influences of the initial configuration, shear rate, temperature and polydispersity on the morphology, interfacial tension, interfacial thickness, the state of dispersion of each of the components in the blends have been investigated by both DPD and MesoDyn theories.

3. The effects of the composition of the UHMWPE/PP blend and content of the hybrid MP (DK-1/PEG) on the morphology, rheological behavior and mechanical

properties of the UHMWPE/PP/MP composite have been investigated. The possible mechanisms of viscosity reduction and enhancement in mechanical properties have been proposed.

4. The complex intercalator of poly (ethylene glycol)/ 2-methacryloyloxyethyl-dodecyldimethylammonium bromide (MDAB) is used to modify Na<sup>+</sup>-montmorillonite through ultrasonic irradiation. The influences of the organo-montmorillonite (OMMT: PM, MM and PMM) content on the phase morphology, and properties of the UHMWPE/PP/OMMT blends are investigated.

F-H theory is applied to investigate the unique thermodynamic properties of binary *A/B* polymer system at the volume fraction  $\phi_A = 1-1/e$  and the effects of chain length, volume fraction and  $\chi$  on the lowest free energy of mixing.

### **1.4.2 Relevant results of this work**

1. Complex intercalator PEG/ MDAB is used to modify MMT through ultrasonic irradiation to obtain PMM. The addition of a small amount of PMM is able to significantly reduce the melt viscosity of UHMWPE/PP (90/10) blend. The UHMWPE nanocomposites exhibit remarkable improvement in mechanical properties such as tensile strengths, elongation at break and yield strength compared with the matrix without clay. TEM shows that the PMM is exfoliated in the matrix, achieving nano-dispersion and improving greatly the mechanical properties and thermal stability of UHMWPE composites. The use of PMM in the blends better balances the compromise between processability improvement of UHMWPE and loss in its mechanical properties.

2. DPD and MesoDyn are first applied to study the mesoscale morphology and processability of UHMWPE and its blends. It is very difficult to investigate the whole phase separation process of UHMWPE blends by experiments because of spatial and temporal scale limitations. On the contrary, DPD simulations allow doing so.

3. An effective way to reduce the melt viscosity is to dilute the UHMWPE with a NMWP. However, there is no general acceptance on the viscosity reduction mechanism of the resulting blends. This work studies the viscosity reduction

mechanism of the blends by both rheological experiments and DPD simulations. Moreover, the Flory-Huggins theory is also adopted to predict the optimum processing conditions (composition, parameter  $\chi$  and molecular weight of NMWP). Since these results have universality, they are supposed to provide guidance for predicting the rheological behavior of other ultra-high molecular weight polymer blends.

4. This work reports on a unique thermodynamic properties of binary  $A/B$  polymer systems at the volume fraction  $\phi_A = 1-1/e$ . For binary polymer systems with a given polymer  $A$  and fixed  $\chi$ , exchange chemical potential curves all pass through a common point and the corresponding volume fraction is  $\phi_A = 1-1/e$  ( $\approx 0.63$ ), whatever the value of  $N_B$ , implying that the exchange chemical potentials at  $\phi_A = 1-1/e$  are independent of  $N_B$ . Moreover, as  $N_B$  decreases the minimum free energy of mixing monotonously decreases and the  $\phi_{Am}$  asymptotically approaches  $\phi_A = 1-1/e$  if  $\chi N_A \neq 2.05$  or is located at  $\phi_A = 1-1/e$  if  $\chi N_A = 2.05$  and  $\chi N_B < 2.65$ . This indicates that the  $\phi_{Am}$  for a polymer solution with a good solvent is close to  $1-1/e$ . It is also worth noting that  $\mu_c$  is crucially dependent on the value of  $\chi N_A$ . More specifically, if  $\chi N_A$  is less than, equal to, or greater than 2.05, the corresponding  $\mu$  is positive, zero and negative, respectively.

## 1.5 References

1. Charnley J. Low friction principle in: Low friction arthroplasty of the hip: theory and practice. Berlin: Springer, 1979
2. Orthopedic Products: Parts 1-3. Smith RC, editor, Medical and healthcare marketplace guide 1995. New York: Investment Dealers' Digest, 1995.
2. Smith P, Lemstra PJ. J Mater Sci 1980,15, 505.
4. Zwijnenburg A, Pennings AJ. Coll Polym Sci 1975, 253, 452.
5. Zwijnenburg A, Pennings AJ. Coll Polym Sci 1976, 254, 868.
6. Smith P, Lemstra PJ. Polymer 1980, 21, 1341.
7. Smith P, Lemstra PJ. Makromol Chem 1979, 180, 2983.
8. Mackley MR, Solbai S. Polymer 1987, 28, 1115.

9. Mackley MR, Solbai S. *Polymer* 1987, 28, 1111.
10. Kanamoto T, Porter RS, Takeda M, Tanaka K, Tsuruta A. *Polym J* 1983, 15, 327.
11. Rotzinger BP, Chanzy HD, Smith P. *Polymer* 1989, 30, 1814.
12. Kanamoto T, Porter RS, Kleintjens LA, Lemstra PJ. eds., *Integration of Fundamental Polymer Science and Technology*, Applied Science, London 1989.
13. Zachariades AE, Watts MPC, Porter RS. *Polym Eng Sci* 1980, 20, 555.
14. Wang LH, Porter RS. *J Polym Sci Polym Phys Ed* 1990, 28, 2411.
15. Farrar DF, Brain AA. *Biomaterials* 1997, 18, 1677.
16. Wu JJ, Buckley CP et al. *J Mater Sci & Lett* 2000, 20, 473.
17. Wu JJ, Buckley CP et al. *Biomaterials* 2002, 23, 3773.
18. Gao P, Mackley MR. *Polymer* 1994, 35, 5210.
19. Parasnis NC, Ramani K, *J Mater Sci Mater in Med* 1998, 9, 165.
20. Gul RM, McGarry FJ. *Polym Eng Sci* 2004, 44, 1848.
21. Gao P, Cheung MK, Leung TY. *Polymer* 1996, 37, 3265.
22. Leung TY, PhD. thesis, The Hong Kong University of Science and Technology, Hong Kong, 1995.
23. Zachariades AE, Watts MPC, Porter RS. *Polym Eng Sci* 1980, 20, 555.
24. Capiati N, Kojima S, Perkins W, Porter RS. *J Mater Sci* 1977, 12, 334.
25. Waddon AJ, Keller A. *J Polym Sci Part B Polym Phys* 1990, 28, 1063.
26. Maruyama S, Imada K, Takayanagi M. *Int J Polymeric Mater* 1973, 2, 105.
27. Gibson AG, Ward IM, Cole BN, Parsons B. *J Mater Sci Lett* 1974, 9, 1193.
28. Gibson AG, Ward IM. *J Polym Sci Polym Phys Ed* 1978, 16, 2015.
29. Predecki P, Statton WO. *Polym Lett* 1972, 10, 87.
30. Woodhams et al, USP5399308, 1995.
31. Hatzikiriakos SG, Dealy JM, *J Rheology* 1991, 35, 497.
32. Kalika DS, Denn MM. *J Rheology* 1987, 31, 815.
33. Hill DA, Hasegawa T, Denn MM. *J Rheology* 1990, 34, 891.
34. Shih CK. *Polym Eng Sci* 1976, 18, 742.
35. Aiello R, Mantia FPL. *Macromol Mater Eng* 2001, 286, 176.
36. Nakajima et al. USP4487875, 1984.

37. Vadhar P, Kyu T. *Polym Eng Sci* 1987, 27, 202.
38. George G. et al, USP3219728, 1965.
39. Scheetz et al, USP4281070, 1981.
40. Liu GD, Chen YZ, Li HL. Study on Processing of Ultrahigh Molecular Weight Polyethylene/ Polypropylene Blends. *Journal of Applied Polymer Science* 2004, 94, 977.
41. Liu GD, Chen YZ, Li HL. Study on Processing of Ultrahigh Molecular Weight Polyethylene/ Polypropylene Blends: Capillary Flow Properties and Microstructure. *Journal of Applied Polymer Science* 2004, 92, 3894.
42. Liu GD, Li HL. Extrusion of Ultrahigh Molecular Weight Polyethylene Under Ultrasonic Vibration Field. *J Appl Polym Sci* 2003, 89, 2628.
43. Isayev, A. I.; Wong, C. M.; Zeng, X. SPE ANTEC Tech Pap 1987, 33, 207.
44. Isayev, A. I. In Processing of the 23rd Israel Conference of Mechanical Engineering, 1990, p 1.
45. Isayev, A. I.; Wong, C. M.; Zeng, Z. *Adv Polym Technol* 1990, 10, 31.
46. Keishiro, O. *Jpn Pat.* 91,253,323, 1991.
47. Peshkovskii SL, Feidman ML, Tukachinskii AI. *Polym Compos* 1983, 4, 126.
48. Giannelis EP, Krishnamoorti R, Manias E. Polymer-silicate nanocomposites: model systems for confined polymers and polymer brushes. *Adv Polym Sci* 1999, 138, 107.
49. LeBaron PC, Wang Z, Pinnavaia TJ. Polymer-layered silicate nanocomposites: an overview. *Appl Clay Sci* 1999, 15, 11.
50. Vaia RA, Price G, Ruth PN, Nguyen HT, Lichtenhan J. Polymer/layered silicate nanocomposites as high performance ablative materials. *Appl Clay Sci* 1999, 15, 67.
51. Giannelis EP. Polymer-layered silicate nanocomposites: synthesis, properties and applications. *Appl Organomet Chem* 1998, 12, 675.
52. Bharadwaj RK. Modeling the barrier properties of polymerlayered silicate nanocomposites. *Macromolecules* 2001, 34, 1989.
53. Messersmith PB, Giannelis EP. Synthesis and barrier properties of poly(1 - caprolactone) -layered silicate nanocomposites. *J Polym Sci, Part A Polym Chem*

1995, 33, 1047.

54. Yano K, Usuki A, Okada A, Kurauchi T, Kamigaito O. Synthesis and properties of polyimide–clay hybrid. *J Polym Sci, Part A Polym Chem* 1993, 31, 2493.

55. Gilman JW. Flammability and thermal stability studies of polymer-layered silicate (clay) nanocomposites. *Appl Clay Sci* 1999, 15, 31.

56. Dabrowski F, Bras ML, Bourbigot S, Gilman JW, Kashiwagi T. PA-6 montmorillonite nanocomposite in intumescent fire retarded EVA. Proceedings of the Eurofillers' 99, Lyon-Villeurbanne, France; 6–9 September 1999.

57. Sinha Ray S, Yamada K, Okamoto M, Ueda K. New polylactide/layered silicate nanocomposite: a novel biodegradable material. *Nano Lett* 2002, 2, 1093.

58. LeBaron PC, Wang Z, Pinnavaia TJ. Polymer–layered silicate nanocomposites: an overview. *Appl Clay Sci* 1999, 15, 11.

59. Wang X, Wu QY, Qi ZN. Unusual rheology behaviour of ultra high molecular weight polyethylene/kaolin composites prepared via polymerization-filling. *Polym Int* 2003, 52, 1078.

60. Wen JP, Yin P, Zhen MH. Friction and wear properties of UHMWPE/ nano-MMT composites under oilfield sewage condition. *Materials Letters* 2008, 62, 4161.

61. Tiller AR, Gorella B. *Polymer* 1994, 35, 3251.

62. Fan CF, Olafson BD, Blanco M, Hsu SL. *Macromolecules* 1992, 25, 3667.

63. Lee S, Lee JG, Lee H, Mumby SJ., *Polymer* 1990, 40, 5137.

64. Yang H, Li ZS, Lu ZY, Sun CC. *Eur Polym J* 2005, 41, 2956.

65. Groot RD, Madden TJ. *J Chem Phys* 1998, 108, 8713.

66. Ortiz V, Nielsen SO, Discher DE, Klein ML, Lipowsky R, Shillcock J. *J Phys Chem B* 2005, 109, 17708.

67. Ryjkina E, Kuhn H, Rehage H, Müller F, Peggau J. *Angew Chem Int Ed* 2002, 41, 983.

68. Kranenburg M, Nicolas JP, Smit B. *Phys Chem Chem Phys* 2004, 6, 4142.

69. Hoogerbrugge PJ, Koelman JMVA. *Europhys Lett* 1992, 19, 155.

70. Koelman JMVA, Hoogerbrugge PJ. *Europhys Lett* 1993, 21, 363.

71. Kong Y, Manke CW, Madden WG, Schlijper AG. *Int J Thermophys* 1994, 15,

- 1093.
72. Schlijper AG, Hoogerbrugge PJ, Manke CW. *J Rheol* 1995, 39, 567.
  73. Español P, Warren PB. *Europhys Lett* 1995, 30, 191.
  74. Groot RD, Warren PB. *J Chem Phys* 1997, 107, 4423.
  75. Flory PJ, *Principles of Polymer Chemistry* Cornell University Press, Ithaca, New York, 1953.
  76. Hildebrand JH, Scott RL. *The Solubility of Non-Electrolytes* (Reinhold), New York, 1949.
  77. Case F, Honeycutt JD. *Trends Polym Sci* 1994, 2, 259.
  78. Abu-Sharkh B, AISunaidi A. *Macromol. Theory Simul.* 2006, 15, 507.
  79. Yamamoto S, Maruyama Y, Hyodo SA. *J Chem Phys* 2002, 116, 5842.
  80. Fraser B, Denniston C, Müser MH. *J Chem Phys* 2006, 124, 104902.
  81. Visser DC, Hoefsloot HCJ, Iedema PD. *J Comput Phys* 2006, 214, 491.
  82. Matsen MW, Bates FS. *Macromolecules* 1996;29:1091.
  83. Qian HJ, Lu ZY, Chen LJ, Li ZS, Sun CC. *Macromolecules* 2005; 38:1395.
  84. Cao X, Xu G, Li Y, Zhang Z. *J Phys Chem A* 2005, 109, 10418.
  85. Won YY, Davis HT, Bates FS, Agmalian M, Wignall GD. *J Phys Chem B* 2000;104:7134.
  86. Xu Y, Feng J, Liu HL, Hu Y. *J East China Univ Sci Tech* 2006; 32:133.
  87. Rekvig L, Kranenburg M, Vreede J, Hafskjold B, Smit B. *Langmuir* 2003, 19, 8195.
  88. Schulz SG, Kuhn H, Schmid G, Mund C, Venzmer J. *Colloid Polym Sci* 2004, 283, 284.
  89. Jakobs B, Sottmann T, Strey R, Allgaier J, Willner L, Richter D. *Langmuir* 1999;15:6707.
  90. Qian HJ, Chen LJ, Lu ZY, Li ZS, Sun CC. *J Chem Phys* 2006;124: 14903.
  91. Qian HJ, Chen LJ, Lu ZY, Li ZS, Sun CC. *Europhys Lett* 2006; 74:466.
  92. Malfreyt P, Tildesley DJ. *Langmuir* 2000, 16, 4732.
  93. Xu JB, Wu H, Lu DY, He XF, Zhao YH, Wen H. *Mol Simul* 2006, 32, 357.

# CHAPTER 2 Experiments and Simulation Methods

## 2.1 Experimental Section

### 2.1.1 Materials

Main materials and the relative information are listed in Table 2.1.

**Table 2.1** Main materials and the relative information.

Materials	Manufacturers	Remark
UHMWPE (M-II)	Beijing No. 2 Auxiliary Agent Factory (Beijing, China)	average viscosity molecular weight of $2.5 \times 10^6$ and a mean particle diameter of about $300\mu\text{m}$
HDPE (6098)	Shandong Qilu Petrochemical Engineering Co. (Shandong, China)	MFR of 7.8g/10 min (230°C, 2.16kg load)
PP (F401)	Lanzhou Chemical Industry Factory (Lanzhou, China)	MFR of 2.0g/10 min (230°C, 2.16kg load)
LDPE (2426K)	Lanzhou Chemical Industry Factory (Lanzhou, China)	20-28 branches/1000 long chain carbons
PEG	Liaoyang Aoke Chemical Co. (Liaoning, China)	average viscosity molecular weight of 6000
OMMT (DK-1)	Zhejiang Fenghong clay Chemicals Co. (Zhejiang, China)	
DM	Chengdu Kelong Chemical Reagents Factory (Chengdu, China)	
1-bromododecane	Chengdu Kelong Chemical Reagents Factory (Chengdu, China)	
Ethyl acetate	Bodi Chemieals (Tianjin, China)	
MMT	Zhejiang Fenghong clay Chemicals Co. (Zhejiang, China)	

### 2.1.2 Sample preparation

#### 2.1.2.1 Preparation of MP (Chapter 5)

PEG was first added to alcohol to form a uniform solution. The as-received organophilic montmorillonite DK-1 powders were subsequently added to the above solution. The mixture was then heated to 60°C for 3 hours and under vigorous stirring. The resulting homogeneous DK-1/PEG suspension was dried in a 50°C oven for four days and then pulverized. The DK-1/PEG hybrid was obtained. The hybrids with weight ratios of 1:1, 1:2 and 2:1 were donated as MP11, MP12 and MP21, respectively.

### **2.1.2.2 Preparations of MDAB, PM, MM and PMM (Chapter 6)**

A cationic surfactant 2-methacryloyloxyethyl dodecyldimethylammonium bromide (MDAB) was synthesized by quaternarization reaction (see Figure 2.1). 2-(Dimethylamino)ethyl methacrylate and 1-bromododecane (1:1 molar ratio) were reacted at 40°C for 80h. The product was insoluble to either of the ingredients and thus precipitated. The white powder-like precipitant was purified by filtering and washing using ethyl acetate. It was then dried under vacuum at ambient temperature for 24 h.

OMMT was prepared by the ion exchange reaction. PEG (10g) and MDAB (10g) were first added to deionized water (800mL) in order to form a uniform solution, to which the as-received MMT powder was subsequently added. The system was subjected to ultrasonic irradiation (acoustic intensity, 9.54 W/cm<sup>2</sup>) for 1h (Figure 1). Then, the exchanged MMT was filtered and redispersed in deionized water. This procedure was repeated several times till no bromide ion was detected with 0.1 N AgNO<sub>3</sub> solution. The filter cake was finally vacuum-dried at room temperature and crushed into powder. This OMMT is denoted as PMM. The preparation of other kinds of OMMT [PEG/MMT (PM) or MDAB/MMT (MM)] are similar to that for PMM.

### **2.1.2.3 Preparations of UHMWPE blends and composites**

All components of both UHMWPE/PP and its composites were physically mixed, and then extruded by a general three-section single-screw extruder (D = 25 mm, L/D = 25) through a circle die. The temperatures were 190, 210, and 220°C for each

section of the barrel and 210°C for the die. The extrudates were then made pellets and compression molded into 1 and 4 mm plates. Compression molding was carried out in the following conditions: preheated at 200°C for 5 min at low pressure, compressed for 5 mins at 13 MPa at the same temperature, and then cooled to ambient temperature with the cooling rate 30°C/min in the mold at 13 MPa. Specimens for tensile test or izod-notched impact tests were got from the 1 and 4 mm plates respectively.

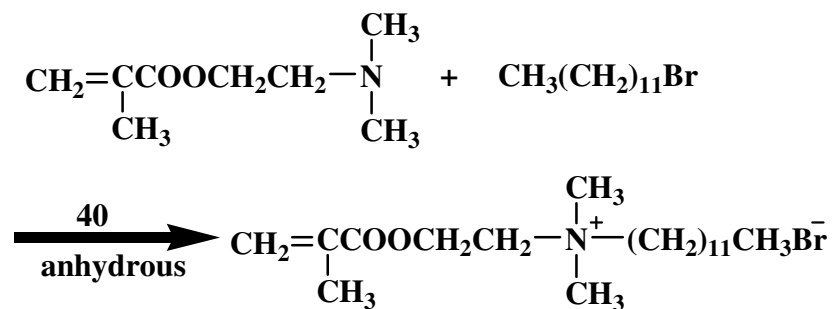


Figure 2.1 Scheme for the synthesis of MDAB.

## 2.1.3 Instruments

### 2.1.3.1 Rheological experiments

The rheological measurements were carried out on a Gottfert Rheograph 2002 (Gottfert Co., Germany). The capillary diameter and its length-to-diameter ratio are 1 mm and 30, respectively. Entrance pressure losses were assumed to be negligible for such a long capillary die. Therefore no Bagley corrections were made. The flow properties of these specimens were measured at 230°C.

### 2.1.3.2 Scanning electron microscope (SEM)

A JSM 5900 LV scanning electron microscope (Tokyo, Japan) was used to observe the morphologies of UHMWPE blends and composites. Before the SEM observation, the specimens were prepared by brittle fracturing in liquid nitrogen, and then etched in a solution of 1.3 wt %  $\text{KMnO}_4$  dissolved in a  $\text{H}_2\text{SO}_4/\text{H}_3\text{PO}_4/\text{H}_2\text{O}$  (10/4/1) mixture to eliminate the amorphous phase.

### 2.1.3.3 Mechanical properties

Tensile tests were carried out at room temperature according to GB/T 1040-92 standard on an Instron model 4302 machine (Instron Co., U.K.). Tensile strength, elongation at break and yield strength were measured at a cross-head speed of 50mm/min. Notched izod impact strength was measured with XJ-40AX (Wuzhong Material Testing Technical Co., China) at room temperature according to GB 1843-80 standard.

#### **2.1.3.4 Thermal analysis**

Crystallization studies were performed on a Netzsch DSC 204 (Netzsch Co., Germany) differential scanning calorimeter under constant nitrogen flow. The sample masses were small (3-4mg) for all measurements. All samples were first heated to 190°C, held at 190°C for 5 min, and then cooled to 60°C with a rate 10°C /min and held at 60°C for 5 min. They were then scanned from 60 to 190°C at a rate of 10°C.

#### **2.1.3.5 Transmission electron microscopy (TEM)**

TEM observations were carried out with an H-7100 (Tokyo, Japan) instrument with an accelerating voltage of 100 kV. The ultrathin sections with a thickness of 100nm were microtomed in liquid nitrogen by a Reichert Ultracut cryoultramicrotome without staining.

#### **2.1.3.6 Wide-angle X-ray diffraction (WAXD)**

WAXD spectra were recorded with a Philip X'pert prd diffractometer (Japan). The X-ray beam was nickel-filtered Cu Ka ( $\lambda=0.1542\text{nm}$ ) radiation operated at 40kV and 100mA. MMT, MP, PM, MM, or PMM were studied in the form of powder. Samples of UHMWPE composites were cut from 1 mm plates. The scanning range was varied from  $2\theta = 1^\circ$  to  $11^\circ$  with a rate of  $5^\circ/\text{min}$ .

#### **2.1.3.7 Ultrasonic irradiation instrument**

The ultrasonic irradiation instrument was VC-1500 (Sonic and Material, USA). It had the following features: standard titanium horn with a diameter of 22 mm, an

adjustable power output, a replaceable flat stainless steel tip, and a digital thermometer to determine temperature. The power output was  $9.54\text{W}/\text{cm}^2$  in this work (Figure 2.2)

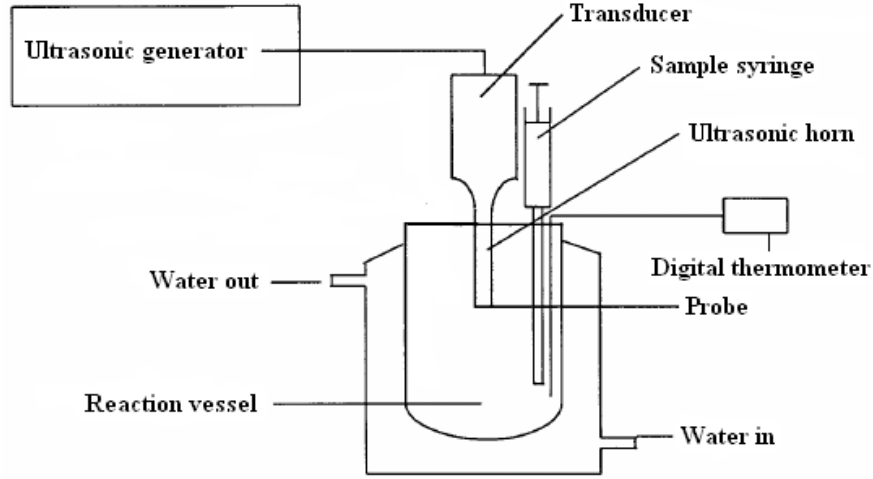


**Figure 2.2** Schematic diagram of the apparatus used for the preparation of OMMT.

## 2.2 Theoretical background

### 2.2.1 Thermodynamics of mixing

#### 2.2.1.1 Flory-Huggins theory

The F-H expression for the free energy density of mixing of component 1 with component 2 is given by <sup>[1-4]</sup>:

$$\frac{F_{mix}}{k_B T} = \frac{\phi_1}{N_1} \ln \phi_1 + \frac{\phi_2}{N_2} \ln \phi_2 + \chi \phi_1 \phi_2 \quad (2.1)$$

where  $k_B$  is Boltzmann constant,  $T$  is the absolute temperature,  $\phi_i$  and  $N_i$ , are the volume fractions and the numbers of segments per molecule, and  $\chi$  is interaction parameter. An implicit condition associated with this equation is that the lattice is filled completely, hence  $\phi_1 + \phi_2 = 1$ . Under this condition,  $\phi_2 = 1 - \phi_1$ ,  $\phi_1$  being the only degree of freedom. The first two terms in the free energy of mixing [Eq. (2.1)] have entropic origin and always act to promote mixing, although with blends of long-chain polymers these terms are quite small. The last term has energetic origin, and can be positive (opposing mixing), zero (ideal mixtures), or negative (promoting

mixing) depending on the sign of the interaction parameter  $\chi$ .

If there is a net attraction between species (i.e. they like each other better than they like themselves),  $\chi < 0$  and a single-phase mixture is favourable for all compositions. More often there is a net repulsion between species (they like themselves more than each other) and the Flory interaction parameter is positive  $\chi > 0$ . In this case the equilibrium state of the mixture depends on the functional dependence of this free energy on the composition  $\phi$  for the whole range of compositions. This functional dependence  $F_{\text{mix}}(\phi)$  also depends on the value of the Flory interaction parameter  $\chi$  as well as on the degrees of polymerization of both molecules  $N_1$  and  $N_2$ .

For non-polar mixtures with species interacting mainly by dispersion forces, the interaction parameter  $\chi$  can be estimated by Eq. (2.2).

$$\chi \approx v_0 \frac{[\delta_1^2 + \delta_2^2 - 2\delta_1\delta_2]}{k_B T} = \frac{v_0(\delta_1 - \delta_2)^2}{k_B T} \quad (2.2)$$

It is based on the solubility parameter  $\delta$  related to the energy of vapourization  $\Delta E$  of a molecule. For example, for a molecule of species  $i$  the solubility parameter is defined as

$$\delta_i \equiv \sqrt{\frac{\Delta E_i}{v_i}} \quad (2.3)$$

Where  $v_i$  and  $v_0$  are the  $i$  molecular volume, lattice site volume, respectively. The energy of vapourization  $\Delta E_i$  of a molecule  $i$  is the energy of all the interactions between the molecule and its neighbours. The cohesive energy density  $\Delta E_i/v_i$  is the interaction energy per unit volume between the molecules in the pure  $i$  state.

The above approach works reasonably well for non-polar interactions, which only have van der Waals forces between species, and does not work in mixtures with strong polar or specific interactions, such as hydrogen bonds.

Graessley et al <sup>[5]</sup>. determined the values of  $\chi$  from SANS data in the single-phase region for two series of blends, H97/D88 and H88/D78, using the random phase approximation and the F-H expression for free energy of mixing. The components were prepared by saturating the double bonds of nearly monodisperse polybutadienes (78, 88, and 97% vinyl content) with H<sub>2</sub> and D<sub>2</sub>. Those values were

found to be insensitive to the component volume fractions for  $\phi = 0.25, 0.50$  and  $0.75$ . Likewise,  $\chi$  should in principle be independent of chain length as well as other features of the large scale chain architecture. Empirically, the temperature dependence of the F-H interaction parameter is often written as the sum of two terms:

$$\chi = a + \frac{b}{T} \quad (2.4)$$

where  $a$  and  $b$  specify the enthalpic and entropic parts of  $\chi$ . In addition, the parameters  $a$  and  $b$  are often found to depend weakly on chain lengths and composition. The Flory-Huggins equation contains all of the thermodynamic information needed to decide the equilibrium state of a mixture and whether any metastable states are possible, as discussed next.

### 2.2.1.2 Phase diagrams

A phase diagram can be constructed to summarize the phase behavior of the mixture, showing regions of stability, instability, and metastability. The binodal curve is determined by the common tangent of the free energy at the compositions  $\phi^I$  and  $\phi^{II}$  corresponding to the two equilibrium phases

$$\left( \frac{\partial F_{mix}}{\partial \phi} \right)_{\phi=\phi^I} = \left( \frac{\partial F_{mix}}{\partial \phi} \right)_{\phi=\phi^{II}} \quad (2.5)$$

The derivative of the free energy of mixing per site with respect to the volume fraction of component 1 is

$$\begin{aligned} \frac{\partial F_{mix}}{\partial \phi_1} &= \mu \\ &= k_B T \left[ \frac{\ln \phi_1}{N_1} + \frac{1}{N_1} - \frac{\ln(1-\phi_1)}{N_2} - \frac{1}{N_2} + \chi(1-2\phi_1) \right] \end{aligned} \quad (2.6)$$

where  $\mu$  is the exchange chemical potential (or more briefly the exchange potential) <sup>[6]</sup>. Notice that this purely entropic contribution diverges at both extremes of composition ( $\partial F_{mix}/\partial \phi_1 \rightarrow -\infty$  as  $\phi_1 \rightarrow 0$  and  $\partial F_{mix}/\partial \phi_1 \rightarrow \infty$  as  $\phi_1 \rightarrow 1$ ). This divergence means that a small amount of either species will always dissolve even if there are strong unfavourable energetic interactions.

Many demixed states have lower free energy than the homogeneous state, but the

lowest free energy state defines the equilibrium state. Straight lines connecting the two phase compositions determine the free energy of the phase separated state. In order to minimize the free energy, the system chooses the compositions that have the lowest possible straight line, which is a common tangent. The phases present are thus determined by the common tangent rule. This common tangent minimization of the free energy of mixing effectively requires that the chemical potential of each species in both phases are balanced at equilibrium. The two equilibrium compositions  $\phi_p$  and  $\phi_q$  correspond to the tangency points of a common tangent line. For any overall composition in the miscibility gap between  $\phi_p$  and  $\phi_q$ , the system can minimize its free energy by phase separating into two phases of composition  $\phi_p$  and  $\phi_q$ . The amounts of each phase are determined by the lever rule. The composition ranges  $0 < \phi < \phi_p$  or  $\phi_q < \phi < 1$  are outside the miscibility gap and the homogeneously mixed state is the stable equilibrium state for these blend compositions.

The binodal curve is calculated by simultaneously solving the following two equations

$$\ln\left(\frac{\phi_1^I}{\phi_1^{II}}\right) + (\phi_1^{II} - \phi_1^I)(1 - N_1 / N_2) + \chi N_1 [(1 - \phi_1^I)^2 - (1 - \phi_1^{II})^2] = 0 \quad (2.7)$$

$$\ln\left(\frac{1 - \phi_1^I}{1 - \phi_1^{II}}\right) + (\phi_1^I - \phi_1^{II})(1 - N_2 / N_1) + \chi N_2 [(\phi_1^I)^2 - (\phi_1^{II})^2] = 0 \quad (2.8)$$

where  $\phi_1^I$  and  $\phi_1^{II}$  are the volume fractions of polymer 1 in the two coexisting phases labeled I and II.

The second derivative of the free energy with respect to  $\phi_1$  is given by

$$\frac{\partial^2 F_{mix}}{\partial \phi_1^2} = k_B T \left[ \frac{1}{N_1 \phi_1} + \frac{1}{N_2 (1 - \phi)} - 2\chi \right] \quad (2.9)$$

Returning to the general case of an asymmetric blend, the inflection points in  $F_{mix}(\phi)$  can be found by equating the second derivative of the free energy Eq. (2.10) to zero:

$$\partial^2 F_{mix} / \partial \phi_1^2 = 0 \quad (2.10)$$

The curve corresponding to the inflection point is the boundary between unstable

and metastable regions and is called the spinodal.

## 2.2.2 DPD simulation

In the DPD simulation, the time evolution of motion for a set of interacting particles is solved by Newton's equation <sup>[7]</sup>:

$$\frac{d\mathbf{r}_i}{dt} = \mathbf{v}_i; \quad \frac{d\mathbf{v}_i}{dt} = \mathbf{f}_i. \quad (2.11)$$

where  $\mathbf{r}_i$  and  $\mathbf{v}_i$  are the position and velocity of the  $i$ th particle. For this method, the force acting on a particle contains three pairwise additive parts:

$$\mathbf{f}_i = \sum_{j \neq i} (\mathbf{F}_{ij}^C + \mathbf{F}_{ij}^D + \mathbf{F}_{ij}^R) \quad (2.12)$$

where  $\mathbf{F}^C$ ,  $\mathbf{F}^D$  and  $\mathbf{F}^R$  respectively represent conservative, dissipative, and random forces, and the sum runs over all other particles within a certain cutoff radius  $r_c$ . As this is the only length-scale in the system, cutoff radius is always used as the unit of length,  $r_c = 1$ . The different parts of the forces are given by

$$\mathbf{F}_{ij}^C = \begin{cases} a_{ij}(1 - r_{ij})\mathbf{e}_{ij} & (r_{ij} < 1) \\ 0 & (r_{ij} \geq 1) \end{cases} \quad (2.13)$$

$$\mathbf{F}_{ij}^D = -\gamma\omega^D(r_{ij})(\mathbf{e}_{ij} \cdot \mathbf{v}_{ij})\mathbf{e}_{ij} \quad (2.14)$$

$$\mathbf{F}_{ij}^R = \sigma\omega^R(r_{ij})\zeta_{ij}\Delta t^{-1/2}\mathbf{e}_{ij} \quad (2.15)$$

where  $\mathbf{r}_{ij} = \mathbf{r}_i - \mathbf{r}_j$ ,  $r_{ij} = |\mathbf{r}_{ij}|$ ,  $\mathbf{e}_{ij} = \mathbf{r}_{ij}/r_{ij}$ , and  $\mathbf{v}_{ij} = \mathbf{v}_i - \mathbf{v}_j$ .  $\zeta_{ij}$  is a random number with zero mean and unit variance.  $a_{ij}$  is a constant which describes the maximum repulsion between interacting beads.  $\omega^D$  and  $\omega^R$  stand for  $r$ -dependent weight functions for the dissipative and random forces, respectively, and they vanish for  $r > r_c = 1$ . Unlike the conservative force, the weight functions  $\omega^D(r_{ij})$  and  $\omega^R(r_{ij})$  of the dissipative and random forces couple together to form a thermostat. Español and Warren have shown that there is the following fluctuation-dissipation theorem in the dissipative force and the random force <sup>[8]</sup>:

$$\omega^D(r) = [\omega^R(r)]^2 \quad \sigma^2 = 2\gamma k_B T \quad (2.16)$$

The weight functions are chosen simply by:

$$\omega^D(r) = [\omega^R(r)]^2 = \begin{cases} (1-r)^2 & (r < 1) \\ 0 & (r \geq 1) \end{cases} \quad (2.17)$$

A modified version of the velocity-Verlet algorithm <sup>[9]</sup> is used here:

$$\begin{aligned} \mathbf{r}_i(t + \Delta t) &= \mathbf{r}_i(t) + \Delta t \mathbf{v}_i(t) + (\Delta t)^2 \mathbf{f}_i(t)/2, \\ \mathbf{v}_{\square i}(t + \Delta t) &= \mathbf{v}_i(t) + \lambda(\Delta t) \mathbf{f}_i(t), \\ \mathbf{f}_i(t + \Delta t) &= \mathbf{f}_i(\mathbf{r}(t + \Delta t), \mathbf{v}_{\square i}(t + \Delta t)), \\ \mathbf{v}_i(t + \Delta t) &= \mathbf{v}_i(t) + \Delta t(\mathbf{f}_i(t) + \mathbf{f}_i(t + \Delta t))/2. \end{aligned} \quad (2.18)$$

In particular, herein, we choose  $\lambda = 0.65$  and  $\Delta t = 0.05$  <sup>[10]</sup>.

The soft-sphere interactions of DPD can be mapped onto Flory-Huggins theory through the  $\chi$  parameter <sup>[11]</sup>. If the system has  $i$  and  $j$  components or beads interacting with each other and if one chooses  $a_{ii} = a_{jj}$  and assumes that  $\rho_i + \rho_j$  is approximately constant, then, according to Groot and Warren, the mapping relation is

$$\chi = \frac{2\alpha(a_{ij} - a_{ii})(\rho_i + \rho_j)}{k_B T} \quad (2.19)$$

where  $\alpha$  is a parameter related to the pair-correlation function  $g(r)$ , which is expressed as a function of the reduced coordinate  $r = \mathbf{r}/r_c$ , and  $\rho_i + \rho_j = \rho$  is the density of the system.

The conservative interaction strength  $\alpha_{ij}$  was chosen according to the linear relation with Flory–Huggins  $\chi$  parameters for polymers

$$\alpha_{ij} = \alpha_{ii} + 3.27\chi_{ij} \quad (\rho = 3) \quad (2.20)$$

The interaction parameter between the same type beads  $\alpha_{ii}$  equals 25.

The DPD simulations of the UHMWPE/NMWP blends were performed in a cell of size  $30 \times 30 \times 30$ , with the bead density  $\rho=3$ . Periodic boundary conditions were applied and the shear flow was simulated by means of Lees–Edwards boundary conditions which were illustrated in Figure 2.3 <sup>[12]</sup>. For convenience, the particle mass  $m$ , and  $k_B T$  were all taken as unit. The time step  $\Delta t$  was taken as 0.05 <sup>[13]</sup>, and adjacent particles in the polymer chain interacted via a linear spring with a harmonic spring constant of 4.0, according to Groot and Liu <sup>[14-16]</sup>. Moreover the friction coefficient  $\gamma$  was chosen as 4.5 <sup>[16]</sup>.

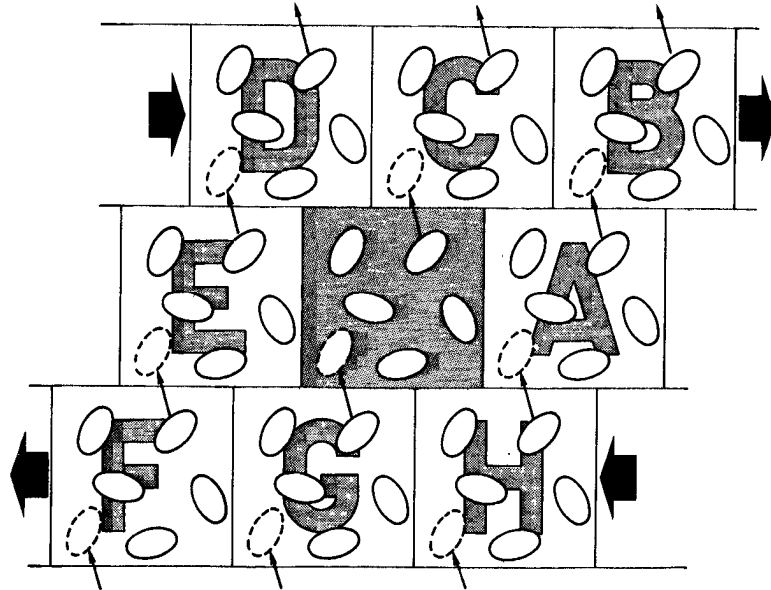


**Figure 2.3** Lees–Edwards boundary conditions. The infinite periodic system is subjected to a uniform shear in the  $xy$  plane. The simulation box and its images centred at  $(x, y) = (\pm kL, 0)$ , ( $k$  is positive integer), (e.g. A, E) are taken to be stationary. Boxes in the layer above,  $(x, y) = (\pm kL, mL)$ , ( $m$  is positive integer), (e.g. B, C, D) are moving at a speed  $(dv_x/dr_y)L$  in the positive  $x$  direction. Boxes in the layer below,  $(x, y) = (\pm kL, -mL)$ , (e.g. F, G, H) move at a speed  $-(dv_x/dr_y)L$  in the negative  $x$  direction.

SEM observations show that the as-received M-II powder is made of major particles with an average diameter of about  $300 \mu\text{m}$ . These major particles are in turn made of minor particles with diameters of about  $10 \mu\text{m}$ . The minor particles are aggregates of yet smaller, submicron particles. Some fibrillar bridges between these discrete particles indicate partial melting during synthesis (Figure 2.4). Additionally, it is easier for NMWP to be plasticized, compared with UHMWPE. Therefore, UHMWPE is encapsulated completely by NMWP in the initial configuration, which is described as a core-shell initial configuration. A so-called random initial configuration, namely, UHMWPE and NMWP are randomly distributed, is also adopted.

The number of beads in each mesoscale molecule is determined by the degree of polymerization and the characteristic ratio ( $C_n$ ) of the polymer. Table 2.2 lists the characteristic ratios, molecular weights and the corresponding DPD chain lengths of the species in this work.

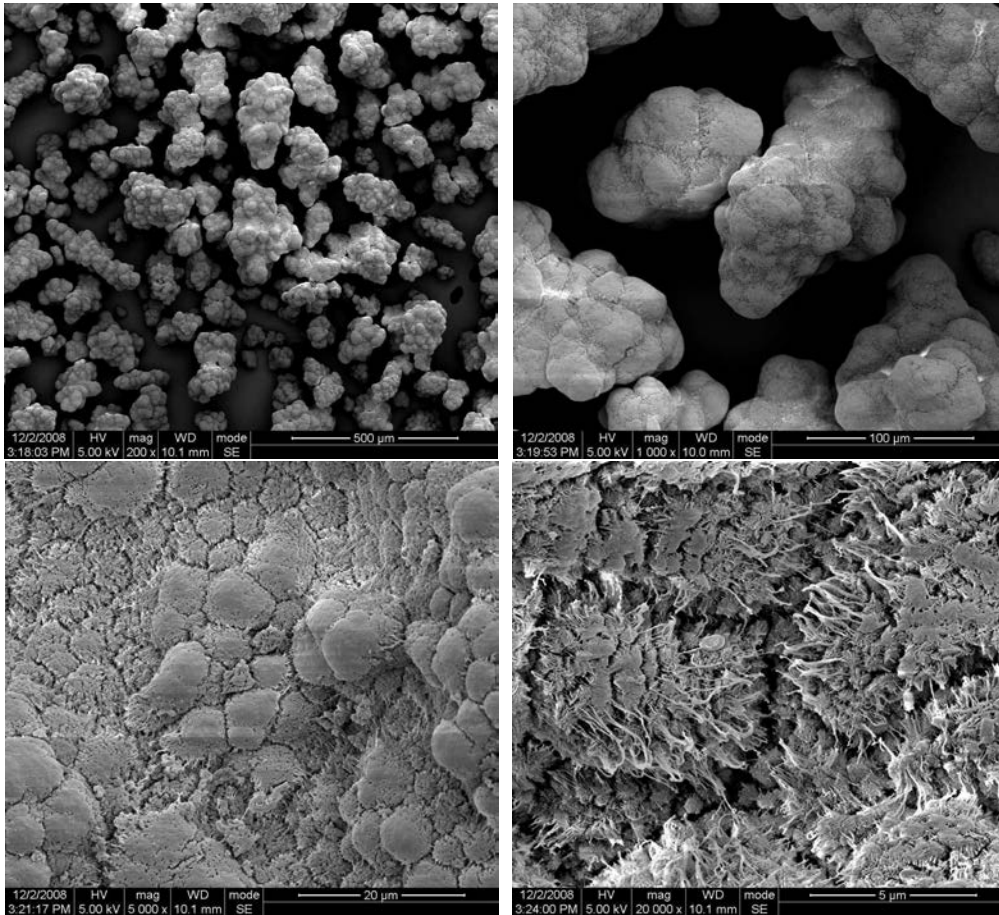


**Figure 2.4** SEM of UHMWPE powder.

**Table 2.2** Characteristic ratios, molecular weights and the corresponding DPD chain lengths of the species in the UHMWPE blends.

Species	$M_p$	$C_n$	$N_{DPD}$
UHMWPE	$2.5 \times 10^6$	7.7	11600
PP	$7.3 \times 10^4$	6.9	250
HDPE	$5.4 \times 10^4$	7.7	250
PEG	$5.5 \times 10^4$	5.0	250

### 2.2.3 MesoDyn simulation

The basic idea in the MesoDyn method is the density function theory. The latter is based on the concept that the free energy  $F$  of an inhomogeneous liquid is a function of the local density function  $\rho$ . From the free energy, all thermodynamic functions can be derived.

The model used in the MesoDyn project consists of beads of various types, I, J, ..., with interactions described by harmonic oscillator potentials for the intramolecular interactions (Gaussian chain) and a mean-field potential for all other interactions <sup>[17]</sup>. Each bead is a certain component type representing covalently bonded groups of atoms such as those given by one or a few structural units of a polymer chain. The dynamics of the system is described by a set of functional Langevin equations, and these equations are the diffusion equations in the component densities, which take account of the noise in the system.

On a coarse-grained time scale,  $\rho_1^0(r)$  is defined as a collective concentration field of the beads of type I at an instant in time and serve as a reference level. There will be a certain distribution of bead positions, defined as  $\Psi(R_{11}, \dots, R_{nN})$ , where  $R_{\gamma s}$  is the position of a bead  $s$  from chain  $\gamma$ . Given the distribution  $\Psi$ , we can define the collective concentration of beads  $s$  from all chains by the average of a microscopic density operator:

$$\rho_1[\Psi](r) \equiv \sum_{\gamma=1}^n \sum_{s=1}^N \delta_{1s}^K Tr \Psi \delta(r - R_{\gamma s}) \quad (2.21)$$

Where  $\delta_{1s}^K$  is the Kronecker function with a value of 1 when bead  $s$  is of type I and 0 otherwise. It is assumed that in the slowly relaxing liquid the interactions do not depend on the momentum.

A set of distribution functions  $\Psi$  with the constraint  $\rho_1[\Psi](r) = \rho_1^0(r)$ :

$$\Omega = \left\{ \Psi(R_{11}, \dots, R_{nN}) \mid \rho_1[\Psi](r) = \rho_1^0(r) \right\} \quad (2.22)$$

All distributions  $\Psi$  of the set  $\Omega$  lead to the same density  $\rho_1^0(r)$ . On the basis of this set of distribution functions, an intrinsic free-energy functional  $F[\Psi]$  can be defined:

$$F[\Psi] = Tr(\Psi H^{id} + \beta^{-1} \Psi \ln \Psi) + F^{nid}[\rho^0] \quad (2.23)$$

The first term is the average value of the Hamiltonian for internal Gaussian chain interactions <sup>[18, 19]</sup>. The second term in the free energy functional represents the Gibbs entropy of the distribution  $-k_B T \Psi \ln \Psi$ . The third term  $F^{nid}[\rho^0]$  is the mean-field nonideal contribution.

The key rudiment of dynamic density functional theory is that now on a coarse-grained time scale, the distribution function  $\Psi$  is such that the free-energy functional  $F[\Psi]$  is minimized. Hence,  $\Psi$  is independent of the history of the system and is fully characterized by the constraints that it represents the density distribution and minimizes the free-energy functional. This constraint on the density fields is realized by means of an external potential  $U_I$ .

The constraint minimization of the free-energy functional leads to an optimal distribution, which in turn, and by the one-to-one relation between densities, distributions, and external potential, can be written as

$$\beta F[\rho] = n \ln \Phi + \beta^{-1} \ln n! - \sum_I \int U_I(r) \rho_I(r) dr + \beta F^{\text{nid}}[\rho] \quad (2.24)$$

Finally, the non-ideal free energy function is introduced,

$$F^{\text{nid}}[\rho] = \frac{1}{2} \int \int \left[ \epsilon_{AA}(|r-r'|) \rho_A(r) \rho_A(r') + \epsilon_{AB}(|r-r'|) \rho_A(r) \rho_B(r') + \epsilon_{BA}(|r-r'|) \rho_B(r) \rho_A(r') + \epsilon_{BB}(|r-r'|) \rho_B(r) \rho_B(r') \right] dr dr' \quad (2.25)$$

where  $\epsilon_{IJ}(|r-r'|)$  is a mean-field energetic interaction between beads of type I at  $r$  and type J at  $r'$ .

The mean-field intrinsic chemical potentials can easily be derived by functional differentiation of the free energy:  $\mu_I(r) = \delta F / \delta \rho_I(r)$ . At equilibrium,  $\mu_I(r) = \text{constant}$ , which results in the familiar self-consistent-field equations for the mean-field Gaussian chain model. In general, these equations have many solutions, one of which is a state of lowest free energy, most states being metastable. On the basis of these equations, the generalized time dependent Ginzburg-Landau theory can be set up.

The following functional Langevin equations for diffusive dynamics of the density fields are also introduced:

$$\frac{\partial \rho_A}{\partial t} = M \nu_B \nabla \rho_A \rho_B \nabla [\mu_A - \mu_B] + \eta \quad (2.26)$$

$$\frac{\partial \rho_B}{\partial t} = M \nu_B \nabla \rho_A \rho_B \nabla [\mu_B - \mu_A] + \eta \quad (2.27)$$

Here,  $M$  is a bead mobility parameter. The kinetic coefficient  $M \nu_A \nu_B$  models a local exchange mechanism.

The distribution of the Gaussian noise satisfies the fluctuation-dissipation

theorem:

$$\langle \eta(r, t) \rangle = 0 \quad (2.28)$$

$$\langle \eta(r, t) \eta(r', t') \rangle = -\frac{2Mv_B}{\beta} \delta(t-t') \nabla_r \times \delta(t-t') \rho_A \rho_B \nabla_{r'} \quad (2.29)$$

The Langevin equations are constructed for an incompressible system with dynamic constraint:

$$(\rho_A(r, t) + \rho_B(r, t)) = \frac{1}{v_B} \quad (2.30)$$

where  $v_B$  is the average bead volume.

In the MesoDyn method, the molecules are defined on a coarse-grained level as “Gaussian chains of beads”. Each bead is of a certain component type representing covalently bonded groups of atoms such as those given by one or a few monomers of a polymer chain. Chemically specific information about the molecular ensemble enters MesoDyn via material parameters such as the self-diffusion coefficients of the bead components, the Flory-Huggins interaction parameters, the bead sizes, and the molecular architecture (chain length, branching, etc.).

The dynamics of the system is described by a set of so-called functional Langevin equations. In simple terms, these are diffusion equations in the component densities that take account of the noise in the system. By means of numerical inversions, the evolution of the component densities is simulated, starting from an initially homogeneous mixture in a cube and with periodic boundary conditions. The dimensions of the simulation lattice were  $30 \times 30 \times 30$ . All bead diffusion coefficients are  $1.0 \times 10^{-7} \text{ cm}^2 \text{ s}^{-1}$ . The simulation temperature was 298 K, and the time step was 50.0 ns.

## 2.3 References

1. Staverman AJ, Van Saten JH. Recl Trav Chim 1941, 60, 76.
2. Huggins ML. Some Properties of Solutions of Long-chain Compounds. J Phys Chem 1942, 46, 151.
3. Flory P J. Thermodynamics of High Polymer Solutions. J Chem Phys 1942, 10,

- 51.
4. Michael rubinstein, Colby RH. Polymer Physics. Oxford University Press, 2003. p143.
  5. Balsara NP, Fetters LJ, Hadjichristidis N, Lohse DJ. Thermodynamic interactions in model polyolefin blends obtained by small-angle neutron scattering. *Macromolecules* 1992, 25, 6137.
  6. Pierre-Gilles de Gennes. Scaling Concepts in Polymer Physics. CORNELL UNIVERSITY PRESS, Ithaca and London, 1979.
  7. Groot RD, Warren PB. Dissipative particle dynamics: Bridging the gap between atomistic and mesoscopic simulation. *J Chem Phys* 1997, 107, 4423.
  8. Español P, Warren PB. Statistical Mechanics of Dissipative Particle Dynamics. *Europhys Lett* 1995, 30, 191.
  9. Allen MP, Tildesley DJ. Computer Simulation of Liquids. Clarendon, Oxford, 1987.
  10. Huang CI, Chiou YJ, Lan YK. Phase behavior of an amphiphilic molecule in the presence of two solvents by dissipative particle dynamics. *Polymer* 2007, 48, 877.
  11. Groot RD, Madden TJ. Dynamic simulation of diblock copolymer microphase separation. *J Chem Phys* 1998, 108, 8713.
  12. Allen MP, Tildesley DJ. Computer Simulation of Liquids (Clarendon, Oxford, 1987).
  13. Liu DH, Zhong CL. Cooperative Self-Assembly of Nanoparticle Mixtures in Lamellar Diblock Copolymers: A Dissipative Particle Dynamics Study. *Macromol Rapid Commun* 2006, 27, 458.
  14. Groot RD. Electrostatic interactions in dissipative particle dynamics - simulation of polyelectrolytes and anionic surfactants. *J Chem Phys* 2003, 118, 11265.
  15. Özen AS, Sen U, Atilgan C. Complete mapping of the morphologies of some linear and graft fluorinated co-oligomers in an aprotic solvent by dissipative particle dynamics. *J Chem Phys* 2006, 124, 064905.
  16. Liu DH, Zhong CL. Multicompartment micelles formed from star-dendritic triblock copolymers in selective solvents: A dissipative particle dynamics study.

Polymer 2008, 49, 1407.

17. Doi M, Edwards SF, The theory of polymer dynamics. Oxford Science Publications: Oxford, 1986.

18. Barber MN, Ninham BW. Random and Restricted Walks; Gordon and Breach: New York, 1970.

19. Etelvino JH, Bechara AlfonsL, Baumstark. Therese Wilson Tetraethyldioxetane and 3,4-dimethyl-3,4 -di-n-butyl-1,2-dioxetane. High ratio of triplet to singlet excited products from the thermolysis of both dioxetanes. J Am Chem Soc 1976, 98, 6468.

# CHAPTER 3 Phase Morphologies and Rheological Behaviors of UHMWPE/NMWP Blends

## 3.1 Introduction

As stated in Chapter 1, UHMWPE and its composites are widely used as bearing components, gears, guide rails and medical materials in total joint replacement hydrophobic nature, chemical resistance and mechanical properties. However, processing UHMWPE is problematic due to its high molecular weight. It induces a very high melt viscosity that prevents UHMWPE from being processed by conventional melt processes (extrusion and injection molding).

An effective way to reduce the melt viscosity is to dilute the UHMWPE with normal molecular weight polymer (NMWP) <sup>[1, 2]</sup>. On the basis of previous investigations <sup>[3 - 6]</sup>, this chapter reports on the mechanism of viscosity reduction of the UHMWPE/NMWP binary blends is further studied by SEM observations, DPD simulations and rheological measurements. Conventional PE (HDPE and LDPE) and PP are used as examples to show the effects of the interaction parameter  $\chi$  on the morphology of the UHMWPE/NMWP binary blend. The Flory-Huggins theory is also adopted to predict the optimum processing conditions including the composition, the parameter  $\chi$  and molecular weight of NMWP in the binary blends.

## 3.2 Results and discussion

### 3.2.1 Morphology of the UHMWPE/NMWP blends

Generally, the rheological behavior of polymer blends strongly depends on their mesoscopic structures in the melt state <sup>[7]</sup>. In this section, we use DPD simulation to

investigate the effects of the parameter  $\chi$ , chain length and the volume fraction of NMWP on the mesoscopic morphology and the rheological behavior of the blends of UHMWPE with HDPE ( $\chi = 0$ ), PP ( $\chi = 9 \times 10^{-3}$ ) and LDPE [the measured  $\chi$  values for PE blends with small differences in branch contents ( $< 30$ ) from SANS are usually less than  $6 \times 10^{-4}$ ] [8]

### 3.2.1.1 UHMWPE/HDPE blends

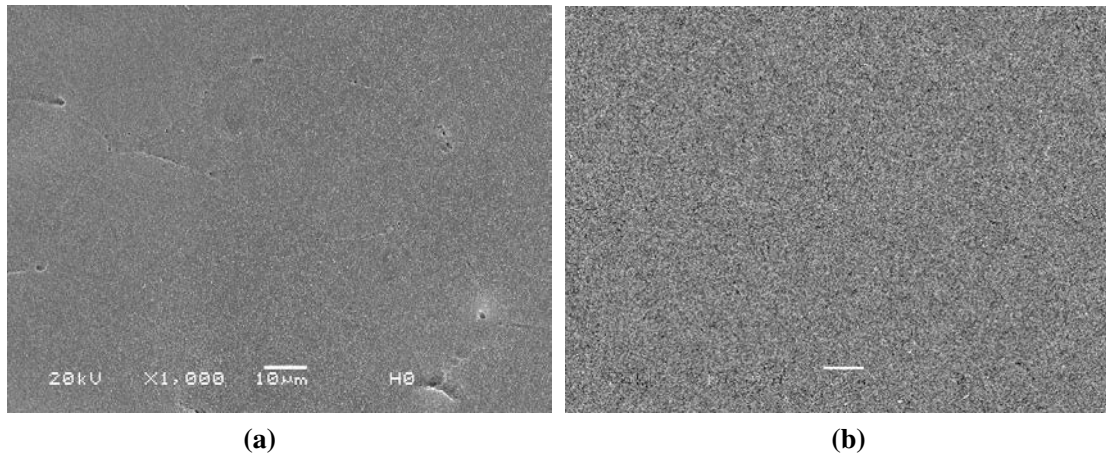


**Figure 3.1** SEM micrographs of cryogenically fractured surfaces of UHMWPE after etching. The scale bars in (a) and (b) are 10 and 1 μm, respectively.

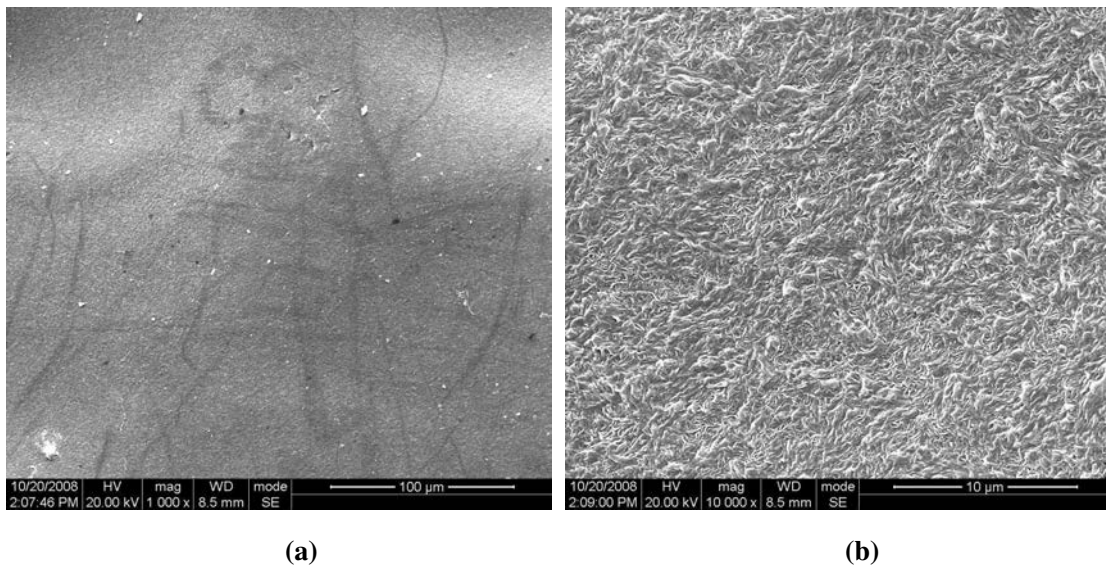


**Figure 3.2** SEM micrographs of cryogenically fractured surfaces after etching for the HDPE. The scale bars in (a) and (b) are 100 and 10 μm, respectively.

The unique difference between UHMWPE and HDPE resides in molecular weight. Their microstructures are supposed to be identical. Hence, HDPE is usually used to disentangle UHMWPE chains and improve its processability. However, both two-phase and homogeneous phase structures are reported for the UHMWPE/HDPE blend. Hence, the effects of HDPE on the morphologies of UHMWPE blends are investigated by both DPD simulations and SEM observations.

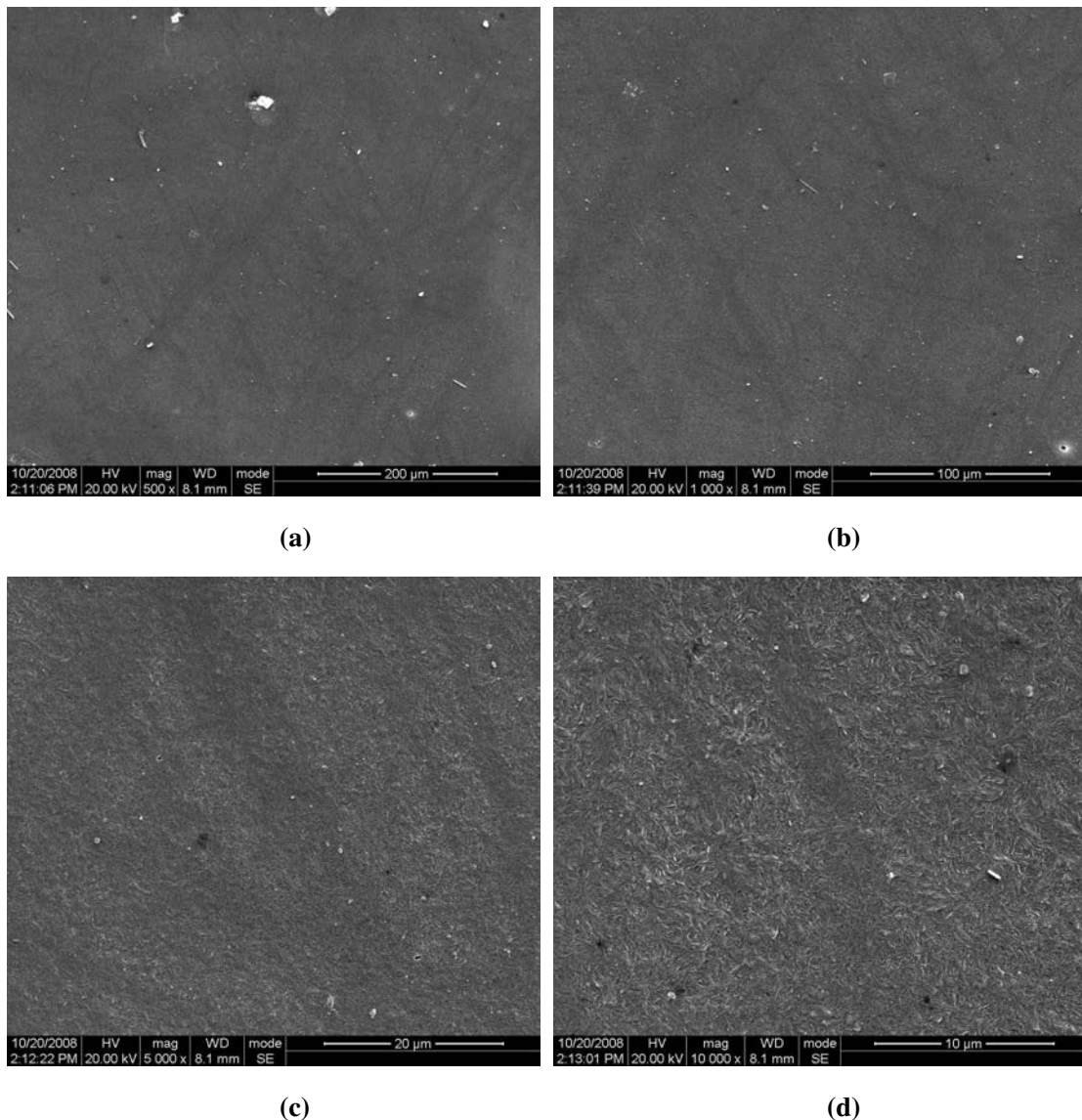


**Figure 3.3** SEM micrographs of cryogenically fractured surfaces after etching for the UHMWPE/HDPE blend mixed for 5 minutes. The scale bars in (a), (b), (c) and (d) are 200, 100, 20 and 10 μm, respectively.

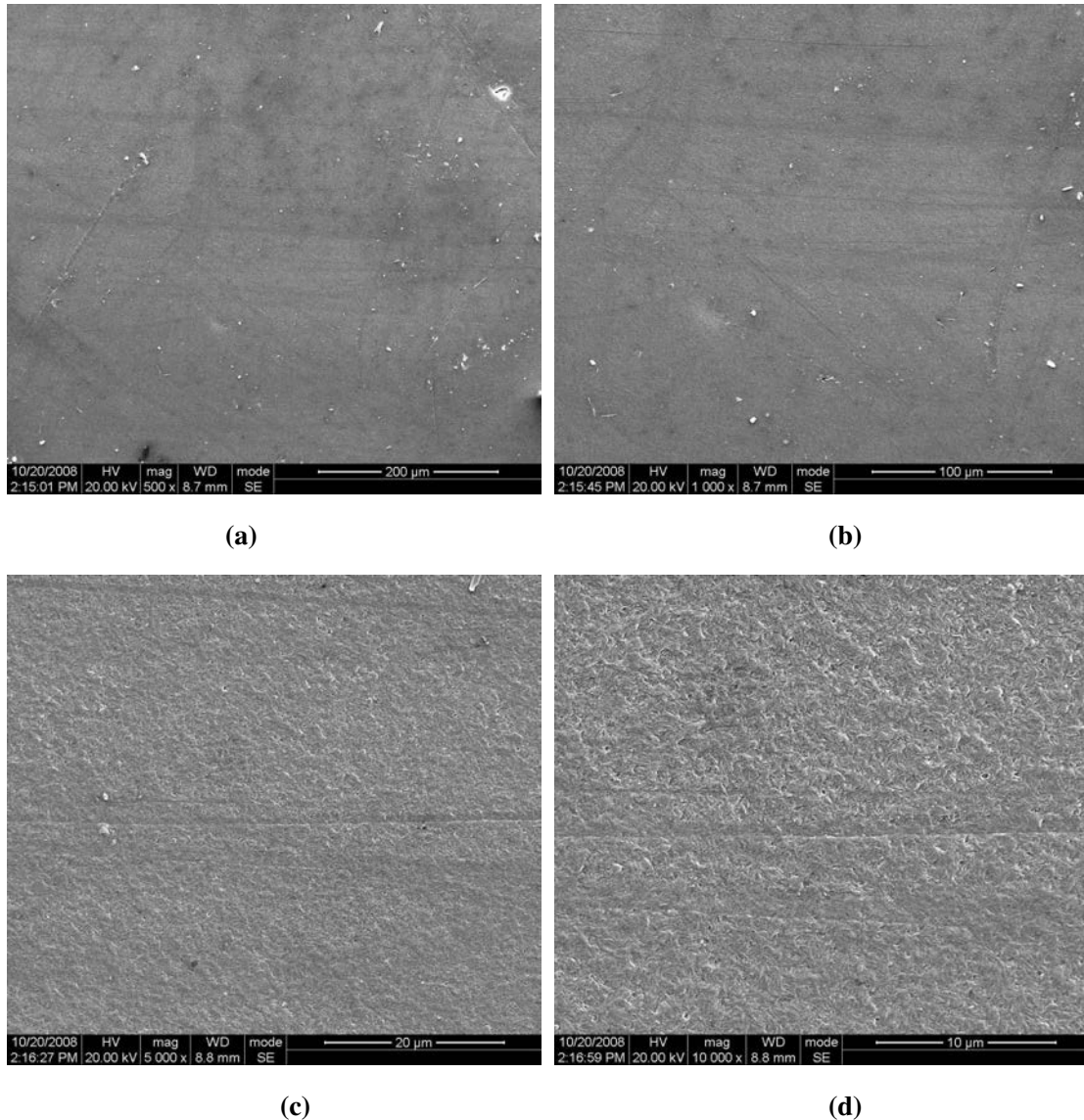


**Figure 3.4** SEM micrographs of cryogenically fractured surfaces after etching for the UHMWPE/HDPE blend mixed for 40 minutes. Scale bars are like in Figure 3.3.

Figures 3.1 – 3.4 show the SEM micrographs of the cryogenically fractured surfaces at different magnifications of UHMWPE, HDPE and the UHMWPE/HDPE (50/50) blend with the amorphous phase being etched. Both UHMWPE and HDPE show characteristic fibril-like crystal morphology (Figures 3.1 and 3.2). However, the lamellas of UHMWPE are more uniform than those of HDPE. After 5 minutes of mixing, the crystal domains of HDPE and UHMWPE could not be distinguished in the UHMWPE/HDPE (50/50) blend (Figure 3.3). Furthermore, as the plasticating time increases to 40 minutes, the change in the homogeneous phase structure is minor, suggesting that the diffusion of HDPE into UHMWPE is fast and that the miscibility

between HDPE and UHMWPE is good (Figure 3.4).

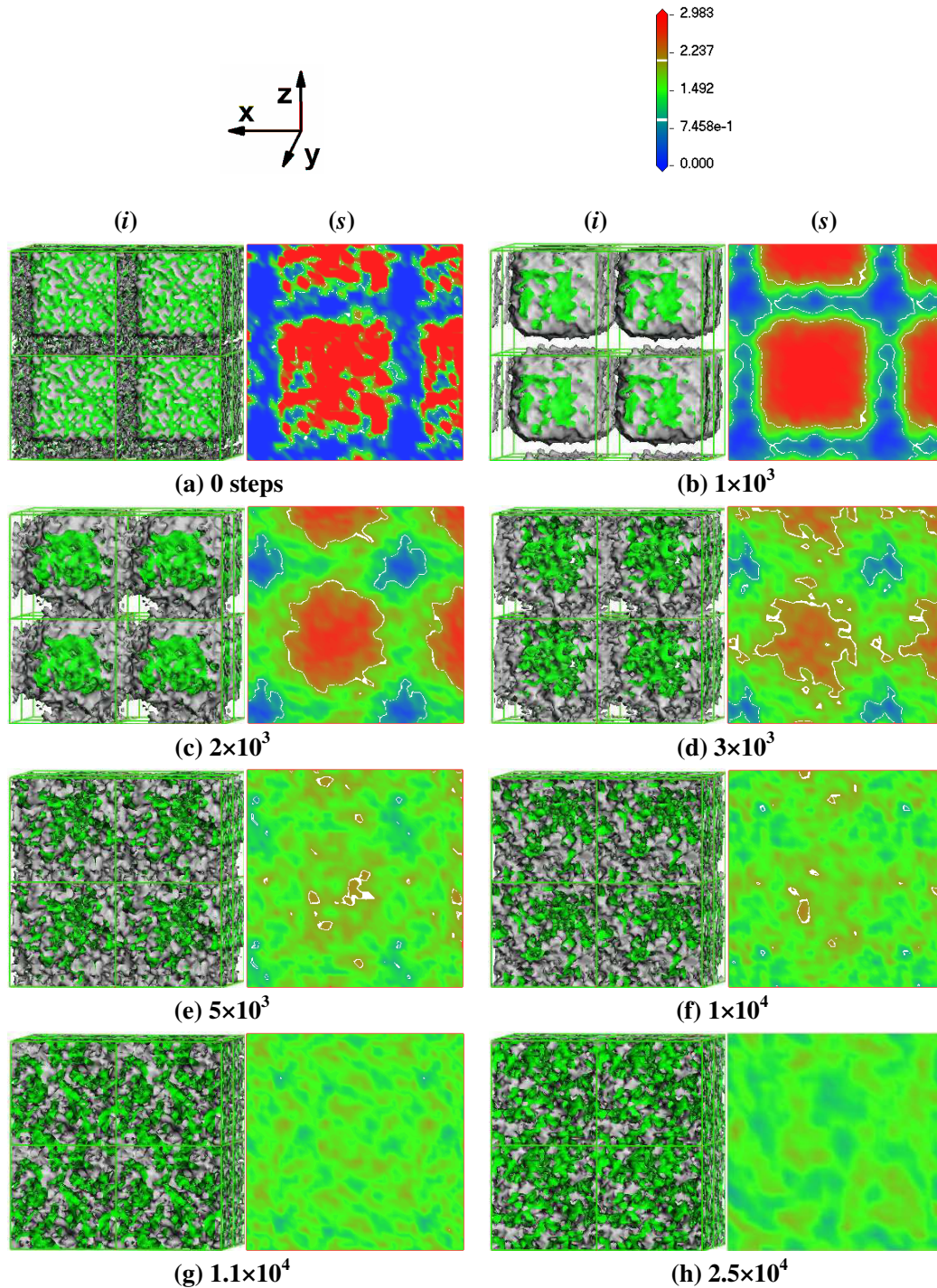


**Figure 3.5** The UHMWPE/HDPE (50/50) blend is simulated from a core-shell initial configuration (UHMWPE and HDPE are the core and shell, respectively). (i): time evolution of iso-density surfaces of HDPE, The outward surfaces of the HDPE phases are colored with green, and the rests are UHMWPE phases; (s): the corresponding slices perpendicular to y axis (the legend shows the magnitudes of density in the slices denoted by different colors that vary from 0.000 to 3.000); the high density region of the UHMWPE are colored with red; the iso-density line of the UHMWPE for  $\rho = 1.00$  and  $2.00$  are colored with white.

The DPD simulations originated from the core-shell initial configuration are used to evaluate the evolution of the morphology with time for the UHMWPE/HDPE blend. The one with a composition of 50/50 was taken as an example. Figure 3.5 shows snapshots of the morphologies of the blend in the evolution process. Figures 3.5(a) - (d) show an obvious increase in the interface thickness after  $1 \times 10^3$  steps of simulation, confirming good miscibility between the two polymers. From Figure 3.5(e), the interfacial thickness increases continuously. Additionally, the high density region ( $\rho \geq 2.000$  DPD units) of the HDPE has almost disappeared whereas that of the UHMWPE remains relatively important in the blend. In the next stage, both the interface and high density region of the UHMWPE vanish, and the UHMWPE/HDPE (50/50) blend approximately possesses a homogeneous phase after  $1.1 \times 10^4$  time steps [Figure 3.5(g)]. At last this structure evolves very little with time. Finally the blend reaches a homogeneous phase in Figure 3.5(h). The homogeneous phase morphology of the UHMWPE/HDPE (50/50) blend is also corroborated by its density profile. There is virtually no fluctuation in density distributions for the UHMWPE and HDPE after  $1.1 \times 10^4$  time steps [Figure 3.6]. The evolution process of the morphology for the UHMWPE/HDPE (50/50) blend suggests that the initial diffusion rates for both UHMWPE and HDPE are very rapid and they become slow after 5000 time steps, which is totally consist with the SEM observations.

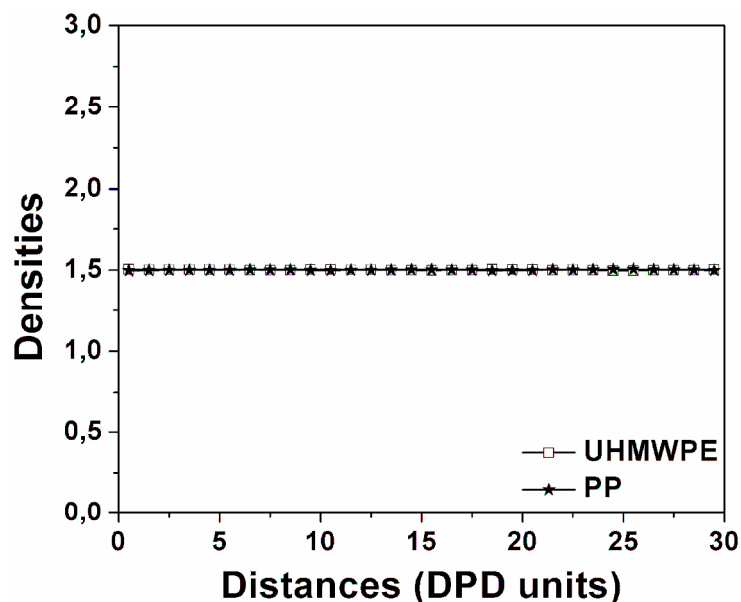


**Figure 3.6** Density profiles of the simulated UHMWPE/HDPE (50/50) blend after  $1.1 \times 10^4$  time steps.

A random initial configuration is also adopted to investigate the effect of the initial configuration on the equilibrium state morphology of the UHMWPE/HDPE (50/50) blend. As shown in Figure 3.7, the morphology resulting from the random initial configuration is also a homogeneous phase, suggesting that the simulation time together with  $2.5 \times 10^4$  steps is enough to obtain the equilibrium state structure of the UHMWPE/HDPE (50/50) blend.

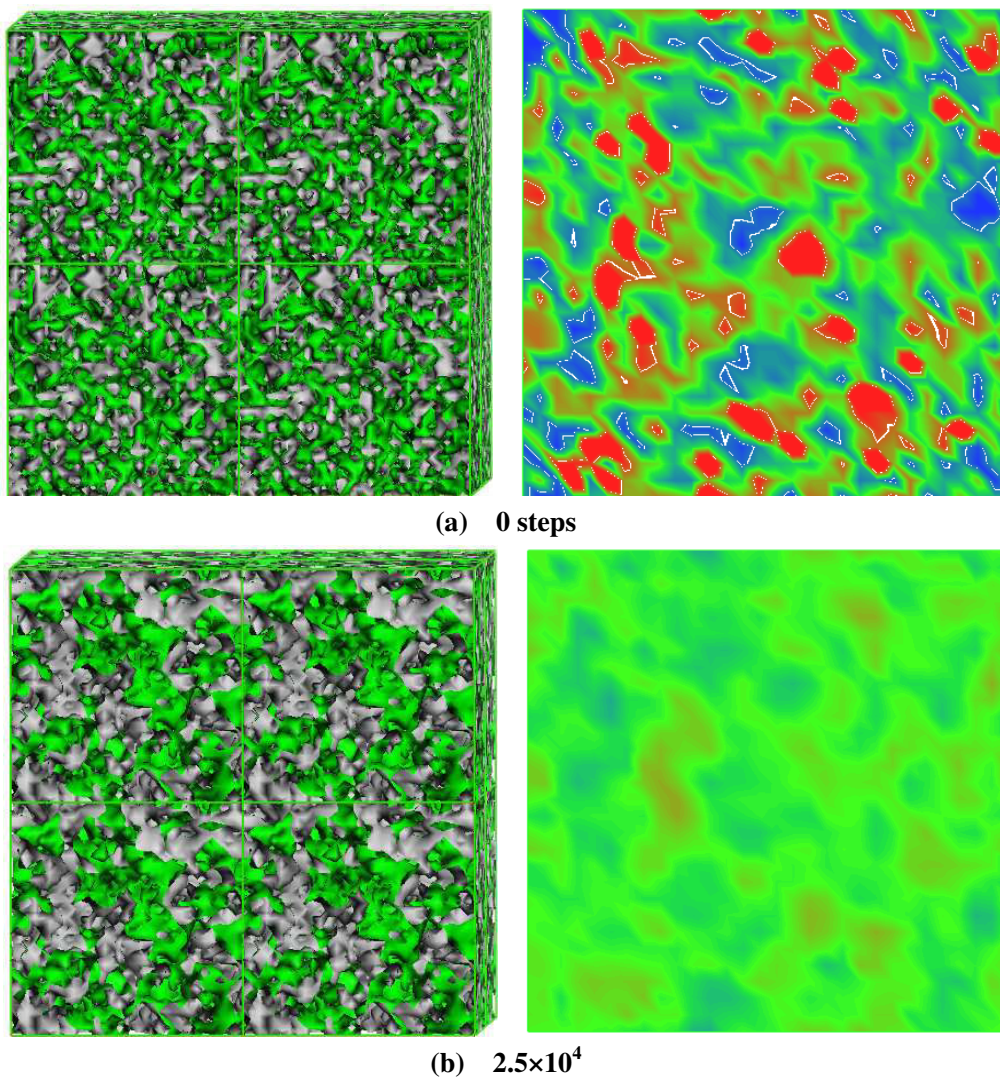


**Figure 3.7** The UHMWPE/HDPE (50/50) blend is simulated from a random initial configuration. The others are the same as those in Figure 3.5.

### 3.2.1.2 UHMWPE/LDPE blends

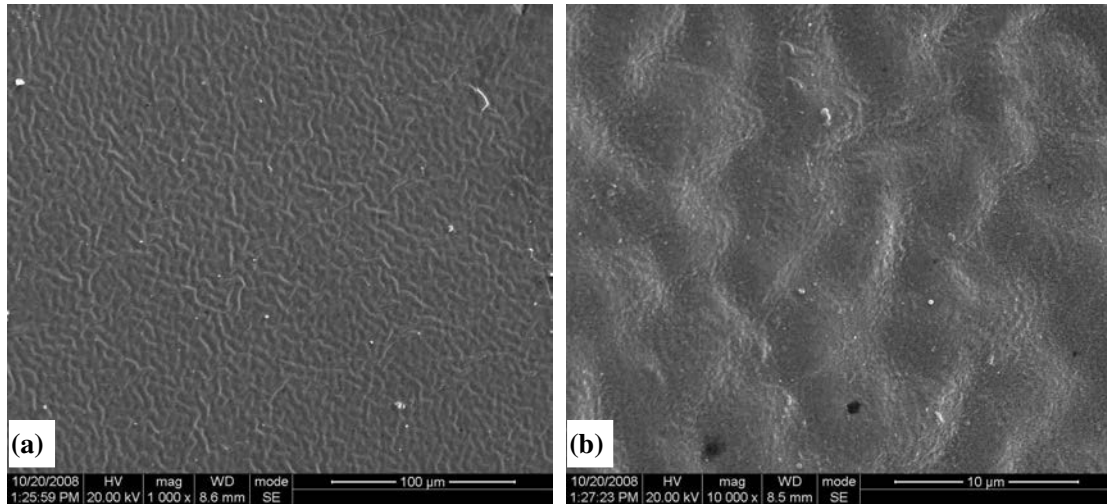


**Figure 3.8** SEM micrographs of cryogenically fractured surfaces of LDPE after etching. The scale bars in (a) and (b) are 100 and 10  $\mu\text{m}$ , respectively.

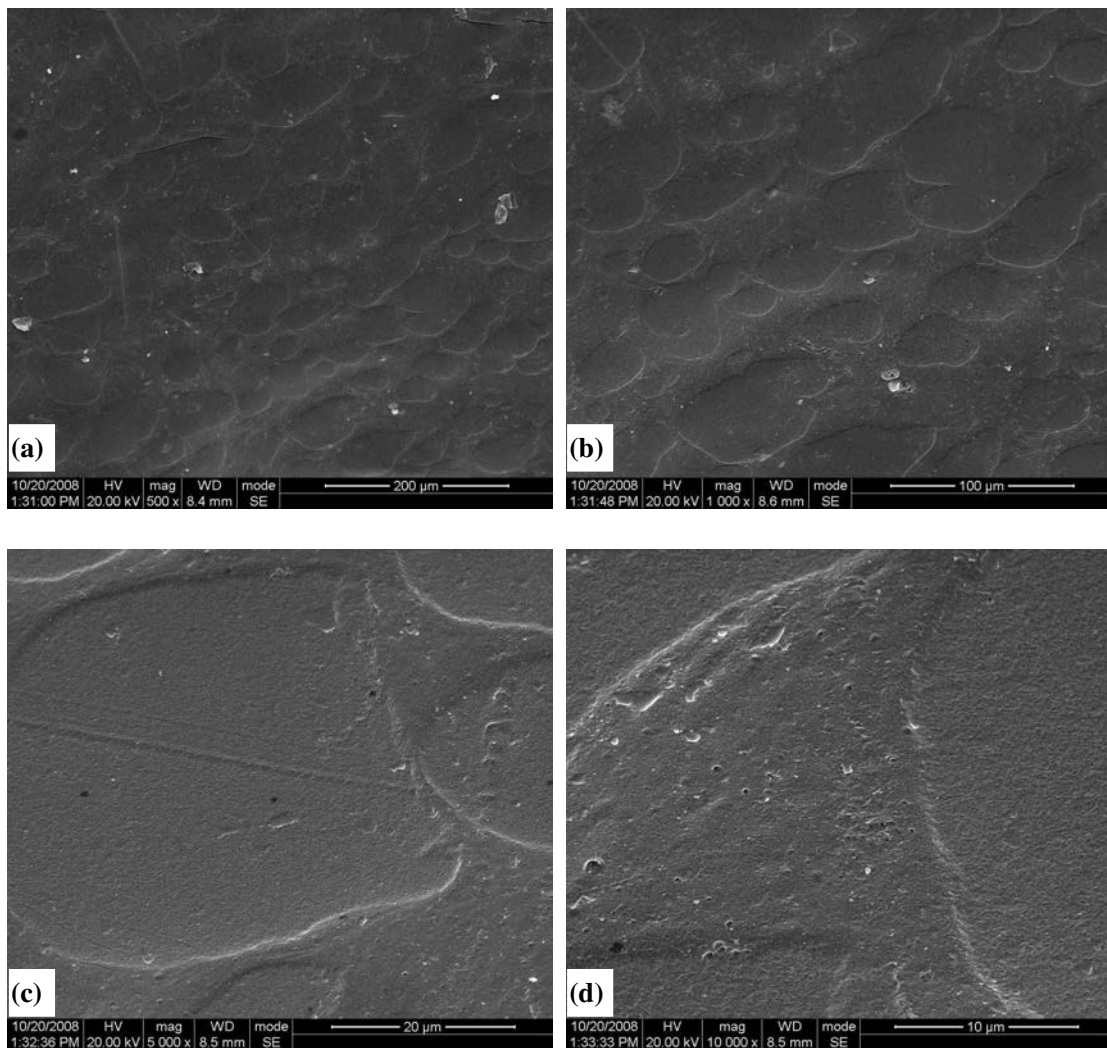


**Figure 3.9** SEM micrographs of cryogenically fractured surfaces after etching for the UHMWPE/LDPE (50/50) blend mixed for 3 mins. The scale bars in (a), (b), (c) and (d) are 200, 100, 20 and 10  $\mu\text{m}$ , respectively.

PE-PE miscibility has been a topic of great academic and commercial interest for the past decade owing to its relevance to the understanding of processing and performance properties of blends containing different types of PEs. Opposing views exist over this issue, ranging from complete homogeneity<sup>[9 - 10]</sup> to total phase separation<sup>[11 - 18]</sup> for blends composed of HDPE and LDPE as well as HDPE and LLDPE. Nevertheless, in the case of the HDPE/LDPE blends, there is a general consensus that the average number of branches per backbone or the branch content of LDPE is the major molecular factor that controls miscibility<sup>[9, 16-18, 19]</sup>. In this section, both the SEM and the DPD simulation are used to investigate the morphologies of the UHMWPE/LDPE blends.

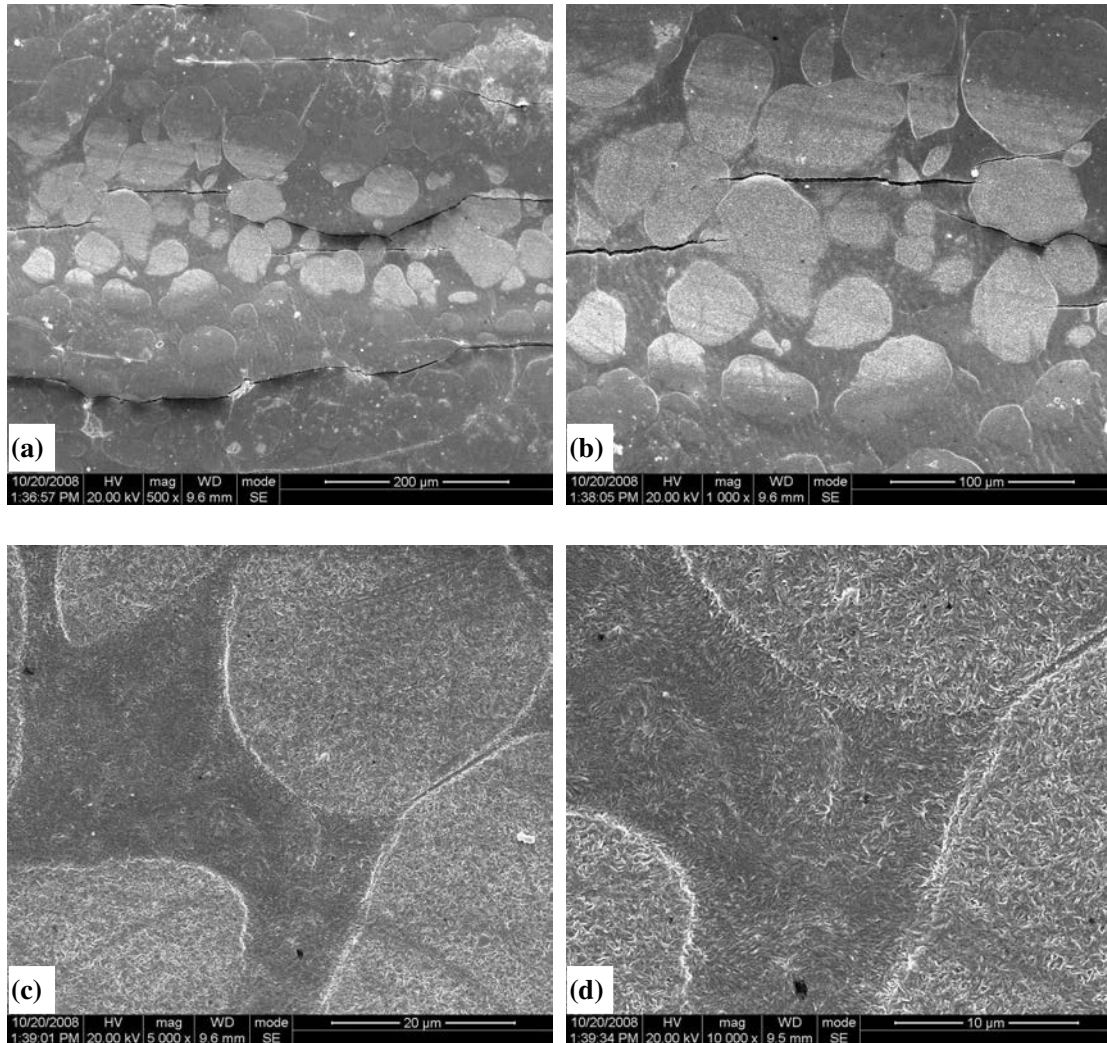


**Figure 3.10** SEM micrographs of cryogenically fractured surfaces after etching for the UHMWPE/LDPE (50/50) blend mixed for 9 mins. Scale bars are like in Figure 3.9.

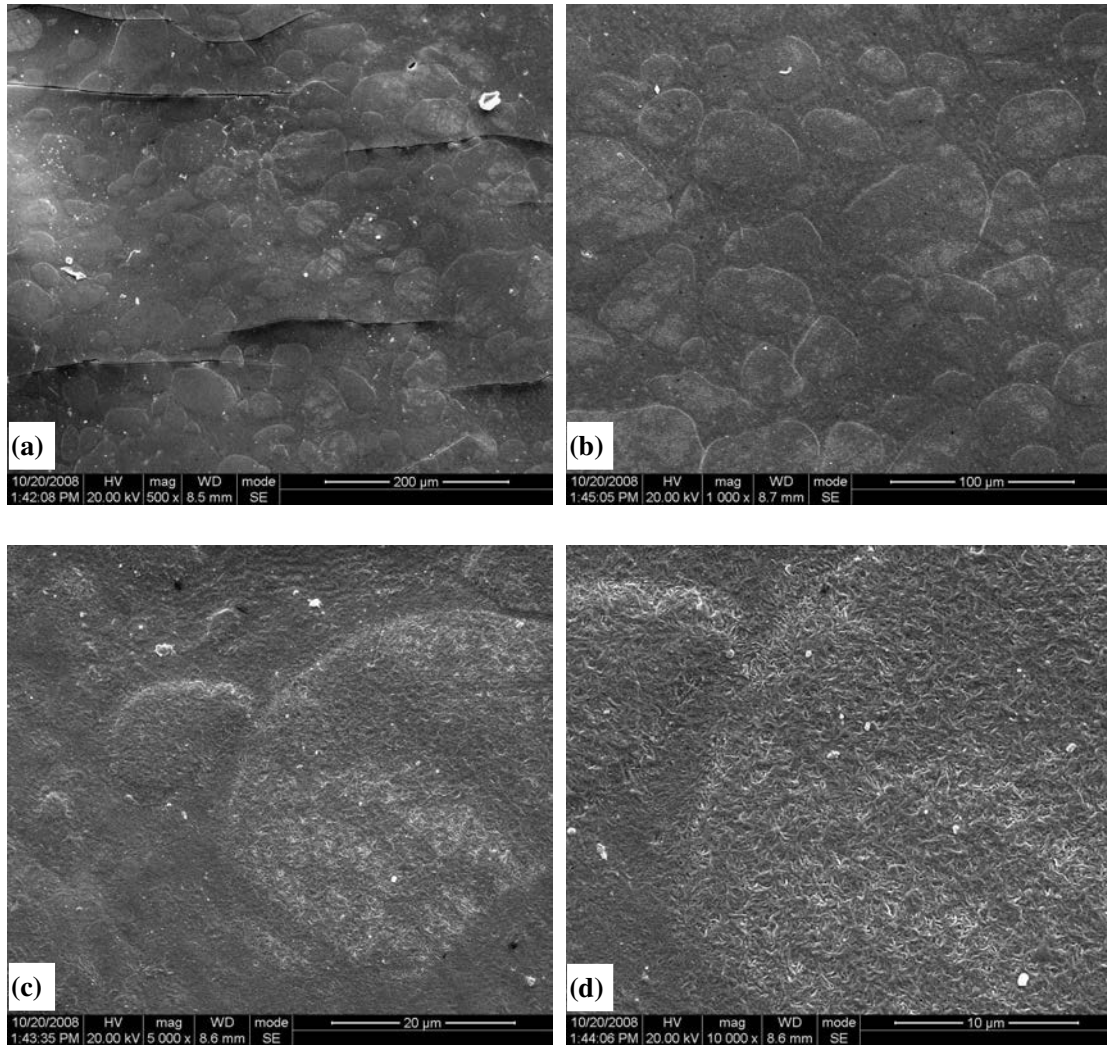


**Figure 3.11** SEM micrographs of cryogenically fractured surfaces after etching for the UHMWPE/LDPE blend mixed for 15 mins. Scale bars are like in Figure 3.9.

Figures 3.8 – 3.11 shows SEM micrographs of the cryogenically fractured surfaces of the LDPE and the UHMWPE/LDPE (50/50) blend with the amorphous phase etched. Figure 3.8 indicates that there is not obvious fibril-like crystal morphology in LDPE, which is totally different from HDPE and UHMWPE (Figures 3.1 and 3.2). For the UHMWPE/LDPE (50/50) blend, the morphologies at different magnifications show an abundance of particles, as shown in Figure 3.9 – 3.11. From Figure 3.9, the surfaces of the particles differ from those of the UHMWPE but similar to those of LDPE. This may be ascribed to the fact that the melt LDPE crystallizes on the surface of UHMWPE particles before it could have totally penetrated UHMWPE within 3 min. When the plasticating time is increased to 9 min (Figures 3.10), the classical morphologies of UHMWPE particles occur with shape interfaces, which

might be attributed to the fact that the LDPE now has started penetrating the UHMWPE particles. As the plasticating time is increased to 15 min, the interfaces between LDPE and UHMWPE become very fuzzy, suggesting that the most of LDPE in between UHMWPE particles have penetrated the particles. The comparison of Figures 3.9 – 3.11 with Figure 3.3 indicates that the diffusion rate of LDPE is much lower than that of HDPE in UHMWPE. In the experimental time scale (from Figure 3.9 to 3.11), the penetration process of LDPE into UHMWPE particles is not complete. Therefore, the UHMWPE/LDPE (50/50) blend likely did not reach its equilibrium structure. Hence, the DPD simulation is used to address the morphology development process.

The core-shell initial configuration is adopted to simulate by DPD the morphological evolution of the UHMWPE/LDPE (50/50) blend. Since the branch content of the LDPE was from 20 to 28 was used for the SEM observations, the LDPE with a branch content of 25 is adopted to calculate the solubility parameters of components for the DPD simulations. Figure 3.12 shows the time evolution of iso-density surfaces of LDPE in the blend. From the snapshots of the evolution process, within  $3 \times 10^3$  time steps the morphologies of the blend are still core-shell structures and the interface thickness increases rapidly as time runs, which is very similar to that of the UHMWPE/HDPE within the same time steps [Figures 3.5(b) - (d) and 3.12(b) - (d)]. However, both Figures 3.5 and 3.12 indicate that the diffusion rates of UHMWPE and LDPE in the UHMWPE/LDPE (50/50) blend is remarkably slower than those of UHMWPE and HDPE in the UHMWPE/HDPE (50/50) blend after  $5 \times 10^3$  time steps. This agrees well with the SEM observations. For example, the UHMWPE/LDPE (50/50) blend dose not form a homogeneous phase until  $2.5 \times 10^4$  time steps, which is much later than that of the UHMWPE/HDPE (50/50) blend ( $1.1 \times 10^4$  time steps). The difference in the dynamic process between the two blends might be attributed to the difference in miscibility between LDPE and HDPE with UHMWPE, which basically depends on the solubility parameters of components.

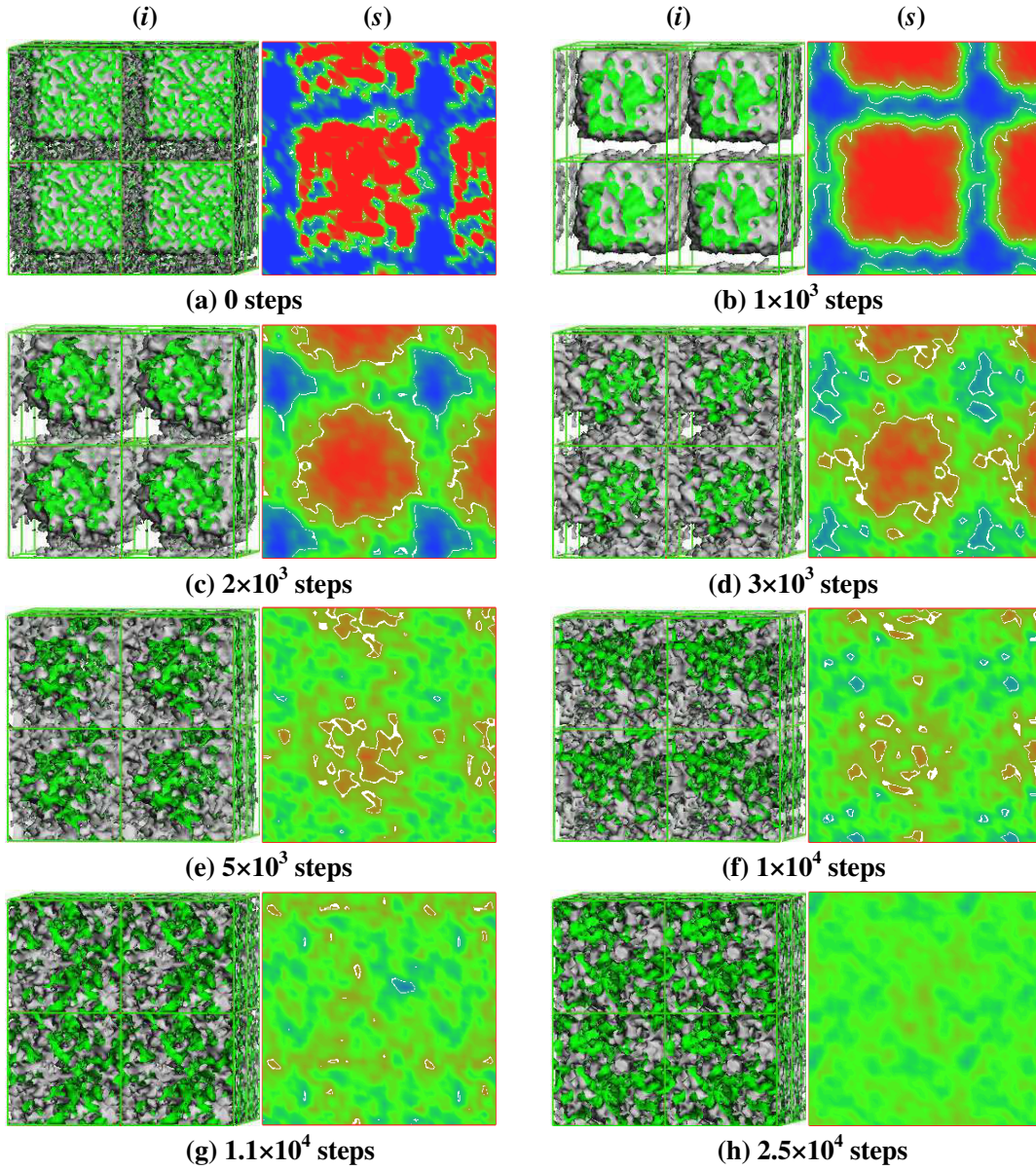


**Figure 3.12** The UHMWPE/LDPE (50/50) blend is simulated from a core-shell initial configuration (UHMWPE and LDPE are core and shell, respectively). (i): time evolution of iso-density surfaces of LDPE; (s): the corresponding slices. Others are same with Figure 3.5.

The effect of the branch content might be understood by the Hildebrand solubility parameter formalism. It is well-known that the solubility parameter is not only determined by the interaction energy potential,  $u(r)$ , but also the local arrangement of the molecules,  $g(r)$ , as depicted in the following expression:

$$\delta = \sqrt{\frac{\Delta E_v}{V}} = \sqrt{\frac{2\pi n^2}{V^2} \int_0^\infty u(r)g(r)r^2 dr} \quad (3.1)$$

where  $\delta$  is the Hildebrand solubility parameter;  $\Delta E_v/V$  is the cohesive energy density;

$n$  is the number of molecules;  $u(r)$  is the interaction energy potential; and  $g(r)$  is the radial distribution function. As one can conceive, PE with different branching characteristics and/or contents should exhibit different local morphology [i.e. different  $g(r)$ ]. Therefore, it is not surprising that  $\delta$  values of different PEs can differ and such differences can lead to differences in dynamic processes of the UHMWPE/HDPE and UHMWPE/LDPE blends.

On the basis of molecular dynamics (MD), Choi et al. showed that if the branch content of LDPE is less than 30, HDPE/LDPE blends form homogenous mixtures. However, when the branch content is higher than 30, the blends phase separate<sup>[8]</sup>. It is worth noting that the molecule of HDPE has the same microstructure with that of UHMWPE. Hence, the DPD results are consistent with the MD predictions.

The slight difference between DPD results and the SEM observation might be related to the fact that samples for the SEM observation correspond to some of the intermediate states in the structure evolution, such as Figure 3.12(d).

### **3.2.1.3 UHMWPE/PP blends**

Figures 3.13 show SEM micrographs of the cryogenically fractured surfaces of the specimens with etching of the amorphous phase. For the UHMWPE/PP (70/30) blend, the morphologies at different magnifications show an abundance of particles. Inspection of the SEM micrographs shows that the morphology of the dispersed particles is similar to that of pure UHMWPE. These dispersed particles are the crystal domains of UHMWPE. Comparison of Figure 2.3 with Figure 3.11 suggests that the major UHMWPE particles are divided into minor particles by PP in the blend. A further increase in the PP concentration of PP only increases the thickness of the PP phase. Consequently, 30 wt.% of PP in the blend is high enough to pack the minor particles. The critical composition strongly affects the rheological behavior of the UHMWPE/NMWP blends, as will be discussed in section 3.2.3. Considering the fact that the PP-rich phase in between UHMWPE particles can reduce the viscosity of the blend, the PP-rich phase is described as lubricating phase.

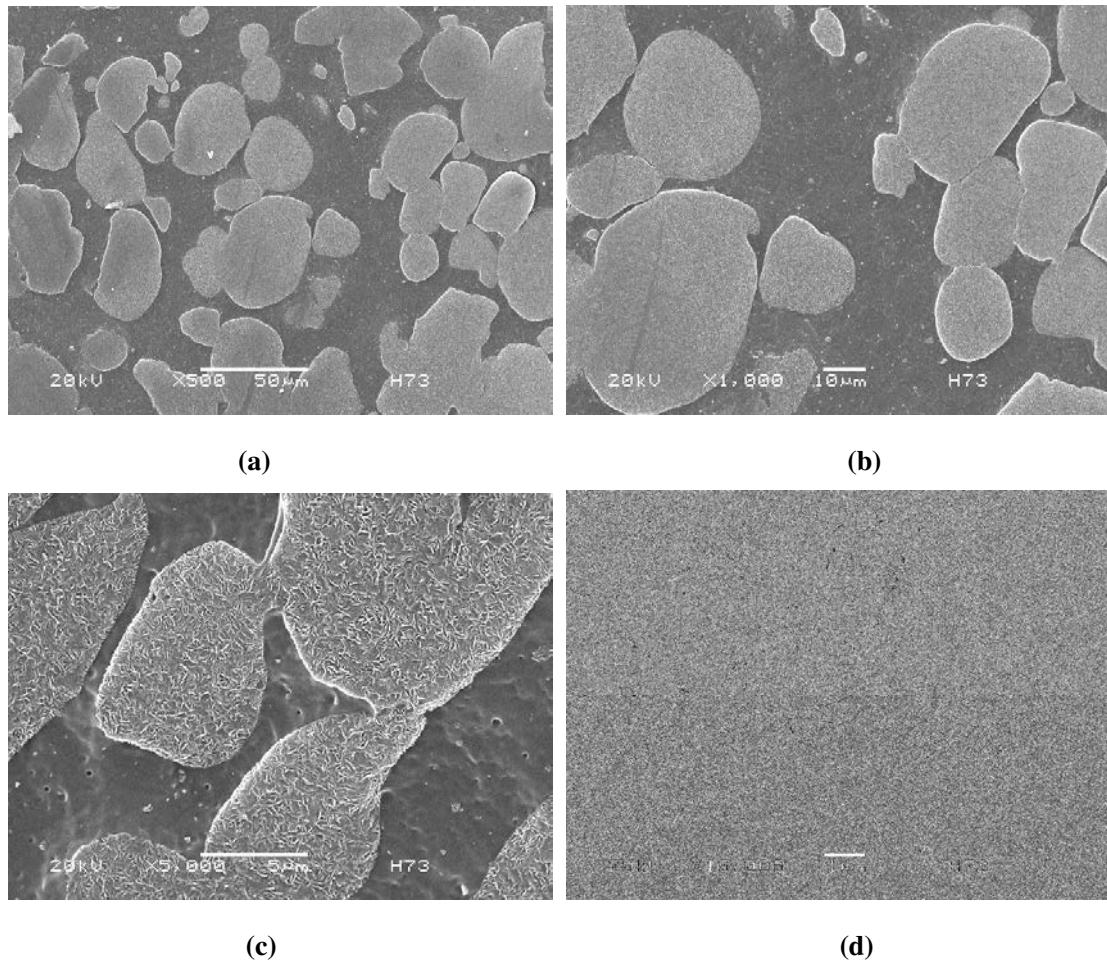


**Figure 3.13** SEM micrographs of cryogenically fractured surfaces of the UHMWPE/PP (70/30) after etching mixed for 3 minutes. The scale bars in (a), (b), (c) and (d) are 50, 10, 5 and 1  $\mu\text{m}$ , respectively.

In order to determine the equilibrium state structure and the dynamics of the morphology of the UHMWPE/PP (70/30) blend, the core-shell initial configuration is also adopted in the DPD simulations. Figure 3.14 shows the time evolution of the iso-density surfaces of PP in the blend. From the snapshots of the evolution process the morphologies of the blend are still core-shell structures within  $10^3$  time steps [Figures 3.14(a), (b)]. However, in the range of  $2 \times 10^3$  -  $8 \times 10^3$  time steps, the blend shows bicontinuous phase structures. After that, perforated lamella (PL) morphologies occurs, and the system changes slowly to overcome the defects formed in the previous stage [Figures 3.14(c) - (g)]. At last, this structure does not changes much anymore as time runs and the PL morphologies are obtained after  $4 \times 10^5$  steps [Figures 3.9(h)]. The simulation further shows that when the morphology of (h) is subjected to a shear

rate of 0.8 (DPD unit) for  $1 \times 10^5$  steps and then without shear for  $4 \times 10^5$  steps, the PP is dispersed as spherical particles in UHMWPE. This agrees well with that obtained the random initial configuration after  $4 \times 10^5$  steps, as will be discussed in Chapter 4.

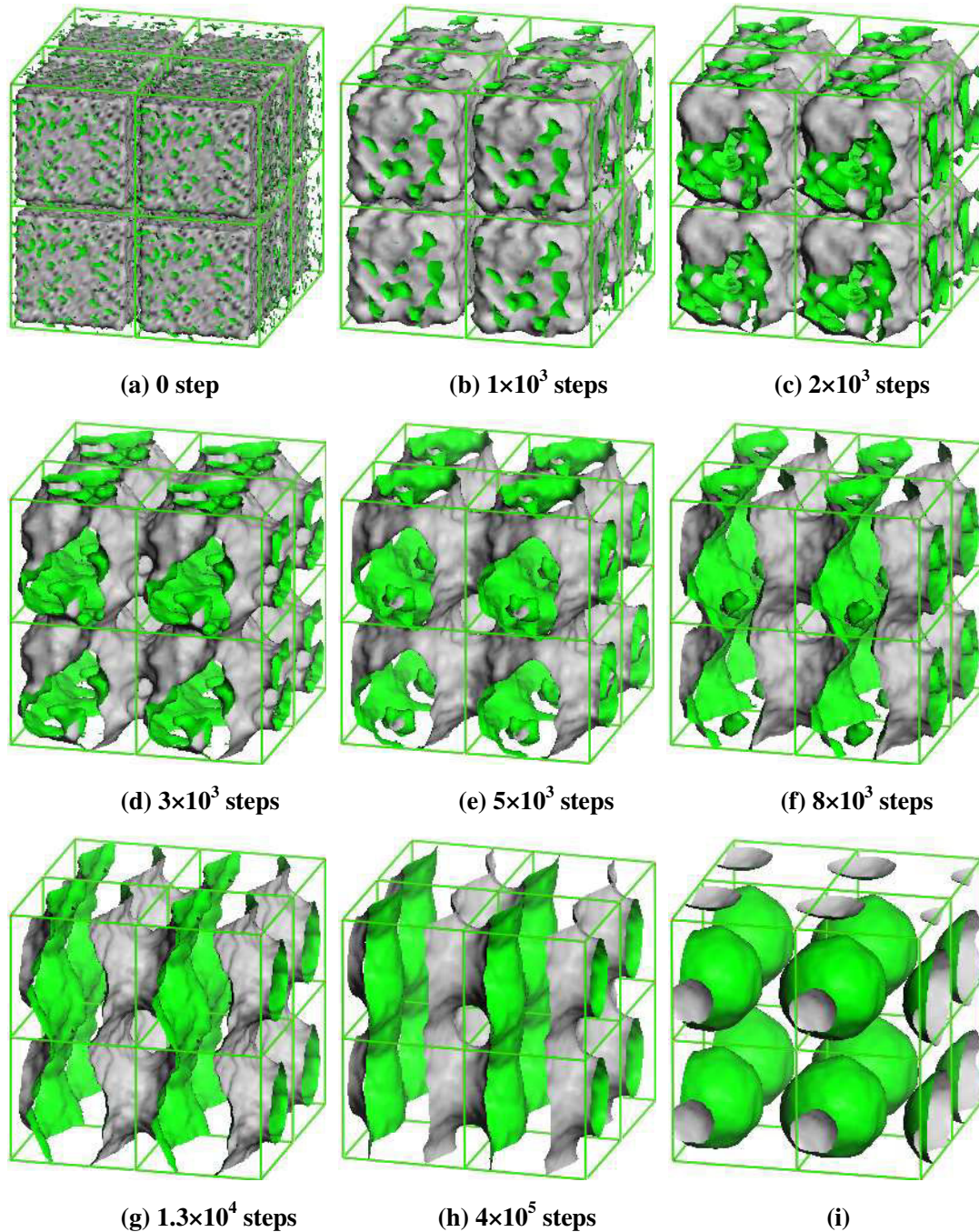


**Figure 3.14** Time evolution of iso-density surfaces of PP in the UHMWPE/PP (70/30) blends simulated from the core-shell initial configuration (UHMWPE and PP are core shell, respectively). The outward surfaces of PP phase are colored with green, and the rests are UHMWPE phase. (i) the blends with morphology of (h) is simulated under shear rate of 0.8 for  $1 \times 10^5$  steps, and then without shear rate for  $4 \times 10^5$  steps.

The morphological evolution process of the UHMWPE/PP (70/30) blend indicates two things. First, the PL morphology is not the most stable state but is stable enough when time is not very long and shear is not very strong. Note that the blend of UHMWPE with HDPE or LDPE does not show any stable intermediate states during the phase mixing process. Second, the PL morphology would be more efficient than the spherical morphology at reducing the viscosity of the UHMWPE/PP (70/30) blend. However, the mechanical properties of the UHMWPE/PP (70/30) blend with PL morphology might be lower than that with the spherical morphology. The slight difference between the DPD results and the SEM observations might be attributed to the fact that the samples for the SEM observation are far from the equilibrium state. In other words, Figure 3.13 might correspond to one of the intermediate states, such as Figure 3.14(c), in the phase separation process.

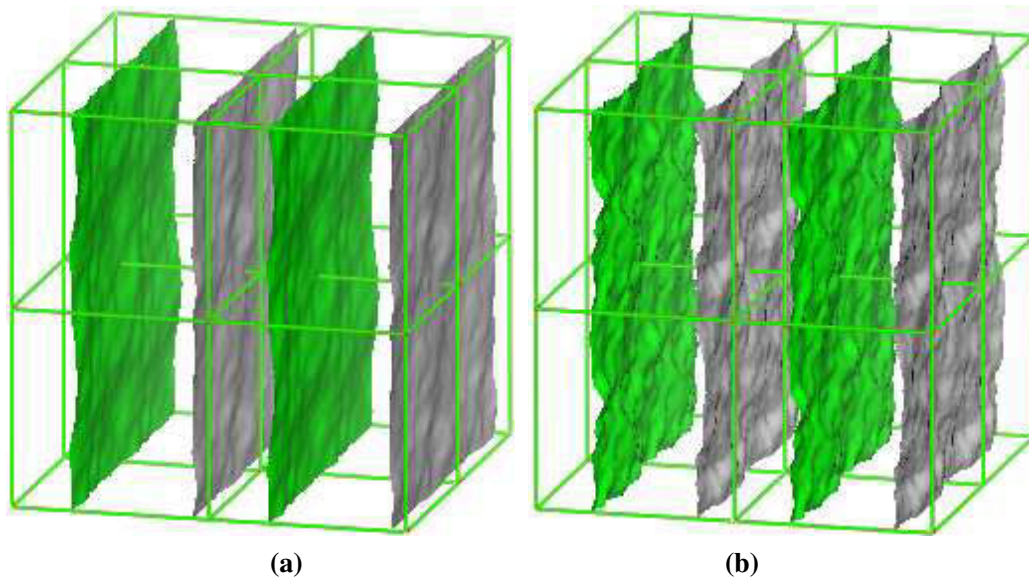


**Figure 3.15** The time evolution of iso-density surfaces of PP for the UHMWPE/PP blend simulated from a core-shell initial configuration. The outward surfaces of PP phases are colored with green, and the rests are UHMWPE phases. Each system contains  $8.1 \times 10^4$  DPD beads: (a) UHMWPE/PP (60/40), (b) UHMWPE/PP (50/50).

The DPD simulation is also performed on the UHMWPE/PP (60/40) UHMWPE/PP (50/50) blends with the core-shell initial configuration to investigate the effects of the compositions on the morphologies. Figure 3.15 shows the iso-density surfaces of PP after  $4 \times 10^5$  time steps. Comparison of Figures 3.14 with Figure 3.15 shows that the sizes of the UHMWPE domains [pores in Figures 3.14(h)]

in PP lamellar phase decrease with increasing  $\phi_{PP}$ . When  $\phi_{PP}$  reaches 40% the pores disappear completely and the lamellar morphology occurs. A further increase of  $\phi_{PP}$  to 50% only increases the thickness of the PP phase and the lamellar morphology is retained. Liu's studies <sup>[20]</sup> indicated that some of the mechanical properties of the UHMWPE/PP blends, such as tensile strength and izod-notched impact strength, decrease with increasing  $\phi_{PP}$  when  $\phi_{PP} > 10\%$ , which might originate from the simultaneous decrease of UHMWPE domains in PP phase.

Figure 3.16 shows the distribution of each of the polymer components of the UHMWPE/PP (50/50) blend. No UHMWPE is located in the PP-rich phase while there is a significant amount of PP in the UHMWPE-rich domains. The former prevents the viscosity of PP from increasing and the latter favors the disentanglement of UHMWPE chains and consequently its viscosity reduction (see section 3.2.3). These distributions are supported by DPD simulations and predictions based on Flory-Huggins theory (see section 3.2.3).

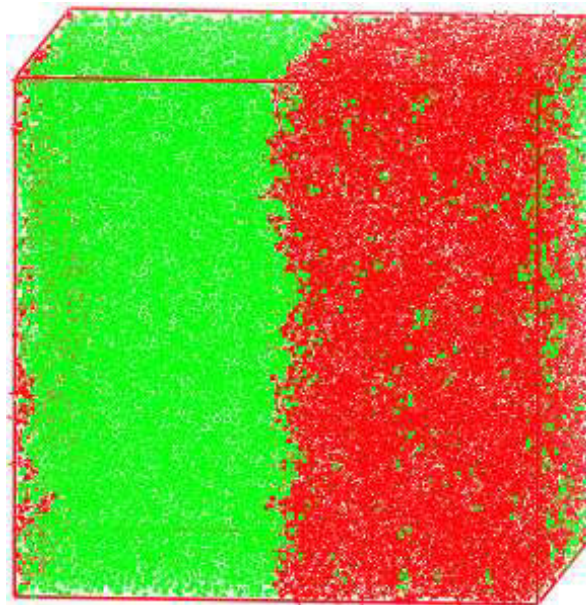


**Figure 3.16** The UHMWPE/PP (50/50) blend is simulated from a core-shell initial configuration for  $4 \times 10^5$  steps. The green and red beads represent PP and UHMWPE, respectively.

### **3.2.2 Mechanisms of the viscosity reduction of the UHMWPE/ NMWP blends**

Figure 3.17 shows the effects of PP, LDPE and HDPE on the rheological properties of UHMWPE. The melts of pure UHMWPE and the UHMWPE/HDPE (50/50) blend flew unsteadily at lower shear rate, and no steady rheological data could be obtained at higher shear rates because of the pressure fluctuation. It was confirmed that plasticating the UHMWPE/HDPE (50/50) blend in a screw extruder is very difficult. Blockade and melt fracture seriously occur [Figure 3.18]. This is because the miscibility between HDPE and UHMWPE is good. The molten HDPE can rapidly penetrate the UHMWPE domains within the first few minutes during processing [Figure 3.3 – 3.5]. With increasing plasticating time, the amount of the HDPE melt on the skins of the specimens and the gaps between the UHMWPE particles becomes less and less, UHMWPE particles may aggregate again, preventing the viscosity of the blend from decreasing.

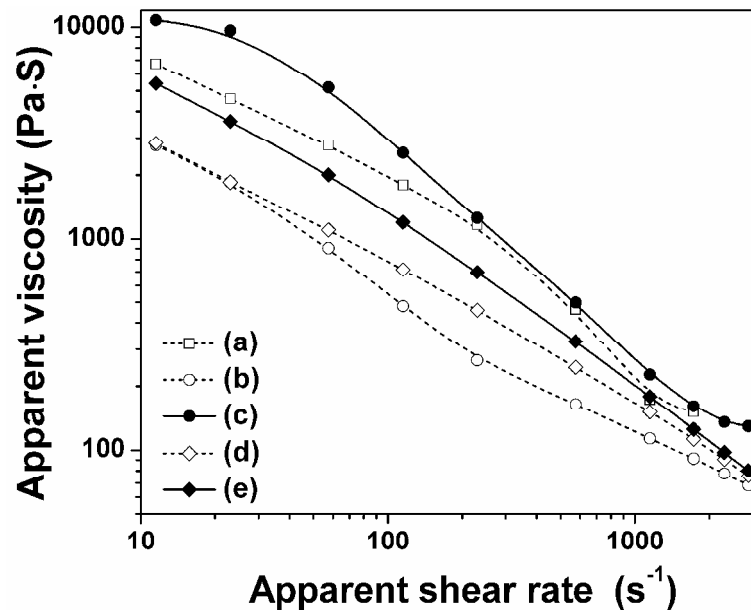


**Figure 3.17** Plot of the logarithm of the apparent viscosity versus the logarithm of the apparent shear rate for (a) HDPE, (b) LDPE, (c) UHMWPE/LDPE (50/50), (d) PP, and (e) UHMWPE/PP (50/50). Both blends are mixed for 15 minutes.

It is very interesting to note that the addition of the same concentration PP into UHMWPE effectively solves the problems facing the UHMWPE/HDPE blend during extrusion. The viscosity of the UHMWPE/PP (50/50) blend is significantly reduced and the surfaces of extrudates are smooth [Figure 3.19]. As stated in section 3.2.1. (Figure 3.16), only a small fraction of the molten PP penetrates the UHMWPE-rich

phase because of the immiscibility between UHMWPE and PP. Most of the molten PP prefers to flow in between the UHMWPE particles, acting as a lubricant and increasing the adhesion between them. In the case of the UHMWPE/LDPE (50/50) blend, the viscosity is evidently higher than that of the UHMWPE/PP (50/50) blend although the viscosity of pure LDPE is lower than that of PP (Figure 3.17). When the LDPE concentration is decreased to 30%, the blend can not be processed with a general three-section double-screw extruder because of the very high melt viscosity. On the other hand, there is no problem for the UHMWPE/PP (90/10) blend in which UHMWPE still forms particles between which PP acts as the lubricant (Figure 3.20).



**Figure 3.18** Extrudates of the UHMWPE/HDPE (50/50) blend.



**Figure 3.19** Extrudates of the UHMWPE/PP (50/50) blend mixed for 15 mins.

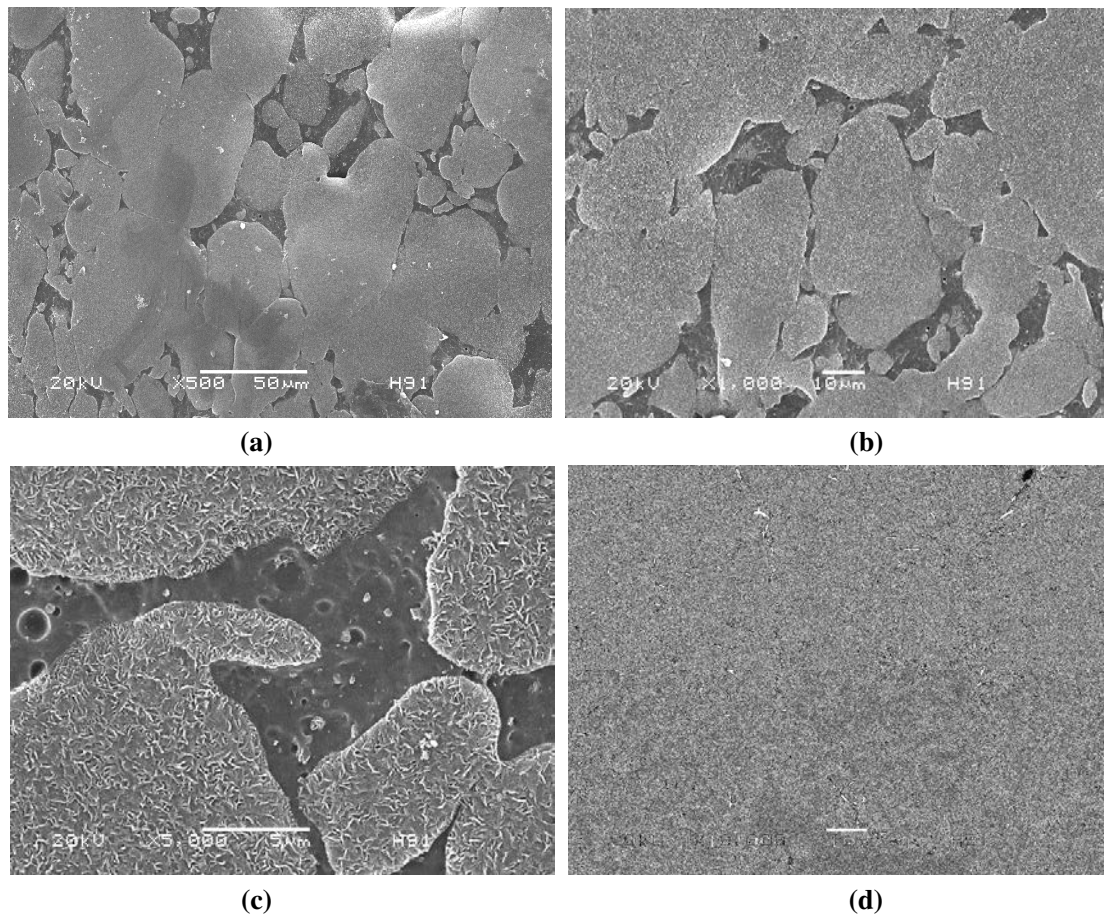


**Figure 3.20** SEM micrographs of cryogenically fractured surfaces after etching for the UHMWPE/PP (90/10) blend mixed for 3 minutes. The scale bars in (a), (b), (c) and (d) are 50, 10, 5 and 1  $\mu\text{m}$ , respectively.

It is obvious that UHMWPE and LDPE are superior to PP in disentangling UHMWPE chains than that of PP. On the other hand, PP is shown to be much more effective than HDPE and LDPE at decreasing the viscosity of the UHMWPE. Therefore, the formation of the lubrication phase between the UHMWPE particles with the addition of NMWP might be the dominant factor of the viscosity reduction. In what follows, a phase diagram approach based on Flory-Huggins theory is adopted to investigate in detail the effects of the concentration, the parameter  $\chi$ , molecular weight of NMWP on the formation of the lubrication phase and the viscosity of the UHMWPE/NMWP blends.

### 3.2.3. Rheological behaviors predictions based on phase diagram

Figure 3.21 shows the interaction parameter  $\chi$  as a function of the volume fraction  $\phi_{NMWP}$  for various  $N_1$  (50, 250 and 1000), and fixed  $N_2$  (11600);  $N_1$  and  $N_2$  correspond to the chain lengths of the NMWP and UHMWPE, respectively (Chapter 2, Table 2.1). The phase diagrams, the binodal and spinodal curves together with the critical points are shown. In view of the fact that all the blends of NMWP and UHMWPE with different  $N_1$  possess similar properties, a representative one ( $N_1 = 250$ ;  $N_2 = 11600$ ) is plotted to show the general properties of binary polymer systems with a given  $N_2$ . It is seen that the parameters  $\chi$  of the UHMWPE/HDPE (50/50) blend and that of the UHMWPE/PP (50/50) blend lie below the binodal curve and above the spinodal one, respectively. Therefore the corresponding equilibrium states are homogeneous phase and two-phase morphologies, respectively. This is in agreement with the DPD simulations and the SEM observations.

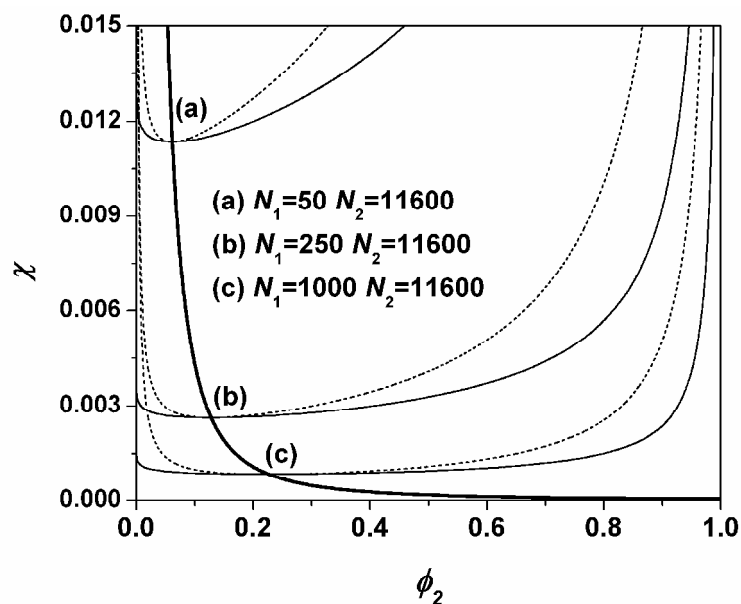


**Figure 3.21** Binodals (solid curves) and spinodals (dashed curves) of polymer blends with fixed  $N_2$  (11600) and various  $N_1$ . (a), (b) and (c) are critical points, and the bold solid curve are composed of critical points.

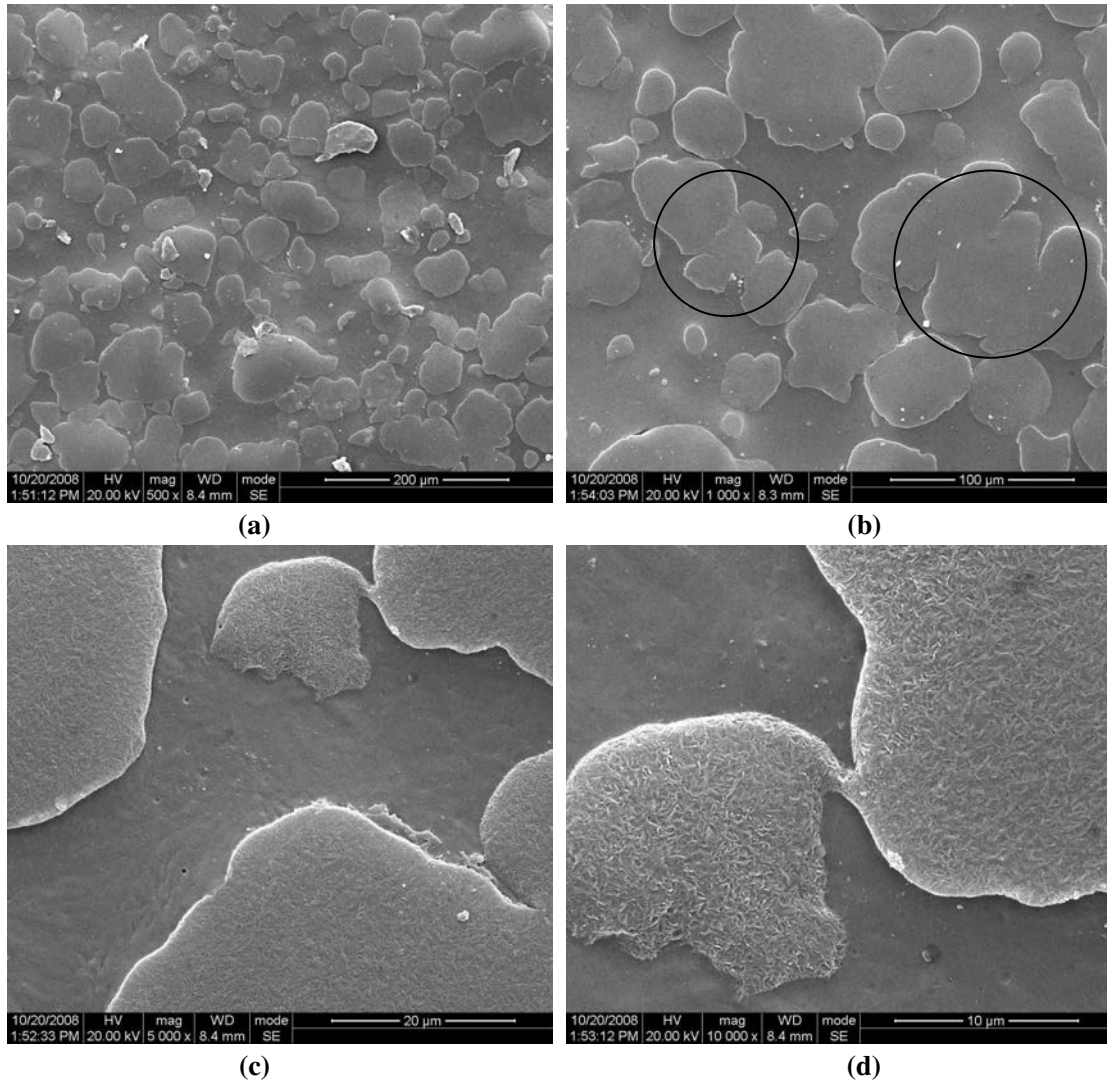


**Figure 3.22** SEM micrographs of cryogenically fractured surfaces after etching for the UHMWPE/PP (50/50) blend mixed for 3 minutes. The scale bars in (a), (b), (c) and (d) are 200, 100, 20 and 10  $\mu\text{m}$ , respectively.

As shown in Figure 3.21, the composition of each of the phases in the UHMWPE/PP blend can be determined from the lever rule. The volume fractions of the UHMWPE in each of the phases are about 0 and 90%, respectively. They match well the DPD simulations shown in Figure 3.16. This implies that if  $\phi_{PP} > 10$ , about 10% of the PP may have penetrated the UHMWPE phase and nearly no UHMWPE is located in the PP phase, which is beneficial to the viscosity reduction of the UHMWPE. Indeed the PP forms the lubricating phases between the UHMWPE particles. Therefore the apparent viscosity of the UHMWPE/PP blend mostly depends on that of the PP phase when  $\phi_{PP} > 10$ . As the plasticating time increases, most of the major UHMWPE particles are divided into the minors and PP is more uniformly

distributed in between the UHMWPE particles (Figures 3.22 - 3.24). Consequently, its effect of PP on the viscosity reduction of the UHMWPE/PP (50/50) blend is expected to be more significant. This is confirmed by the rheological measurements (Figure 3.25). However, according to Figure 3.14, excessive shear (too long time and/or too strong) will transform the PL structure of PP into spherical one which might prevent the viscosity of the blend from decreasing. Alternatively, when  $\phi_{PP}$  is less than about 10%, the blend will show homogeneous phase morphology which makes viscosity reduction thermodynamically impossible when processing UHMWPE/PP blends.

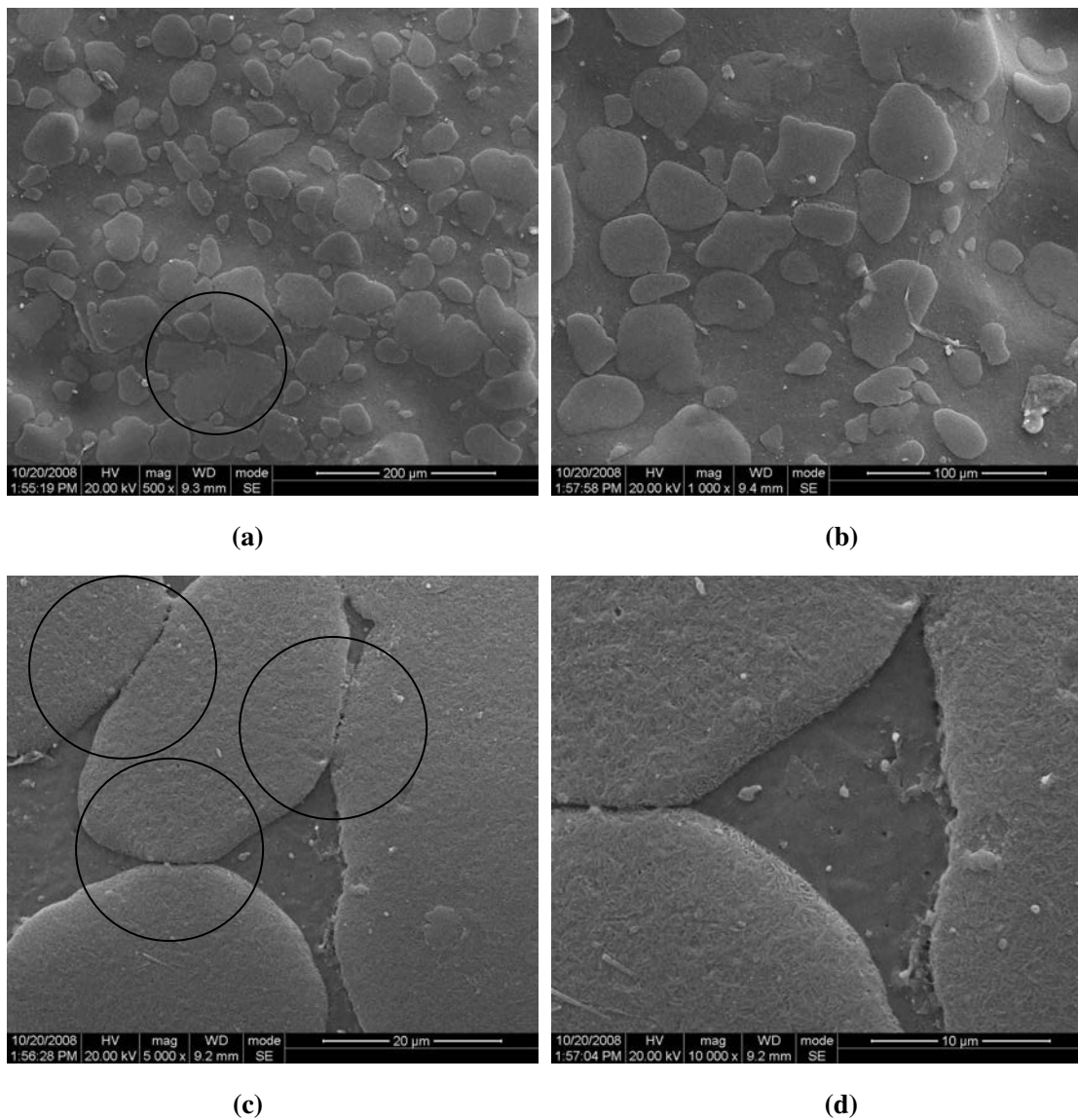


**Figure 3.23** SEM micrographs of cryogenically fractured surfaces after etching for the UHMWPE/PP (50/50) blend mixed for 9 minutes. Scale bars are like in Figure 3.22.

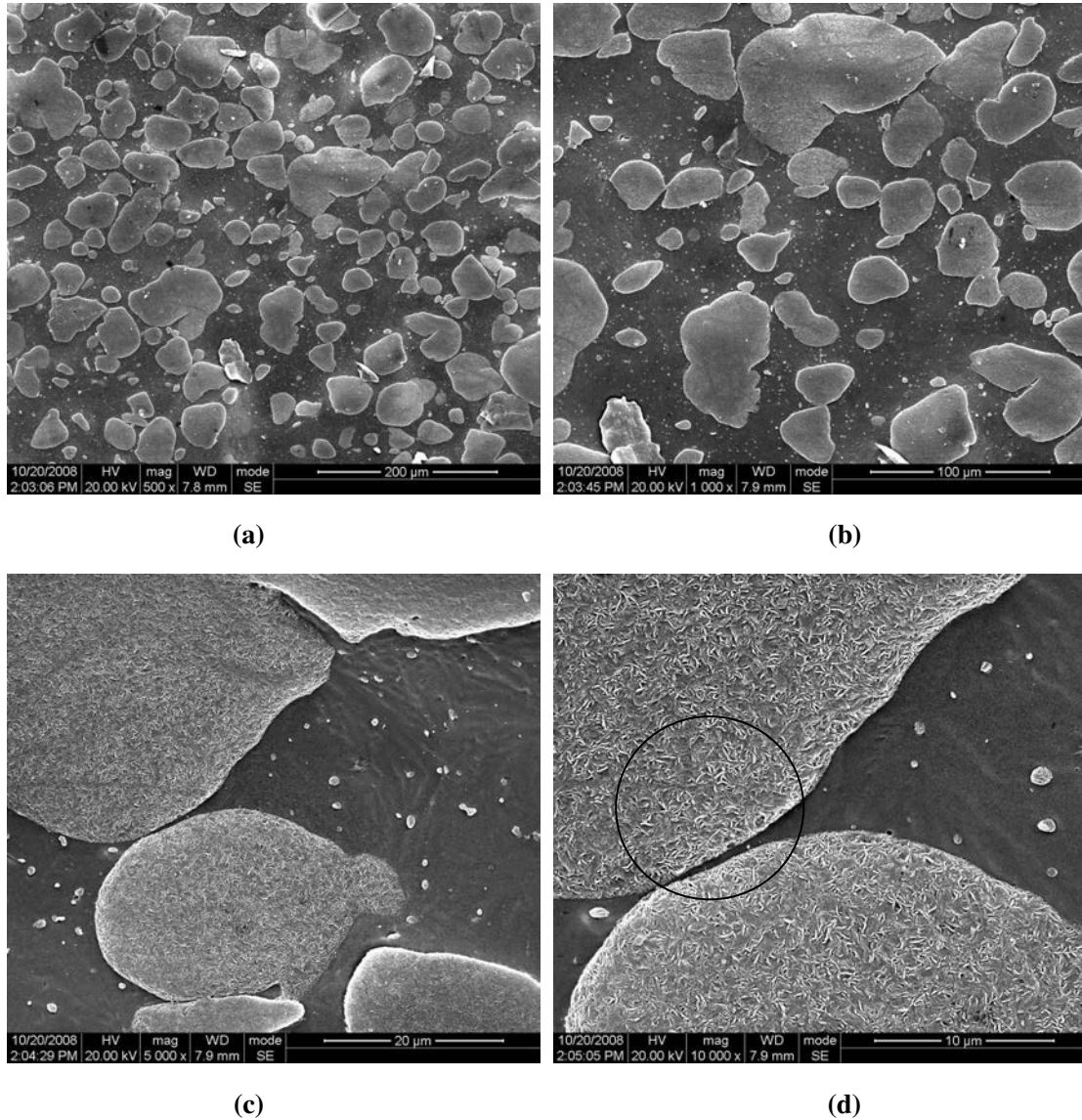


**Figure 3.24** SEM micrographs of cryogenically fractured surfaces after etching of the UHMWPE/PP (50/50) blend mixed for 15 minutes. Scale bars are like in Figure 3.22.

When the parameter  $\chi$  lies below the binodal curve, the viscosity of the UHMWPE/NMWP blend increases with increasing plasticating time. This is because more and more NMWP penetrates the UHMWPE phase and less and less NMWP will be available to form lubricating phases between the UHMWPE particles. This is the reason that a high-pressure and rapid molding technology is applied to processing UHMWPE/HDPE blends (Figure 3.5). The  $\chi$  values of PE blends with small differences in branch contents ( $< 30$ ) measured by SANS are usually less than  $6 \times 10^{-4}$ . Therefore, the two-phase interface becomes fuzzy (Figures 3.9 – 3.11), the content of LDPE between UHMWPE particles decreases and the apparent viscosity of the

UHMWPE/LDPE (50/50) blend increases with increasing the plasticating time (Figure 3.26).

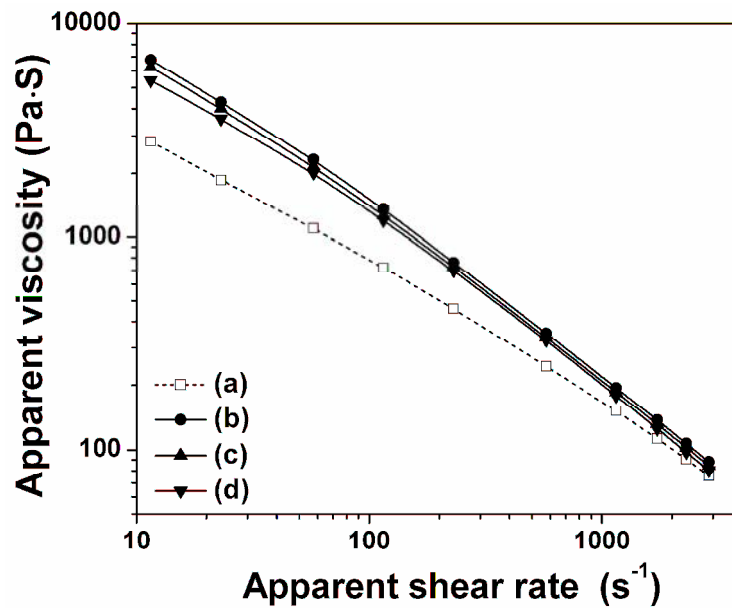


**Figure 3.25** Plot of the logarithm of the apparent viscosity versus the logarithm of the apparent shear rate for (a) PP, and (b), (c), (d) are UHMWPE/PP (50/50) blend mixed for 3, 9 and 15 minutes, respectively.

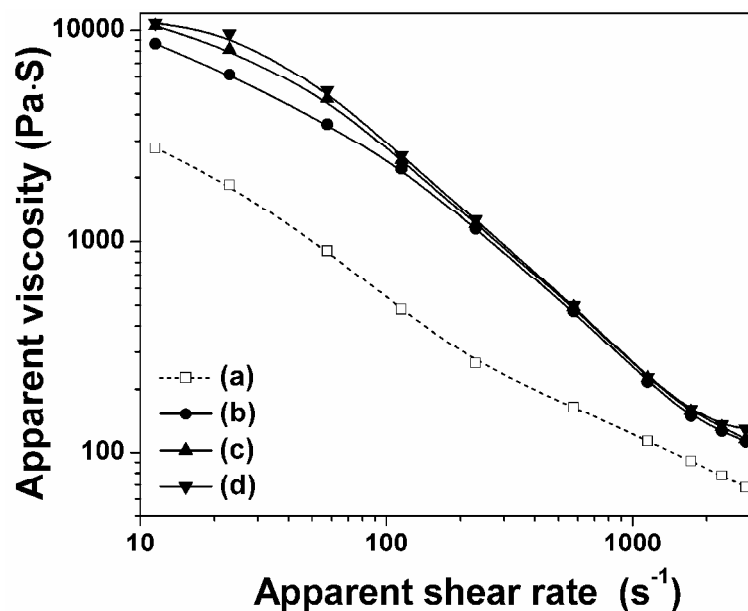


**Figure 3.26** Plot of the logarithm of the apparent viscosity versus the logarithm of the apparent shear rate for (a) LDPE, and (b), (c), (d) are UHMWPE/LDPE blend (50/50) mixed for 3, 9 and 15 minutes, respectively.

As stated in chapter 1, an excess in the amount of NMWP might bring about

important deterioration in some of the most desirable properties of UHMWPE. Therefore, it is necessary to investigate the effect of the fraction of NMWP on the rheological behavior of the UHMWPE/NMWP blend. As shown in Figure 3.27, when the PP volume fraction is less than 10%, no remarkable viscosity reduction occurs. This is because under this composition the UHMWPE and PP form a homogeneous phase. As the PP volume fraction increases, the UHMWPE/PP blend exhibits a very different rheological behavior, depending strongly on the shear rate. The viscosity of the blend is reduced to a significant degree when the shear rate is in the range of 256.9 to 1999.8s<sup>-1</sup> [Figures 3.27(e) - (g)]. Moreover, when  $\phi_{PP} \geq 0.1$  the flow is smooth and no pressure fluctuation has occurred. When the shear rate varies from 23.0 to 92.4s<sup>-1</sup>, there appear two distinct rheological behaviors for the UHMWPE/PP blend [Figures 3.27(a) - (d)]. The viscosity of the blends decreases dramatically with  $\phi_{PP}$  increasing from 0.1 to 0.3. This is because when  $\phi_{PP} > 0.1$ , about 10% PP would penetrate the UHMWPE phase and the rest forms a lubricating phase between the UHMWPE particles. An increase in the PP volume fraction leads to an increase in the amount of the PP available for forming that lubricating phase and consequently a reduction in the apparent viscosity of the blend. Nevertheless, the viscosity of the blends varies only slightly when the PP volume fraction exceeds 30%. This could be explained by the fact that 30% PP is enough to form the lubrication phase between UHMWPE particles. An excess in PP can only increase the thickness but not the area of the lubrication phase. This has been certificated by the DPD simulations (Figure 3.15). However, there is slightly difference of the critical composition between the experimental measurements and the simulation results, which might attributed to the fact that the samples for the rheological measurements are far from the equilibrium state. Besides, the critical composition (for example,  $\phi_{PP} = 0.3$ ) has been described as the maximum packing fraction of filler particles <sup>[21]</sup>. The range of  $0.3 \geq \phi_{PP} \geq 0.1$  is thus called composition sensitive region - CSR of low shear rates for the UHMWPE/PP blends. Consequently, for a given NMWP with fixed parameter  $\chi$  and molar mass, the optimum composition should be located in the CSR of the blends for low shear rates, and above but close to the corresponding binodal curve for high shear rates. It is

worth noting that all the ranges for the low shear rate, high shear rate and CSR rigorously depend on the rheological behavior of the blend. From Figure 3.21, the metastable region for the UHMWPE/PP blend is located in the corresponding CSR. Thus the CSR, which may not always be easily measured in practice, can be approximately replaced by the metastable region provided that the viscosity of the blend is low enough for processing within the metastable region.

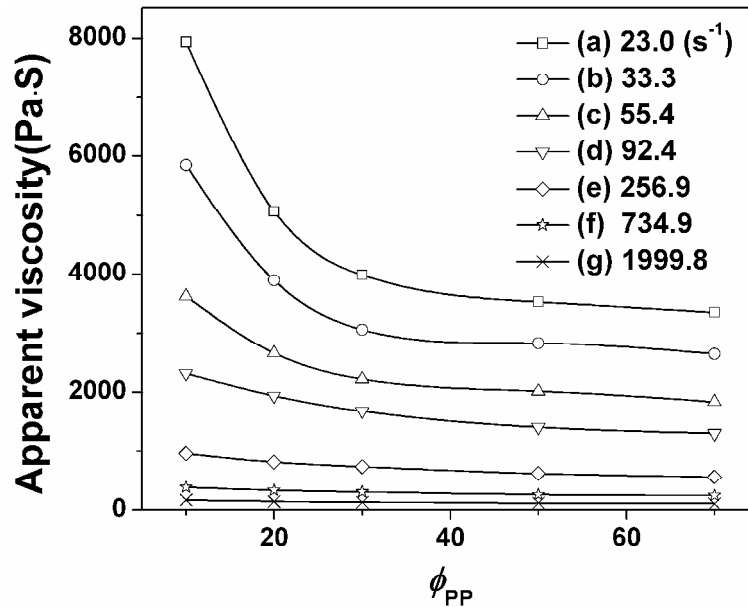


**Figure 3.27** Plot of the apparent viscosity versus the concentration of PP for UHMWPE/PP (50/50) blend mixed for 3 mins.

Figure 3.21 shows that an increase in the parameter  $\chi$  favors the formation of a two-phase structure. At the same time, it accelerates the rate with which the NMWP molecules migrate toward the surface of the blends during processing. As a result, the NMWP can no longer effectively act as a lubricant agent between UHMWPE particles. Moreover, the interfacial thickness will decrease (Chapter 7), leading to worse mechanical properties. Therefore, for UHMWPE/NMWP blends with fixed composition and molar mass of each of the components, the optimum value of the parameter  $\chi$  should be above but close to the corresponding binodal curve (Figure 3.21). This Figure also shows that for a polymer blend with fixed parameter  $\chi$ , both the corresponding binodal and spinodal curves shift downwards with increasing  $N_1$ , indicating that increasing molar mass of the NMWP in a certain range can improve

the processability of the UHMWPE owing to the formation of a lubricating phase between the UHMWPE particles [Figure 3.21(a) - (c)].

Figure 3.28 also shows the parameter  $\chi$  as a function of the volume fraction  $\phi_2$  for various  $N_2$  (1160, 4640 and 23200), and fixed  $N_1$  (250). For the phase diagram, as  $N_2$  increases, both binodal and spinodal curves shift downwards, which suggest that the increase of  $N_{UHMWPE}$  is favorable to the phase separation of the UHMWPE/PP blends. Furthermore, the effect of  $N_2$  will be discussed in Chapter 5 and the thermodynamic properties of the blends will be discussed in Chapter 7.

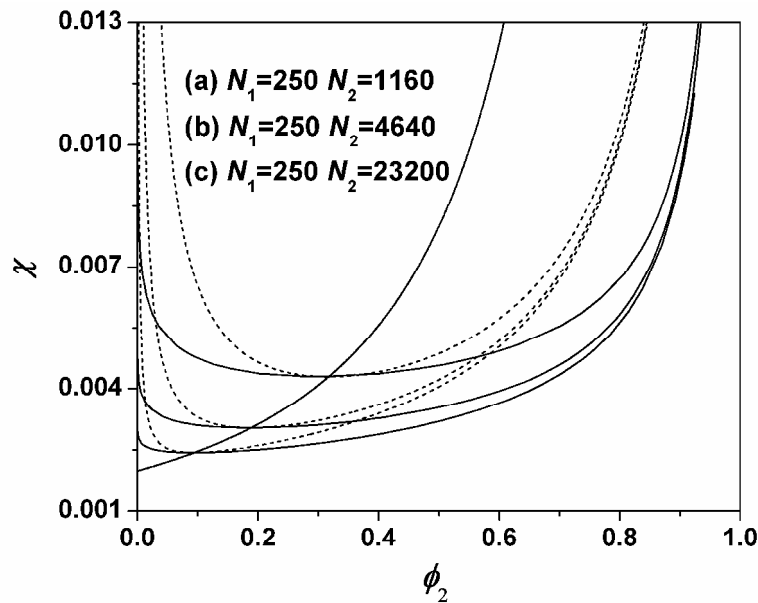


**Figure 3.28** Binodals (solid curves) and spinodals (dashed curves) of polymer blends with fixed  $N_1$  (250) and various  $N_2$ . (a), (b) and (c) are critical points, and the bold solid curve are composed of critical points.

### 3.3 Conclusion

In this work, we have investigated the effects of NMWP on the morphologies and rheological behaviors of the UHMWPE blends by experimental measurements and theoretical predictions. It is obvious that HDPE and LDPE are better than PP to disentangle the UHMWPE chains. On the other hand, PP is proved to more effective than HDPE and LDPE in decreasing the viscosity of the UHMWPE/LDPE blends in our research. Therefore, the formation of the lubrication phase between the UHMWPE particles with the adding of NMWP might be the dominant factor of the

viscosity reduction.

Rheological measurements show that with increasing plasticating time the viscosity of the UHMWPE/PP (50/50) blend decreases and that of UHMWPE with the same contents of LDPE increases, which should be attributed to the fact that these two blends form two-phase and homogeneous phase equilibrium state structures, respectively.

Moreover, phase diagram is adopted to investigate in detail the effects of the composition, the parameter  $\chi$ , molecular weight on the lubrication phase and the viscosity of blends. Results show that the optimum composition should be located in CSR of the blends for low shear rate, and above and close to the corresponding binodal curve for high shear rate. It is worth noting that all of the ranges for low shear rate, high shear rate and CSR rigorously depend on the rheological measurements of specimens. The phase diagram also shows that for a polymer blend with a given parameter  $\chi$ , both the corresponding binodal and spinodal curves shift downwards with increasing  $N_1$ , indicating that increasing molecular weight of NMWP in a certain range can improve the processability of blends because of the existence of the lubrication phase in between the UHMWPE particles. Besides, it is hoped that these results would provide guidance to studying the rheological behavior of other ultra-high molecular weight polymer blends.

### 3.4 References

1. Dumoulin MM, Utracki LA, Lara J. Rheological and mechanical behavior of the UHMWPE/MDPE mixtures Polym Eng Sci 1984, 24, 117.
2. Kyu T, Vadhar P. Cocrystallization and miscibility studies of blends of ultrahigh molecular weight polyethylene with conventional polyethylenes. J Appl Polym Sci 1986, 32, 5575.
3. Liu GD, Chen YZ, Li HL. Study on Processing of Ultrahigh Molecular Weight Polyethylene/Polypropylene Blends. Journal of Applied Polymer Science 2004, 94, 977.

4. Liu GD, Chen YZ, Li HL. Study on Processing of Ultrahigh Molecular Weight Polyethylene/Polypropylene Blends: Capillary Flow Properties and Microstructure. *Journal of Applied Polymer Science* 2004, 92, 3894.
5. Xie M, Li HL. Viscosity reduction and disentanglement in ultrahigh molecular weight polyethylene melt: Effect of blending with polypropylene and poly(ethylene glycol). *European Polymer Journal* 2007, 43, 3480.
6. Xie M, Liu XL, Li HL. Influence of Poly(ethylene glycol)-Containing Additives on Extrusion of Ultrahigh Molecular Weight Polyethylene/Polypropylene Blend *Journal of Applied Polymer Science*, 2006, 100, 1282.
7. Alamo RG, Londono JD, Mandelkern L, Stehling FC, Wignall GD. Phase behavior of blends of linear and branched polyethylenes in the molten and solid states by small-angle neutron scattering. *Macromolecules* 1994, 24, 411.
8. Zhengang JF, Michael C, Williams, Choi P. A molecular dynamics study of the effects of branching characteristics of LDPE on its miscibility with HDPE. *Polymer*, 2002, 43, 1497.
9. Alamo RG, Graessley WW, Krishnamoorti R, Lohse DJ, Londono JD, Mandelkern L, Stehling FC, Wignall GD. Small Angle Neutron Scattering Investigations of Melt Miscibility and Phase Segregation in Blends of Linear and Branched Polyethylenes as a Function of the Branch Content. *Macromolecules* 1997, 30, 561.
10. Agamalian M, Alamo RG, Kim MH, Londono JD, Mandelkern L, Wignall GD. Phase Behavior of Blends of Linear and Branched Polyethylenes on Micron Length Scales via Ultra-Small-Angle Neutron Scattering. *Macromolecules* 1999, 32, 3093.
11. Barham PJ, Hill MJ, Keller A, Rosney CCA. Phase separation in polyethylene melts. *J Mater Sci Lett* 1988, 7, 1271.
12. Hill MJ, Barham PJ, Keller A, Rosney CCA. Phase segregation in melts of blends of linear and branched polyethylene. *Polymer* 1991, 32, 1384.
13. Hill MJ, Barham PJ, Keller A. Phase segregation in blends of linear with branched polyethylene: the effect of varying the molecular weight of the linear polymer. *Polymer* 1992, 33, 2530.

14. Hill MJ, Barham PJ. Liquid-liquid phase separation in melts of blends of linear with branched polyethylenes: morphological exploration of the phase diagram. *Polymer* 1992, 33, 4099.
15. Hill MJ. Liquid-liquid phase separation in binary blends of a branched polyethylene with linear polyethylenes of differing molecular weight. *Polymer* 1994, 35,1991.
16. Hill MJ, Barham PJ, van Ruiten J. Liquid-liquid phase segregation in blends of a linear polyethylene with a series of octene copolymers of differing branch content. *Polymer* 1993, 34, 2975.
17. Barham PJ, Hill MJ, Goldbeck-Wood G, van Ruiten J. The effect of thermal ageing on impact-modified engineering resins. *Polymer* 1993, 34, 2981.
18. Hill MJ, Barham PJ. Interpretation of phase behaviour of blends containing linear low-density polyethylenes using a ternary phase diagram. *Polymer* 1994, 35, 1802.
19. Morgan RL, Hill MJ, Barham PJ. Morphology, melting behaviour and co-crystallization in polyethylene blends: the effect of cooling rate on two homogeneously mixed blends. *Polymer* 1999, 40, 337.
20. Liu GD. A study on processing and enhancing properties of ultrahigh molecular weight polyethylene. PhD dissertation of Sichuan University in China, 2003.
21. 徐佩弦. 高聚物流变学及其应用. 化学工业出版社 2003.7 第一版.

# CHAPTER 4 Structures and Properties of UHMWPE/PP blends

## 4.1 Introduction

On the bases of the investigations in chapter 3, it can be seen that melt viscosity can be reduced by diluting the UHMWPE with conventional PE (HDPE, LDPE, and LLDPE) under the condition of a high-pressure and rapid molding technology. It is, nevertheless, unable to spare an attendant disadvantage in the process since effective amounts of intermediate molecular weight polyethylene cause a remarkable decrease in some of the most desirable properties. The original excellent mechanical properties, such as mechanical property, are not easy to maintain. Fortunately, UHMWPE with 10~30% polypropylene (PP) could be extruded by a conventional single extruder, and its mechanical and tribological properties were as good as or even better than that of pure UHMWPE.

In this chapter, the effects of initial configurations, temperatures and shear rates on the morphologies and properties of the UHMWPE/PP blends were studied by the applications of DPD and MesoDyn theories. It is well known that the knowledge of interface is very important to improve some properties of two-phase blends<sup>[1 - 2]</sup>. Hence, the influence of composition polydispersity on the interfacial properties of the UHMWPE/PP blends was also investigated by DPD theory.

## 4.2 Results and Discussion

### 4.2.1 Effects of initial configurations

With the determination of the effects of initial configurations on the dynamics of phase separation, the random initial configuration is also adopted in the DPD simulations on the UHMWPE/PP (70/30) blend, and the time evolution of iso-density

surfaces of PP in the blends is shown in Figure 4.1. Consequently, the morphology resulting from the random initial configuration is spherical structure which matches well with that from the core-shell initial configuration, suggesting that the simulation time together with  $4 \times 10^5$  steps is enough to obtain the equilibrium state structure of the UHMWPE/PP blend. In view of the fact that the core-shell initial configuration is closer to the real UHMWPE/NMWP blends than the random initial configuration, hence, the former is adapted to investigate the dynamic of phase mixing for the blends in chapter 3. However, it is very time cost to reach the equilibrium morphologies simulated from the core-shell initial configuration. With the determination of equilibrium morphologies, only random initial configuration is used in this section.

First, DPD simulations of the effects of PP on the morphologies of the UHMWPE/PP blends are performed with random initial configuration by varying the proportion of UHMWPE/PP from 95:5 to 1:99. Figure 4.1 shows the morphologies of the UHMWPE/PP blends obtained after  $4 \times 10^5$  time steps DPD simulation. Apparently a totally disorder and homogeneous phase occurs when 5 percents of PP are added into UHMWPE, as shown in Figure 4.1(a). Between the totally disordered region and the ordered phases there are some melted structures, such as micelle-like. There is no symmetry in the phases, thus, we describe them as droplets (no matter large or small) of the minor moiety in disordered phases. Groot and Madden<sup>[3, 4]</sup> distinguished processes on three different length and time scales in the formation of polymer mesophases: (1) phase separation on the mesoscopic bead level, (2) organization of polymers into micelles, and (3) the organization of these micelles into a superstructure with its own particular symmetry. For the UHMWPE/PP (90/10) blends, a micelle-like phase is found between the disordered and ordered phases. This corresponds to the level (2) ordering in Groot and Madden's scheme. Nevertheless, for the UHMWPE/PP (90/10) blend, although the melted structures occurs after  $4 \times 10^5$  time steps DPD simulation, the blend approximately possesses a homogeneous phase before  $2 \times 10^5$  time steps. Hence, the phase separation is very slow in the UHMWPE/PP (90/10) blend [Figure 4.1(b)].

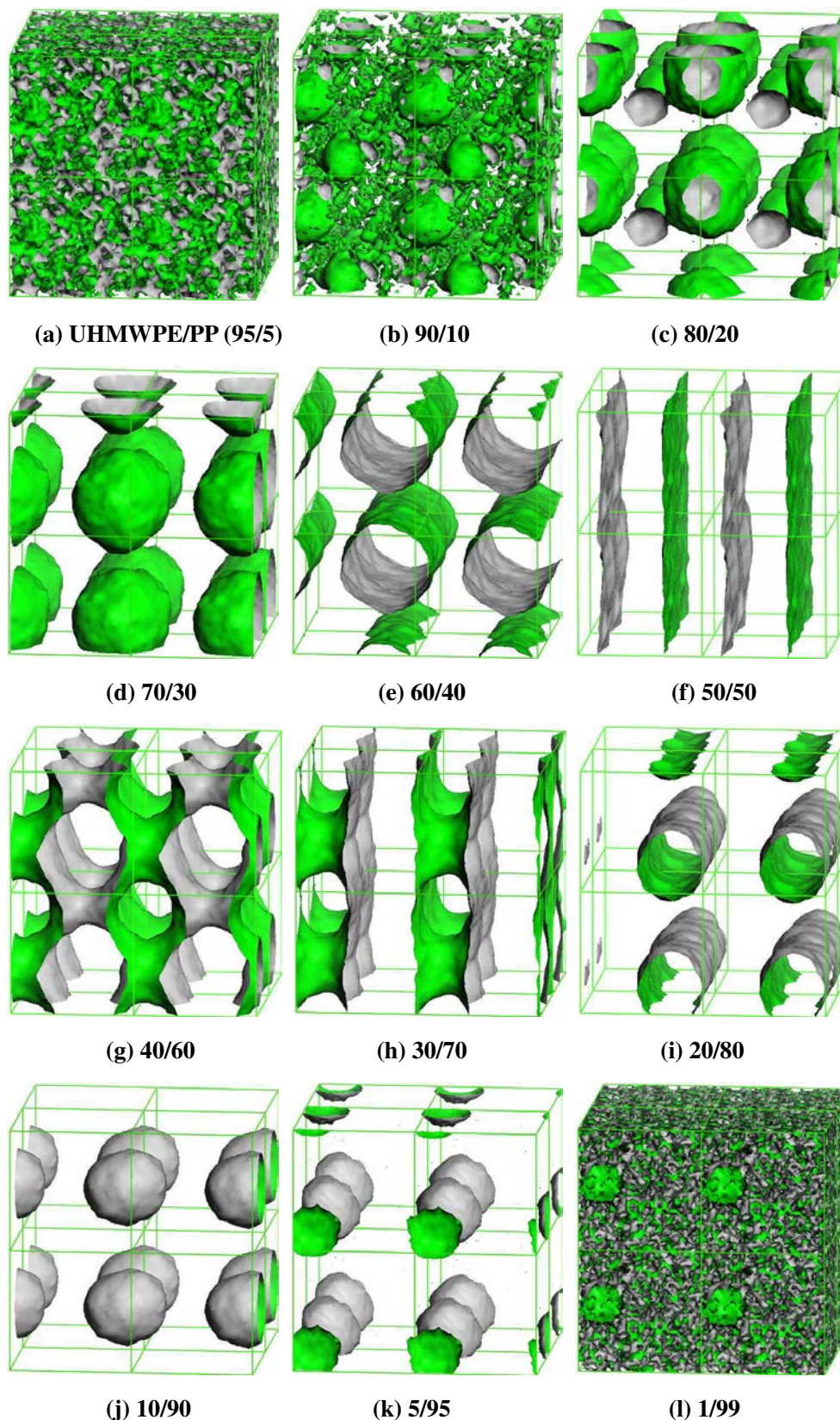


**Figure 4.1** Iso-density surfaces of PP for the UHMWPE/PP blends obtained after  $4 \times 10^5$  steps DPD simulation from random initial configuration. The outward surfaces of PP phases are colored with green, and the rests are UHMWPE phases.

As the concentration of PP increases, some different classical and nonclassical morphologies appear. For example, spherical structure formed in the UHMWPE/PP (80/20), (70/30), (10/90) - (1/99) blends [Figures 4.1(c), (d), (j)-(l)]. As shown in Figures 4.1(e) and (i), PP and UHMWPE tends to form columnar phases in the UHMWPE/PP (60/40) and (20/80) blends, separately. At 70% concentration of PP, two phases including continuous phase of PP and stable perforated lamella (PL) structures of UHMWPE occur. Moreover, the UHMWPE/PP (40/60) blend always shows bicontinuous phase before  $4 \times 10^5$  time steps DPD simulation.

Both PP and UHMWPE show lamellar phases in the UHMWPE/PP (50/50) blend. The isodensity surface of PP divides the blends into PP-rich domain and the UHMWPE-rich domain [Figure 4.1(f)]. The time evolution of the morphology for the UHMWPE/PP blends was investigated by the DPD simulations to give a direct visualization of the underlying dynamic process, for which the phase separation of the UHMWPE/PP (50/50) blends was adopted as an example. Some snapshots of the structures of the blends in the evolution process are given in Figure 4.2. Details of the evolution process can be shown by a comparative scrutiny of Figure 4.2. In Figure 4.2(a), a structure of bicontinuous phase can be identified after  $1 \times 10^4$  steps simulation. As shown in Figure 4.2(b), which is plotted after  $1.9 \times 10^5$  steps of Figure 4.2(a), the holes in both PP-rich and UHMWPE-rich phases become smaller gradually, i.e. PP and UHMWPE transfer to their rich domain, respectively. But the holes in the UHMWPE phase are smaller than that in the PP phase, which might attribute to the fact that the diffusivities of PP are faster than that of UHMWPE [Figure 4.3]. In the next stage, the bicontinuous structures of the blends vanish, and the PL structures of PP appear [Figure 4.2(c)]. Moreover, both PP and UHMWPE show lamella structures after  $3 \times 10^5$  steps. At last this structure changes a little as time runs, and finally we obtain the lamellar phases as shown in Figure 4.1(f). Consequently, both UHMWPE and PP will separate from each other to form their own rich domains with the time increasing although both of them are randomly mixed together at the beginning of the simulation.

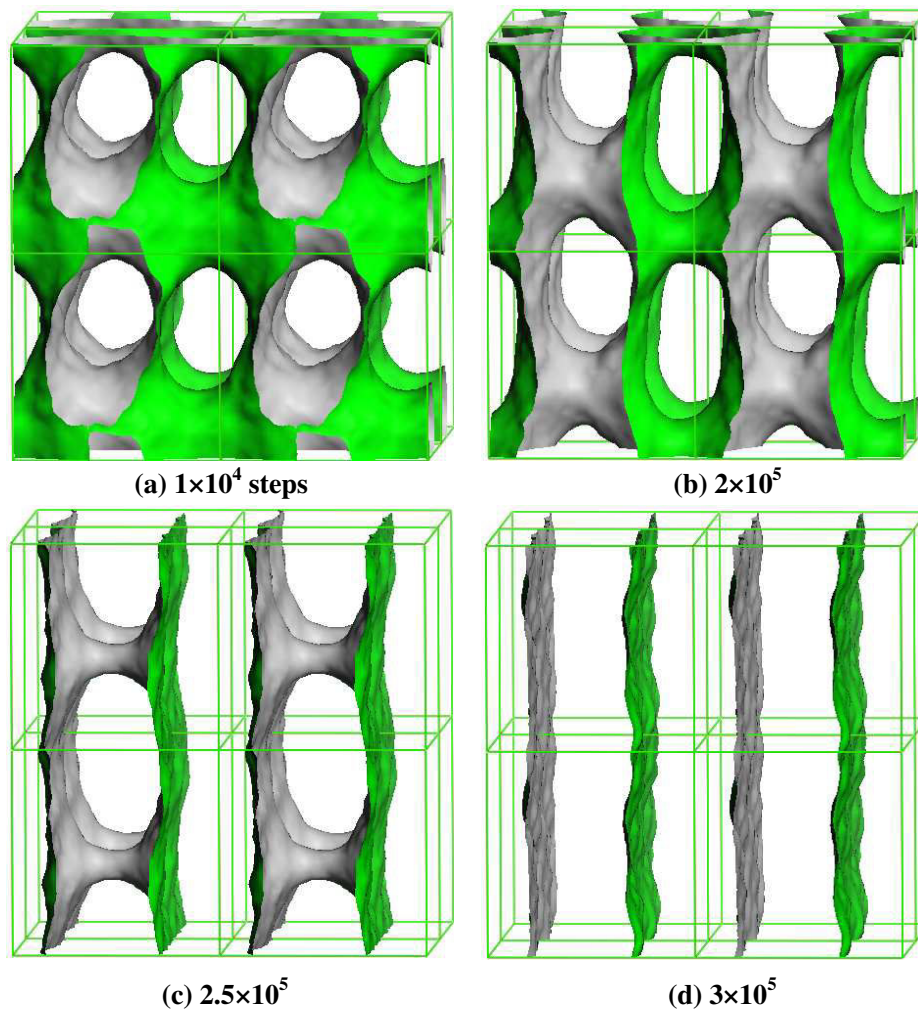


**Figure 4.2** Time evolution of iso-density surfaces of PP in the UHMWPE/PP (50/50) blends from random initial configuration. The outward surfaces of PP phases are colored with green, and the rests are UHMWPE phases.

Figure 4.3 represents the changes in diffusivities of UHMWPE and PP with respect to the variation of PP concentration in the UHMWPE/PP blends. The chain length of UHMWPE is larger than that of PP, and molecule diffusivity of PP is better than that of UHMWPE [Figures 4.3(a) and (b)]. Hence, UHMWPE is easier to accumulate and separate phase than PP, which are directly demonstrated by the comparisons of morphologies for two blends with reciprocal relation of compositions, such as between Figures 4.1(a) and (k), (b) and (j), (c) and (i), (d) and (h), as well as (f) and (g). Moreover, the diffusivities for both PP and UHMWPE increase with the

increasing of PP concentration in the UHMWPE/PP blends (Figures 4.3). Our previous experimental observations <sup>[5-7]</sup> showed that the melt apparent viscosity of the UHMWPE/PP blends decreased with the increase of PP content in the blends. So the enhancements of diffusivities for both PP and UHMWPE might be beneficial to the viscosity reduction of the blends.

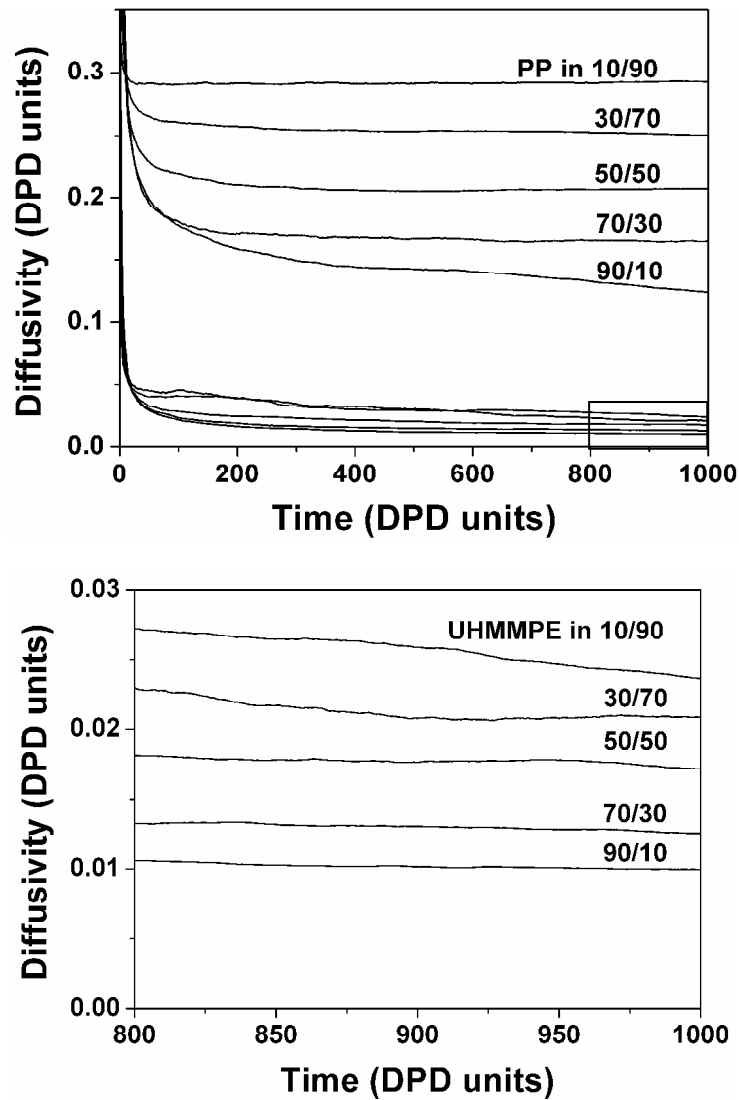


**Figure 4.3** Time evolution of diffusivities of PP and UHMWPE in the UHMWPE/PP blends with varying the proportion of the UHMWPE/PP blends from 90/10 to 10/90.

#### 4.2.2 Effect of temperature

The order parameter  $P$ , represents the characteristics of phase separation. It is

defined as

$$P = \frac{\int_V \sum_I [\theta_1^2(r) - (\theta_1^0)^2] dr}{V} \quad (4.1)$$

where  $\theta$  is the polymer volume fraction and  $V$  is the volume of cells.  $P$  is the mean-squared deviation from homogeneity in the system, which captures the effects of phase separation. In order to show the process of phase separation at different temperatures and concentrations more distinctly, it is helpful to analyze the order parameter changes during the phase separations.

In the MesoDyn simulations, the random initial configuration is also adapted to investigate the effect of temperatures on the morphologies of the UHMWPE/PP blends. The time evolutions of order parameters of the UHMWPE/PP (50/50) blend at 298, 503 and 573K are shown in Figures 4.4, which exhibits three stages [I, II, and III in Figure 4.4(b)] in the phase evolvment. These are very close to the results of Chen's studies on the microphase separation of the binary mixture of tri-block copolymer P123 ((EO)20(PO)70(EO)20) and water<sup>[8]</sup>. Based on Chen's studies, we take the order parameters of the UHMWPE/PP (50/50) blend at 503K as example to state the possible dynamic process of the three stages. In the first stage (I), the order parameter changes little, corresponding to the nucleation of several polymer aggregates. Then, the order parameter increases rapidly, indicating the formation of their approximate morphology at the second stage (II). The final stage (III) is time-consuming, at which the system changes slowly to overcome the defects formed in the previous stage. Experimental evidence comes from time-resolved x-ray scattering<sup>[9]</sup>. These experiments reveal the presence of two processes, a fast process that is believed to be related to the local segregation of the blends [stages I and II] and a slow process that leads to long-ranged order [stage III]. Besides, for systems with other compositions, the order parameters go through in a similar way.

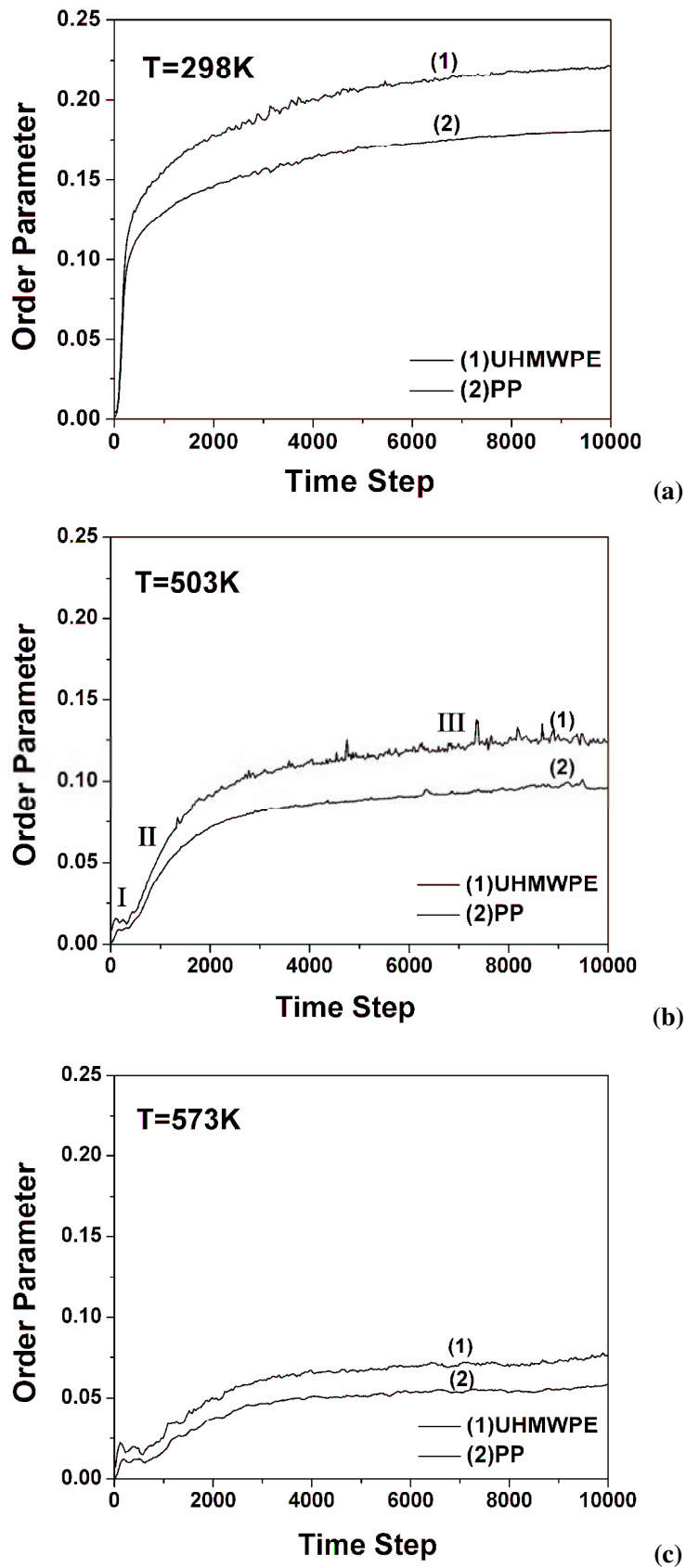


**Figure 4.4** Time evolution of the dimensionless order parameters of the UHMWPE/PP (50/50) blends at different temperatures: (a) 298, (b) 503 and (c) 573K.

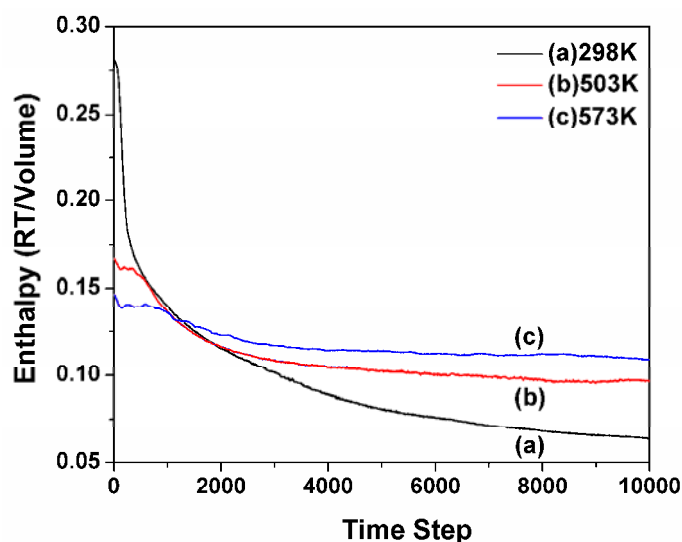


**Figure 4.5** Mixed enthalpy of the UHMWPE/PP (50/50) blends with time evolution at temperatures of (a) 298, (b) 503 and (c) 573K.

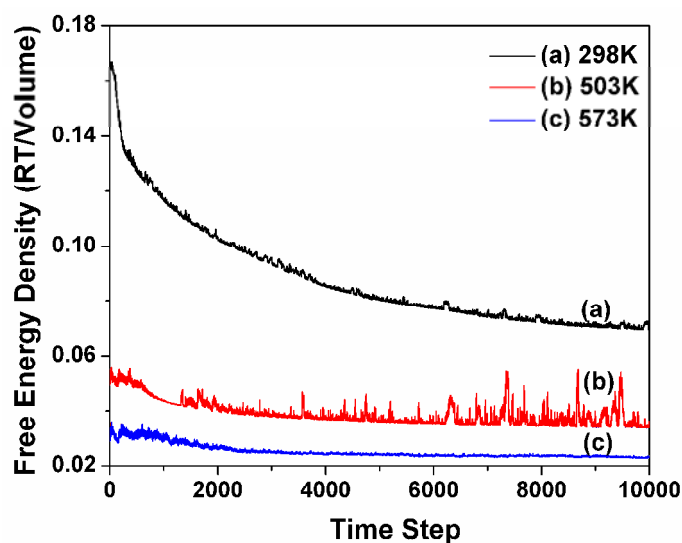


**Figure 4.6** Mixed free energy of the UHMWPE/PP (50/50) blends with time evolution at temperatures of (a) 298, (b) 503 and (c) 573K.

On the basis of Figure 4.4 (a) – (c), it is indicated that the rate of the formation of two-phase structure becomes slower with increasing temperature. However, the morphology of the blend is still two-phase structure although the order parameter of resultant state is very low at 573 K [Figure 4.4 (c)]. With the combination of free energy formula  $\Delta G = \Delta H - T\Delta S$  and Figure 4.4, it can be concluded that the phase separation of the blend is exothermic, which also can be concluded from Figure 4.5.

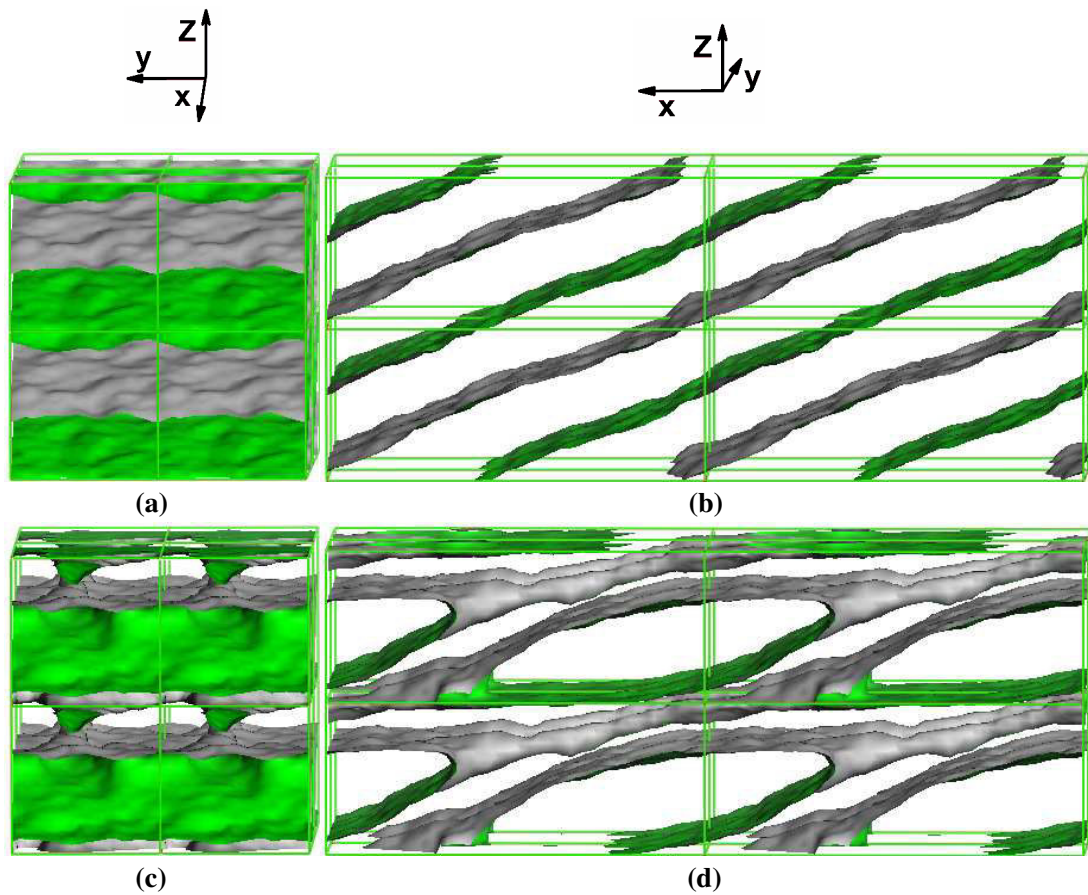
Furthermore, the order parameters of the blends decrease on heating, so the critical point is the upper temperature of phase separation [upper critical solution temperature (UCST) behavior] for the UHMWPE/PP blends, which is consistent with the prediction based on Flory-Huggins theory (Figure 3.21). The effects of temperature on the phase behavior can be understood from the fact that the parameter  $\chi$  of the blend decreases. Therefore, the miscibility of UHMWPE and PP increases at increasing temperature. As shown in Figure 4.6, all of the mixed free energies of the UHMWPE/PP (50/50) blend at different temperatures are positive, leading to the two-phase structure. The mixed free energies remarkably decrease with the increasing temperature, so the separated free energies will increase and the phase separation becomes difficult, which intrinsically agrees with the changes of order parameters for the blend at various temperatures.

### **4.2.3 Effects of shears rates on morphologies**

In this work, the DPD simulations on the UHMWPE/PP (50/50) blend are performed, and the shear rates vary from 0.005 to 0.5 (DPD unit). The simulated isosurfaces of PP in the UHMWPE/PP (50/50) blend are shown in Figure 4.7. When shear flow is added, the UHMWPE/PP (50/50) blends show various morphologies and orientations, depending on the shear flow. At a low shear rate of 0.005, the morphologies of both PP and UHMWPE are lamellar structures [Figure 4.7(a) and (b)], and the lamellar normal is not parallel the velocity gradient direction. Nevertheless, when the shear rate increases to 0.01, the PL structure of UHMWPE and continuous structure of PP occur simultaneously, and the acute angle between the lamellar normal and the velocity gradient direction decreases gradually without reaching zero [Figure 4.7(c) and (d)]. With the shear rate of 0.1, both PP and UHMWPE in the UHMWPE/PP (50/50) blend gives parallel lamellar alignment again, whose normal is parallel to the velocity gradient direction (parallel) [Figure 4.7(e) and (f)]. As shown in Figure 4.7(a) - (f), it can be seen that not only the angles between the lamellar normal and the velocity gradient direction decreases, but also the shapes of the layers changes with increasing the shear rates. When the shear rates increase to

0.2, the lamellar is still parallel the velocity direction, but its normal is not parallel the velocity gradient direction any more [Figure 4.7(g) and (h)]. Furthermore, the blends show cylindrical morphology with shear rates of 0.5 [Figure 4.7(i) and (j)] and the morphology dose not change any more although bigger shear rates are used. Hence, it can be concluded that the evolution of the morphologies is very sensitive to shear rate within 0.005 – 0.5.

In early studies, only parallel alignment was found <sup>[10]</sup>. More recent experiments on polyolefin diblocks showed that perpendicular alignment (lamellar normal is parallel to the x-z plane) could also be produced <sup>[11]</sup>. In this work, the perpendicular alignment is absent, while the cylindrical morphology appears in the DPD simulation on the UHMWPE/PP (50/50) blend.



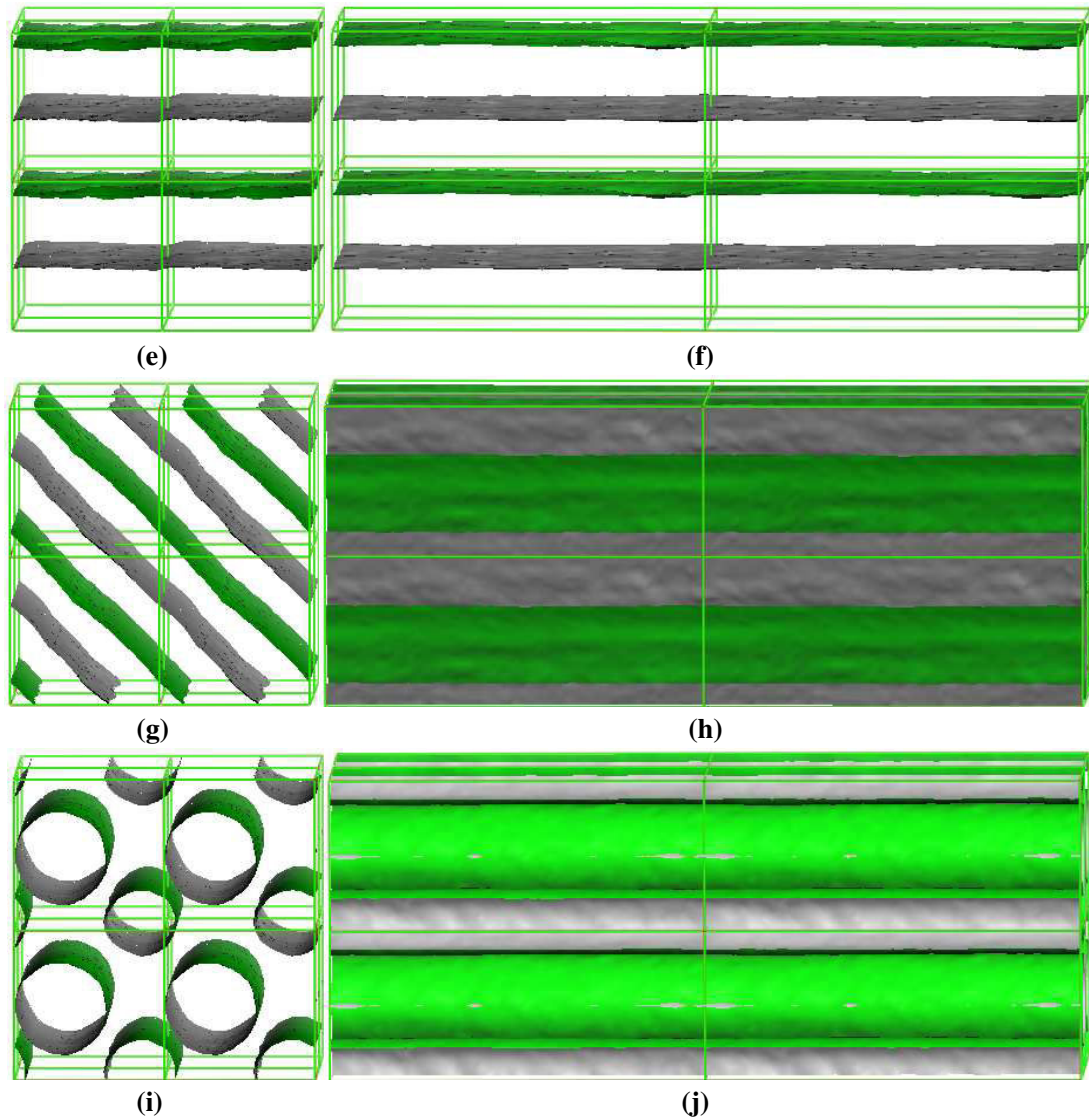


**Figure 4.7** Iso-density surfaces of PP for the UHMWPE/PP (50/50) blends obtained after  $4 \times 10^5$  steps DPD simulation. The outward surfaces of PP phases are colored with green, and the rests are UHMWPE phases. (a) and (b) 0.005 (DPD units), (c) and (d) 0.01, (e) and (f) 0.1, (g) and (h) 0.2, (i) and (j) 0.5. In this work, x-axis and z-axis are shear direction and the shear gradient direction, respectively.

#### 4.2.4 Effect of polydispersity on interface properties

Real polymer samples are polydisperse. It is therefore of interest to investigate the effect of polydispersity on interfacial properties. In this section the interface between polydisperse polymers is analyzed by considering the simplest molten polydisperse system: PE and PP melts are both binary mixtures. In the blends the long PE (UHMWPE) and PP (HMWPP) chains as well as the small PE (NMWPE) and PP (NMWPP) chains are composed by 11600, 1000, 250 and 250 beads, respectively. In

spite of this simplicity, we expect it to exhibit the same features that would be found in more general polydisperse systems.

Figures 4.8 – 4.10 show the density profiles of the UHMWPE/ NMWPE/ HMWPP/ NMWPP blends with different compositions. It can be seen that both UHMWPE and HMWPP prefer to be in their own rich phases. Both NMWPE and NMWPP, however, are not only located in their own rich phases, but also in the neighbor phases (Figure 4.8).

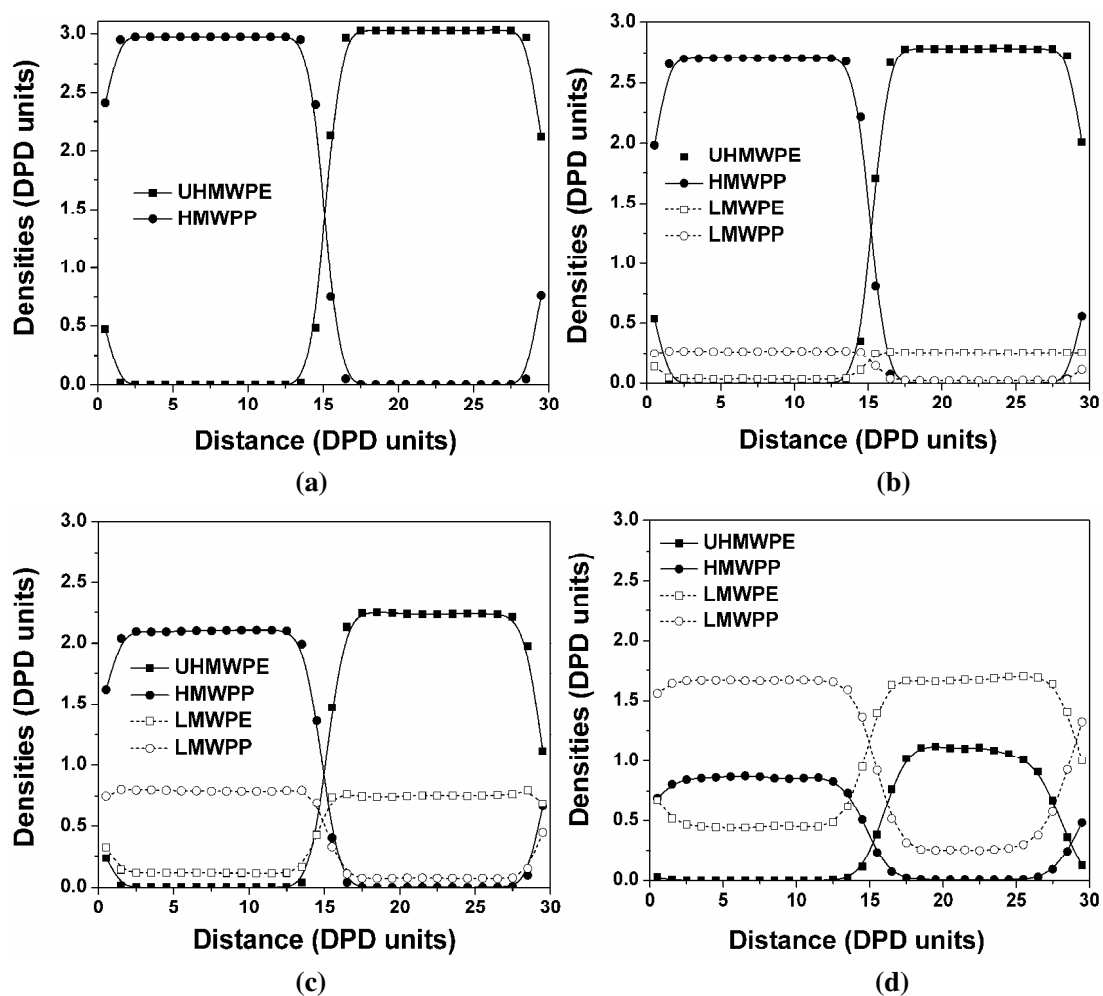


**Figure 4.8** Density profiles of each component for the blends: (a) UHMWPE/ HMWPP (50/50); (b) UHMWPE/ NMWPE/ HMWPP/ NMWPP (45/5/45/5); (c) UHMWPE/ NMWPE/ HMWPP/ NMWPP (35/15/35/15); (d) UHMWPE/ NMWPE/ HMWPP/ NMWPP (15/35/15/35).

Besides, there is a significant accumulation of small chain at the interface as indicated in Figure 4.9. This accumulation of the small chains at the interface push the long chains further away from the interface with increasing the concentration of the

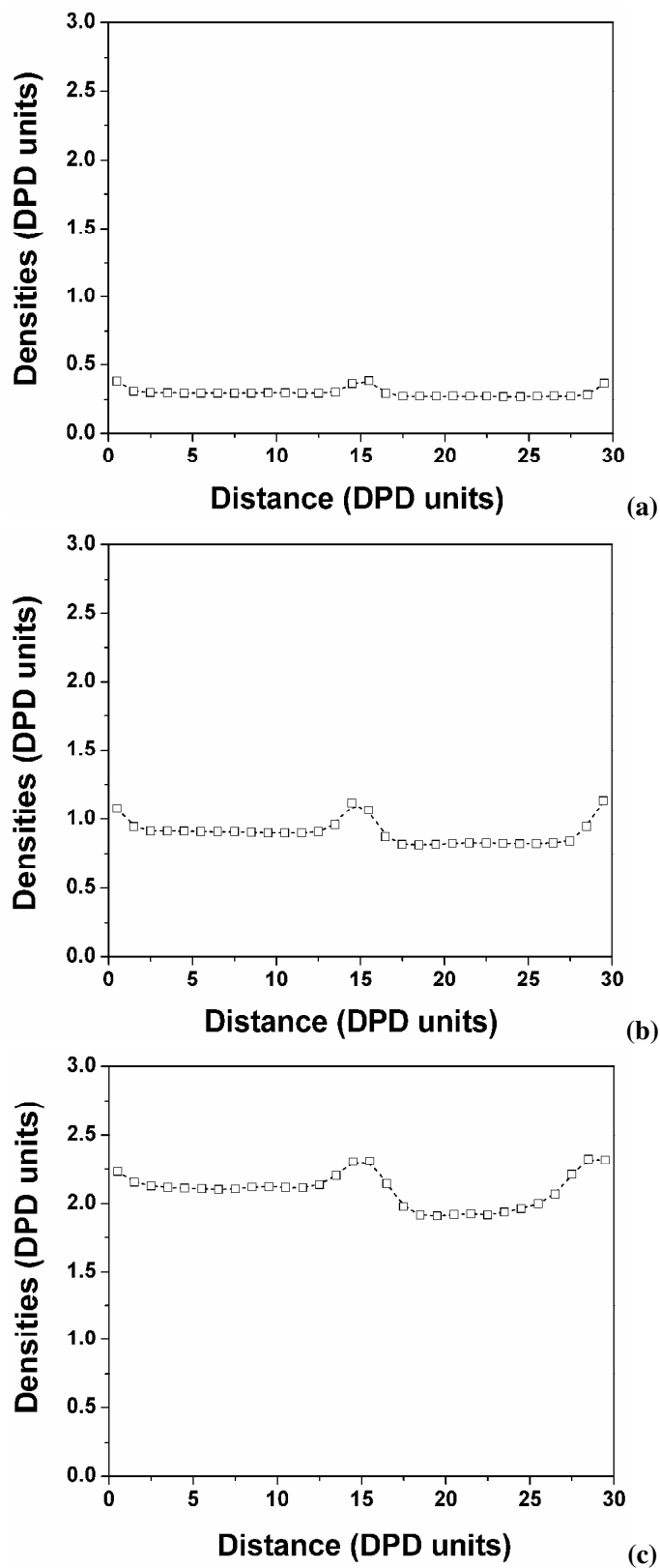


**Figure 4.9** The sum of the densities of NMWPE and NMWPP for the blends: (a) UHMWPE/ NMWPE/ HMWPP/ NMWPP (45/5/45/5); (b) UHMWPE/ NMWPE/ HMWPP/ NMWPP (35/15/35/15); (c) UHMWPE/ NMWPE/ HMWPP/ NMWPP (15/35/15/35).

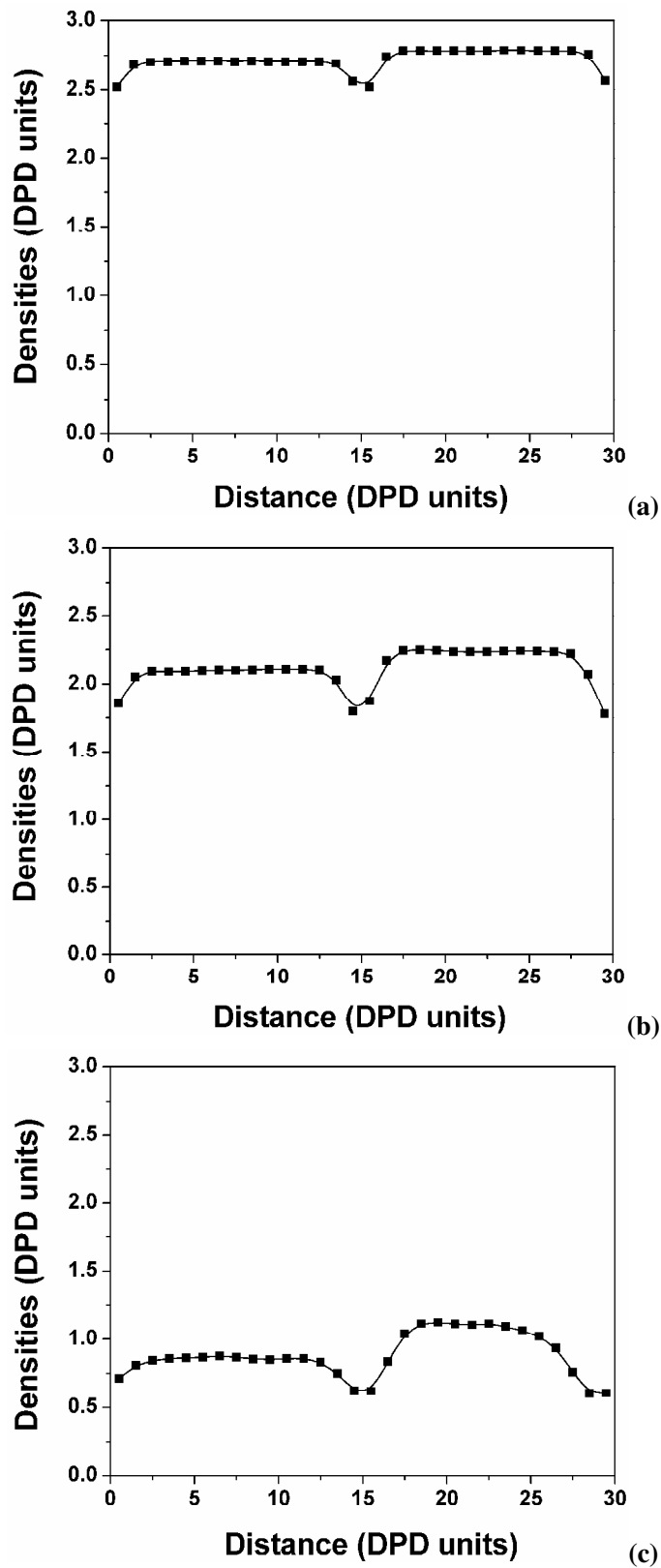


**Figure 4.10** The sum of the densities of UHMWPE and HMWPP for the blends: (a) UHMWPE/ NMWPE/ HMWPP/ NMWPP (45/5/45/5); (b) UHMWPE/ NMWPE/ HMWPP/ NMWPP (35/15/35/15); (c) UHMWPE/ NMWPE/ HMWPP/ NMWPP (15/35/15/35).

small chains (Figure 4.10). One interesting quantity is the volume fraction of small chains,  $\phi_{\text{NMWPE}} + \phi_{\text{NMWPP}}$ . We have represented on Figure 4.11 the small-chain excess

$$\varepsilon(x) = \phi_{\text{NMWPE}}(x) + \phi_{\text{NMWPP}}(x) - \overline{\phi_{\text{NMWPE}}} - \overline{\phi_{\text{NMWPP}}} \quad (4.2)$$

as a function of  $x$  for different polydisperse systems. Our calculations indicate that the function of  $\varepsilon(x)$  has a positive maximum at the interface ( $x = 0$  and  $15$ ). For example both  $\varepsilon(0)$  and  $\varepsilon(15)$  are about 0.075 for the UHMWPE/ NMWPE/ HMWPP/ NMWPP (15/35/15/35) blend. Thus, at the interface, 22% of the monomers belong to long chains and 78% to small chains.

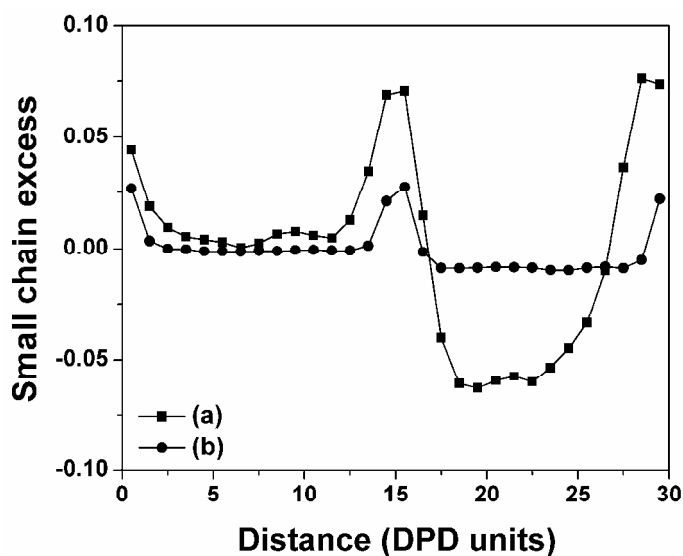


**Figure 4.11** The small chain excess (NMWPE and NMWPP) for the blends: (a) UHMWPE/ NMWPE/ HMWPP/ NMWPP (15/35/15/35); (b) UHMWPE/ NMWPE/ HMWPP/ NMWPP (45/5/45/5).

More precisely, the DPD calculations indicate that the small-chain excess at the interface (I) decreases when the concentrations of small chains for NMWPE and NMWPP decreases (Figures 4.11); (II) decreases when both small chain lengths simultaneously increase (Figures 4.9). Indeed, when both chains become very long, the variation in chain lengths does not play any role (see chapter 7). The physical reason of the accumulation might be attributed to the fact that having more small chains at the interface has the effect of lowering the interfacial tension. Besides, it is clear that the interface thickness depends strongly upon the concentration of small

chains. As the concentration of small chains increases, the interface thickness of the blend increases dramatically (Figure 4.11).

The normal and transversal components of the pressure tensor [ $P_n(x)$  and  $P_t(x)$ ] are calculated complying with the definition of Irving and Kirkwood <sup>[12]</sup>. Only the pairs of particles whose centers of mass connecting line passes through the infinitesimal interface should contribute to the local pressure tensor. For a planar interface, the expressions <sup>[13, 14]</sup> take the forms as

$$P_n(x) = \rho(x)k_B T + \frac{1}{A} \left\langle \sum_{i<j} \frac{\mathbf{F}_{ij}^x \cdot \mathbf{r}_{ij}^x}{r_{ij}^x} \theta \left( \frac{r^x - r_i^x}{r_{ij}^x} \right) \theta \left( \frac{r_j^x - r^x}{r_{ij}^x} \right) \right\rangle,$$

$$P_t(x) = \rho(x)k_B T + \frac{1}{2A} \left\langle \sum_{i<j} \frac{\mathbf{F}_{ij}^y \cdot \mathbf{r}_{ij}^y + \mathbf{F}_{ij}^z \cdot \mathbf{r}_{ij}^z}{r_{ij}^x} \theta \left( \frac{r^x - r_i^x}{r_{ij}^x} \right) \theta \left( \frac{r_j^x - r^x}{r_{ij}^x} \right) \right\rangle. \quad (4.3)$$

Here  $\rho(x)$  denotes the density at  $x$  averaged over tangential coordinates  $y$  and  $z$  and  $\theta(x)$  denotes the Heaviside step function. For the term  $\mathbf{F}_{ij}^\alpha \cdot \mathbf{r}_{ij}^\alpha$  ( $\alpha = x, y, z$ ) we only count the contributions from the conservative forces  $\mathbf{F}^C$  and the harmonic forces  $\mathbf{F}^S$  because our system corresponds to the correct Boltzmann distribution <sup>[15]</sup>. The interfacial tension in each slab is obtained by dividing the simulation box into 30 slabs parallel to the interface, and the pressure tensor is calculated by:

$$2\gamma_s = \int_{slab} [P_n(x) - P_t(x)] dx \quad (4.4)$$

In the left side of this equation, an additional factor 2 arises from the existence of two interfaces in the system due to the periodic boundary conditions.

Figure 4.12 shows that the interfacial tension is lowered by the presence of small chains and decreases remarkably with increasing the concentration of the small chains, which is consistent with the density distributions of all components at the interface. Small chains in fact play a surfactant role.

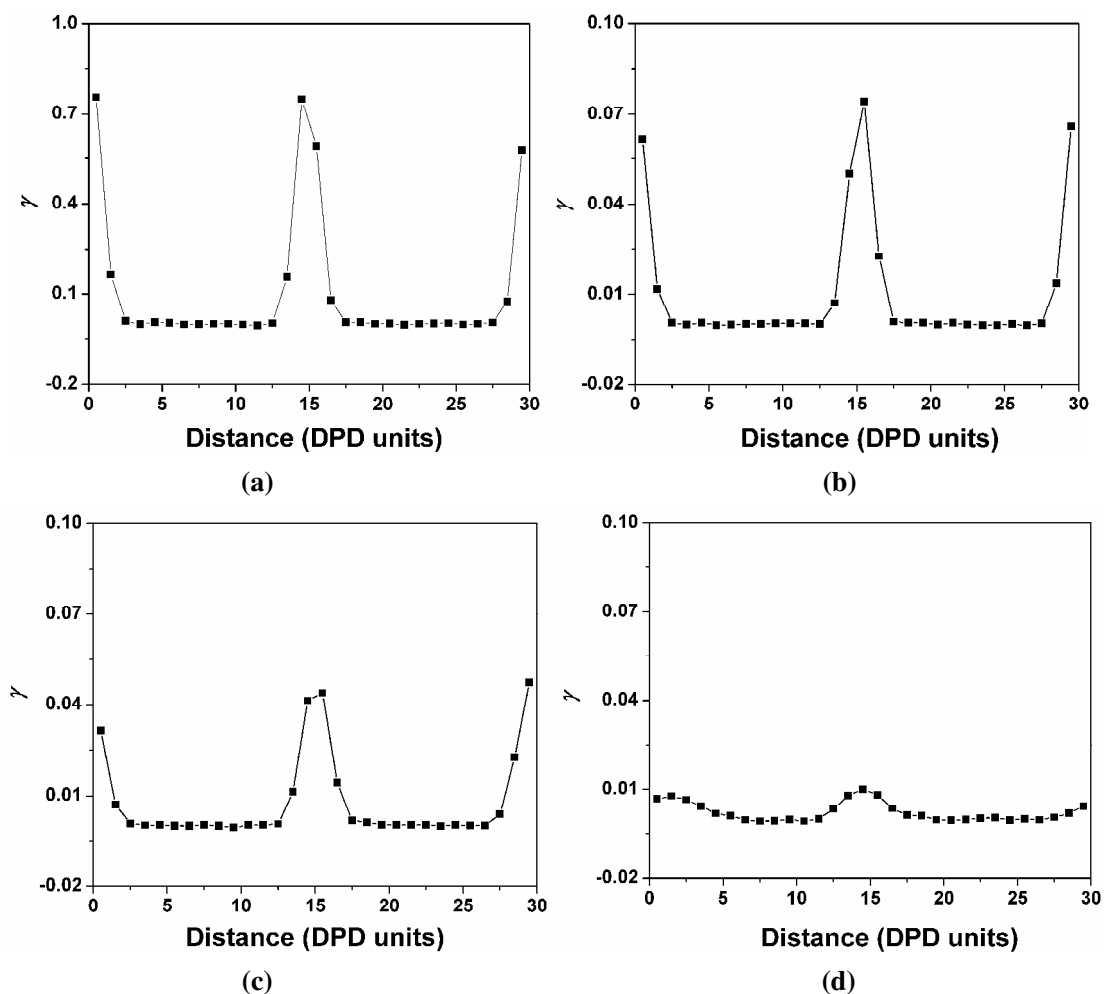


**Figure 4.12** Interfacial tension in each slab calculated from Eqs. (4.3) and (4.4) for: (a) UHMWPE/ HMWPP (50/50); (b) UHMWPE/ NMWPE/ HMWPP/ NMWPP (45/5/45/5); (c) UHMWPE/ NMWPE/ HMWPP/ NMWPP (35/15/35/15); (d) UHMWPE/ NMWPE/ HMWPP/ NMWPP (15/35/15/35).

Figures 4.8 – 4.12 has shown the importance of molecular weight and polydispersity effects on the properties of polymer-polymer interfaces. The origin of these effects is purely entropic. The loss of translational entropy due to the confinement of the chains into one-half space is more severe for small chains. As a result the interface is broader for small chains, and for a polydisperse system, it is more advantageous to expel large chains from the interface.

### 4.3 Conclusions

In this section, the effects of initial configurations, shear rates, temperature and polydispersity have been investigated by both DPD and MesoDyn theories, leading to

the following conclusions:

Experimental observations showed that the melt apparent viscosity of the UHMWPE/PP blends decreased with the increase of PP content in the blends. So the enhancements of diffusivities for both PP and UHMWPE might be beneficial to the viscosity reduction of the blends.

The simulation by MesoDyn theory suggests that the time evolutions of dimensionless order parameters of the UHMWPE/PP (50/50) blend at each value of temperature exhibit three stages. Experiments reveal the presence of two processes, a fast process that is believed to be related to the local segregation of the blends [stages I and II] and a slow process that leads to long-ranged order [stage III].

On the bases of the studies on the effects of shear rates, it can be concluded that the evolution of the morphologies is very sensitive to shear rate within 0.005 – 0.5. Particularly, the perpendicular alignment is absent, while the cylindrical morphology appears in the DPD simulation on the UHMWPE/PP (50/50) blend.

For the UHMWPE/NMWPE/HMWPP/NMWPP blends with different compositions, it can be seen that both PE and PP with relatively high molecular weight prefer to be in their own rich phases. Nevertheless, the other components are not only located in own rich phases, but also in the neighbor phases.

The physical reason of the accumulation of small chains might be attributed to the fact that having more small chains at the interface has the effect of lowering the interfacial tension. Small chains in fact play a surfactant role. Besides, as the concentration of small chains increases, the interface thickness of the blend increases dramatically.

## References

1. Hu WC, Brown HR, Koberstein JT, Bhatia R, Lingelser JP, Gallot Y. Adhesion enhancement of polymer blend interfaces by reactive block copolymer brushes. *C R Chimie* 2006, 9, 45.

2. Molau GE, in: Aggarwal SL Ed., Block copolymers, Plenum Press, New York, 1970, p. 79.
3. Groot RD, Madden TJ. Dynamic simulation of diblock copolymer microphase separation. *J. Chem. Phys.* 108, 8713 (1998).
4. Groot RD, Madden TJ, Tildesley DJ. On the role of hydrodynamic interactions in block copolymer microphase separation. *J Chem Phys* 1999, 110, 9739.
5. Liu GD, Chen YZ, Li HL. Study on Processing of Ultrahigh Molecular Weight Polyethylene/Polypropylene Blends. *Journal of Applied Polymer Science* 2004, 94, 977.
6. Liu GD, Chen YZ, Li HL. Study on Processing of Ultrahigh Molecular Weight Polyethylene/Polypropylene Blends: Capillary Flow Properties and Microstructure. *Journal of Applied Polymer Science* 2004, 92, 3894.
7. Xie M, Li HL. Viscosity reduction and disentanglement in ultrahigh molecular weight polyethylene melt: Effect of blending with polypropylene and poly(ethylene glycol). *European Polymer Journal* 2007, 43, 3480.
8. Zhao YR, Chen X, Yang CJ, Zhang GD. Mesoscopic Simulation on Phase Behavior of Pluronic P123 Aqueous Solution. *J Phys Chem B* 2007, 111, 13937.
9. Balsara NP, Garetz BA, Newstein MC, Bauer BJ, Prosa TJ. Evolution of Microstructure in the Liquid and Crystal Directions in a Quenched Block Copolymer Melt. *Macromolecules* 1998, 31, 7668.
10. Koppi KA, Tirrell M, Bates FS, Almdal K, Colby RH. Lamellae orientation in dynamically sheared diblock copolymer melts. *J Phys France II* 1992, 2, 1941.
11. Gupta VK, Krishnamoorti R, Kornfield JA, Smith SD. Evolution of Microstructure during Shear Alignment in a Polystyrene-Polyisoprene Lamellar Diblock Copolymer. *Macromolecules* 1995, 28, 4464.
12. Irving JH, Kirkwood JG. The Statistical Mechanical Theory of Transport Processes. IV. The Equations of Hydrodynamics. *J Chem Phys* 1950, 18, 817.
13. Rao M, Berne BJ. On the location of surface of tension in the planar interface between liquid and vapour. *Mol Phys* 1979, 37, 455.
14. Varnik F, Baschnagel J, Binder K. Molecular dynamics results on the pressure

tensor of polymer films. *J Chem Phys* 2002, 113, 4444.

15. Groot RD, Warren PB. Dissipative particle dynamics: Bridging the gap between atomistic and mesoscopic simulation. *J Chem Phys* 1997, 107, 4423.

# CHAPTER 5 The UHMWPE/PP/MP Composites

## 5.1 Introduction

The results in chapter 3 indicated that the UHMWPE/PP (90/10) blend could be extruded by a conventional single extruder. However, the melt fluidity of the UHMWPE/PP blend was still low. Besides, its mechanical and tribological properties were as good as or even better than that of pure UHMWPE<sup>[1,2]</sup>. Xie's investigation suggested that the addition of a small amount of PEG could also significantly reduce the die pressure and melt viscosity of UHMWPE/PP blend, but the tensile strength of the blend would sharply decrease when more than 2phr PEG was added<sup>[3,4]</sup>. Wu et al reported that UHMWPE/kaolin composites prepared by polymerization-filling showed better dynamic rheological properties<sup>[5]</sup>. When the kaolin content was more than 15 wt %, the composite melts behaved like general polymer melts and could be extruded at low shear rate. When the kaolin content was less than 10 wt %, nevertheless, a common viscoelastic flow zone was absent from the flow curve of the composites. In addition, the stress vibration started at a low shear rate, and a coarse surface of the extrudate appeared. In view of the fact that both kaolin and MMT have layer structures, it is hoped that the synergistic effect of PEG and MMT on reducing the viscosity is achieved.

In this chapter, both PEG and the OMMT of DK-1 are used to prepare the hybrid MP. The effects of the weight ratio of the UHMWPE/PP blends and content of the hybrid MP on the morphologies, rheological behaviours and mechanical properties of the UHMWPE/PP/MP composites have been investigated. The possible mechanisms of viscosity reduction and enhancement in mechanical properties have been proposed.

## 5.2 Results and discussion

### 5.2.1 The dispersion characteristics of OMMT in the UHMWPE/PP/MP composites

Figure 5.1 compares the WAXD patterns of MP21, MP11, UHMWPE/PP/MP21 (90/10/3), UHMWPE/PP/MP11 (90/10/3) and DK-1. The mean interlayer spacing of the (001) plane ( $d_{(001)}$ ) for the DK-1 sample estimated by Bragg's formula  $n\lambda = 2d\sin\theta$  is 2.29 nm ( $2\theta \approx 3.85^\circ$ ) [Figure 5.1(a)]. The identification of the (001) diffraction peaks is summarized for all investigated samples in Table 5.1.

**Table 5.1** (001) diffraction peaks and corresponding d-spacing of DK-1 and various composites

Samples	001	
	$2\theta$	d-spacing
DK-1	3.85	2.29
MP11	2.61	3.39
MP21	2.73	3.22
UHMWPE/PP/MP11(90/10/3)	no peak	-
UHMWPE/PP/MP21(90/10/3)	no peak	-

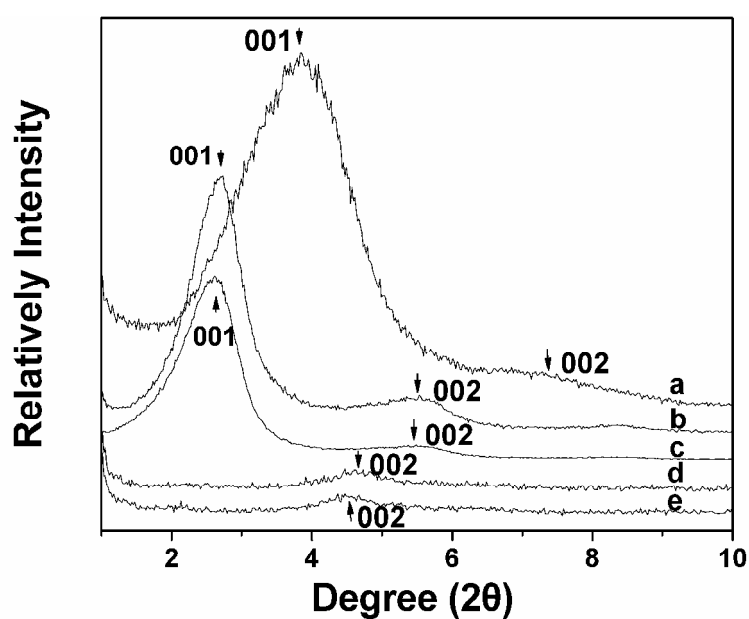


**Figure 5.1** Wide-angle X-ray diffraction patterns of (a) DK-1, (b) MP21, (c) MP11, (d) UHMWPE/PP/MP21 (90/10/3) and (e) UHMWPE/PP/MP11 (90/10/3).

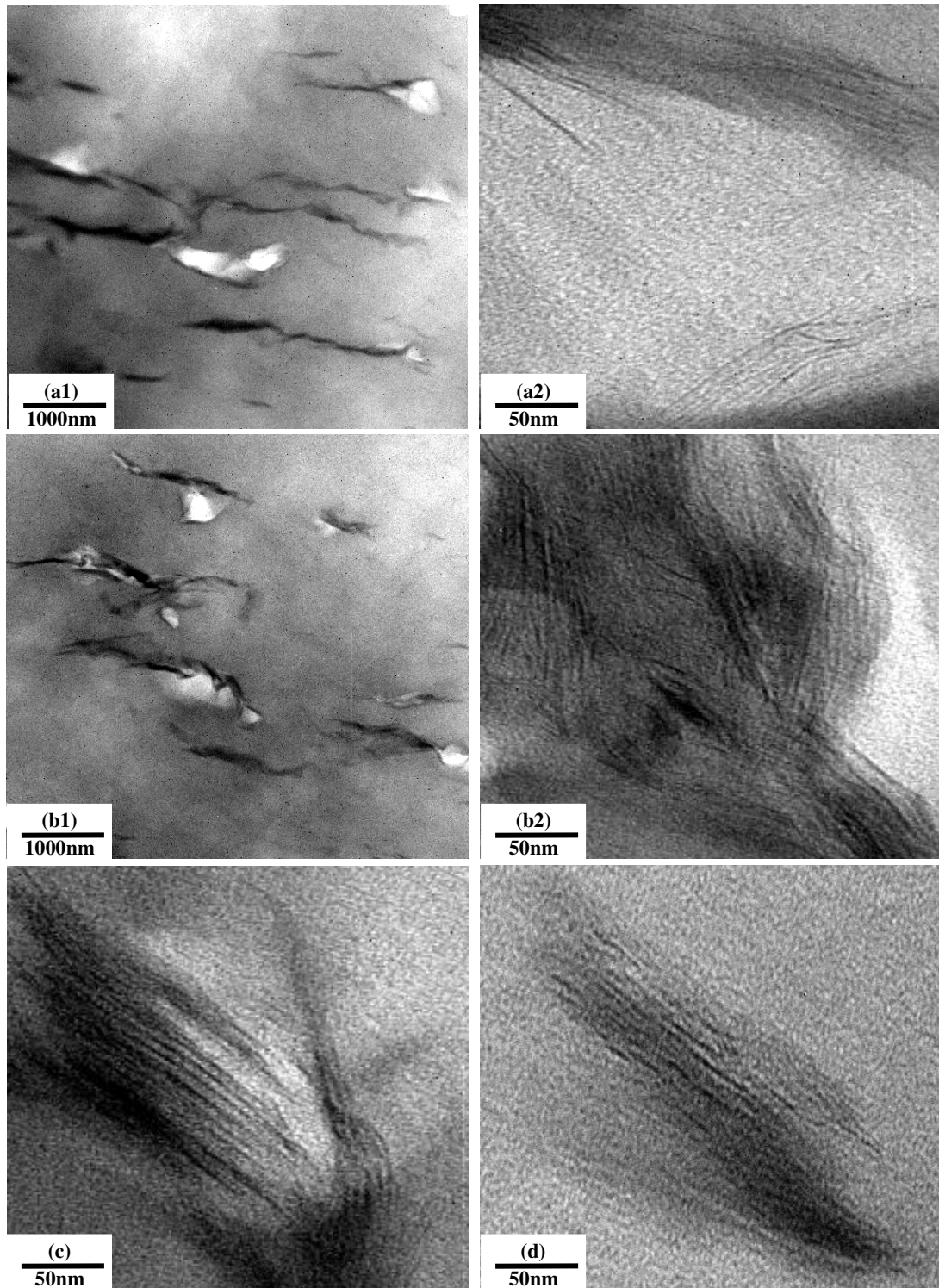


**Figure 5.2** Transmission electron micrographs of (a1) and (a2) UHMWPE/PP/MP11 (90/10/3), (b1) and (b2) UHMWPE/PP/MP21 (90/10/3), (c) MP11 and (d) MP21.

As it is shown in Figure 5.1 and Table 5.1, the peaks of (001) plane shifted to lower angles in both MP11 and MP21, and the peak of (001) plane disappeared in UHMWPE/PP/MP11 and UHMWPE/PP/MP21. The shifts established the formation

of exfoliated and intercalated structure for UHMWPE/PP/MP, as opposed to an intercalated structure for MP systems. Figure 5.1 and Table 5.1 also indicate that the d-spacing of MP11 is slightly larger than that of MP21.

Figure 5.2 shows the transmission electron micrographs of UHMWPE/PP/MP11 (90/10/3), UHMWPE/PP/MP21 (90/10/3), MP11 and MP21. As can be seen in Figure 5.2 (a2) and (b2), apart from intercalated MMT, the exfoliated layers are also present in UHMWPE/PP/MP11 (90/10/3) and UHMWPE/PP/MP21 (90/10/3). But only intercalated structure was able to be observed in MP11 and MP21 [Figure 5.2 (c) and (d)].

Aranda and Greeland et al. have found that polymers containing the groups capable of associative interactions, such as hydrogen bonding, lead to intercalation [6, 7]. FTIR spectra for DK-1 is given in Figure 5.3, in which the absorption band at ca.  $3432.50\text{ cm}^{-1}$  represents the hydroxyl (-OH) group. The driving force of the intercalation originates from the strong hydrogen bonding between the oxygen groups of PEG and hydroxyl groups from DK-1. Besides, the complexation of PEG with Na<sup>+</sup> between MMT layers facilitates the intercalation of PEG into MMT [8].

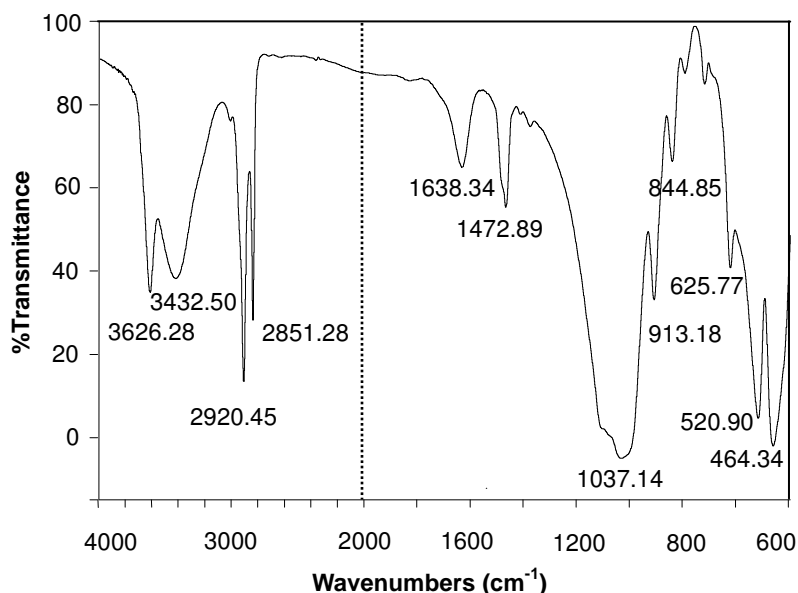


**Figure 5.3** FTIR spectra for DK-1.

The surface modifier for DK-1 lowers the surface energy of the inorganic host and converts the normally hydrophilic silicate surface to an organophilic one, making

the intercalation and exfoliation of MMT possible.

## 5.2.2 Analysis of phase structure formation

### 5.2.2.1 Phase structure of the UHMWPE/PP/PEG blends

#### 5.2.2.1.1 Phase behaviors in the Absence of shear

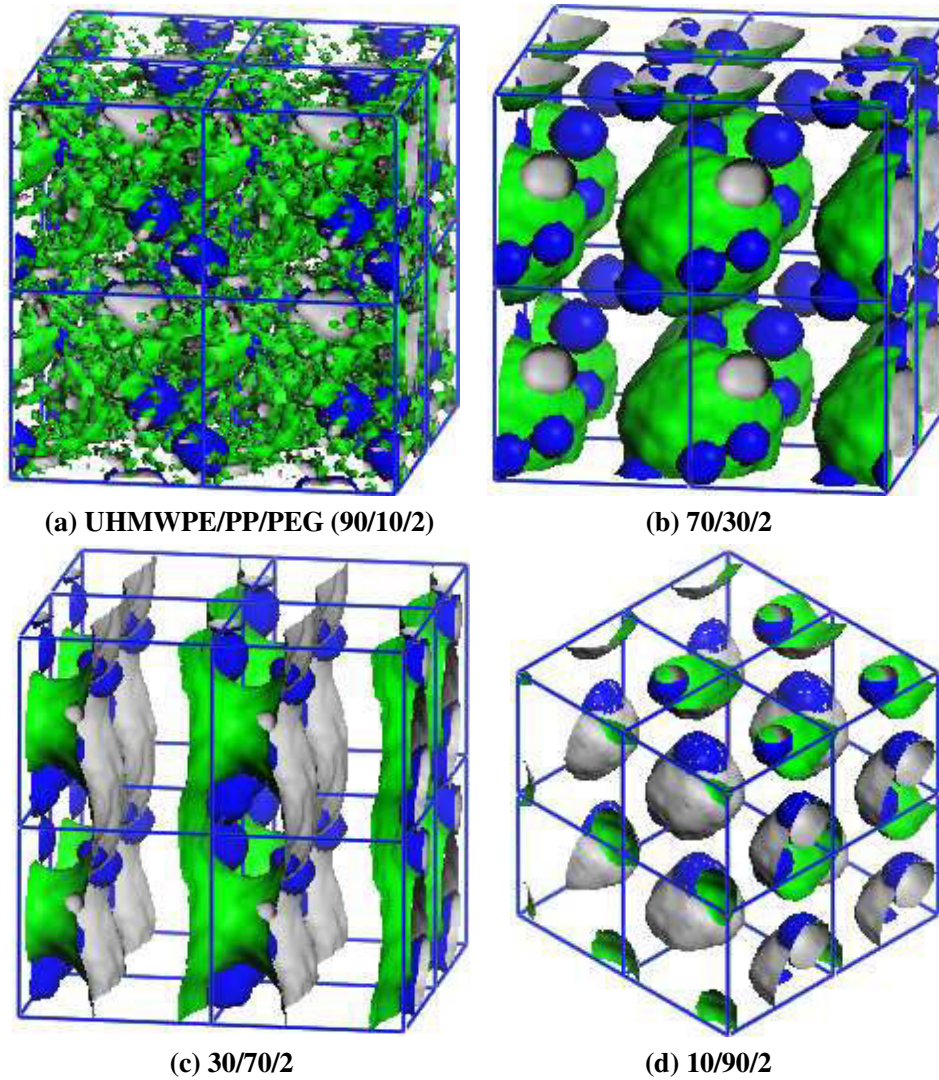


**Figure 5.4** Iso-density surfaces of PP and PEG for UHMWPE/PP blends obtained after  $4 \times 10^5$  steps DPD simulation. The outward surfaces of PP phases are colored with green, the outward surfaces of PEG phases are colored with blue, and the rests are UHMWPE phases.

DPD simulations of the effects of PEG on the morphologies of the UHMWPE/PP blends are performed by varying the concentrations of PP from 10 to 90. The concentration of PEG is 2 per hundred parts of UHMWPE/PP by weight (phr).

The morphologies of the UHMWPE/PP/PEG blends obtained after  $4 \times 10^5$  time steps DPD simulation are shown in Figure 5.4. Obviously, PEG prefers to distribute in the UHMWPE phase regardless of variation of PP concentration in UHMWPE/PP/PEG blends (Figure 5.4). For example, the phase morphology of the UHMWPE/PP/PEG (30/70/2) blend is also corroborated by its density profile. PEG can hardly be located in the PP-rich phase (Figure 5.5). By careful observation it was determined that PP in UHMWPE/PP/PEG blends exhibits morphology similar to that in the corresponding UHMWPE/PP blends (Figure 4.1 in Chapter 4) except for the 10/90/2 blends, for which a hexagonal spheres morphology is observed [Figure 5.4(d)]. Due to the presence of aether bond segments in PEG chains, UHMWPE and PP have very different polar character with PEG. Therefore, they would prefer to be located as far from each other as possible, leading to a phase separation of the ternary UHMWPE/PP/PEG systems. On the other hand, Flory–Huggins parameters  $\chi_{UHMWPE/PEG}$  (0.191) is much lower than  $\chi_{PP/PEG}$  (0.412), which leads PEG to be concentrated more preferably in the phase of UHMWPE instead of PP.

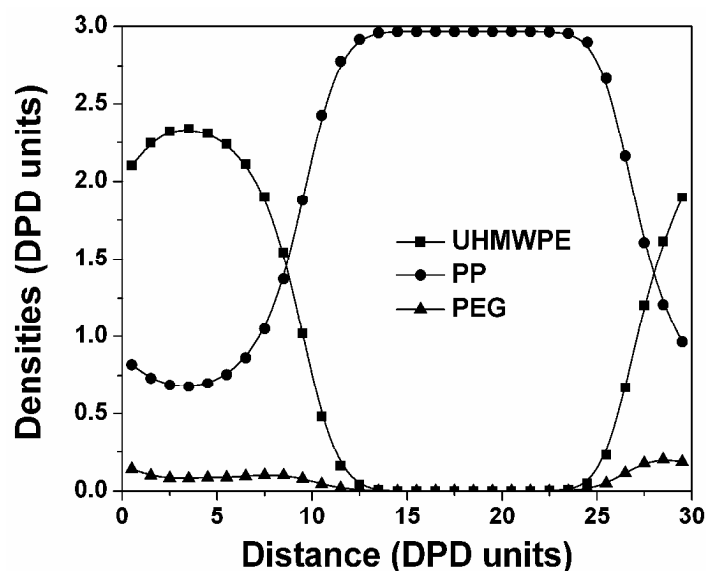


**Figure 5.5** Density profiles of each component for the blends UHMWPE/PP/PEG (30/70/2).

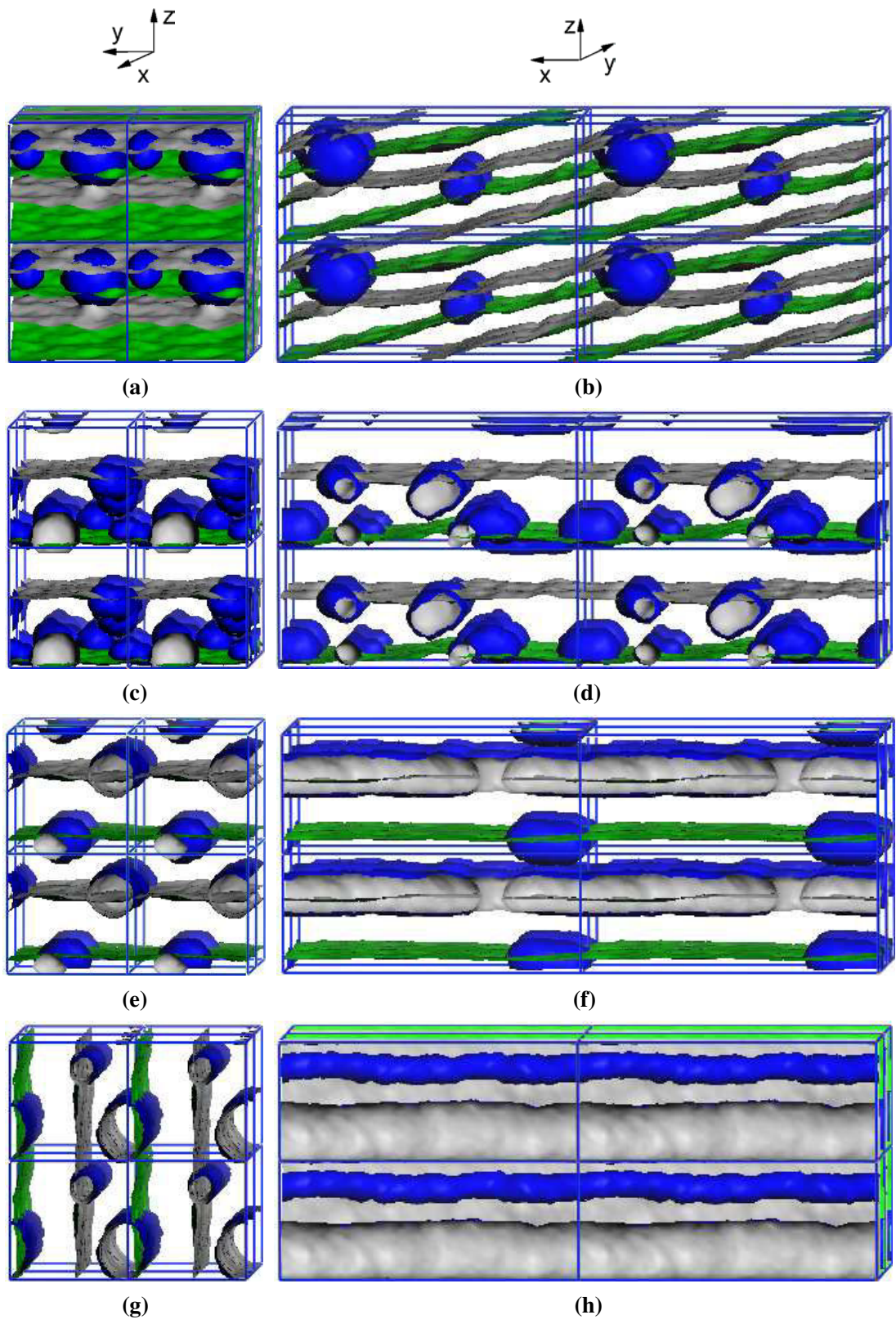
### 5.2.2.1.2 Phase behaviors in the presence of shear

The DPD simulations on the UHMWPE/PP/PEG (50/50/2) blends are performed, and the shear rates vary from 0.005 to 0.5. The simulated isosurfaces of both PP and

PEG in the UHMWPE/PP/PEG (50/50/2) blends are shown in Figure 5.6. When shear flow is added, the UHMWPE/PP/PEG (50/50/2) blends show very different morphologies as well as orientations, depending on the strength of shear flow. At a low shear rate of 0.005, the morphologies of both PP and UHMWPE are lamellar structures [Figure 5.6(a) and (b)] and the lamellar normal is not parallel to the velocity gradient direction, which is very similar with the corresponding morphology of the UHMWPE/PP (50/50) blend [Figure 4.7(a) and (b)]. Within the shear rate of 0.01-0.05, both PP and UHMWPE in the UHMWPE/PP/PEG (50/50/2) blend always give parallel lamellar alignment, whose normal is parallel to the velocity gradient direction. However, this morphology only appears at relatively large shear rate in the UHMWPE/PP (50/50) blend [Figure 4.7(e) and (f)]. Nevertheless, when the shear rate is more than 0.3, the UHMWPE/PP/PEG (50/50/2) blend shows perpendicular alignment, which does not appear in the UHMWPE/PP blends. Koppi and coworkers reported that the main reason of the transformation from the parallel alignment to perpendicular alignment is attributed to the increase of shear rate<sup>[9, 10]</sup>. Consequently, it can be decided that the addition of PEG and the increase of shear rate have the similar effects on the morphologies of the UHMWPE/PP blends by the comparison of Figure 4.7 and 5.6.

From Figure 5.6 it can be seen that PEG in the UHMWPE/PP/PEG (50/50/2) blends turns into a spherical structure and concentrates more in the UHMWPE phase under the condition of shear rate from 0.0 to 0.01. When the shear rate increases to 0.05, PEG localizes preferably in the interface between PP and UHMWPE phases, and ellipsoidal and discontinuous cylindrical morphology appear gradually, as shown in Figure 5.6(e) and (f). At a high shear rate of 0.3, PEG totally forms with cylindrical morphologies, and concentrates mostly in PP phase with only a part locating at the interface of UHMWPE and PP phases [Figure 5.6(g) - (j)]. In conclusion, with the increasing of shear flow, PEG phase translates preferably from UHMWPE phase to PP phase, which is probably attributed to two reasons: (1) Flory–Huggins parameters [ $\chi_{UHMWPE/PEG}$  (0.191) <  $\chi_{PP/EG}$  (0.412)] dominate the location of PEG at a low shear

rates; (2) the obviously closer viscosity of PEG to that of PP than that of UHMWPE forms the main factor at a high shear rates.



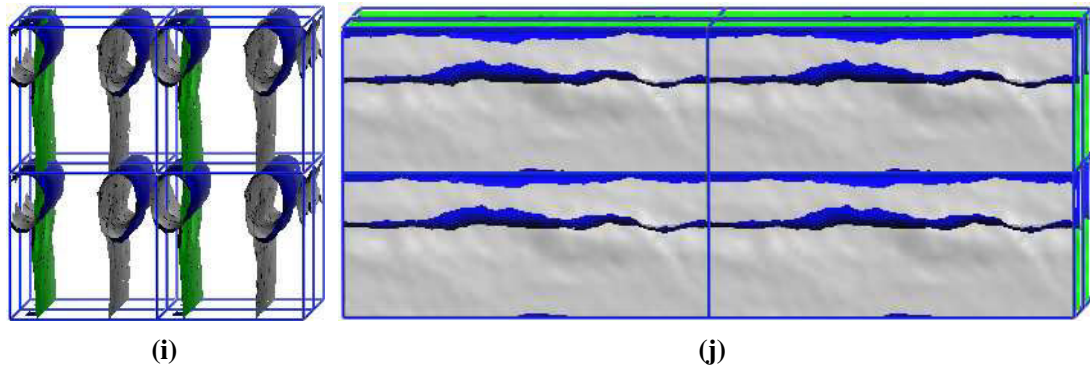


**Figure 5.6** Iso-density surfaces of PP and PEG for the UHMWPE/PP/PEG (50/50/2) blends obtained after  $4 \times 10^5$  steps DPD simulation. The outward surfaces of PP phases are colored with green, the outward surfaces of PEG phases are colored with blue, and the rests are UHMWPE phases. (a) and (b) 0.005 (shear rate), (c) and (d) 0.01, (e) and (f) 0.05, (g) and (h) 0.3, (i) and (j) 0.5. x-axis and z-axis are shear direction and the shear gradient direction, respectively.

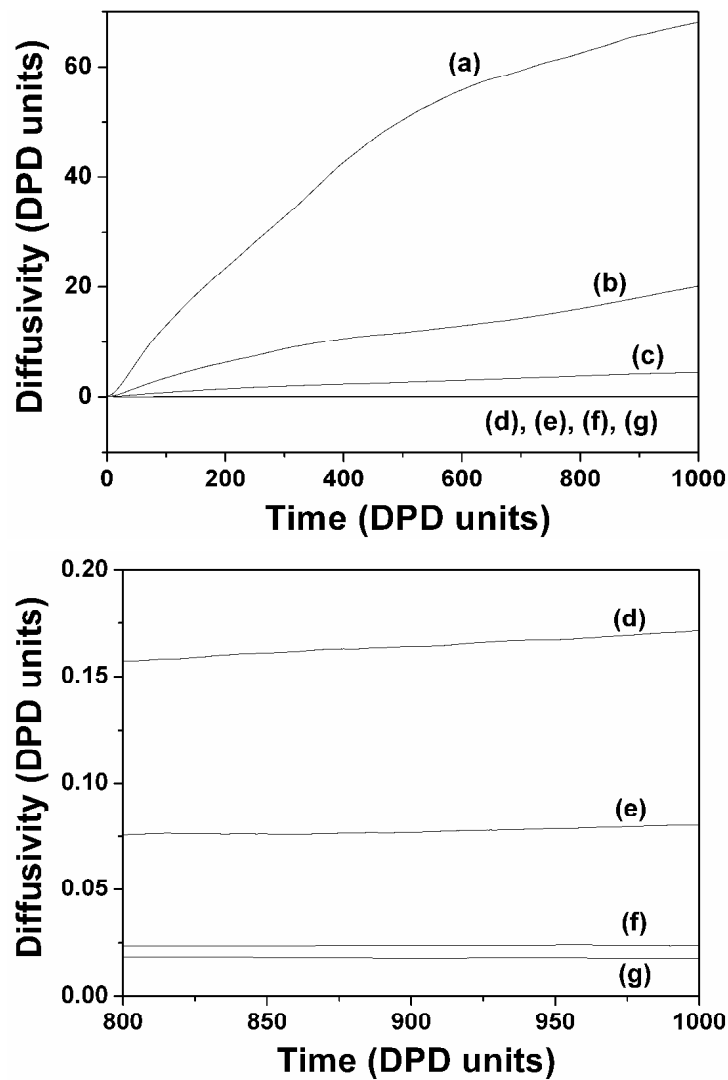


**Figure 5.7** Time evolution of diffusivities of UHMWPE in the UHMWPE/PP/PEG (50/50/2) blends with varying the shear rate: (a) 0.2 (DPD units), (b) 0.1, (c) 0.05, (d) 0.01, (e) 0.005, (f) 0.001 and (g) 0.0.

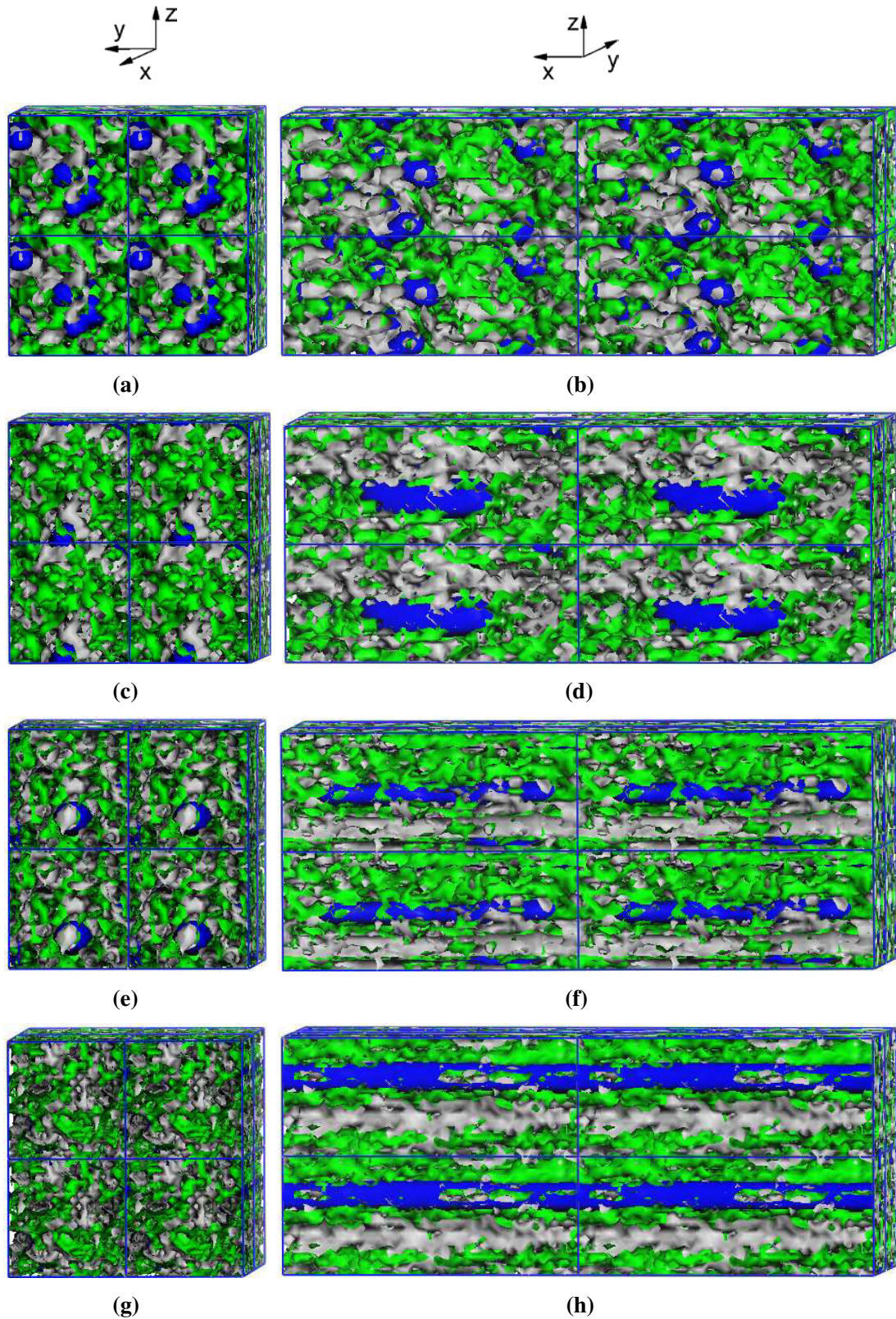


**Figure 5.8** Iso-density surfaces of PP and PEG for the UHMWPE/PP/PEG (90/10/2) blends obtained after  $2 \times 10^5$  steps DPD simulation. The outward surfaces of PP phases are colored with green, the outward surfaces of PEG phases are colored with blue, and the rests are UHMWPE phases. (a) and (b) 0.01 (shear rate), (c) and (d) 0.05, (e) and (f) 0.1, (g) and (h) 0.2. x-axis and z-axis are shear direction and the shear gradient direction, respectively.

The simulated diffusivities of UHMWPE for the UHMWPE/PP/PEG (50/50/2) as a function of shear rate are shown in Figure 5.7. It is evident that the diffusivity of UHMWPE increases with increasing shear rate, which illustrates that the viscosities of the blends decrease to a certain extent under shear flow. When the shear rate is higher than 0.05, the diffusivities of UHMWPE increase rapidly. Our previous experimental investigations on the UHMWPE/PP/PEG blends showed that shear thinning appears at higher shear rates, and the blends exhibit a non-Newtonian behavior <sup>[3]</sup>, which probably should be attributed to the increasing of diffusivities for UHMWPE in the blends.

DPD simulations for a large amount of UHMWPE in blends have been further performed by varying shear rate from 0.01 to 0.2. In the case of the UHMWPE/PP/PEG (90/10/2) blends, as shown in Figure 5.8, the morphologies of PEG are more sensitive to shear rates, and spherical and cylindrical morphology occur in turn with the increasing of shear rates (Figure 5.8). It is well known that PEG has very low viscosity and good lubricating property. PEG with spherical and cylindrical morphologies in the UHMWPE/PP (90/10) blends might act as a lubricant to induce interphase slippage of the blends.

### 5.2.2.1.3 Effects of molecular weight of UHMWPE

First, we fix  $N_{PP} = 250$  and vary  $N_{UHMWPE}$  from 4640 to 23200 to study the effect of molecular weight of UHMWPE on the morphologies the UHMWPE/PP blends, as shown in Figure 5.9. As  $N_{UHMWPE}$  increases from 4640 to 23200, both PP and UHMWPE always show lamellar structures and PEG shows spherical structure for the fixed composition of 50/50/2 [Figure 5.9(a) and (c)]. The morphologies change dramatically with increasing  $\phi_{UHMWPE}$ , for example, a two-phase structure occurs in the blend with  $N_{UHMWPE}$  of 23200 [Figure 5.9(b)], but an approximate homogeneous phase structure will appear when  $N_{UHMWPE}$  is 4640 [Figure 5.9(d)]. This indicates that the increase of  $N_{UHMWPE}$  is favorable to the phase separation of the UHMWPE/PP/PEG blends, which is consistent with the prediction of phase diagram

based on Flory-Huggins theory (Figure 3.28).

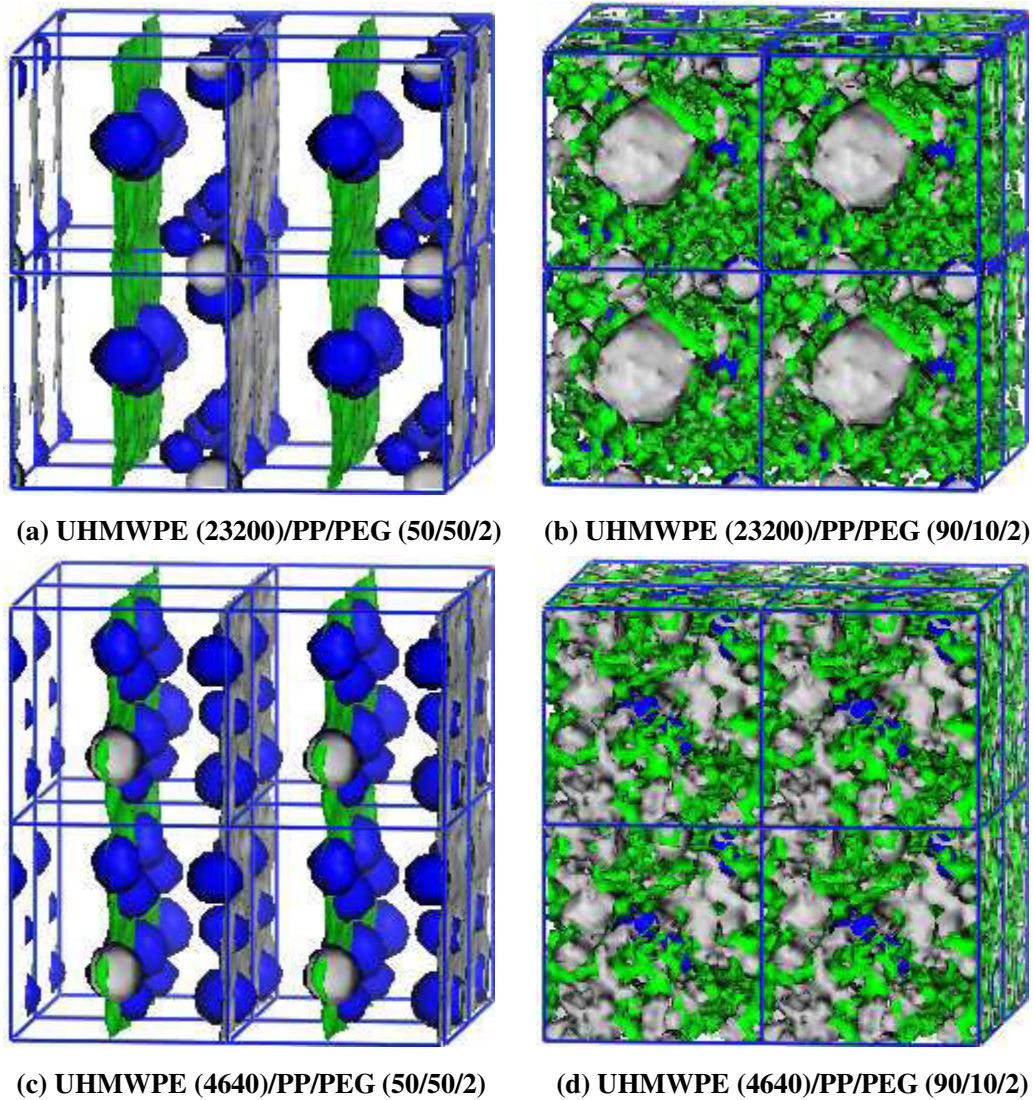


**Figure 5.9** Iso-density surfaces of PP and PEG for UHMWPE/PP blends obtained after  $4 \times 10^5$  steps DPD simulation. The outward surfaces of PP phases are colored with green, the outward surfaces of PEG phases are colored with blue, and the rests are UHMWPE phases.

The above results also can be confirmed by the time evolution of the order parameter  $P$  based on MesoDyn simulations with random initial configuration. The time evolutions of dimensionless order parameters of the UHMWPE/PP/PEG blends with different compositions and molecular weights of UHMWPE are shown in Figures 5.10. By comparing Figure 5.10(a) and (c) or (b) and (d), it is easy to find that the higher molecular weight of UHMWPE will make the phase separation faster. However, the comparisons of the order parameters of system Figure 5.10(a) and (b) or (c) and (d) suggest that the influence extents of the molecular weight to the dynamic

of phase separation of the composites are remarkably different for various compositions. The time necessary for phase separation to start in system (b) and (d) are longer than these in system (a) and (c), respectively.

Furthermore, to probe the influence of compositions and molecular weight of UHMWPE on the extent of phase separation, the parameters  $P$  for different systems are compared at the same time step in Figure 5.10. It is clear that the parameter  $P$  of PEG in every system with the same concentration of PEG is almost unchanged, which suggests that the effect of the variations of composition and the molecular weight of UHMWPE on the extent of phase separation of PEG is slight.

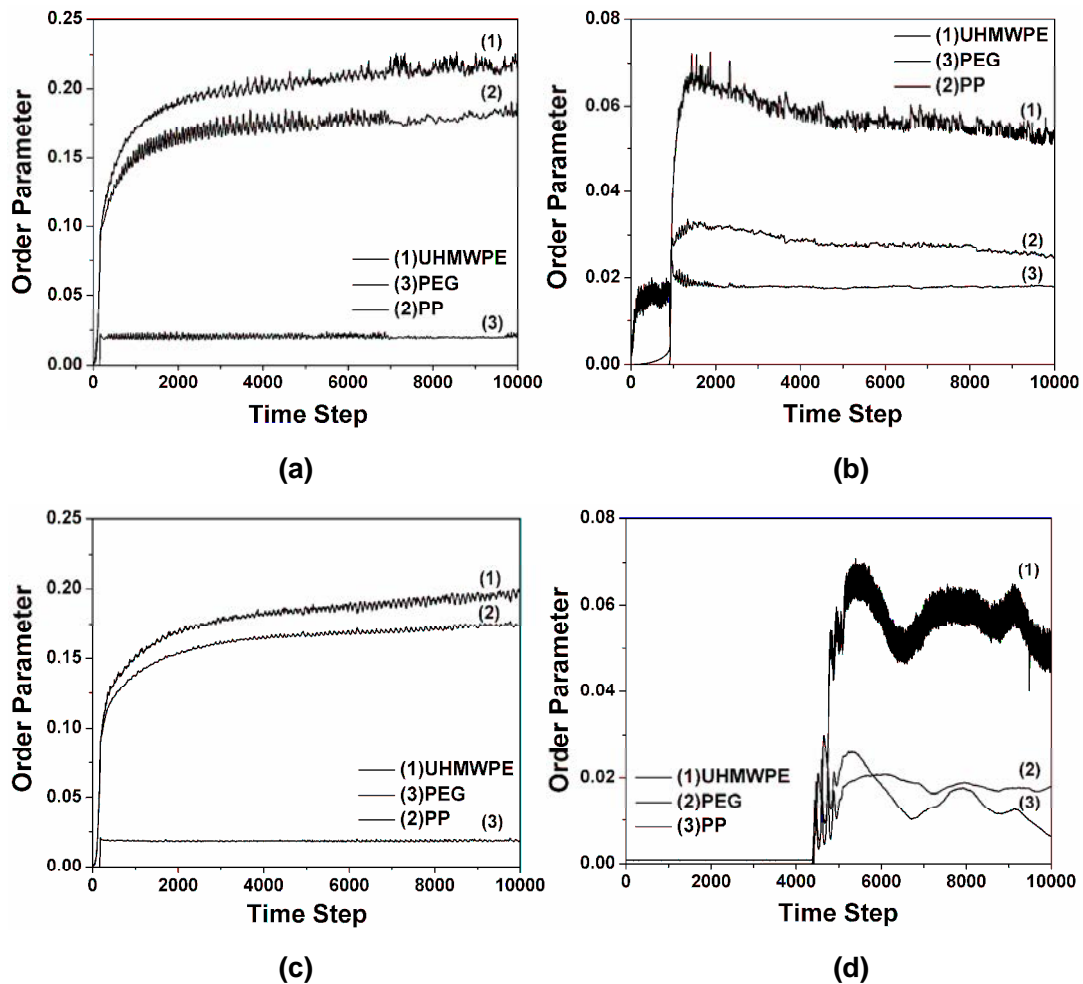


**Figure 5.10** Time evolution of the dimensionless order parameters for: (a) UHMWPE (11600)/PP (50/50/2); (b) UHMWPE (11600)/PP (90/10/2); (c) UHMWPE (2320)/PP (50/50/2); (d) UHMWPE (2320)/PP (90/10/2).

### 5.2.2.2 Phase structure of the UHMWPE/PP/MP composites

Premphet and Horanont showed that in filled blends with two immiscible polymers the filler distributed selectively in the polymer-phase with which it had the lowest interfacial tension <sup>[11]</sup>. An extension of this qualitative approach has been provided by Sumita <sup>[12]</sup>. They introduced a wetting coefficient,  $W_a$ , which allows predicting the selectivity of filler.

$$W_a = \frac{\gamma_{filler-B} - \gamma_{filler-A}}{\gamma_{A-B}} \quad (5.1)$$

where,  $\gamma_{filler-A}$  and  $\gamma_{filler-B}$  are the interfacial tensions between the fillers and polymer  $A$  or  $B$ , and  $\gamma_{A-B}$  is the interfacial tension between polymer  $A$  and  $B$ . In this equation,  $A$  is PEG and  $B$  is PP or UHMWPE. If  $W_a > 1$ , the filler distributes within  $A$ -phase; if  $-1 < W_a < 1$ , the filler is located at the interface; if  $W_a < -1$ , the filler is selective for the  $B$ -phase.

**Table 5.2** Surface tensions at 200°C of the polymers and filler used

Material	Surface tension(mN/m)		
	Total ( $\gamma$ )	Disperse Component ( $\gamma^d$ )	Polar Component ( $\gamma^p$ )
PEG	28.5	20.4	8.1
PP	19.6	19.3	0.4
UHMWPE	26.6	26.6	0.0
OMMT	257.7	94.7	163.0

**Table 5.3** Interfacial Tensions ( $\gamma_{A-B}$ ) and Wetting Coefficients ( $W_a$ ) of all possible polymer-polymer- and polymer-filler-pairs

System	Possible pairs	$\gamma_{A-B}$ (mN/m)	$W_a$	Final phase structure
	UHMWPE/PEG	8.9		
UHMWPE/OMMT/PEG	UHMWPE/OMMT	183.9	6.6	Encapsulation
	PEG/OMMT	125.6		
PP/OMMT/PEG	PP/OMMT	176.0	7.1	Encapsulation
	PP/PEG	7.1		

The interfacial tensions between polymers are determined with the harmonic mean equation of Wu <sup>[13, 14]</sup> [Eq. (5.2)], where  $A$  and  $B$  are the two polymers:

$$\gamma_{AB} = \gamma_A + \gamma_B - \frac{4\gamma_A^d \gamma_B^d}{\gamma_A^d + \gamma_B^d} - \frac{4\gamma_A^p \gamma_B^p}{\gamma_A^p + \gamma_B^p} \quad (5.2)$$

Here  $\gamma_A$  and  $\gamma_B$  are surface tensions of the two materials in contact, and  $d$  and  $p$  superscripts denote the dispersion and polar components of the surface tensions.

For the calculation of the interfacial tensions between filler and polymers the geometric mean equation of Wu <sup>[13]</sup> [Eq. (5.3)] is used since it is recommended for systems of a high-energy material, OMMT, and a low-energy material, such as the polymers used:

$$\gamma_{AB} = \gamma_A + \gamma_B - 2(\gamma_A^d \gamma_B^d)^{\frac{1}{2}} - 2(\gamma_A^p \gamma_B^p)^{\frac{1}{2}} \quad (5.3)$$

The corresponding values of the surface tensions at 200°C are listed in Table 5.2<sup>[13, 15]</sup>. The resulting interfacial tensions for the possible pairs are given in Table 5.3.

To apply Eq. (5.1) to the UHMWPE/PP/PEG/OMMT system, we studied the UHMWPE/OMMT/PEG and PP/OMMT/PEG composites, respectively. Table 5.3 shows that the interfacial tension between the OMMT and PP (or OMMT and UHMWPE) is by 50.4 mN/m (or 58.3 mN/m) larger than the corresponding value for the pair OMMT-PEG. According to Refs. <sup>[11, 16]</sup>, this indicates a large affinity of the OMMT to the PEG than to PP or UHMWPE in the blend. The concept of the wetting coefficient also confirms this tendency: Eq. (5.1) yields wetting coefficients of 7.1 and 6.6 in PP/OMMT/PEG and UHMWPE/OMMT/PEG system, respectively. Consequently, in the extrusion of the UHMWPE/PP/MP system, PEG molecules still covered on OMMT layers, instead of being replaced by PP or UHMWPE molecules. Hence, an encapsulation structure of MP was finally found in the UHMWPE/PP/MP composites.

Alternatively, the UHMWPE/PP/MP composites are also investigated by SEM to directly observe the effect of MP on the morphologies, as shown in Figures 5.11 – 5.14. It can be concluded that most of MMT stacks are located in the PP-rich phase by the comparison of Figures 5.12 and 5.13 with the corresponding Figures 3.13 and 5.11. Owing to the encapsulation structures of MP, PEG also should be in the PP-rich phase, which is consistent with Figure 5.6.

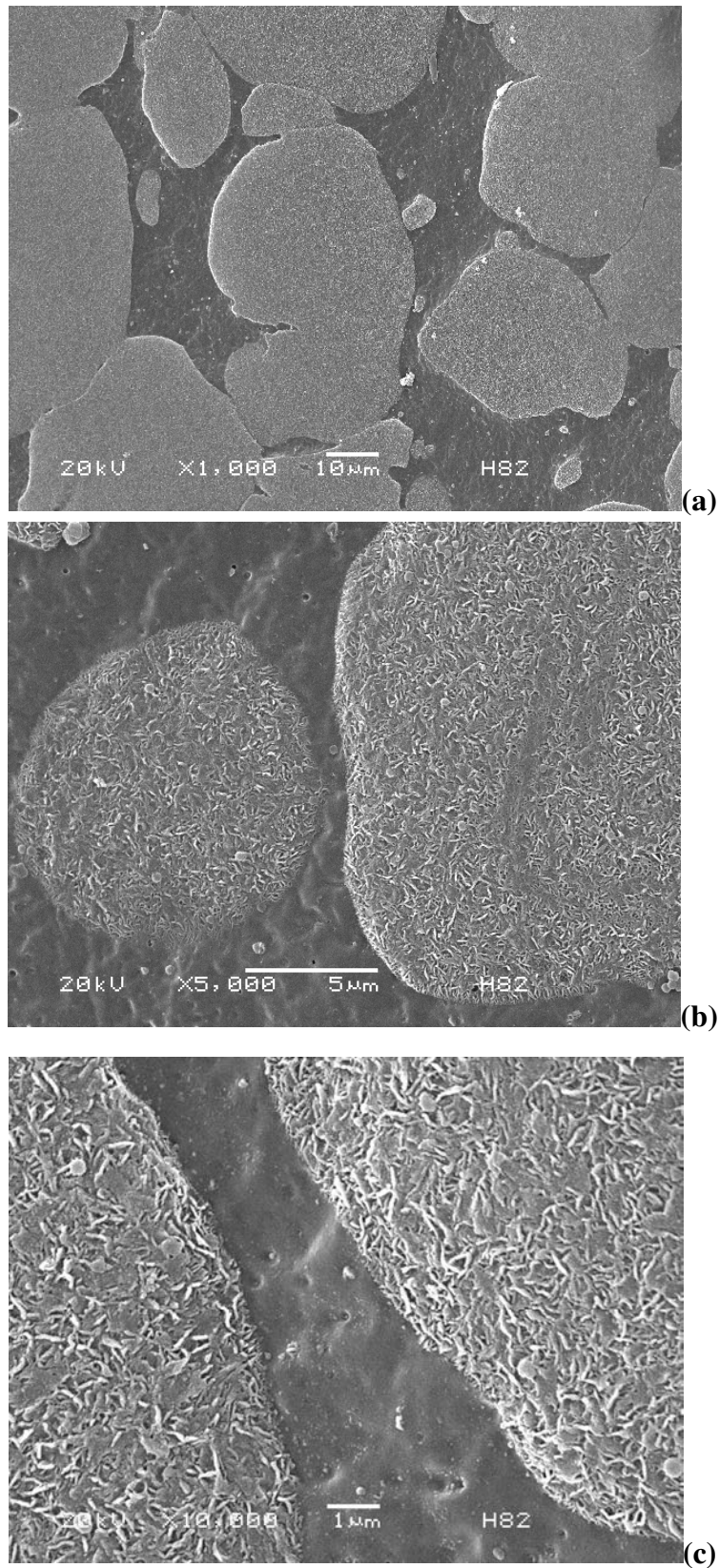


**Figure 5.11** SEM micrographs of cryogenically fractured surfaces of the UHMWPE/PP (80/20) after etching mixed for 3 minutes. The scale bars in (a), (b) and (c) are 10, 5 and 1  $\mu\text{m}$ , respectively.

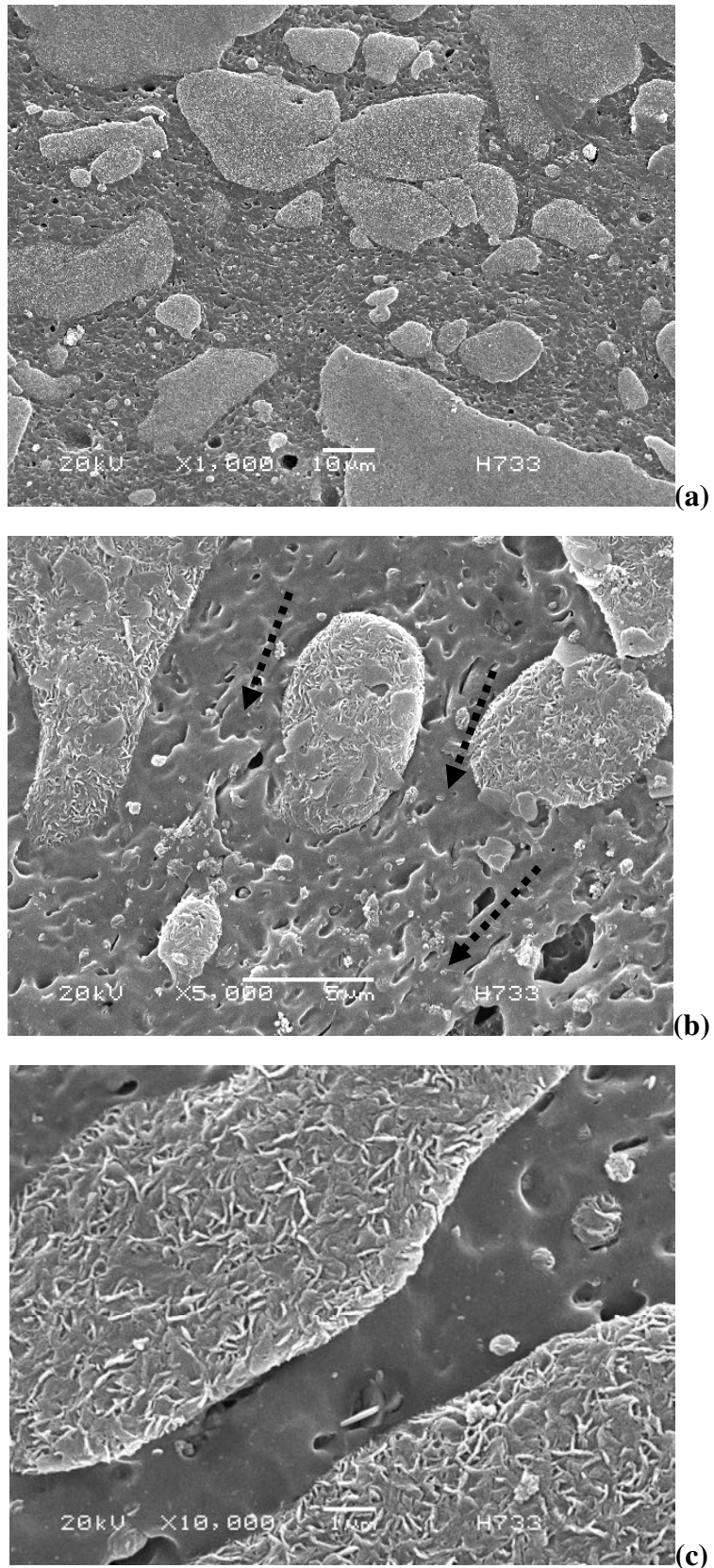


**Figure 5.12** SEM micrographs of cryogenically fractured surfaces of the UHMWPE/PP/MP11 (70/30/3) after etching mixed for 3 minutes. Dish arrows denote MMT layer direction. Scale bars are like in Figure 5.11.

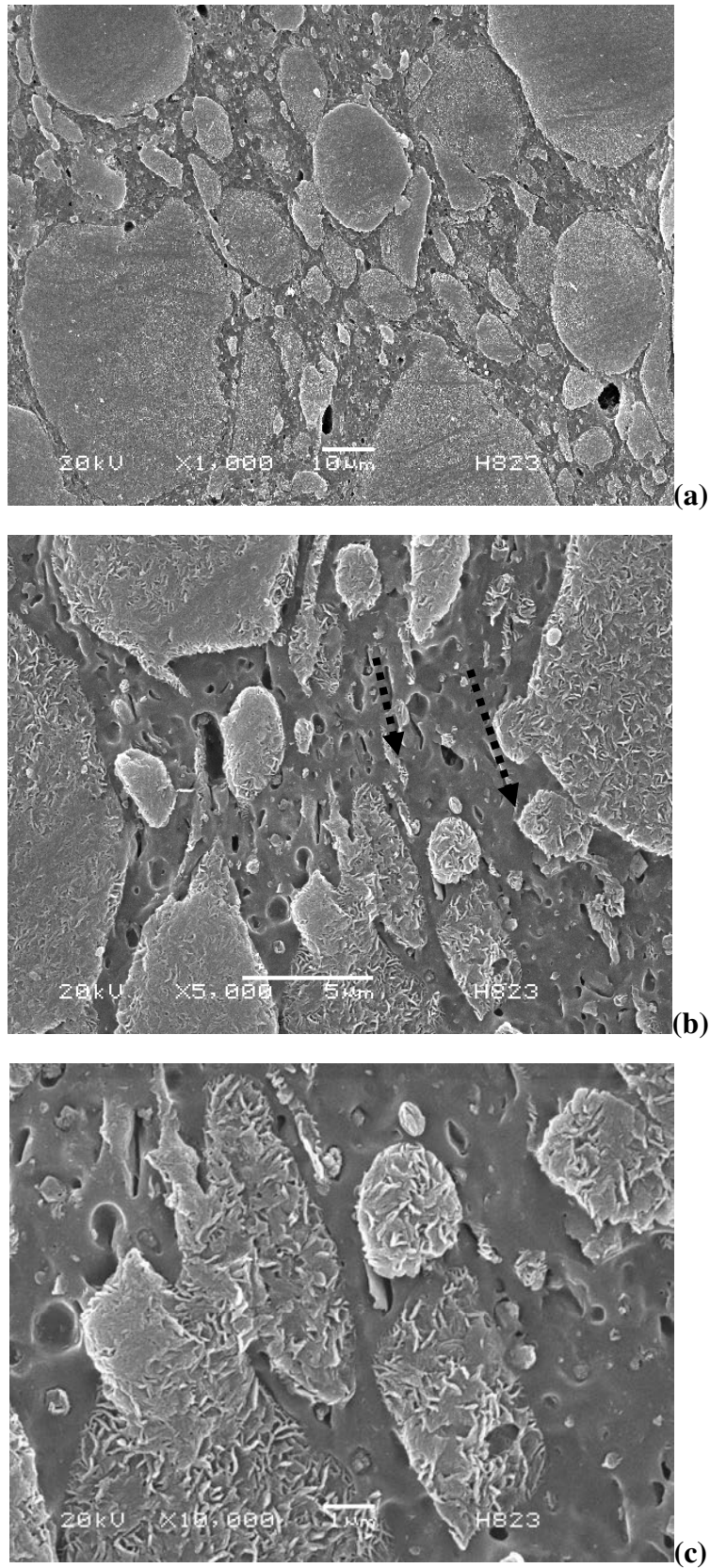


**Figure 5.13** SEM micrographs of cryogenically fractured surfaces of the UHMWPE/PP/MP11 (80/20/3) after etching mixed for 3 minutes. Dish arrows denote MMT layer direction. Scale bars are like in Figure 5.11.

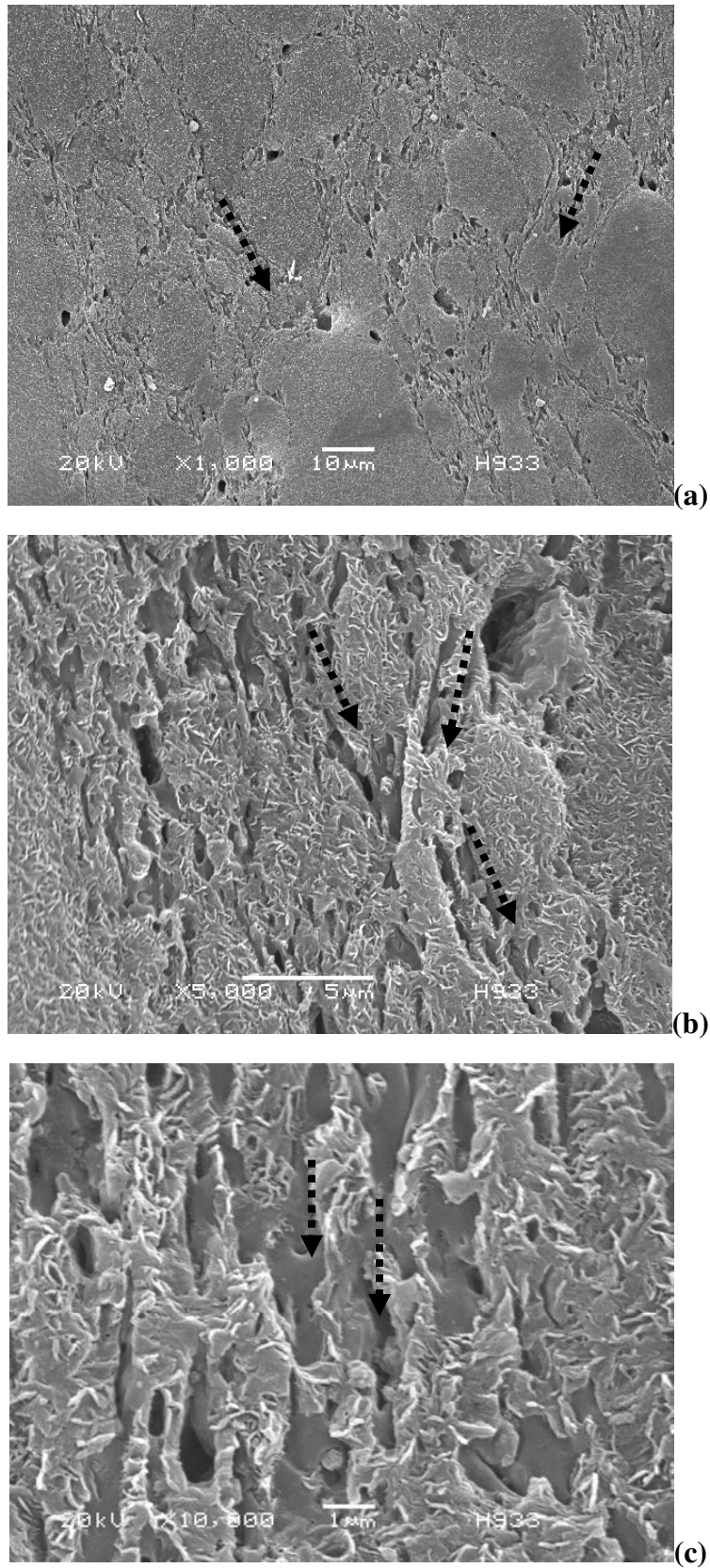


**Figure 5.14** SEM micrographs of cryogenically fractured surfaces of the UHMWPE/PP/MP11 (90/10/3) after etching mixed for 3 minutes. Dish arrows denote MMT layer direction. Scale bars are like in Figure 5.11.

Most of the MP layers are always parallel with the surface of the UHMWPE particles, which have been marked by arrow in Figures 5.12 – 5.14. With decreasing  $\phi_{PP}$ , the PP-rich phase becomes longer, more narrow and more homogeneously disperse between the UHMWPE particles with the addition of MP11 (compare Figure 5.14 with 3.20). For the UHMWPE/PP/MP11 (90/10/2) composite, almost all of the minor UHMWPE particles have been packed by PP and MP (Figure 5.14), while most of the particles still stack together in the UHMWPE/PP (90/10) blends (Figure 3.20).

### 5.2.3 Rheological behaviors and mechanism of viscosity reduction

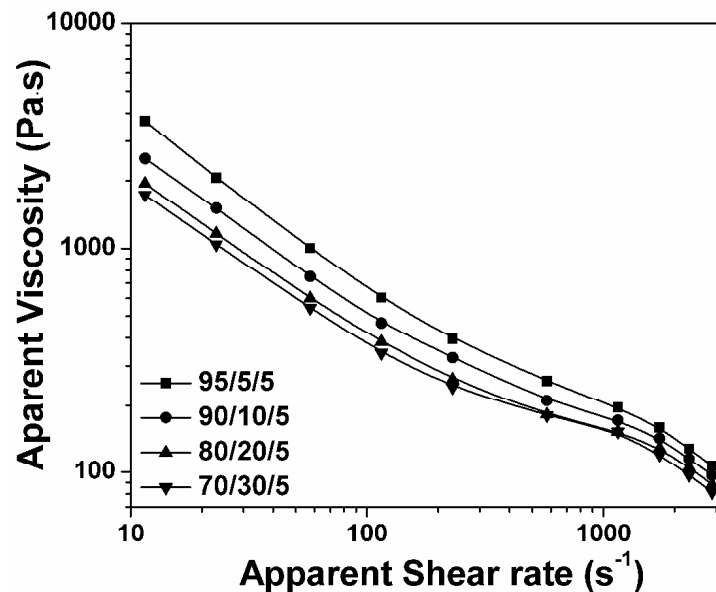


**Figure 5.15** Plot of the logarithm of the apparent viscosity versus the logarithm of the apparent shear rate for UHMWPE/PP/MP11.

The effect of MP and PP on the rheological properties of UHMWPE was investigated, as is shown in Figures 5.15 and 5.16. It can be seen that as  $\phi_{PP}$  increase, the melt apparent viscosities of the UHMWPE/PP/MP11 composites decrease. Moreover, with 5 wt % PP and 5 wt % MP11 in the UHMWPE/PP/MP11 composites, the apparent melt viscosity was much lower than that of pure UHMWPE, and no pressure vibration occurred throughout the whole range of shear rate [Figure 5.15(c)]. Nevertheless, it is impossible to process the UHMWPE/PP (95/5) blends at the same

conditions. Besides, with more addition of MP, more viscosity reduction of UHMWPE/PP occurs (Figure 5.16).

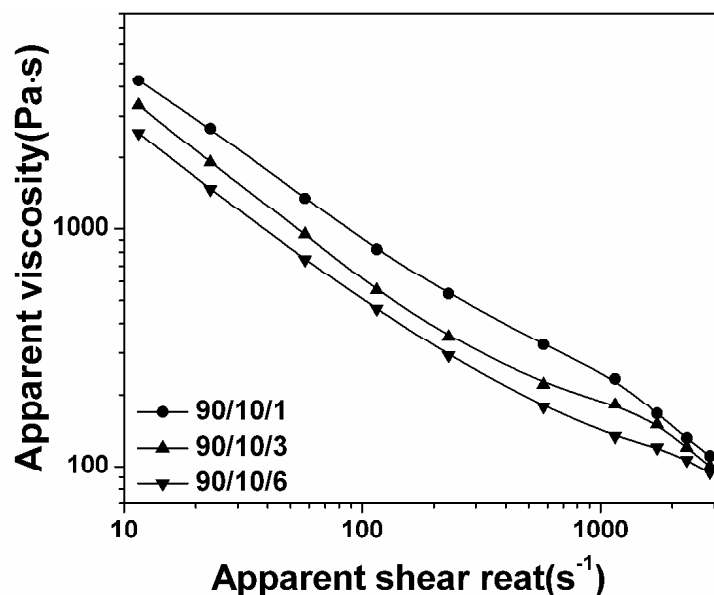


**Figure 5.16** Plot of the logarithm of the apparent viscosity versus the logarithm of the apparent shear rate for UHMWPE/PP/MP11.

On the bases of the studies in chapter 3, we have concluded it is necessary to form the lubrication phase between UHMWPE particles in the processing, while, many problems occur simultaneously. For example, an increase in the parameter  $\chi$  favors the phase separation. At the same time, it accelerates the rate with which the NMWP molecules migrate toward the surface of the blends during processing. As a result, the NMWP can no longer effectively act as a lubricant agent between UHMWPE particles. Moreover, the interfacial thickness will decrease, leading to worse mechanical properties. On the contrary, if the parameter  $\chi$  is too small, excessive NMWP is necessary to form the lubrication phase, which will bring about important deterioration in some of the most desirable properties of UHMWPE. Fortunately, the problem can be completely solved by the addition of MP. It is well known that PEG has very low viscosity and good lubricating property, and PEG is incompatible with UHMWPE and PP, i. e., the value of parameter  $\chi$  is large enough to form the lubrication phase. Besides, the OMMT layers serve as PEG carrier in the composite. Consequently, the MP hybrids are preferably located between UHMWPE

particles and act as lubrication phase. Moreover, owing to the parallel arrangement of the MP layers to the surface of UHMWPE particles, a small quantity of MP can significantly reduce the viscosity of the composites. Finally, synergistic effect of PEG and OMMT on reducing the viscosity is achieved. It is worth noting that the addition of NMWP is also necessary because NMWP with relatively small value of parameter  $\chi$  can disentangle the UHMWPE molecules and decrease the sizes of UHMWPE particles, which is in favor of maintenance or enhancement of many mechanical properties, such as izod-notched impact strength and tensile strength.

## 5.2.4 Crystal structure and crystallinity

A series of representative endotherm curves for UHMWPE and its composites were shown in Figure 5.17 and the corresponding values are listed in Table 5.4. The crystallinity of samples,  $\Delta\chi_c$ , can be calculated by Eq.(5.4) <sup>[20]</sup>,

$$\Delta\chi_c = \frac{\Delta H_m}{(1-\phi)\Delta H_m^*} \times 100\% \quad (5.4)$$

where,  $\phi$  is the weight fraction of the filler (specifically, MP and PP in present discussion) in composite,  $\Delta H_m$  is the heat fusion,  $\Delta H_m^*$  denotes heat of fusion for an infinitely large crystal.  $\Delta H_m^*$  of UHMWPE was measured by Wunderlich et al. and it was reported to be 293.0 J/g <sup>[21]</sup>.

**Table 5.4** DSC analysis of pure UHMWPE, UHMWPE/PP and UHMWPE/PP/MP11

Sample	UHMWPE		
	$T_m$	$\Delta H_m$	$\Delta\chi_c$
UHMWPE	137.8	166.4	56.8
UHMWPE/PP(90/10)	139.9	140.3	53.2
UHMWPE/PP(70/30)	138.3	106.6	52.0
UHMWPE/PP/MP11(90/10/1)	139.1	137.9	53.5
UHMWPE/PP/MP11(90/10/3)	138.7	144.6	56.1
UHMWPE/PP/MP11(90/10/5)	138.4	126.0	50.6

Figure 5.17 and Table 4 shows that crystallinity of UHMWPE in UHMWPE/PP blends tends to decrease with increasing PP ratios. In the case of pure UHMWPE,

UHMWPE/PP (90/10) and UHMWPE/PP (70/30) blends, the corresponding crystallinities were 56.8%, 53.2% and 52.0%. However, when 1 phr and 3 phr MP11 was used, the crystallinity of UHMWPE in the UHMWPE/PP (90/10) blends increased to 53.5% and 56.1%, respectively. When 5 phr MP11 was added, the crystallinity of UHMWPE decreased to 50.6% (Table 5.4).

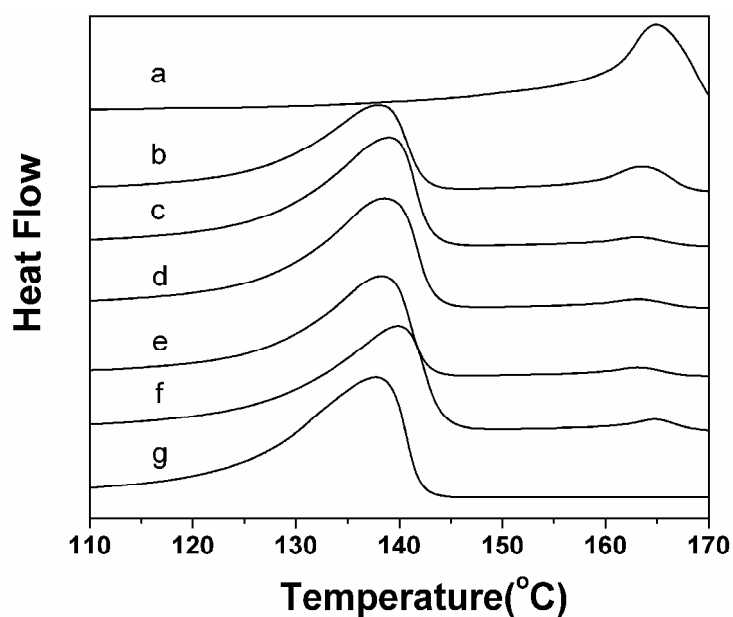


**Figure 5.17** DSC curves of (a) PP, (b) UHMWPE/PP (70/30), (c) UHMWPE/PP/MP11 (90/10/5), (d) UHMWPE/PP/MP11 (90/10/3), (e) UHMWPE/PP/MP11 (90/10/1), (f) UHMWPE /PP (90/10), (g) UHMWPE.

## 5.2.5 Mechanical Properties

**Table 5.5** The mechanical properties of pure UHMWPE, UHMWPE/PP and UHMWPE/PP/MP11

Sample	Tensile strength (MPa)	Elongation at break (%)	Young' modulus (MPa)	Izod-notched impact strength (kJ/m <sup>2</sup> )
UHMWPE	36.0	393.4	740.2	No break
UHMWPE/PP(90/10)	37.9	401.2	750.2	No break
UHMWPE/PP/MP11(90/10/1)	39.2	413.1	876.3	No break
UHMWPE/PP/MP11(90/10/3)	46.2	460.1	1005.0	No break
UHMWPE/PP/MP11(90/10/5)	39.7	428.2	1027.0	No break

Table 5.5 summarizes the mechanical properties of UHMWPE, UHMWPE/PP and UHMWPE/PP/MP11. In the case of UHMWPE/PP (90/10) blend, its mechanical

properties remain nearly unchanged when compared with pure UHMWPE. But apparent enhancement of tensile strength, Elongation at break and Young's modulus of UHMWPE/PP(90/10) blend appeared when 1 phr, 3phr and 5phr MP11 were respectively added into it, except that izod-notched impact strength was without much obvious change. Especially when 3phr of MP11 was added, a 28.3 % increase in tensile strength, 17.0 % increase in elongation at break and 35.8 % increase in Young' modulus were observed. The mechanical properties enhanced as a result of the decrease of defects at boundaries between UHMWPE particles because the sizes of particles decrease with the additions of PP and MP.

### 5.3 Conclusions

In this chapter, the effects of MP on the morphologies and properties of the UHMWPE/PP blends have been studied theoretically and experimentally, and some conclusions have been drawn as follow:

DPD simulations suggest that with the absence of shearing PEG prefers to distribute in the UHMWPE phase regardless of variation of PP concentration in UHMWPE/PP/PEG blends. However, with the increasing of shear flow, PEG phase translates preferably from UHMWPE phase to PP phase. This probably is attributed to two reasons: (I) Flory–Huggins parameters dominate the location of PEG at a low shear rates; (II) the obviously closer viscosity of PEG to that of PP than that of UHMWPE forms the main factor at a high shear rates.

The increase of  $N_{UHMWPE}$  is favorable to the phase separation of the UHMWPE/PP/PEG blends, which is consistent with the prediction of phase diagram based on Flory-Huggins theory.

The concept of the wetting coefficient confirms that in the extrusion of the UHMWPE/PP/MP system, PEG molecules still covered on OMMT layers, instead of being replaced by PP or UHMWPE molecules. Hence, an encapsulation structure of MP was finally found in the UHMWPE/PP/MP composites.

The addition of a small amount of MP11 has been found able to reduce the melt viscosity of UHMWPE/PP (90/10) blend significantly. With 1 wt % MP11 contents in UHMWPE/PP (90/10) blend, the apparent melt viscosity is much lower than that of pure UHMWPE, and no pressure vibration occurs throughout the whole range of shear rate. With more addition of MP11, more viscosity reduction of UHMWPE/PP (90/10) occurs.

The UHMWPE/PP/MP11 (90/10/3) composite has the optimum comprehensive mechanical property. When the amount of MP11 is 1% or 5%, properties such as tensile strength and elongation at break of composites decrease, but they are still higher than those of the pure UHMWPE and UHMWPE/PP blend.

## 5.4 References

1. Gai JG, Li HL. Influence of Organophilic Montmorillonite and Polypropylene on the Rheological Behaviors and Mechanical Properties of Ultrahigh Molecular Weight Polyethylene. *J Appl Polym Sci* 2007, 105, 1200.
2. Gai JG, Li HL. Ultrahigh Molecular Weight Polyethylene/ Polypropylene/ Organo- Montmorillonite Nanocomposites: Phase Morphology, Rheological, and Mechanical Properties. *J Appl Polym Sci* 2007, 106, 3023.
3. Xie M, Li HL. Viscosity reduction and disentanglement in ultrahigh molecular weight polyethylene melt: Effect of blending with polypropylene and poly(ethylene glycol). *European Polymer Journal* 2007, 43, 3480.
4. Xie M, Liu XL, Li HL. Influence of Poly(ethylene glycol)-Containing Additives on Extrusion of Ultrahigh Molecular Weight Polyethylene/Polypropylene Blend *Journal of Applied Polymer Science*, 2006, 100, 1282.
5. 吴其晔, 王新, 胡友良, 漆宗能. 线性聚乙烯及线性聚乙烯/高岭土复合材料的异常流变行为. *青岛化工学院学报* 1999, 20, 316.
6. Aranda P, Eduardo RH. Poly(ethylene oxide)-silicate intercalation materials. *Chem Mater* 1992, 4, 1395.
7. Greeland DJ. Adsorption of poly(vinyl alcohols) by montmorillonite. *J Colloid*

Sci 1963, 18, 647.

8. Suprakas Sinha Ray, Masami Okamoto. Polymer/layered silicate nanocomposites: a review from preparation to processing. *Prog Polym Sci* 2003, 28, 1539.
9. Koppi KA, Tirrell M, Bates FS, Almdal K, Colby RH. Lamellae orientation in dynamically sheared diblock copolymer melts. *J Phys France II* 1992, 2, 1941.
10. Koppi KA, Tirrell M, Bates FS, Almdal K, Colby RH. Lamellae orientation in dynamically sheared diblock copolymer melts. *J Phys France II* 1992, 2, 1941.
11. Premphet K, Horanont P. Phase structure of ternary polypropylene/elastomer /filler composites: effect of elastomer polarity. *Polymer* 2000, 41, 9283.
12. Sumita M, Sakata K, Asai S, Miyasaka K, Nakagawa H. Dispersion of fillers and the electrical conductivity of polymer blends filled with carbon black. *Polym Bull* 1991, 25, 265.
13. Wu S. *Polymer interface and adhesion*; Marcel Dekkar: New York, 1982.
14. Wu S. Formation of dispersed phase in incompatible polymer blends: Interfacial and rheological effects. *Polym Eng Sci* 1987, 27, 335.
15. Pukanszky B, Fekete E. *Adhesion and Surface Modification*. *Adv Polym Sci* 1999, 139, 109.
16. Schuster RH, Issel HM, Peterseim VI. *Rubber Chem Technol* 1996, 69, 769.
17. Wunderlich B, Cormier CM. Heat of fusion of polyethylene. *J Polym Sci Part B: Polym Phys* 1967, 5, 987.

# CHAPTER 6 UHMWPE/PP/PMM Nanocomposites

## 6.1 Introduction

Polymer-clay nanocomposites continue to be an area of great interest due to the many improvements in properties that these materials have over traditional composites<sup>[1-10]</sup>. It is generally assumed that exfoliation of the clay is preferred for the greatest increases in nanocomposite properties<sup>[11,12]</sup>. In the pristine state, layered silicates are only miscible with hydrophilic polymers. Unfortunately, the polymer in which natural clay is to be dispersed is often hydrophobic. The addition of surfactants lowers the surface energy of the inorganic host and improves the wetting characteristics of the polymer matrix, resulting in a larger interlayer spacing, and making the intercalation of many engineering polymers possible.

In this paper, the complex intercalator Poly (ethylene glycol)/2-methacryloyloxyethyl dodecyldimethylammonium bromide was used to modify Na<sup>+</sup>-montmorillonite through ultrasonic irradiation. The influences of the OMMT (PM, MM and PMM) content on the phase morphology, and properties of the UHMWPE/PP/OMMT composites were investigated.

## 6.2 Results and discussion

### 6.2.1 Structure of OMMT platelets in the composites

The dispersion state and structure of OMMT platelets in the UHMWPE/PP/OMMT composites have dramatic influences on its mechanical and rheological performances. Hence, the structure of the composites in the nanometer range has typically been elucidated using WAXD and TEM.

### 6.2.1.1 Structure analysis on the bases of WAXD results

Figure 6.1 shows the respective X-ray diffraction traces for the Na<sup>+</sup>-MMT, PM, MM powders and various representative composites, exhibiting a shift of (001) diffraction peaks towards the lower diffraction angles in different manners. The (001) diffraction peak for PM powder is found to shift, in a comparatively short range, from  $2\theta = 5.57^\circ$  ( $d_{001} = 1.58$  nm) to  $4.75^\circ$  ( $d_{001} = 1.86$ nm). On the other hand, the (001) diffraction peak for the MM powder shifts to  $2\theta = 2.71^\circ$  ( $d_{001} = 3.26$  nm) (Table 6.1). With increasing clay content, these peaks (001) become stronger, and slightly shift towards higher diffraction angles, at  $2.43^\circ$  ( $d_{001} = 3.64$  nm),  $2.47^\circ$  ( $d_{001} = 3.56$  nm) and  $2.51^\circ$  ( $d_{001} = 3.51$  nm) for UHMWPE/PP blended with 1, 3 and 5phr MM, respectively (Figure 6.1 and Table 6.1). These shifts of the (001) diffraction peak are probably attributed to the intercalation of PEG, MDAB, PP or UHMWPE chains snaking into silicate galleries.

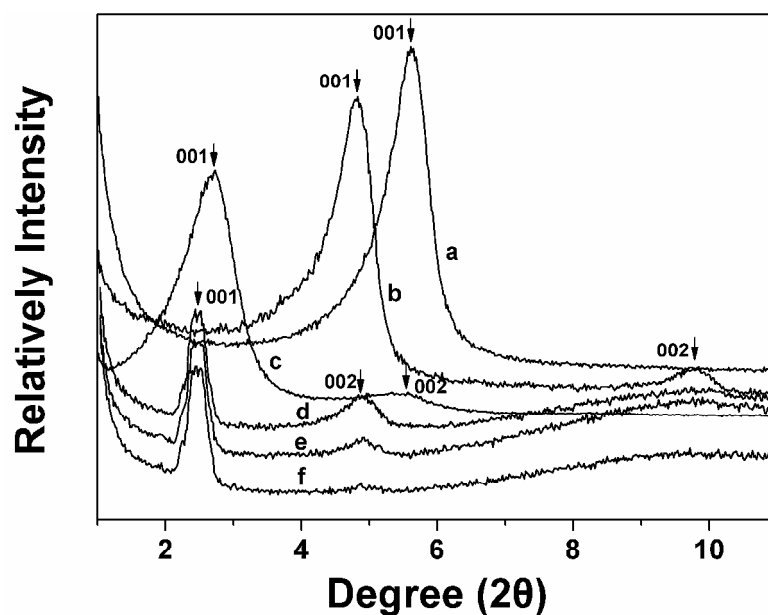


**Figure 6.1** Wide-angle X-ray diffraction patterns: (a) Na<sup>+</sup>-MMT; (b) PM; (c) MM; (d) UHMWPE/PP/MM (90/10/5); (e) UHMWPE/PP/MM (90/10/3) and (f) UHMWPE/PP/MM (90/10/1).

For PM, MM, UHMWPE/PP/MM (90/10/5), UHMWPE/PP/MM (90/10/3) and UHMWPE/PP/MM (90/10/1) samples respectively, sharp peaks observed at  $2\theta = 9.79^\circ$ ,  $5.54^\circ$ ,  $4.93^\circ$ ,  $4.90^\circ$  and  $4.88^\circ$  are confirmed to be (002) plane ( $d_{002}$ ) (Figure 6.1).

The existence of the (001) and (002) diffraction peaks shows that the MM in the composites still retains an ordered structure after melt mixing despite that the interlayer spacing increased significantly compared to that of MM powder.

**Table 6.1** (001) diffraction peaks, corresponding d-spacing,  $h_{001}$ , and  $n_C$  of various MMT and their composites

Samples	peak position( $2\theta$ )	d-spacing(nm)	$h_{001}$	$n_C$ (nm)
MMT	5.57	1.58	-	-
PM	4.75	1.86	-	-
MM	2.71	3.26	-	-
UHMWPE/PP/MM(90/10/5)	2.51	3.51	31.27	9.9
UHMWPE/PP/MM(90/10/3)	2.47	3.56	25.54	8.2
UHMWPE/PP/MM(90/10/1)	2.43	3.64	22.56	7.2
PMM	2.21	3.98	-	-
UHMWPE/PP/PMM(90/10/5)	no peak	-	-	-
UHMWPE/PP/PMM(90/10/3)	no peak	-	-	-
UHMWPE/PP/PMM(90/10/1)	no peak	-	-	-

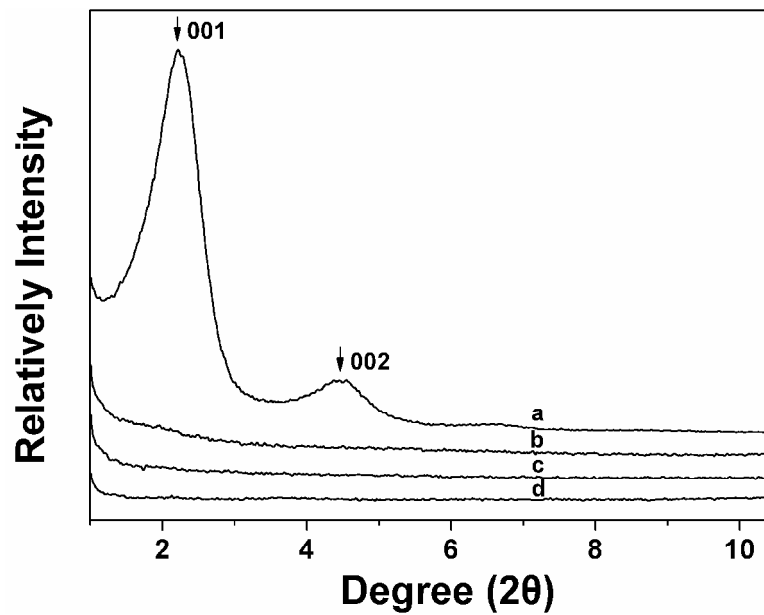


**Figure 6.2** Wide-angle X-ray diffraction patterns: (a) PMM; (b) UHMWPE/PP/PMM (90/10/5); (c) UHMWPE/PP/PMM (90/10/3) and (d) UHMWPE/PP/PMM (90/10/1).

As it is shown in Figure 6.2 and Table 6.1, the peak of (001) plane of PMM shifts to lower angle ( $2\theta = 2.21^\circ$ ) as compared with those of PM or MM. After the melting process, the original (001) together with (002) diffraction peaks disappeared in the

UHMWPE/ PP/ PMM (90/10/1), UHMWPE/ PP/ PMM (90/10/3) and UHMWPE/ PP/ PMM (90/10/5) composites in the range of  $2\theta = 1-11^\circ$ . The disappearance established the formation of exfoliated and better intercalated structure for composites UHMWPE/PP/PMM, as opposed to an intercalated structure for UHMWPE/PP/PM and UHMWPE/PP/MM systems. The structure of PMM in the matrix is probably attributed to the synergistic effects of the complex intercalator (PEG/MDAB) on the intercalation and exfoliation for MMT.

From the WAXD patterns, the crystallite size normal to the (001) plane of the OMMT particles in UHMWPE matrix is calculated by the Scherrer equation <sup>[13]</sup>, written as

$$h_{001} = \frac{K\lambda}{\beta \cos \theta_{001}} \quad (6.1)$$

where  $K$  is a constant (= 0.91),  $\lambda$  the X-ray wavelength (= 0.154 nm),  $\beta$  the width of Bragg diffraction peak determined by the full width at half maximum in radian unit, and  $\theta_{001}$  the half of (001) diffraction angle. From the calculated crystallite size ( $h_{001}$ ), i.e. the thickness of the dispersed clay, the actual number of layers,  $n_c$ , stacked in a clay particle can be approximately calculated as follows <sup>[14]</sup>

$$n_c = \frac{h_{001}}{d_{001}} + 1 \quad (6.2)$$

Table 6.1 also shows the calculated value of  $h_{001}$  and  $n_c$  for the composites UHMWPE/PP/MM. The sample UHMWPE/PP/MM shows that the  $h_{001}$  and  $n_c$  values are in the range of 31.27-22.56 nm and 9.9-7.2 layers.

### 6.2.1.2 Structure analysis on the bases of TEM

The internal structure of the clay in the nanometer scale was observed via TEM analysis. Figures 6.3, 6.4 and 6.6- 6.8 respectively show the typical TEM images of the UHMWPE/PP/MM (90/10/3) and the UHMWPE/PP/PMM (90/10/3) composites. Bright field is the image of polymer, in which dark entities are the cross-section of

intercalated silicate layers <sup>[15]</sup>. Form factors such as average length  $L_{\text{clay}}$ , thickness ( $d_{\text{clay}} \approx h_{001}$ ) of the dispersed clay particles can be obtained from TEM images. On the bases of Figures 6.4, 6.7 and 6.8, the distributions of clay layer length ( $L_{\text{clay}}$ ), thickness ( $d_{\text{clay}}$ ) and their ratios in both the UHMWPE/PP/MM (90/10/3) and the UHMWPE/PP/PMM (90/10/3) composites are obtained and shown in Figure 6.5 and 6.9, respectively.

From Figure 6.3 - 6.5, one can observe the large stacked clay layers. The thicknesses of the MM layers range from 10 to 60nm. Both the TEM and the WAXD results suggest that the MM is hardly exfoliated in the mixing of the composites. The lengths of the stacked MM layers are mainly in the range of 400 – 1000 nm and are partly more than  $1\mu\text{m}$  [Figures 6.4 and 6.5 (a)].

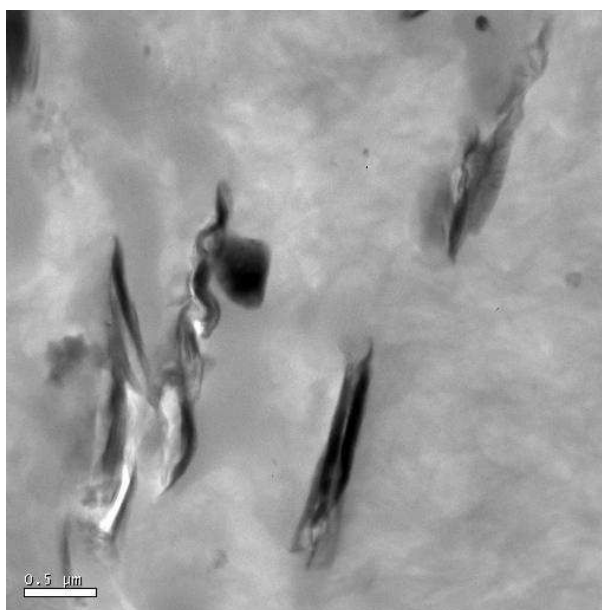


**Figure 6.3** Transmission electron micrographs of the UHMWPE/PP/MM (90/10/3) composites.

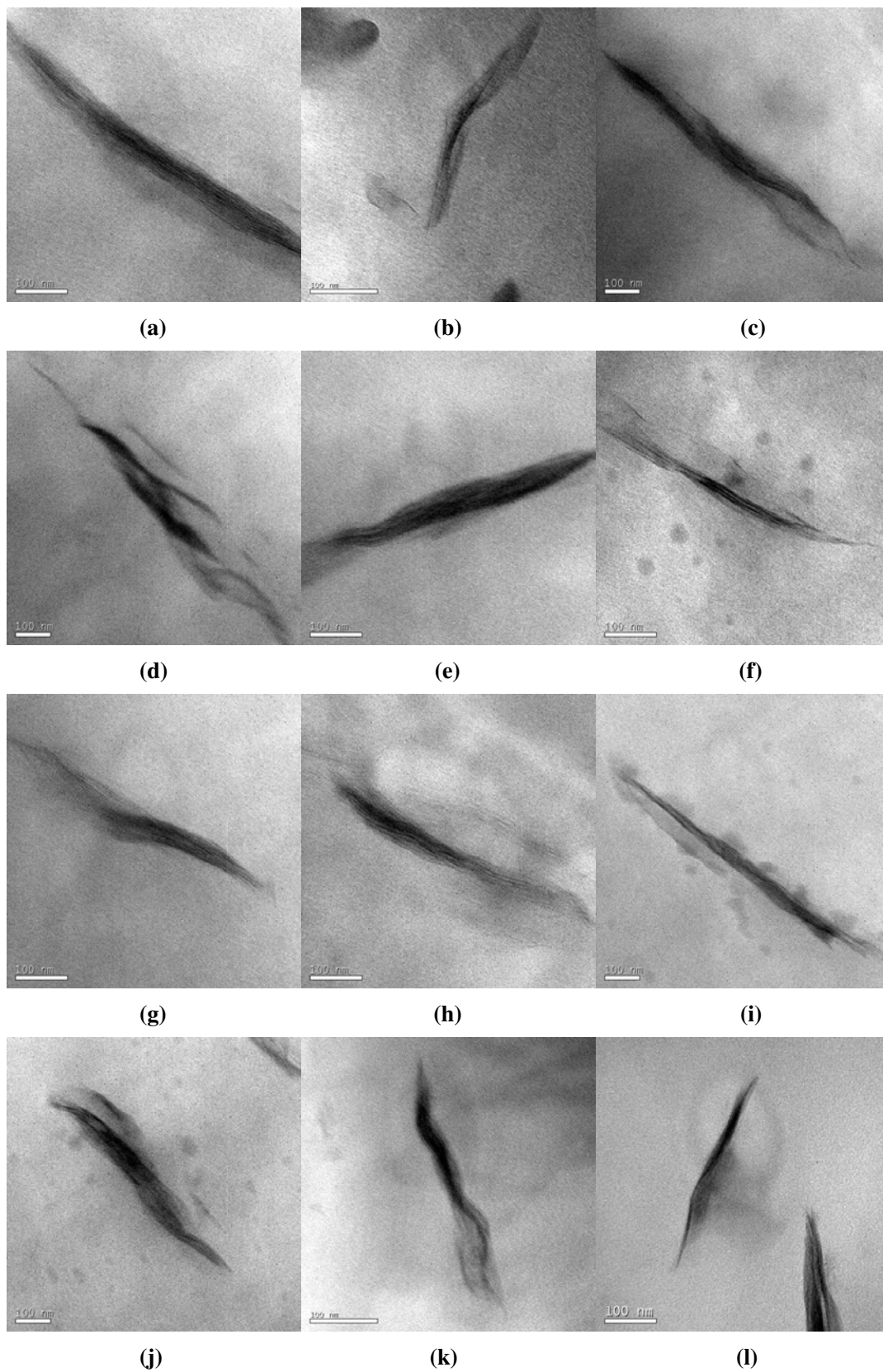


**Figure 6.4** Transmission electron micrographs of the UHMWPE/PP/MM (90/10/3) composites. The micrographs of (a) – (l) denote the different positions of the sample.

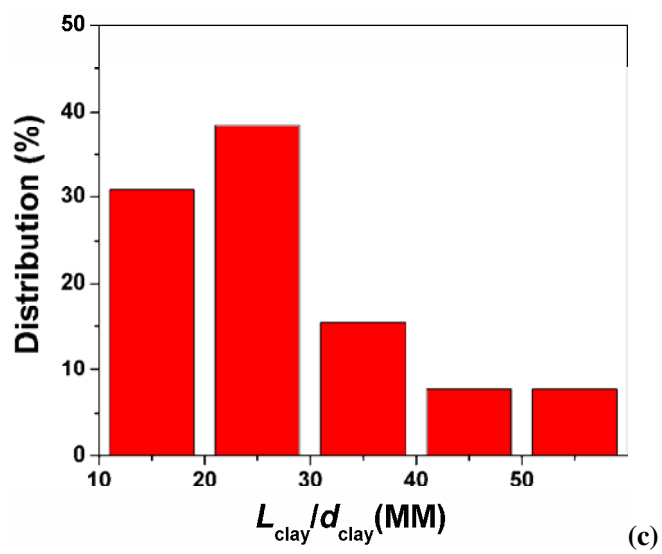
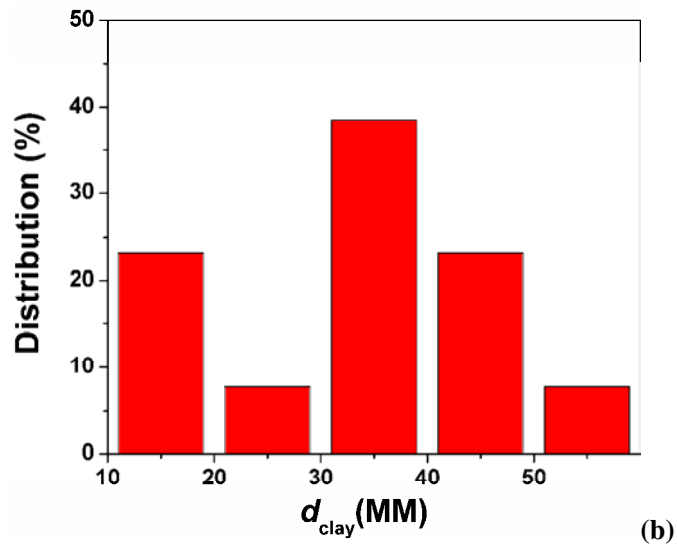
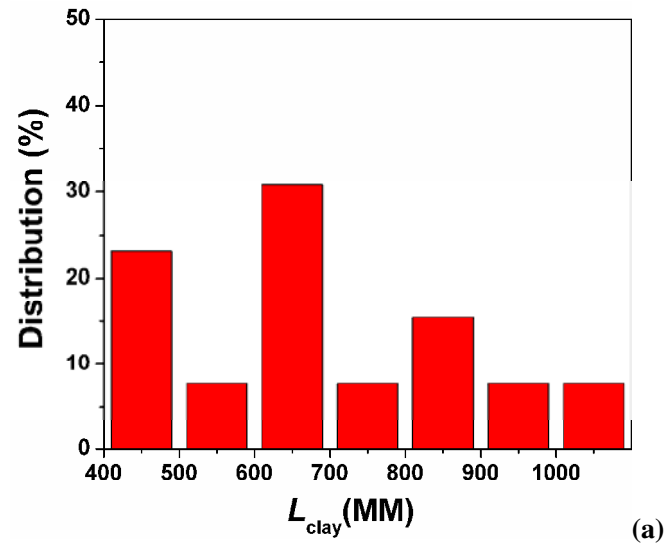


**Figure 6.5** The distributions of: (a) the MM layer length (nm), (b) thickness (nm) and (c) parameter  $L_{\text{clay}}/d_{\text{clay}}$  in the UHMWPE/PP/MM (90/10/3) composite.

For the UHMWPE/PP/PMM (90/10/3) composite, PMM exhibit less stacking than MM in its composites and are little orderly oriented (Figures 6.6 – 6.8). The thicknesses of the PMM layers are mainly located in 1 - 5 nm, while a small part of them is more than 10 nm, such as the stacks in Figure 6.7(d) and (e). Furthermore, the lengths of the PMM layers are in the range of 100 - 400nm which are remarkably shorter than those of MM in its composites [Figure 6.9(a)].

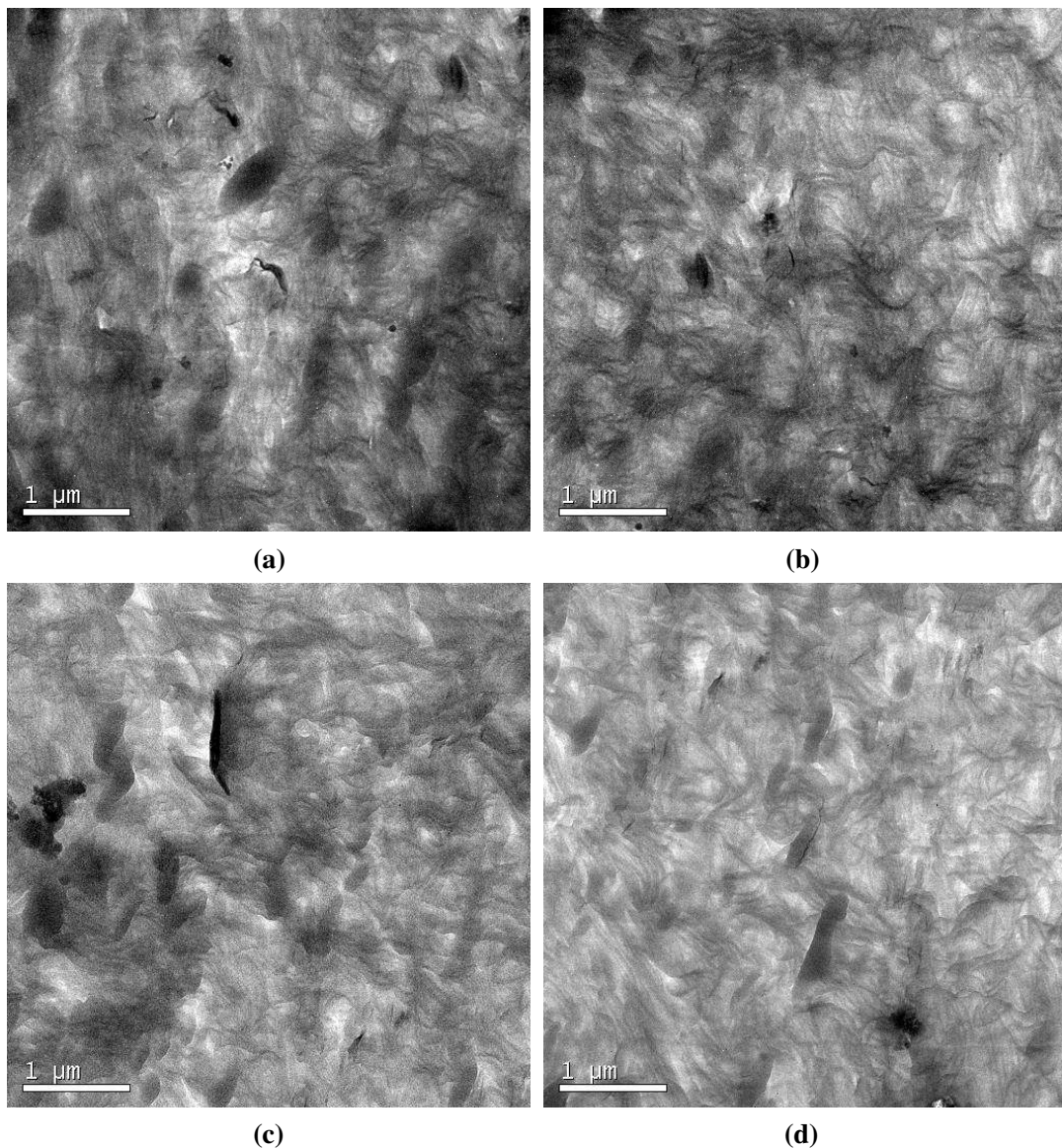


**Figure 6.6** Transmission electron micrographs of the UHMWPE/PP/PMM (90/10/3) composites. The micrographs of (a) – (d) denote the different positions of the sample.

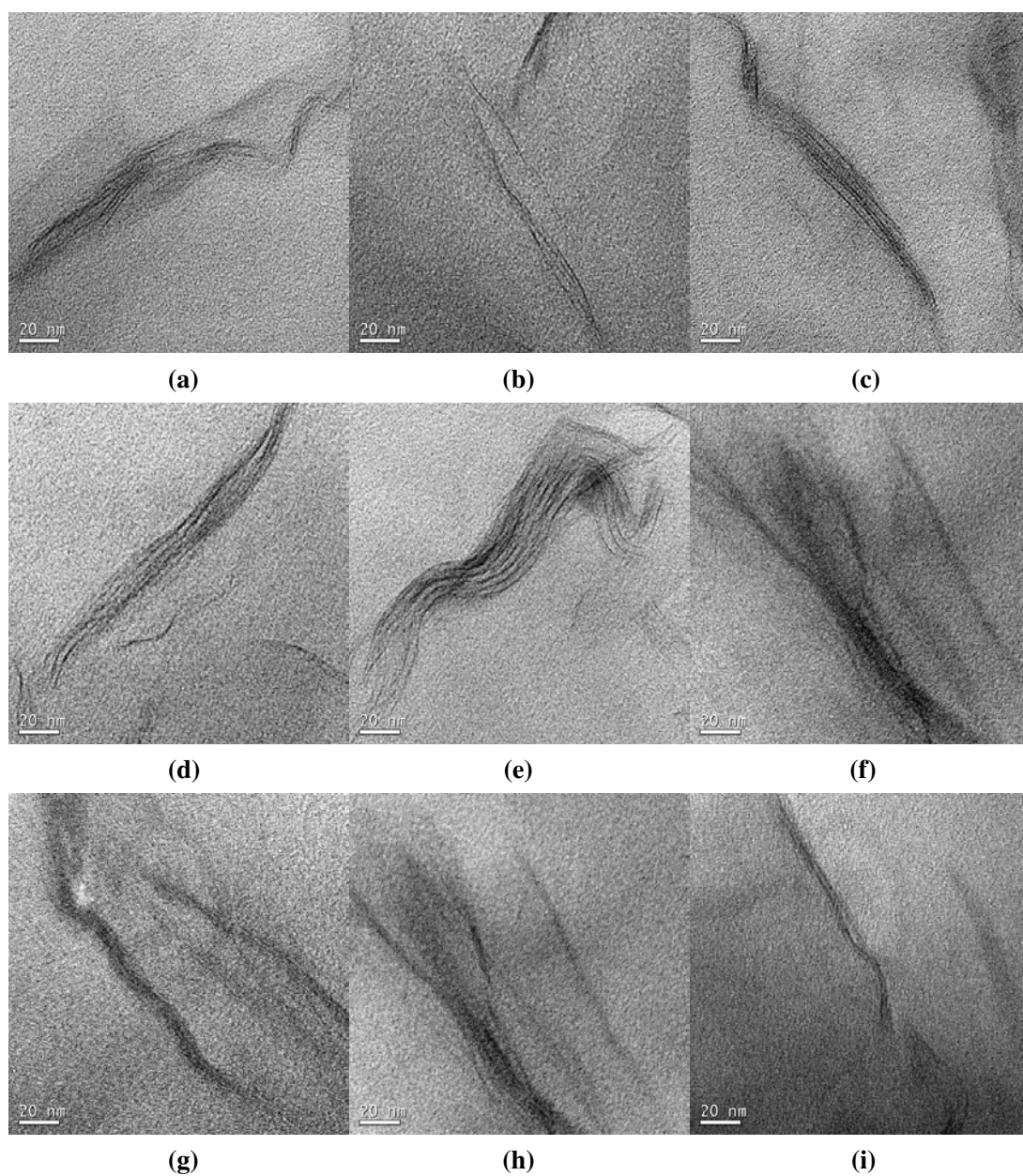


**Figure 6.7** Transmission electron micrographs of the UHMWPE/PP/PMM (90/10/3) composites. The micrographs of (a) – (i) denote the different positions of the sample.

By combining Figures 6.5(c) with 6.9(c), it can be concluded that the value of  $L_{\text{clay}}/d_{\text{clay}}$  (two-dimensional aspect ratio of the dispersed clay particles) of PMM is markedly larger than that of MM in composites. It is worth noting that the ratio plays

an important role in determining the enhancement of mechanical properties of UHMWPE composites <sup>[16]</sup>. Hence, the mechanical properties of the UHMWPE/ PP/ PMM composites might be better than that of the UHMWPE/ PP/ MM composites.

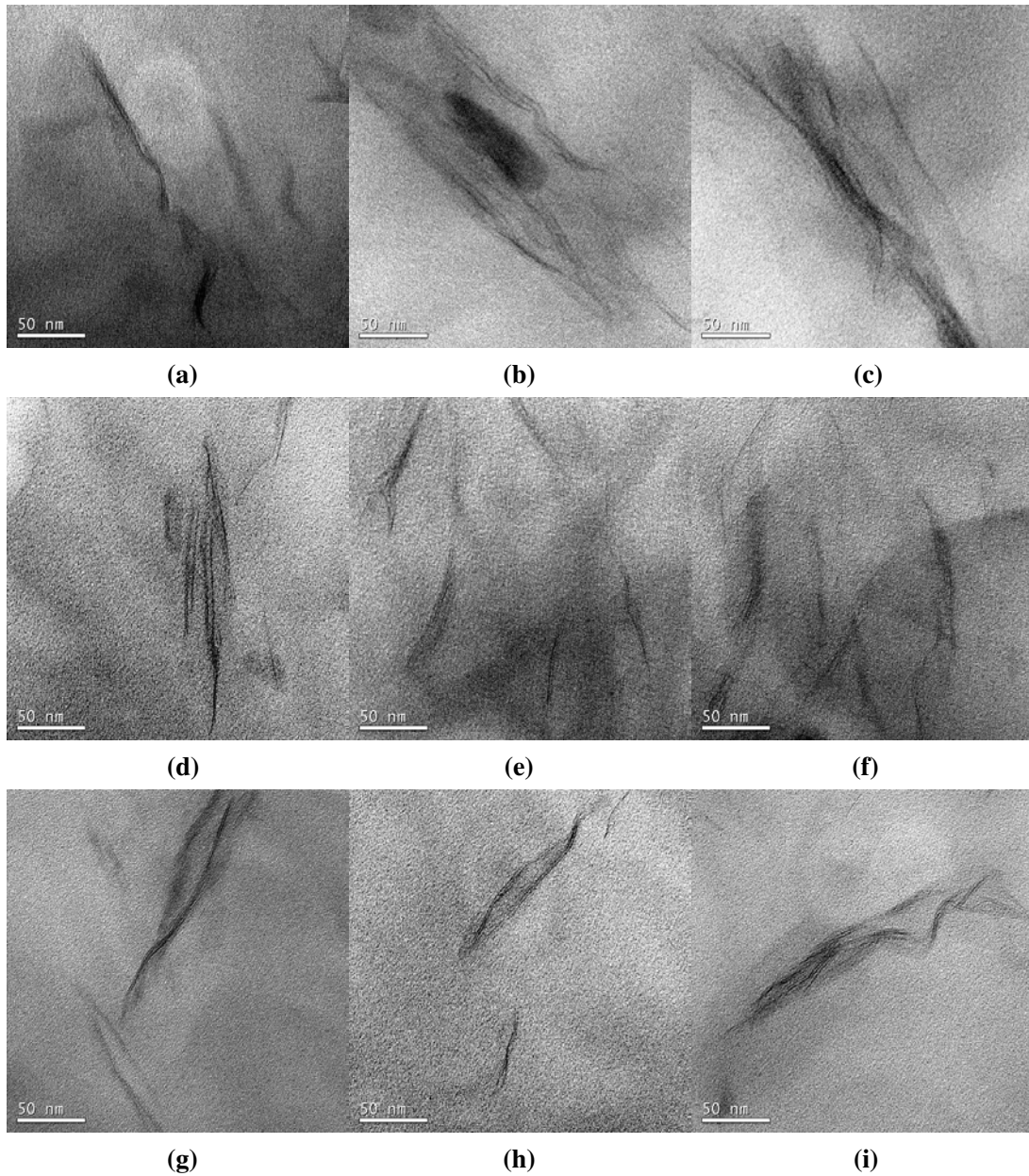


**Figure 6.8** Transmission electron micrographs of the UHMWPE/PP/PMM (90/10/3) composites. The micrographs of (a) – (i) denote the different positions of the sample.

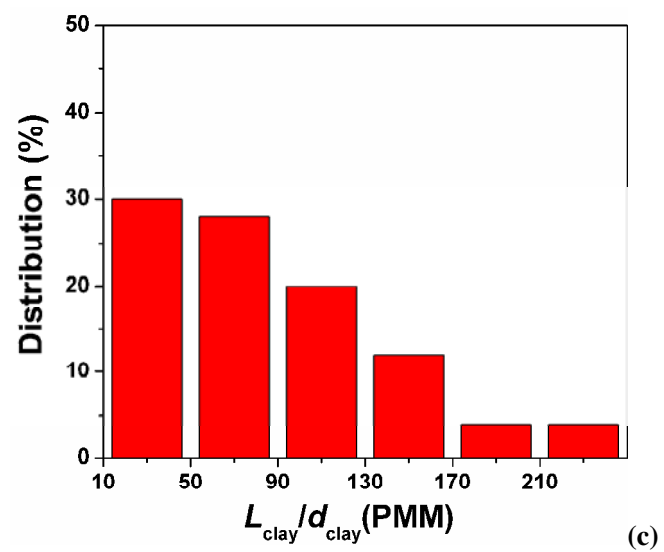
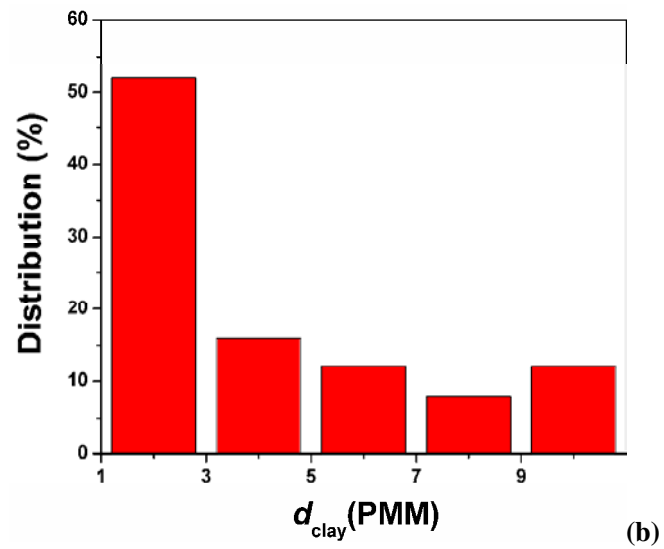
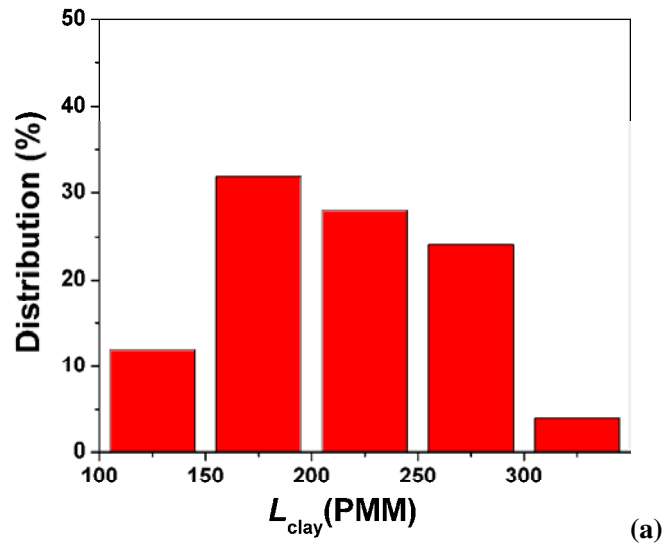


**Figure 6.9** The distributions of: (a) the PMM layer length (nm), (b) thickness (nm) and (c) parameter  $L_{\text{clay}}/d_{\text{clay}}$  in the UHMWPE/PP/PMM (90/10/3) composite.

## 6.2.2 Rheological behaviors

Generally, the rheological behavior of polymer composite melts strongly depends on their interface properties [17], the dispersion-distribution state of clay layers and interfacial properties [18, 19].

The effects of PMM, MM and PM on the rheological properties of UHMWPE were also investigated, as is shown in Figures 6.10 and 6.11. These figures show that the viscosities of the UHMWPE/PP blend, UHMWPE/PP/PM and UHMWPE/PP/PMM composites decrease with increasing shear rate, indicating a feature of pseudoplastic flow. These studies also show that the addition of PM and PMM can significantly reduce the apparent viscosity of the UHMWPE/PP (90/10) blend, and no pressure vibration occurs throughout the whole shear rate range investigated. Moreover, the viscosities of composites tend to decrease with increasing clay concentration. Besides, the surface of extruded bar and pipe of the UHMWPE/PP/PMM (90/10/5) composite are very smooth (Figure 6.12). A comparison of the flow behavior of UHMWPE/PP blend, UHMWPE/PP/PM and UHMWPE/PP/PMM composites shows that the most obvious effect on the viscosity reduction of UHMWPE occurs in UHMWPE/PP/PM (90/10/5).

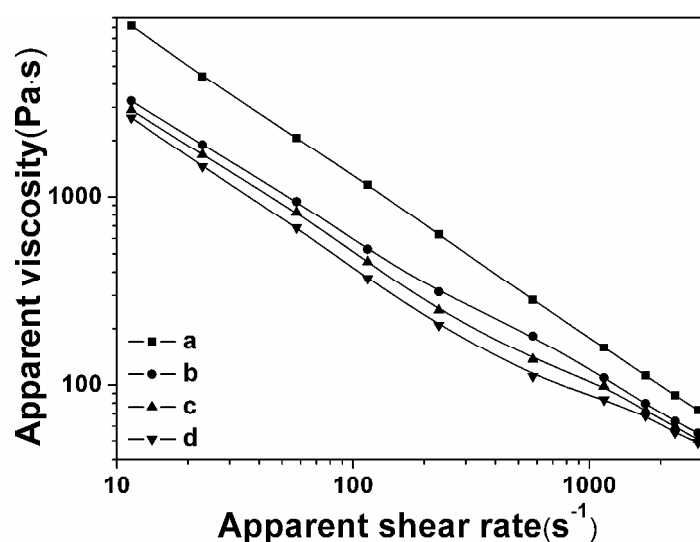


**Figure 6.10** Plot of the logarithm of the apparent viscosity versus the logarithm of the apparent shear rate for (a) UHMWPE/PP (90/10), (b) UHMWPE/PP/PM (90/10/1), (c) UHMWPE/PP/PM (90/10/3) and (d) UHMWPE/PP/PM (90/10/5).

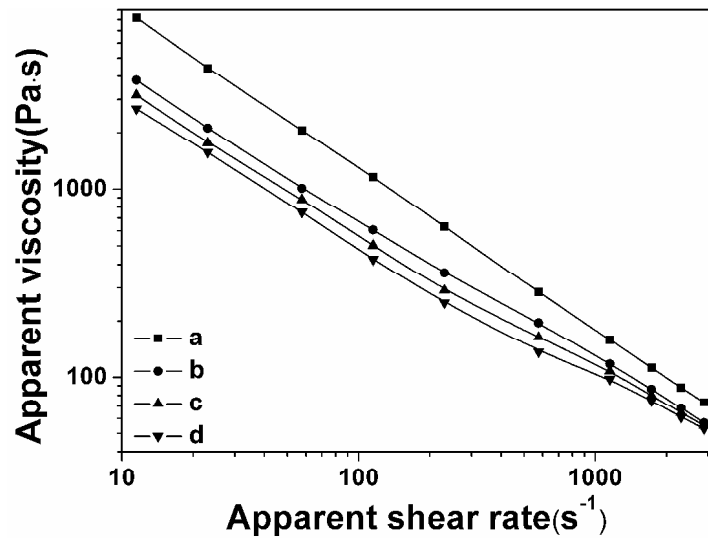


**Figure 6.11** Plot of the logarithm of the apparent viscosity versus the logarithm of the apparent shear rate for (a) UHMWPE/PP (90/10), (b) UHMWPE/PP/PMM (90/10/1), (c) UHMWPE/PP/PMM (90/10/3) and (d) UHMWPE/PP/PMM (90/10/5).



**Figure 6.12** The bar and pipe of the UHMWPE/PP/PMM (90/10/5) composites.

Unlike PM and PMM, the addition of MM to the UHMWPE/PP blend results in a significant increase of melt viscosity, and no steady rheology data could be obtained at shear rates range investigated. This might be attributed to the absence of PEG as lubrication phase. Hence, it is necessary to form the lubrication phase between UHMWPE particles in the viscosity reduction of composites.

### 6.2.3 Mechanical properties

The mechanical properties of composites depend on many factors, including the aspect ratio of the filler, the degree of dispersion of the filler in the matrix and the adhesion at the filler-matrix interface. Table 6.2 summarizes the mechanical properties of UHMWPE and its composites prepared with PMM, PM and MM. In the case of the UHMWPE/PP (90/10) blend, its mechanical properties remain nearly unchanged when compared with pure UHMWPE.

With same MMT loading, the tensile strengths of samples with better dispersed PMM are higher than that of samples with more poorly dispersed PM or MM. For pristine UHMWPE, the tensile strength is 38.71MPa. Addition of 5phr of PMM increases the tensile strength to 47.55MPa, which is 22.84% higher than that of the pristine UHMWPE. For PM or MM based system, tensile strength increases with 1-3phr of clay loading. With 5phr PM or MM content, however, the tensile strength starts to decrease, but they are still higher than those of the pure UHMWPE and UHMWPE/PP blend.

**Table 6.2** The mechanical properties of pure UHMWPE and its composites

Sample	Tensile strength (MPa)	Elongation at break (%)	Yield strength (MPa)	Izod-notched impact strength (kJ/m <sup>2</sup> )
UHMWPE	38.71	396.41	25.85	No break
UHMWPE/PP(90/10)	39.16	431.22	26.02	No break
UHMWPE/PP/PM (90/10/1)	42.33	487.99	26.66	112.86
UHMWPE/PP/PM (90/10/3)	44.12	540.51	27.21	100.91
UHMWPE/PP/PM (90/10/5)	42.85	502.62	28.27	96.93
UHMWPE/PP/MM (90/10/1)	43.13	501.11	27.61	No break
UHMWPE/PP/MM (90/10/3)	44.83	521.35	28.13	No break
UHMWPE/PP/MM (90/10/5)	44.08	517.40	28.44	102.87
UHMWPE/PP/PMM (90/10/1)	44.67	477.98	27.33	No break
UHMWPE/PP/PMM (90/10/3)	46.52	505.88	27.39	No break
UHMWPE/PP/PMM (90/10/5)	47.55	546.19	27.85	No break

With the same OMMT, elongation at break of composite materials almost follows the same trend as the tensile strength. Broadly speaking, yield strength

improves with the increase of clay loading. However, there are not notable differences in the level of yield strength improvement when different OMMT are used. For the UHMWPE/PP/PMM composites, izod-notched impact strengths are without much obvious change, but a slight drop of impact strengths for PM or MM based composites appears with higher clay loading.

As discussed in section 6.2.2, the exfoliation and dispersion of the OMMT in UHMWPE/PP/PMM nanocomposites is remarkably better than that in the UHMWPE/PP/MM composites and the aspect ratio of the former is higher than that of the later (compare Figure 6.3 with Figure 6.6), so PMM is more effective than MM in reinforcement.

## 6.3 Conclusions

The phase morphology, rheological and mechanical properties of the UHMWPE/PP/OMMT composites are investigated in this work, and some conclusions have been drawn as follow:

The WAXD analysis and TEM observation clearly indicate the formation of exfoliated and better intercalated structure for the UHMWPE/PP/PMM composites. The structure of PMM in the matrix is probably attributed to the synergistic effects of the complex intercalator (PEG/MDAB) on the intercalation and exfoliation for MMT.

The addition of a small amount of PM or PMM has been found able to reduce the melt viscosity of UHMWPE/PP (90/10) blend significantly, and PM shows better effect as compared with PMM. With 1phr PM contents in the UHMWPE/PP (90/10) blend, the apparent melt viscosity is much lower than that of pure UHMWPE, and no pressure vibration occurs throughout the whole range of shear rate. With more addition of PM and PMM, more viscosity reduction of UHMWPE/PP (90/10) occurs.

The UHMWPE nanocomposites exhibit remarkable improvement of mechanical properties such as tensile strengths, elongation at break and yield strength compared with the matrix without clay. The dispersed PMM particles exhibited a comparatively

large two-dimensional aspect ratio, which played an important role in determining the enhancement of mechanical properties of UHMWPE composites.

## 6.4 References

1. Giannelis EP, Krishnamoorti R, Manias E. Polymer-silicate nanocomposites: model systems for confined polymers and polymer brushes. *Adv Polym Sci* 1999, 138, 107.
2. LeBaron PC, Wang Z, Pinnavaia TJ. Polymer-layered silicate nanocomposites: an overview. *Appl Clay Sci* 1999, 15, 11.
3. Vaia RA, Price G, Ruth PN, Nguyen HT, Lichtenhan J. Polymer/layered silicate nanocomposites as high performance ablative materials. *Appl Clay Sci* 1999, 15, 67.
4. Giannelis EP. Polymer-layered silicate nanocomposites: synthesis, properties and applications. *Appl Organomet Chem* 1998, 12, 675.
5. Bharadwaj RK. Modeling the barrier properties of polymerlayered silicate nanocomposites. *Macromolecules* 2001, 34, 1989.
6. Messersmith PB, Giannelis EP. Synthesis and barrier properties of poly(1 - caprolactone) -layered silicate nanocomposites. *J Polym Sci, Part A: Polym Chem* 1995, 33, 1047.
7. Yano K, Usuki A, Okada A, Kurauchi T, Kamigaito O. Synthesis and properties of polyimide–clay hybrid. *J Polym Sci, Part A: Polym Chem* 1993, 31, 2493.
8. Gilman JW. Flammability and thermal stability studies of polymer-layered silicate (clay) nanocomposites. *Appl Clay Sci* 1999, 15, 31.
9. Dabrowski F, Bras M Le, Bourbigot S, Gilman JW, Kashiwagi T. PA-6 montmorillonite nanocomposite in intumescent fire retarded EVA. *Proceedings of the Eurofillers'99, Lyon-Villeurbanne, France; 6–9 September 1999.*
10. Sinha Ray S, Yamada K, Okamoto M, Ueda K. New polylactide/layered silicate nanocomposite: a novel biodegradable material. *Nano Lett* 2002, 2, 1093.
11. Nam PH, Maiti P, Okamoto M, Kotaka T, Hasegawa N, Usuki A. A hierarchical structure and properties of intercalated polypropylene/clay nanocomposites. *Polymer* 2001, 42, 9633.

12. Usuki A, Kojima Y, Kawasumi M, Okada A, Fukushima Y, Kurauchi T, Kamigaito O. Synthesis of nylon-6–clay hybrid. *J Mater Res* 1993, 8, 1179.
13. Cullity, B.D. *Element of X-ray diffraction*; Addison-Wesley: London, 1978.
14. Nam PH, Kaneko M, Ninomiya N, Fujimori A, Masuko T. Melt intercalation of poly(l-lactide) chains into clay galleries. *Polymer* 2005, 46, 7403.
15. Suprakas SR, Kazunobu Y, Masami O, Kazue U. New polylactide-layered silicate nanocomposites. 2. Concurrent improvements of material properties, biodegradability and melt rheology. *Polymer* 2003, 44, 857.
16. Nielsen LE. *Mechanical properties of polymer and composites, vol. 2*. New York: Marcel Dekker; 1981.
17. Ray SS, Maiti P, Okamoto M, Yamada K, Ueda K. New Polylactide/Layered Silicate Nanocomposites. 1. Preparation, Characterization, and Properties. *Macromolecules* 2002, 35, 3104.
18. Krishnamoorti R, Giannelis EP. Rheology of end-tethered polymer layered silicate nanocomposites. *Macromolecules* 1997, 30, 4097.
19. Sinha RS, Okamoto K, Okamoto M. Structure–Property Relationship in Biodegradable Poly(butylene succinate)/Layered Silicate Nanocomposites. *Macromolecules* 2003, 36, 2355.

# CHAPTER 7 Unique Thermodynamic Properties of Binary Polymer Blends and Solutions at the Volume Fraction $\phi_A = 1 - 1/e$

## 7.1 Introduction

For many theoretical considerations as well as numerous practical applications, the knowledge of the free energy of mixing as a function of composition is of utmost importance. The phase behavior dictated by the composition dependence of chemical potentials can be utilized to produce interesting and mechanically useful morphologies. Therefore, the obtainment of the free energy of mixing for polymer systems and precise prediction of their phase behaviors are of great interest from both academic and practical viewpoints<sup>[1-7]</sup> and are still challenging both theoretically and experimentally<sup>[8-11]</sup>. Mean-field theories, such as the Flory-Huggins (F-H) theory, have made a considerable contribution to this subject.

The classical F-H theory predictions of phase diagrams are based on the equality of the chemical potentials of the components in the different phases. Many kinds of phase diagrams for both polymer solutions and blends<sup>[12-15]</sup> have been successfully determined by finding the state that minimizes the free energy for any given composition and the F-H interaction parameter. The interaction parameter is often interpreted as an empirical quantity that can be used to bridge the gap between the F-H theory and the diverse range of phase behavior observed experimentally for polymer blends and solutions. Therefore, much attention has been paid to the determination of interaction parameters from both the academic and practical points of view. A large number of experimental methods are available to determine interaction parameters, particularly for polymer solutions<sup>[16-18]</sup>. The use of neutron

scattering is also of particular importance for polymer blends <sup>[19]</sup>.

The need for chemical potentials in the predictions of phase diagrams implies that the knowledge of the free energy of mixing and its derivative with respect to the composition is necessary. Wolf et al. <sup>[20]</sup> applied a headspace sampler and normal gas chromatography to the calculation of phase diagrams exhibiting phase separation. It is convenient to use the mathematical method reported in reference 21 to determine the parameter  $\chi$  from the measured vapor pressures. It requires only the knowledge of the free energy of mixing and not its derivative which is otherwise not easy to obtain if systems contain three or more components.

Zhu et al. has compared the F-H equation with Guggenheim's expression <sup>[22]</sup>, the original Freed's theory <sup>[23, 24]</sup> and the modified non-random two-liquid (NRTL) equation <sup>[25]</sup>. The results showed that the free energies of polymer solutions calculated from Guggenheim's expression and the original Freed's theory are very close to each other and are much higher than those obtained from the modified NRTL equation and F-H equation. However, the volume fractions of the polymer corresponding to the minimum free energy of mixing ( $\phi_{Am}$ ) are almost the same for different theories. This suggests that the variations of  $\phi_{Am}$ s from the different theories are very small and can be neglected. Therefore, for the sake of simplicity and practicability, the F-H equation is adopted when  $\phi_{Am}$  is discussed.

Most previous studies and applications of the F-H theory were prone to focus on the composition dependence of both chemical potential <sup>[13 - 15, 26]</sup> and free energy of mixing for polymer blends and solutions <sup>[20, 22]</sup>, and attention devoted to the direct effects of chain length on them was relatively little <sup>[27]</sup>. To the best of the authors' knowledge, at  $\phi_A = 1-1/e$ , thermodynamic properties with respect to free energy of mixing and chemical potential for polymer blends and solutions have yet been reported up to now. This chapter shows unique thermodynamic properties of binary polymer systems at  $\phi_A = 1-1/e$ . It also reports on the effects of chain length, volume fraction and  $\chi$  on the minimum free energy and  $\phi_{Am}$  by the F-H theory.

## 7.2 Results and discussion

### 7.2.1 Effects of $N$ and $\chi$ on the free energy of mixing

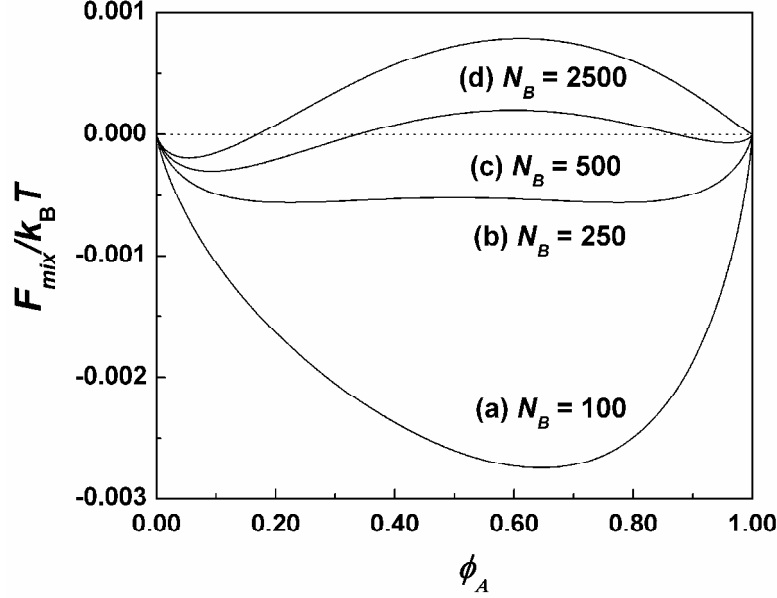


**Figure 7.1** Dependence of free energy of mixing on the volume fraction of component A, for  $N_A = 250$ ,  $\chi = 0.009$ , and  $N_B$  is 100, 250, 500 and 2500, respectively.

For binary  $A/B$  systems, when the contact between  $A$  and  $B$  is not favorable the parameter  $\chi$  is positive; when the contact between  $A$  and  $B$  is more favorable than that between  $A$  and  $A$  or  $B$  and  $B$ , then it is negative. When the value of  $\chi$  is high enough, the free energy develops two minima, separated by a maximum (Figure 7.1). The corresponding requirements for the minimum free energy of mixing are the thermodynamic criteria (7.1) and (7.2).

$$\frac{\partial F_{mix}}{\partial \phi_A} = 0 \quad (7.1)$$

$$\frac{\partial^2 F_{mix}}{\partial \phi_A^2} > 0 \quad (7.2)$$

First, we fix  $N_A = 250$ ,  $\chi = 0.009$  and vary  $N_B$  from 1 to 25000. Figure 7.2 shows the relationship between the calculated  $F_{mix}/k_B T$  from Eq. (2.1) and  $N_B$  for various values of  $\phi_A$ .  $F_{mix}/k_B T$  first increases rapidly with increasing  $N_B$  and then levels off as  $N_B$

further increases. It asymptotically reaches a value of  $\phi_A \ln \phi_A / N_A + \chi \phi_A (1 - \phi_A)$  as can be calculated from Eq. (2.1). Both the abrupt change and the asymptotic value of  $F_{mix}/k_B T$  suggest that the free energy of mixing for binary polymer systems is little affected by  $N_B$  as long as the latter is high enough. In order to determine whether the abrupt change occurs in other thermodynamic properties or not, the effects of  $N_B$  on interfacial tension ( $\gamma$ ) and interface thickness ( $D$ ) are studied by the self-consistent field theory (SCFT).

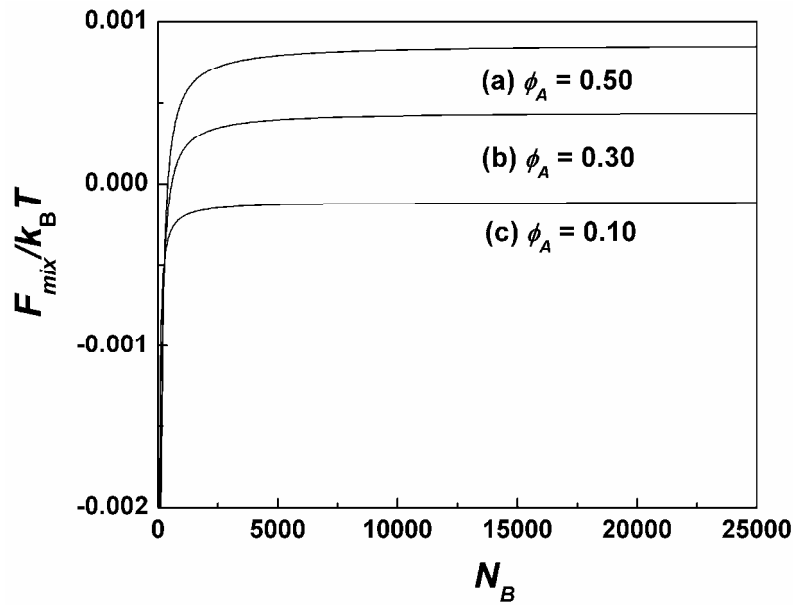


**Figure 7.2** Dependence of free energy of mixing on  $N_B$ , for  $N_A = 250$ ,  $\chi = 0.009$ , and  $\phi_A = 0.10$ , 0.30, and 0.50, respectively. The relatively larger values of  $N_B$  are used to represent the chain lengths of ultrahigh molecular weight polymers.

## 7.2.2 Effects of $N$ and $\chi$ on the interface properties

There are various theories that relate the interfacial properties of two immiscible polymers, e.g.,  $A$  and  $B$ , to the microscopic interactions described by the interaction parameter  $\chi$  between the corresponding monomers. In the early 1970s, the SCFT was employed by Helfand and Tagami <sup>[28]</sup> to study polymer-polymer interfaces. They found very simple expressions relating the interfacial tension  $\gamma_\infty$  and the interface thickness  $D_\infty$  to the interaction parameter  $\chi$  in the limit of infinite chain length,

$$\gamma_\infty = \rho_0 b k_B T (\chi / 6)^{1/2} \quad (7.3)$$

$$D_{\infty} = 2b / (6\chi)^{1/2} \quad (7.4)$$

where  $b$  is the effective length per monomer unit (in this paper,  $b = 1$  equals to the bead size). Broseta et al. [29] then studied the interfacial properties of polymer blends going beyond the usual approximation of infinite chain length. They found the expressions of interfacial tension and interfacial thickness for finite chain length polymer blends as follows:

$$\gamma = \gamma_{\infty} \left[ 1 - \frac{\pi^2}{12} \left( \frac{1}{\chi N_A} + \frac{1}{\chi N_B} \right) \right] \quad (7.5)$$

$$D = D_{\infty} \left[ 1 - 2 \ln 2 \left( \frac{1}{\chi N_A} + \frac{1}{\chi N_B} \right) \right]^{-1/2} \quad (7.6)$$

where  $\gamma_{\infty}$  and  $D_{\infty}$  are given by Eqs. (7.3) and (7.4), respectively.

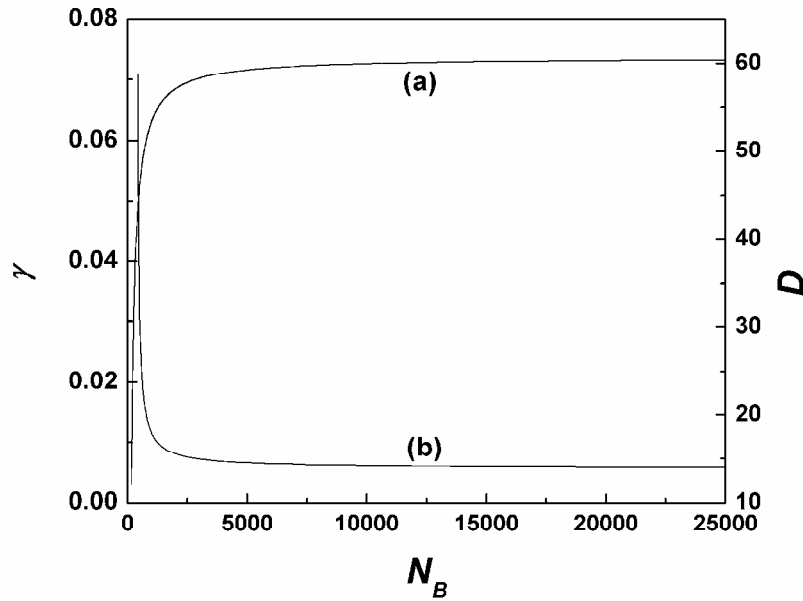


**Figure 7.3** (a) Interface tension from Eq. (7.5) and (b) interface thickness from Eq. (7.6) in binary polymer blends with various  $N_B$ .

Figure 7.3 shows the SCFT predictions of interfacial tension and interfacial thickness calculated from Eqs. (7.5) and (7.6), respectively, for binary polymer blends with  $N_B$  varying from 1 to 25000 (The upper limit of  $N_B$  could correspond to that of ultra-high molecular weight polymer). The results indicate that the SCFT predictions of both interfacial tension and interfacial thickness are also insensitive to the variation

of  $N_B$  when the chain is long enough. That is to say, for UHMWP (ultra-high molecular weight polymer) /NMWP blends, there is a slight effect of the variation of the molecular weight of UHMWP on the interfacial tension and interfacial thickness. Hence, it is necessary to determine the critical value of  $N_B$  in the investigation of the thermodynamic properties of polymer blends.

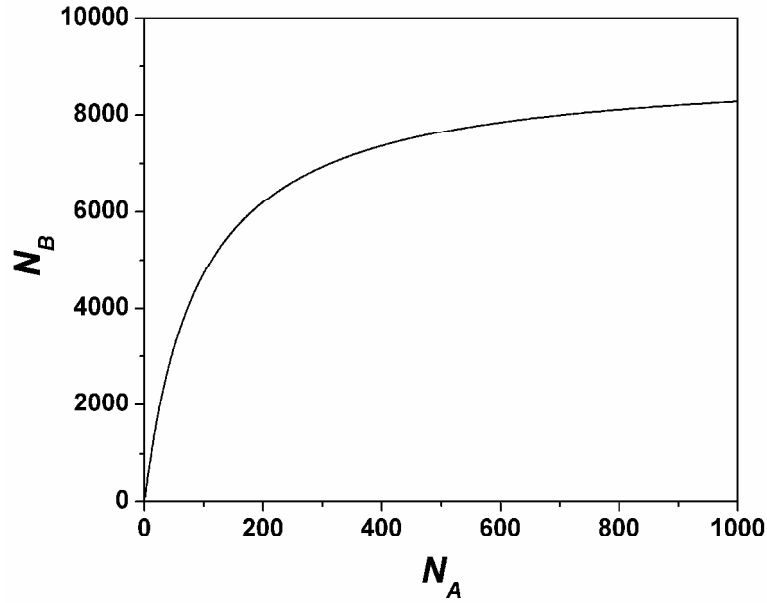


**Figure 7.4** The critical  $N_B$  from thermodynamic criteria (7.7) plotted against  $N_A$ , for  $V = 0.02$  and  $\chi = 0.009$ .

As indicated in Eq. (7.5), it is clear that the value of  $\gamma$  is composed of three parts. The relative contribution of each part ( $C_R$ ) is denoted as the ratio of this part and the sum of the three parts. Consequently, the relative contribution of the third part ( $C_R(N_B)$ ) will be less than a value ( $V$ ), providing that

$$N_B > \frac{(1-V)\pi^2 / (12\chi)}{V + V\pi^2 / (12\chi N_A)} \quad (0 < V < 1) \quad (7.7)$$

For example, consider a polymer blend with  $N_A = 250$  and  $\chi = 0.009$ . When  $N_B > 6620$ , which corresponds to molecular weight of  $1.4 \times 10^6$  for PE,  $C_R(N_B)$  will be less than 1%. If 1% is considered to be in the error, the effect of the variation of  $N_B$  on the interfacial tension of the blend may be neglected for  $N_B > 6620$ . This critical value of  $1.4 \times 10^6$  for PE is approximately consistent with most previous reports<sup>[30]</sup>.

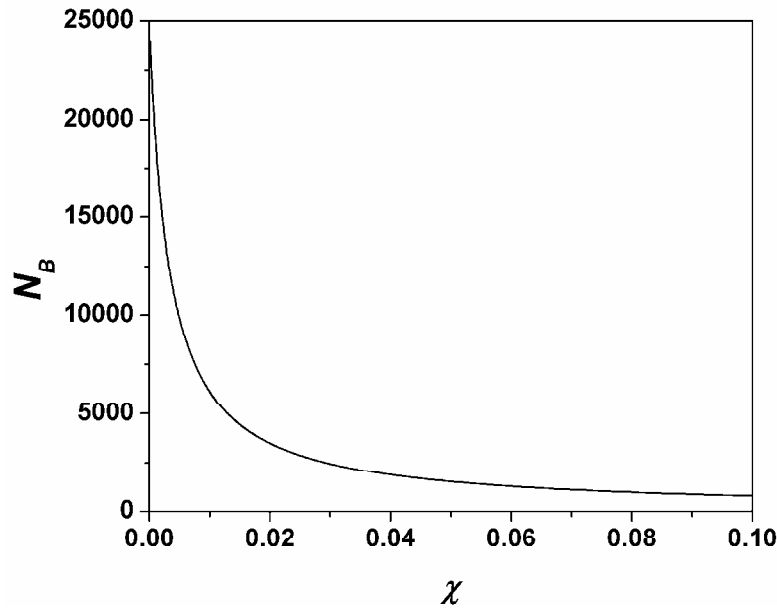


**Figure 7.5** The critical  $N_B$  from thermodynamic criteria (7.7) plotted against the parameter  $\chi$ , for  $V = 0.02$  and  $N_A = 250$ .

As shown in Figure 7.4, the effect of  $N_A$  on the critical  $N_B$  is also investigated on the base of thermodynamic criteria (7.7), which suggest that the critical  $N_B$  is a monotonously increasing function of  $N_A$ , for fixed  $V$  and  $\chi$ . Similarly, for given  $V$  and  $N_A$ , the critical  $N_B$  decreases dramatically with increasing the parameter  $\chi$  (Figure 7.5).

Consequently, all the results based on both SCFT and F-H theories indicate that many thermodynamic properties of binary polymer systems alter very little with the variation of  $N_B$  provided that  $N_B$  is large enough.

Besides, the influence of  $N_A$  is also investigated, as shown in Figures 7.6 and 7.7. These Figures indicate that both interfacial tension and interfacial thickness depends strongly on  $N_A$ . Hence, for the  $A/B$  blend, the determination of  $N_A$  is very important for the enhancement of the properties depending on interfacial tension and interfacial thickness (such as mechanical property). The comparison between (a), (b) and (c) in both Figures 7.6 and 7.7 indicates that the changes of  $\gamma$  and  $D$  when  $N_A$  is in the range of 200 ~ 350 is larger than those when it is in the range of 350 ~ 500.

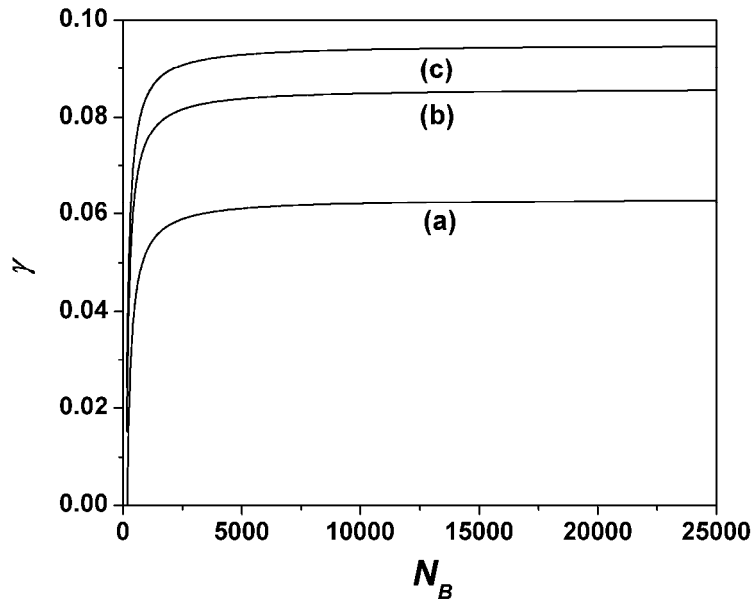


**Figure 7.6** Interface tension from Eq. (7.5) in binary polymer blends with various  $N_B$ , (a):  $N_A = 200$ ; (b):  $N_A = 350$ ; (c):  $N_A = 500$ .

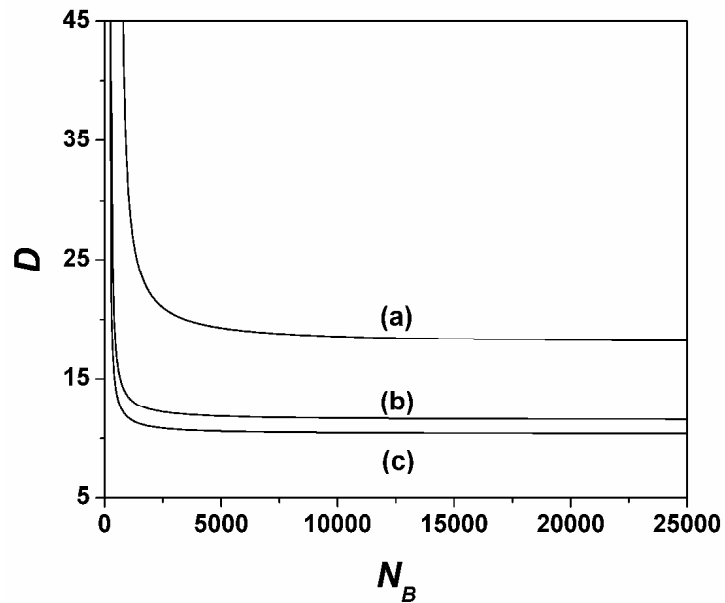


**Figure 7.7** Interface thickness from Eq. (7.6) in binary polymer blends with various  $N_B$ , (a):  $N_A = 200$ ; (b):  $N_A = 350$ ; (c):  $N_A = 500$ .

### 7.2.3 Effects of $N$ and $\chi$ on $\phi_{Am}$

Figures 7.8 – 7.11 shows the exchange chemical potential  $\mu$  of polymer mixtures as a function of the volume fraction  $\phi_A$  for  $N_A = 250$  and  $200$ , and various values of  $N_B$  and  $\chi$ . An interesting observation is that all the  $\mu$  curves pass through a common point

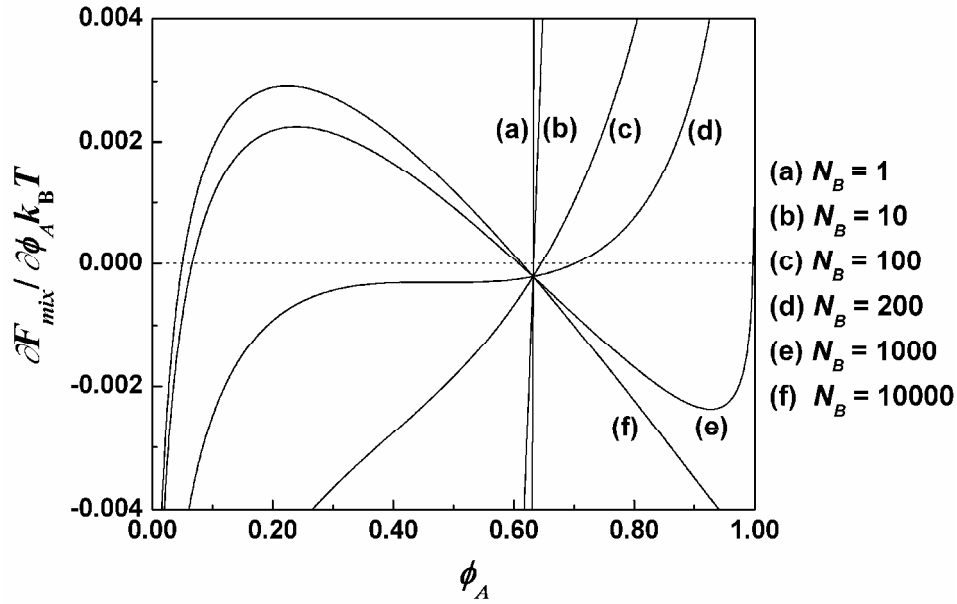


**Figure 7.8** Exchange potential from Eq. (2.6) plotted against the volume fraction of component A, for  $N_A = 250$ ,  $\chi = 0.009$  and  $N_B$  varies from 1 to 10000.

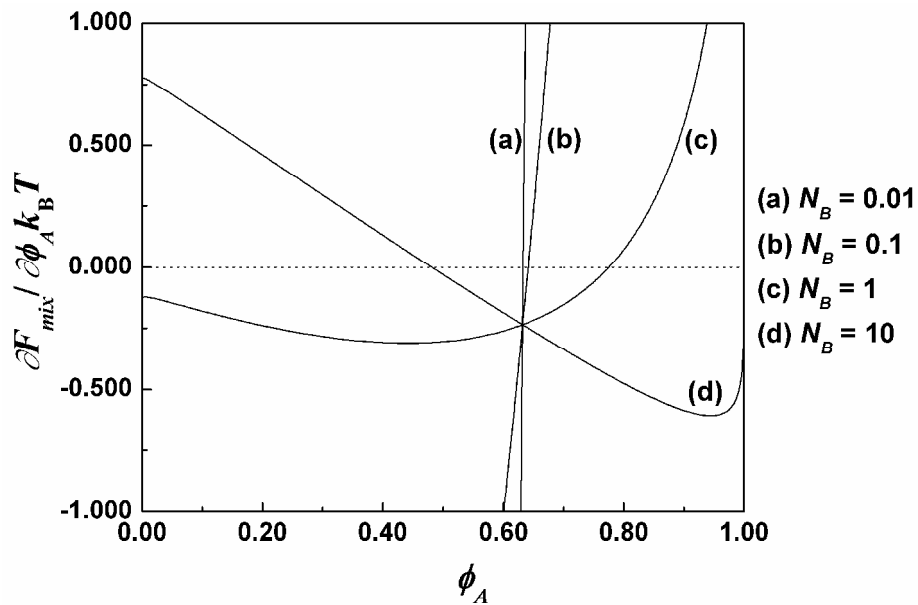


**Figure 7.9** Same as Figure 7.8 but with  $\chi = 0.9$ .

and the corresponding volume fraction  $\phi_A$  is equal to  $1-1/e$ , as can be calculated from Eq. (2.6). This suggests that for systems with fixed  $N_A$  and  $\chi$ , and different values of  $N_B$ , the exchange chemical potentials of mixing are always the same at  $\phi_A = 1-1/e$ . In other words, the exchange chemical potential at  $\phi_A = 1-1/e$  only depends on  $N_A$  and  $\chi$  and not  $N_B$ . In order to further explore the thermodynamic properties of polymer

mixtures at  $\phi_A = 1-1/e$ , we now investigate the effects of both  $N$  and  $\chi$  on the volume fraction of component A corresponding to the minimum free energy of mixing ( $\phi_{Am}$ ).

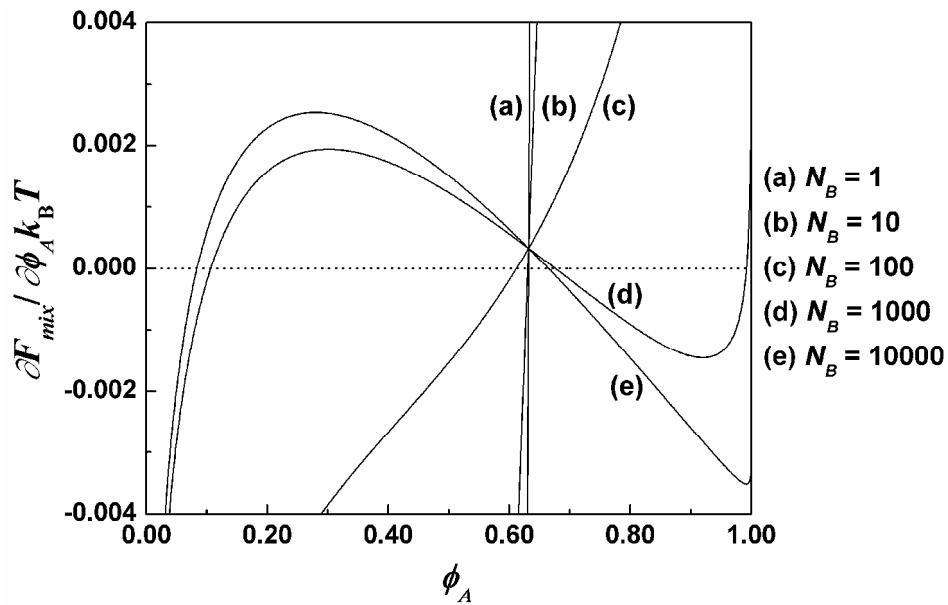


Figure 7.10 Same as Figure 7.8 but with  $N_A = 200$ .

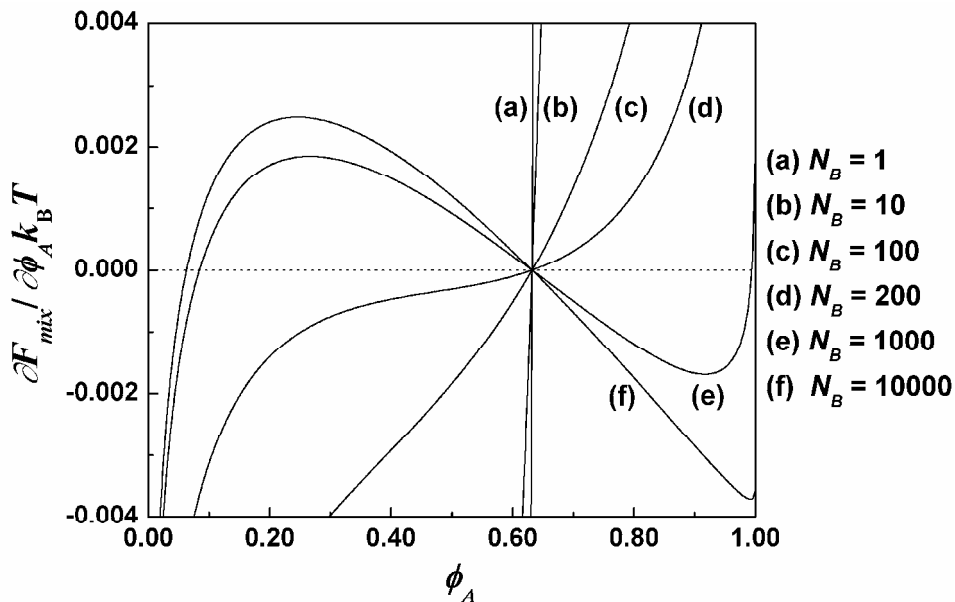
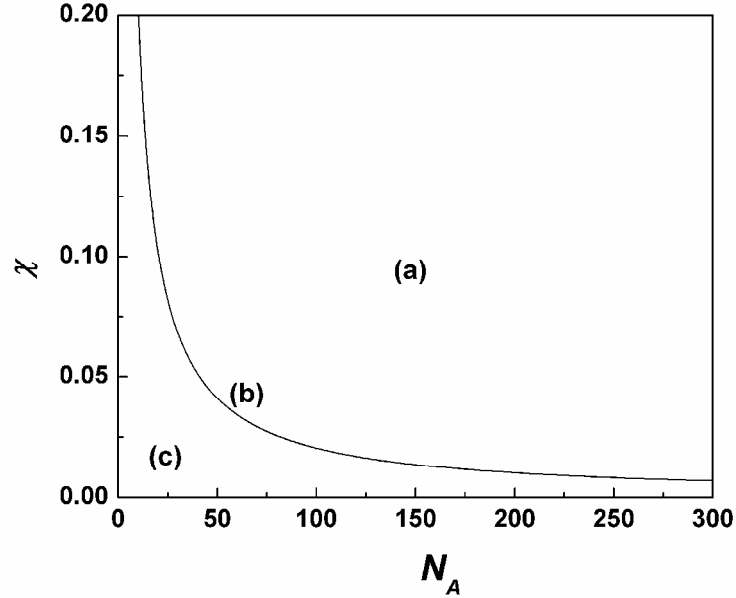


Figure 7.11 Same as Figure 7.8 but with  $N_A = 250$  and  $\chi N_A = 2.05$ .



**Figure 7.12** Plot of  $\chi$  from Eq. (7.9) vs.  $N_A$  at  $\phi_A = 1-1/e$ . (a) the region with  $\chi N_A > 2.0486$ ,  $\mu_c < 0$ ; (b) the line with  $\chi N_A = 2.0486$ ,  $\mu_c = 0$ ; (c) the region with  $\chi N_A < 2.0486$ ,  $\mu_c > 0$ .

Eq. (7.8) is found from the condition  $\phi_A = 1-1/e$  and Eq. (2.6)

$$k_B T \left[ \frac{\ln \phi_A + 1}{N_A} + \chi(1 - 2\phi_A) \right] = 0 \quad (7.8)$$

Therefore,

$$\chi N_A = \frac{\ln \phi_A + 1}{2\phi_A - 1} \Big|_{\phi_A = 1-1/e} \quad (7.9)$$

$$\approx 2.05$$

It is interesting to consider how the common point and  $\phi_{Am}$  behave as the value of  $\chi N_A$  varies. Figures 7.8 – 7.11 indicate that the behaviors of both the common point and  $\phi_{Am}$  are crucially dependent on the value of  $\chi N_A$ , in particular whether or not it is less than, equal to, or greater than the value of 2.05. Figure 7.12 shows the exchange chemical potentials corresponding to the common points ( $\mu_c$ ) for these three scenarios.

In case  $\chi N_A > 2.05$ ,  $\mu_c$  is always negative (Figures 7.8 and 7.9 and Figure 7.12(a)). It is worth noting that the left one of the two minima for the free energy of mixing vanishes with decreasing  $N_B$  [Figure 7.8(a) - (d) and Figure 7.9(a) - (c)]. The corresponding requirements for the critical point ( $N_{Bv}$ ,  $\phi_{Amv}$ ) of the disappearance of

the left minima are the thermodynamic criteria (7.1) and (7.10).

$$\frac{\partial^2 F_{mix}}{\partial \phi_A^2} = 0 \quad (7.10)$$

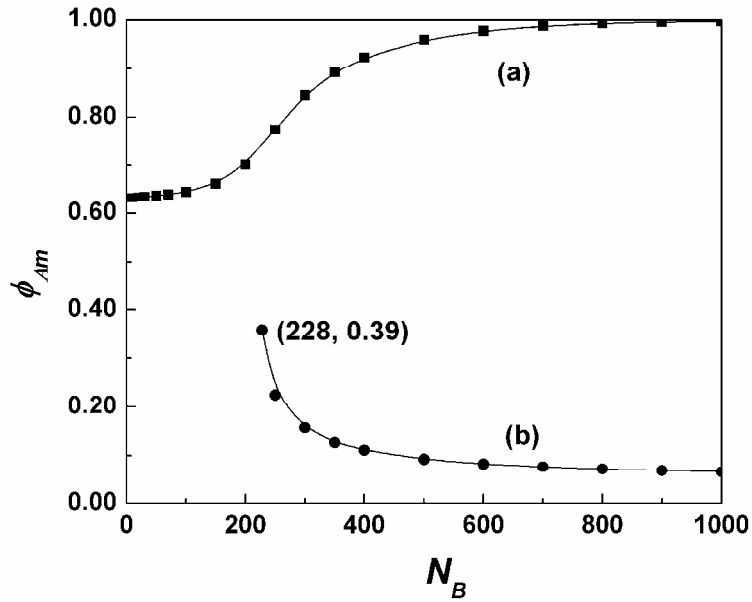


**Figure 7.13** Plot of  $\phi_{Am}$  vs.  $N_B$  for  $N_A = 250$  and  $\chi = 0.009$ . The  $N_B$  and  $\phi_{Am}$  corresponding to the critical point of the disappearance of the left minima are calculated from the thermodynamic criteria (7.1) and (7.10).

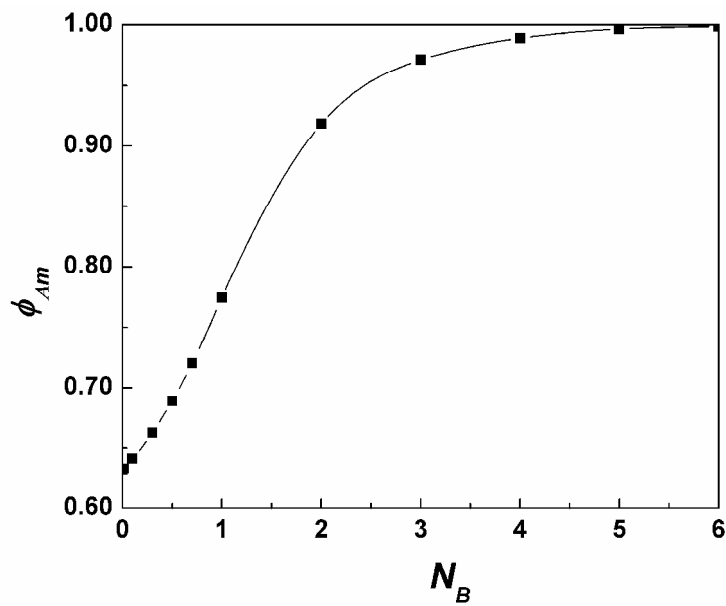


**Figure 7.14** Same as Figure 7.13 but with  $\chi = 0.9$ .

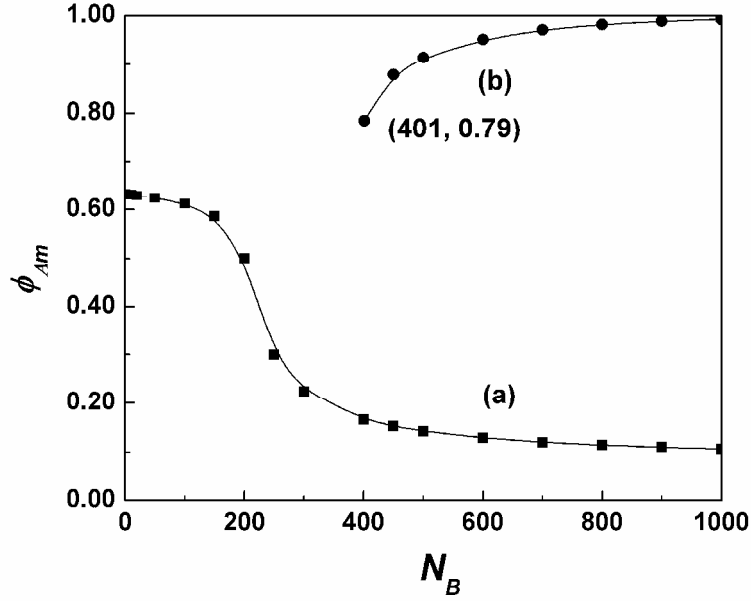


**Figure 7.15** Same as Figure 7.13 but with  $N_A = 200$ .

Figures 7.13 – 7.15 show the plots of  $\phi_{Am}$  versus  $N_B$  for different  $\chi$  and  $N_A$  corresponding to Figures 7.8 – 7.10, respectively. In view of the fact that both Figures 7.13 and 7.14 possess similar properties, a representative Figure 7.13 is reported here to show the general properties of binary polymer systems for the case  $\chi N_A > 2.05$ . The results indicate that the effects of  $N_B$  are three fold. (I)  $\phi_{Am}(N_B)$  monotonously decreases in the order:  $1.00(1000) > 0.92(400) > 0.65(100) > 0.63(10) > 0.63(1)$ , in Figure 7.13(a), based on which it is known that as  $N_B$  decreases  $\phi_{Am}$  asymptotically approaches the limited volume fraction  $1-1/e$ . However, for  $\chi N_A > 2.05$  and  $\mu_c < 0$ ,  $\phi_{Am}$  is not equal to  $1-1/e$ , because  $\mu = 0$  is necessary for the definition of  $\phi_{Am}$ . Moreover, the free energy of mixing is a monotonous increasing function of  $N_B$ , as discussed in section 7.2. (Figures 7.1 and 7.2). Consequently, for binary polymer systems, when  $\chi N_A > 2.05$ , the closer the  $\phi_{Am}$  to  $1-1/e$ , the lower the free energy of mixing. Besides, as  $\phi_{Am}$  increases with  $N_B > N_{Bv}$ , the free energy of mixing decreases for Figure 7.13(b). (II) Another interesting feature of the  $\phi_{Am}$  curve for Figure 7.13(a) is that with decreasing  $N_B$ ,  $\phi_{Am}$  alters very little in both the relatively lower  $N_B$  regions ( $N_B < 100$ ) and higher one ( $N_B > 400$ ). However, the shape of the  $\phi_{Am}$  curve alters dramatically in the range  $100 \leq N_B \leq 400$  which is called a sensitive region of  $\phi_{Am}$ . This is indicated by the steep slope of different regions of the  $\phi_{Am}$  curve. (III) Both the order in (I) and

Figure 7.13 also show that, for  $\chi = 0.009$  and  $N_A = 250$ ,  $\phi_{Am}$  of both polymer blends and solutions is approximately equal to  $1-1/e$  provided that  $N_B \leq 10$ .

The effects of the parameter  $\chi$  on  $\mu$  and  $\phi_{Am}$  can be appreciated upon comparing Figure 7.8 with Figure 7.9, and Figure 7.13 with Figure 7.14, respectively. There is clearly much similarity between two binary polymer systems with different values of  $\chi$ . For example, in both cases  $\mu_c$  is negative and  $\phi_{Am}$  always decreases with decreasing  $N_B$ . In Figure 7.14, however, only one branch of the  $\phi_{Am}$  curves is drawn in that the value of  $\phi_{Amv}$  calculated from the thermodynamic criteria (7.1) and (7.10) is approximately equal to zero and all the values of  $\phi_{Am}$  of the incomplete branch are lower than  $\phi_{Amv}$  [see Figure 7.13(b)]. The comparison of Figure 7.14 with Figure 7.13(a) shows that as  $\chi$  increases, the sensitive region of  $\phi_{Am}$  becomes narrow and the corresponding  $N_B$  decreases dramatically. Moreover, for fixed  $N_A$  and  $N_B$ ,  $\phi_{Am}$  is a monotonously increasing function of  $\chi$ . For example,  $0.63 (N_A = 250, N_B = 1 \text{ and } \chi = 0.009) < 0.77 (N_A = 250, N_B = 1 \text{ and } \chi = 0.9)$ . This is in agreement with Safronov's work <sup>[32]</sup>. In Figure 7.14,  $\phi_{Am}(N_B)$  monotonously decreases in the order:  $1.00 (6) > 0.92 (2) > 0.77 (1) > 0.63 (0.01) > 0.63 (0.001)$ , which shows that  $0.77 (1)$  deviates seriously from the asymptotic volume fraction  $\phi_A = 1-1/e$  and that the value of  $\phi_{Am}$  is close to  $1-1/e$  only if  $N_B \leq 0.01$ . At a first glance, this may be a little surprising because the value of  $N_B$  is not an integer but a fraction. However, it must be noted that since both the chain length  $N$  and the parameter  $\chi$  are defined in terms of energies per site [see Eq. (7.11) and Eq. (2.2)] <sup>[31]</sup>, the lattice site volume must be specified whenever  $N$  and  $\chi$  are discussed.

$$N_i = \frac{v_i}{v_0} \quad (7.11)$$

We now consider the effect of chain length on the  $v_0$  in two regimes. If  $N_B \geq 1$ , molecules  $B$  occupy multiple-connected-lattice sites. However, there will be  $1/N_B$  molecules  $B$  per lattice site provided that  $N_B$  is in the range of  $0 \sim 1$ . Consequently, the new lattice site volume should be  $N_B v_0$  and the corresponding parameter  $\chi$  from Eq. (2.2) and the respective chain lengths calculated from Eq. (7.11) for components  $A$

and  $B$  should be  $\chi N_B$ ,  $N_A/N_B$  and 1, respectively. Moreover, it can be concluded from the thermodynamic criterion (7.1) that the  $\phi_{Am}$  remains unchanged so long as the phase separation parameter  $\chi N$  are fixed. Therefore, the  $\phi_{Am}$  for a polymer solution ( $N_B = 1$ ) must be about  $1-1/e$ , for  $\chi N_A > 2.05$ , so long as  $N_B$  or the parameter  $\chi$  is sufficiently small (component  $B$  is a good solvent). In other words, the smaller the parameter  $\chi$  (or the smaller the volume of molecule  $B$ ), the smaller the deviation of  $\phi_{Am}$  from the asymptotic volume fraction  $\phi_A = 1-1/e$ .

In case where  $\chi N_A < 2.05$ , both Figures 7.10 and 7.12(c) show that  $\mu_c$  is always positive. Moreover, as  $N_B$  decreases the minimum free energy of mixing monotonously decreases, and  $\phi_{Am}$  asymptotically approaches the limited volume fraction  $\phi_A = 1-1/e$  [see Figure 7.10 and 7.15(a)]. These results are very similar with the conclusions for  $\chi N_A > 2.05$ . However,  $\phi_{Am}$  is a monotonous decreasing function of  $N_B$  [see Figure 15(a)] which is opposite to that for the case where  $\chi N_A > 2.05$ .

For  $\chi N_A = 2.05$ , both Figures 7.11 and 7.12(b) show that  $\mu_c$  is always equal to zero at  $\phi_A = 1-1/e$ , regardless of  $N_B$ , implying that the extreme values of the free energy for binary polymer systems are always located at  $\phi_A = 1-1/e$ . Whether or not the extreme values are the maxima or minima depend on  $N_B$ . The range of  $N_B$  corresponding to the minima may be determined from the thermodynamic criteria (7.1) and (7.2). Substitution of Eq. (7.9) into criterion (7.2) leads to:

$$\chi N_B < \frac{\phi_A(1 + \ln \phi_A)}{(1 - \phi_A)[2\phi_A(1 + \ln \phi_A) + 1 - 2\phi_A]} \quad (7.12)$$

where  $\phi_A = 1-1/e$ , therefore

$$\chi N_B < 2.65 \quad (7.13)$$

On the contrary, from Eq. (7.1) and criterion (7.14),

$$\frac{\partial^2 F_{mix}}{\partial \phi_A^2} < 0 \quad (7.14)$$

It is found that for  $\chi N_B > 2.65$  and  $\chi N_A = 2.05$ , the  $\phi_A$  corresponding to the maximum

free energy of mixing for both binary polymer solutions and blends are always located at  $\phi_A = 1-1/e$ .

## 7.2.4 Comparison of the F-H calculations for polymer solutions with experiments and other calculations

Safronov et al. investigated the influence of  $\chi$  on the free energy of mixing for the solutions of polystyrene (PS) in chloroform (a good solvent), ethylbenzene (monomer analog), and cyclohexane (a poor solvent), by isothermal interval vapor sorption [32]. The F-H interaction parameter between the PS and various solvents decrease in the order:  $\chi(\text{cyclohexane}) > \chi(\text{ethylbenzene}) > \chi(\text{chloroform})$ . Their experimental results showed that the values of the free energy were negative for all systems over the entire concentration range and that the second derivative of the free energy was positive. Their investigations for the three PS solutions showed that both  $\phi_{Am}$  and the minimum free energy of mixing monotonously decreased with increasing interaction between the polymer and solvent, which is in good agreement with the result of our theoretical predictions based on F-H theory (see Figures 7.8, 7.9, 7.13 and 7.14). Moreover, for the PS/chloroform solution the  $\phi_{Am}$  was about 0.61 which matched well the H-F theory result of  $1-1/e$  within the experimental errors.

As stated in the theoretical background, for a polymer solution with  $N_A = 100$ ,  $N_B = 1$ , Zhu et al. calculated the free energy as a function of the composition from Guggenheim's expression, the original Freed's theory and the modified NRTL equation, respectively. The results indicated that all the  $\phi_{Am}$  were approximately equal to 0.63, suggesting that the prediction of the limited  $\phi_A = 1-1/e$  from the F-H theory is in consistent with that from other theories.

## 7.3 Conclusions

This paper has reported on unique thermodynamic properties of binary  $A/B$  polymer systems at the volume fraction  $\phi_A = 1-1/e$  and the effects of chain length, volume fraction and  $\chi$  on the lowest free energy of mixing.

The calculated results based on both the SCFT and F-H theory indicate that many thermodynamic properties, such as free energy of mixing, interfacial tension and the interface thickness, are insensitive to  $N_B$  when  $N_B$  is large enough.

Consider a polymer blend with  $N_A = 250$  and  $\chi = 0.009$ . When  $N_B > 6620$ , which corresponds to molecular weight of  $1.4 \times 10^6$  for PE,  $C_R(N_B)$  will be less than 1%. If 1% is considered to be in the error, the effect of the variation of  $N_B$  on the interfacial tension of the blend may be neglected for  $N_B > 6620$ . This critical value of  $1.4 \times 10^6$  for PE is approximately consistent with most previous reports.

For binary polymer systems with a given polymer  $A$  and fixed  $\chi$ , exchange chemical potential curves all pass through a common point and the corresponding volume fraction is  $\phi_A = 1-1/e$  ( $\approx 0.63$ ), whatever the value of  $N_B$ , implying that the exchange chemical potentials at  $\phi_A = 1-1/e$  are independent of  $N_B$ . Moreover, as  $N_B$  decreases the minimum free energy of mixing monotonously decreases and the  $\phi_{Am}$  asymptotically approaches  $\phi_A = 1-1/e$  if  $\chi N_A \neq 2.05$  or is located at  $\phi_A = 1-1/e$  if  $\chi N_A = 2.05$  and  $\chi N_B < 2.65$ . This indicates that the  $\phi_{Am}$  for a polymer solution with a good solvent is close to  $1-1/e$ . For fixed  $N_A$  and  $N_B$ ,  $\phi_{Am}$  is a monotonous increasing function of  $\chi$ , which is in agreement with experimental results. It is also worth noting that  $\mu_c$  is crucially dependent on the value of  $\chi N_A$ . More specifically, if  $\chi N_A$  is less than, equal to, or greater than 2.05, the corresponding  $\mu$  is positive, zero and negative, respectively.

## 7.4 References

1. Saeki S. Calculation of combinatory entropy in complex polymer solutions based on the Flory–Huggins theory. *Fluid Phase Equilib* 1997, 136, 79.
2. Yan QL, Juan JdP. Critical behavior of lattice polymers studied by Monte Carlo simulations. *J Chem Phys* 2000, 113, 5954.
3. Wijmans CM, Smit B, Groot RD. Phase behavior of monomeric mixtures and polymer solutions with soft interaction potentials. *J Chem Phys* 2001, 114, 7644.
4. Povodyrev AA, Anisimov MA, Sengers JV. Crossover Flory model for phase separation in polymer solutions. *Physica A* 1999, 264, 345.

5. Hager JS, Anisimov MA, Sengers JV, Gorodetskii EE. Scaling of demixing curves and crossover from critical to tricritical behavior in polymer solutions. *J Chem Phys* 2002, 117, 5940.
6. Anisimov MA, Agayan VA, Gorodetskii EE. Scaling and crossover to tricriticality in polymer solutions. *JETP Lett* 2000, 72, 578.
7. Anisimov MA, Kostko AF, Sengers JV. Competition of mesoscales and crossover to tricriticality in polymer solutions. *Phys Rev E* 2002, 65, 051805.
8. Brannock GR, Paul DR, Phase behavior of ternary polymer blends composed of three miscible binaries. *Macromolecules* 1990, 23, 5240.
9. Li XF, Denn MM. Surface Effects on the Phase Separation of Binary Polymer Blends. *Ind Eng Chem Res* 2004, 43, 354.
10. Ezequiel R. Soulé, Julio Borrajo, Roberto JJ Williams, Thermodynamic Analysis of a Polymerization-Induced Phase Separation in Nanoparticle–Monomer–Polymer Blends. *Macromolecules* 2007, 40, 8082.
11. Horst R, Wolf BA. Calculation of the phase separation behavior of sheared polymer blends. *Macromolecules* 1992, 25, 5291.
12. Osaheni JA, Jenekhe SA. Efficient blue luminescence of a conjugated polymer exciplex. *Macromolecules* 1994, 27, 3.
13. Clarke N, McLeish TCB, Jenkins SD. Phase Behavior of Linear/Branched Polymer Blends. *Macromolecules* 1995, 28, 13.
14. Frank W, Altena CA. Smolders Calculation of liquid-liquid phase separation in a ternary system of a polymer in a mixture of a solvent and a nonsolvent. *Macromolecules* 1982, 15, 1491.
15. Daisuke Yamaguchi, Hirokazu Hasegawa, Takeji Hashimoto, A Phase Diagram for the Binary Blends of Nearly Symmetric Diblock Copolymers. 2. Parameter Space of Temperature and Blend Composition. *Macromolecules* 2001, 34, 6506.
16. Mumby SJ, Qian C, Eichinger BE. Phase diagrams of quasi-binary polymer systems with LCST/UCST spinodals and hour-glass cloud-point curves. *Polymer* 1992, 33, 5105.
17. Siow KS, Delmas G, Patterson D. Cloud-Point Curves in Polymer Solutions

with Adjacent Upper and Lower Critical Solution Temperatures. *Macromolecules* 1972, 5, 29.

18. Bergmann J, Kehlen H, Ratzsch MT. Critical states in spinodal points with several spinodal directions. *J Phys Chem* 1987, 91, 6567.

19. Riedl B, Prud'homme RE. The determination of the thermodynamic interaction parameter  $\chi$  in polymer blends. *Polym Eng Sci* 1984, 24, 1291.

20. Barth C, Horst R, Wolf BA. (Vapour + liquid) equilibria of (water + dimethylformamide): application of the headspace-gas chromatography for the determination of thermodynamic interactions. *J Chem Thermodynamics* 1998, 30, 641.

21. Horst R. Calculation of vapor pressures not requiring the derivatives of the energy of mixing. *Macromol Theory Simul* 1997, 6, 427.

22. Guggenheim EA, *Mixtures*, The Oxford University Press, Amen House, London, 1952, PP. 183-258.

23. Bawendi MG, Freed KF. Systematic corrections to Flory-Huggins theory: polymer-solvent-void systems and binary blend-void systems. *J Chem Phys* 1988, 88, 2741.

24. Dudowicz J, Freed KF, Madden WG. Role of molecular structure on the thermodynamic properties of melts, blends, and concentrated polymer solutions: comparison of Monte Carlo simulations with the cluster theory for the lattice model. *Macromolecules*, 1990, 23, 4803.

25. Wu You-Ting, Zhu Zi-Qiang, Lin Dong-Qiang, Mei Le-He, A modified NRTL equation for the calculation of phase equilibrium of polymer solutions. *Fluid Phase Equilibria* 1996, 121, 125.

26. Paul CW. Influence of Copolymer Configuration on the Phase Behavior of Ternary Blends. *J Phys Chem B* 2006, 110, 2541.

27. Ubrich JM, Ben Cheikh Larbi F, Halary JL, Monnerie L. Molecular weight effects on the phase diagram of polystyrene-poly(vinyl methyl ether) blends. *Macromolecules* 1986, 19, 810.

28. E. Helfand and Y. Tagami, Theory of the Interface between Immiscible

Polymers. II. J Chem Phys 1972, 56, 3592.

29. Broseta D, Fredrickson GH, Helfand E, Leibler L. Molecular weight and polydispersity effects at polymer-polymer interfaces. *Macromolecules* 1990, 23, 132.

30. Whitehouse C, Liu ML, Gao P. Cold extrusion and in situ formation of self-blends of UHMWPE: Part 1. Processability and thermal characterization. *Polymer* 1999, 40, 1421.

31. Michael rubinstein; Ralph H. Colby, *Polymer Physics*, Oxford University Press, 2003. p143.

32. Safronov AP, Adamova LV. Thermodynamics of dissolution of glassy polymers. *Polymer* 2002, 43, 2653.

## CHAPTER 8 Conclusions

Both computer simulation and experimental analysis are used here to investigate the structures and processing improvement of UHMWPE and its composites. The effects of NMWP on the morphologies and rheological behaviors of the UHMWPE blends have been studied and the viscosity reduction mechanism is proposed. The effects of initial configurations, temperatures and shear rates on the morphologies and properties of the UHMWPE/PP blends were studied by the applications of DPD and MesoDyn simulations. The complex intercalator of PEG/MDAB was used to modify MMT through ultrasonic irradiation. The influences of the OMMT (PM, MM and PMM) content on the phase morphology and properties of the UHMWPE/PP/OMMT blends were investigated. F-H theory is applied to investigate the unique thermodynamic properties of binary  $A/B$  polymer systems at the volume fraction  $\phi_A = 1 - 1/e$ . The main conclusions are stated as follows:

1. Adding HDPE or LDPE is much more efficient at disentangling the UHMWPE chains than PP. However, adding PP is much more efficient at reducing its viscosity than HDPE and LDPE, implying that when a normal molecular weight polymer (NMWP) is added, the formation of a lubricating layer between the UHMWPE particles leads to a significant decrease in viscosity. As the plasticating time increases, the viscosity of the UHMWPE/PP (50/50) blend decreases whereas that of the UHMWPE/LDPE (50/50) increases. This is because the former forms a two-phase structure while the latter a homogeneous one. Moreover, phase diagram is adopted here to investigate in detail the effects of the composition, the parameter  $\chi$ , molecular weight on the lubrication phase and the viscosity of blends. Results show that the optimum composition should be located in CSR of the blends for low shear rate, and above and close to the corresponding binodal curve for high shear rate. The phase diagram also shows that for a polymer blend with fixed parameter  $\chi$ , both the corresponding binodal and spinodal curves shift downwards with increasing  $N_1$ , which indicates that the increasing of molecular weight of NMWP in a certain range can make the blend easy to be phase separation and improve the processability of

blends. Besides, it is hoped that these results would also be proved suitable for researching the rheological behaviors on other ultra-high molecular weight polymer blends.

2. The investigations of the UHMWPE/PP blends based on DPD indicates that the UHMWPE/PP blend forms a homogeneous phase structure when the concentration of PP is below 10%; above that concentration, two-phase structures appear. In the latter cases, no UHMWPE is located in the PP-rich phase while a significant amount of PP is located in the UHMWPE-rich domains. This distribution favors disentanglement of UHMWPE molecules and prevents the viscosity increasing of the PP-rich phase.

3. On the bases of the studies on the effects of shear rates, it can be concluded that the evolution of the morphologies is very sensitive to shear rate within 0.005 – 0.5. For the UHMWPE/NMWPE/HMWPP/NMWPP blends with different compositions, it can be seen that both UHMWPE and HMWPP prefer to be in their own rich phases. Nevertheless, the other components are not only located in own rich phases, but also in the neighbor phases. The physical reason of the accumulation of small chains might be attributed to the fact that having more small chains at the interface has the effect of lowering the interfacial tension. Small chains in fact play a surfactant role.

4. DPD simulations suggest that with the absence of shearing PEG prefers to distribute in the UHMWPE phase regardless of variation of PP concentration in UHMWPE/PP/PEG blends. However, with the increasing of shear flow, PEG phase translates preferably from UHMWPE phase to PP phase. This probably is attributed to two reasons: (I) Flory–Huggins parameters dominate the location of PEG at a low shear rates; (II) the obviously closer viscosity of PEG to that of PP than that of UHMWPE forms the main factor at a high shear rates.

5. The concept of the wetting coefficient confirms that in the extrusion of the UHMWPE/PP/MP system, PEG molecules still covered on OMMT layers, instead of being replaced by PP or UHMWPE molecules. Hence, an encapsulation structure of MP was finally found in the UHMWPE/PP/MP composites. MMT layers are located between the UHMWPE particles and are parallel with the surface of the UHMWPE particles.

6. The WAXD analysis and TEM observation clearly indicate the formation of exfoliated and better intercalated structure for the UHMWPE/PP/PMM composites.

The structure of PMM in the matrix is probably attributed to the synergistic effects of the complex intercalator (PEG/MDAB) on the intercalation and exfoliation for MMT. The addition of a small amount of PMM has been found able to reduce the melt viscosity of UHMWPE/PP (90/10) blend significantly. The UHMWPE nanocomposites exhibit remarkable improvement of mechanical properties such as tensile strengths, elongation at break and yield strength compared with the matrix without clay. The dispersed PMM particles exhibited a comparatively large two-dimensional aspect ratio, which played an important role in determining the enhancement of mechanical properties of UHMWPE composites.

7. The calculated results binary  $A/B$  polymer systems based on both the SCFT and F-H theory indicate that many thermodynamic properties, such as free energy of mixing, interfacial tension and the interface thickness, are insensitive to  $N_B$  when  $N_B$  is large enough. Consider a polymer blend with  $N_A = 250$  and  $\chi = 0.009$ . When  $N_B > 6620$ , which corresponds to molecular weight of  $1.4 \times 10^6$  for PE,  $C_R(N_B)$  will be less than 1%. If 1% is considered to be in the error, the effect of the variation of  $N_B$  on the interfacial tension of the blend may be neglected for  $N_B > 6620$ .

8. For binary polymer systems with a given polymer  $A$  and fixed  $\chi$ , exchange chemical potential curves all pass through a common point and the corresponding volume fraction is  $\phi_A = 1-1/e$  ( $\approx 0.63$ ), whatever the value of  $N_B$ , implying that the exchange chemical potentials at  $\phi_A = 1-1/e$  are independent of  $N_B$ . Moreover, as  $N_B$  decreases the minimum free energy of mixing monotonously decreases and the  $\phi_{Am}$  asymptotically approaches  $\phi_A = 1-1/e$  if  $\chi N_A \neq 2.05$  or is located at  $\phi_A = 1-1/e$  if  $\chi N_A = 2.05$  and  $\chi N_B < 2.65$ . This indicates that the  $\phi_{Am}$  for a polymer solution with a good solvent is close to  $1-1/e$ . It is also worth noting that  $\mu_c$  is crucially dependent on the value of  $\chi N_A$ . More specifically, if  $\chi N_A$  is less than, equal to, or greater than 2.05, the corresponding  $\mu$  is positive, zero and negative, respectively.

AUTORISATION DE SOUTENANCE DE THESE  
DU DOCTORAT DE L'INSTITUT NATIONAL  
POLYTECHNIQUE DE LORRAINE

o0o

VU LES RAPPORTS ETABLIS PAR :

**Monsieur Christian CARROT, Professeur, Université Jean Monnet, Saint Etienne**

**Monsieur Hong-Lai LIU, Professeur, University of Science and Technology, Shanghai, Chine**

Le Président de l'Institut National Polytechnique de Lorraine, autorise :

**Monsieur GAI Jing-Gang**

à soutenir devant un jury de l'INSTITUT NATIONAL POLYTECHNIQUE DE LORRAINE,  
une thèse intitulée :

**"Etudes théoriques et expérimentales de la processabilité du polyéthylène à ultra-haute  
masse molaire"**

en vue de l'obtention du titre de :

DOCTEUR DE L'INSTITUT NATIONAL POLYTECHNIQUE DE LORRAINE

Spécialité : « **Génie des Procédés et des Produits** »

Fait à Vandoeuvre, le 26 juin 2009

Le Président de l'I.N.P.L.

F. LAURENT



NANCY BRABOIS  
2, AVENUE DE LA  
FORET-DE-HAYE  
BOITE POSTALE 3  
F - 5 4 5 0 1  
VANDŒUVRE CEDEX

## **TITRE**

Simulation par CFD et mesure en ligne de la distribution des temps de séjour et la qualité de mélange dans une extrudeuse bi-vis

## **RESUME**

Aujourd'hui le développement de nouveaux matériaux polymères ayant de bonnes propriétés repose de plus en plus sur des procédés de mélange ou de compoundage de polymères au lieu de recourir à la synthèse de nouvelles molécules. L'action du mélange peut fortement influencer sur la morphologie des matériaux polymères multi-constituants. Les extrudeuses bi-vis (TSE) sont souvent utilisées comme mélangeurs/réacteurs pour des procédés de mélange, de compoundage et d'extrusion réactive. Cependant, l'étude sur la qualité du mélange dans les TSE demeure un grand défi en raison de la complexité géométrique et du caractère transitoire de l'écoulement. Cette thèse a pour objet de développer un nouvel instrument en ligne pour mesurer en temps réel la distribution des temps de séjour (DTS) qui caractérise la performance du mélange axial et la capacité de convoyage de différents types d'éléments de vis basées sur l'analyse de l'écoulement transitoire et l'évaluation systématique de la théorie de mélange dans les TSE. Le mélange distributif des polymères fondus est caractérisé par la génération de l'aire des interfaces, un paramètre difficile à mesurer expérimentalement. Alors on fait appel à des simulations numériques de type CFD.

## **MOTS-CLES**

CFD ; extrudeuse bi-vis ; distribution des temps de séjour ; qualité du mélange.

## **TITLE**

CFD simulation and online measurement of the residence time distribution and mixing in twin screw extruders

## **ABSTRACT**

The development of new materials with improved properties seems to rely nowadays more on blending and compounding than on the synthesis of chemically new polymers. Mixing may have a great effect on the morphology and structure of multi-component polymer materials. Twin-screw extruders (TSE) are widely used as mixers/reactors for blending, compounding, and reactive processing. This work aimed at developing a new instrument to measure in real time the residence time distribution (RTD) which characterizes the axial mixing and transport abilities of different screw elements based on the analysis of the transient flow pattern and systematic evaluation of mixing theory in TSE. Distributive mixing of polymer melts is characterized by the generation of interfacial area, which is experimentally much more difficult to measure. This 3D numerical simulation based on CFD is adopted.

## **KEY WORDS**

CFD; twin screw extruder; residence time distribution; mixing.